Inverted Coaxial Detectors for Legend

Modeling and characterization for the search of neutrinoless double beta decay

Tommaso Comellato

Technische Universität München

Fakultät für Physik

**Inverted Coaxial Detectors for Legend -
Modeling and characterization for the search of neutrinoless double beta
decay**

Tommaso Comellato

Vollständiger Abdruck der von der Fakultät für Physik der Technischen Universität München zur Erlangung des akademischen Grades eines

Doktors der Naturwissenschaften (Dr. rer. nat.)

genehmigten Dissertation.

Vorsitzender:	Prof. Dr. Alejandro Ibarra
Prüfer der Dissertation:	1. Prof. Dr. Stefan Schönert
	2. Hon.-Prof. Dr. Allen Caldwell

Die Dissertation wurde am 29.06.2022 bei der Technischen Universität München eingereicht und durch die Fakultät für Physik am 27.07.2022 angenommen.

A Grazia, Giovanni e Mosè
...e tutta la squadra

ABSTRACT

The hypothesis of the existence of the neutrino was raised to explain the energy spectrum of β-decay. Once again, a nuclear transition could shed light on the nature of this elusive particle: the simultaneous β-decay of two neutrons inside a nucleus without accompanying neutrinos. This transition has been called *neutrinoless double beta decay (0νββ)* and, if observed, would determine that neutrinos are Majorana particles, i.e. they are indistinguishable from antineutrinos.

The Germanium Detector Array (GERDA) experiment has searched for this nuclear transition in ^{76}Ge, by operating bare high purity germanium (HPGe) detectors in a liquid argon (LAr) bath, which was instrumented as an active shield. After fulfilling all the design goals in a decade of operation, GERDA ended its experimental program and stopped the data taking in November 2019. With the lowest background level in the field, it achieved operation in the background-free regime, thus allowing to explore half-life sensitivities above 10^{26} yr with *only* 44.2 kg of high purity germanium (HPGe) detectors enriched in ^{76}Ge. The Large Enriched Germanium Experiment for Neutrinoless double beta Decay (LEGEND) experiment will take over the search with a factor of 5 more isotope mass, in its first stage. Its baseline detector geometry is the inverted coaxial (IC): these detectors have the same electrode structure as the broad energy germanium (BEGe) detectors of GERDA, but have masses which are a factor 3 higher. This gives a similar factor in the reduction of the dead material (cables, holders, electronics) deployed in the setup to instrument the detectors, which is a known source of background.

This dissertation accompanied the transition of this geometry from being a *prototype* to baseline design for LEGEND. With an extensive modeling campaign, it has been shown that the collective motion of the charge carriers in a cluster creates features on the pulse shape which were not observed in other geometries. Such modeling allowed to evaluate the tagging efficiency of 0νββ events for the standard event discrimination technique in IC detectors with high accuracy.

The experimental characterization campaign of a prototype IC detector proved that this geometry exhibits excellent performances in terms of energy resolution (2.1 keV full width at half maximum (FWHM) at 2 MeV), charge collection and pulse shape discrimination (PSD). Their values are competitive with the best detectors from the previous generation. Thanks to these encouraging results, five IC detectors of ~2 kg each have been produced from material enriched to 88% in ^{76}Ge, for future use in LEGEND.

Their performance in the vendor's cryostat have been tested comparable to the prototype in all the investigated fields. To benchmark their behavior in LAr, they have been deployed in the GERDA apparatus, where they accumulated an exposure of $8.5\,\mathrm{kg \cdot yr}$ in one year of operation. They proved a remarkable stability in the energy scale and PSD parameters. The energy resolution in the GERDA setup was 2.76–3.00 keV FWHM at 2 MeV and their PSD performances exceeded those of most BEGes. With a background level of $(4.9^{+7.3}_{-3.4}) \cdot 10^{-4}$ cts/(keV $\cdot$ kg $\cdot$ yr), they contributed to keep GERDA operating in the background-free regime and thus to set the limit on the half-life of $0\nu\beta\beta$ to $T_{1/2}^{0\nu\beta\beta} > 1.8 \cdot 10^{26}$ yr at 90% C.L..

ZUSAMMENFASSUNG

Die Hypothese der Existenz des Neutrinos wurde aufgestellt, um das Energiespektrum des β-Zerfalls zu erklären. Wieder einmal könnte ein nuklearer Übergang Licht auf die Natur dieses schwer fassbaren Teilchens werfen: der gleichzeitige β-Zerfall von zwei Neutronen innerhalb eines Kerns ohne begleitende Neutrinos. Dieser Übergang wird als *neutrinoless double beta decay (0νββ)* bezeichnet und würde, wenn er observiert wird, zeigen, dass Neutrinos Majorana-Teilchen sind, d. h. sie sind nicht von Antineutrinos zu unterscheiden.

Das Germanium Detector Array (GERDA)-Experiment hat nach diesem Kernübergang in ^{76}Ge gesucht, indem nackte high purity germanium (HPGe)-Detektoren in einem liquid argon (LAr)-Bad betrieben wurden, das als aktiver Schild instrumentiert war. Nachdem GERDA in einem Jahrzehnt des Betriebs alle Planungsziele erfüllt hatte, beendete es sein experimentelles Programm und stellte die Datenaufnahme im November 2019 ein. Mit dem niedrigsten Hintergrundniveau im Feld erreichte es den Betrieb im hintergrundfreien Bereich und ermöglichte so die Erforschung von Halbwertszeiten über 10^{26} yr mit *nur* 44.2 kg von high purity germanium (HPGe) Detektoren, die mit ^{76}Ge angereichert sind. Das Experiment Large Enriched Germanium Experiment for Neutrinoless double beta Decay (LEGEND) wird in seiner ersten Phase die Suche mit einem Faktor von 5 mehr Isotopenmasse übernehmen. Seine Basisdetektorgeometrie ist die des inverted coaxial (IC): Diese Detektoren haben die gleiche Elektrodenstruktur wie die broad energy germanium (BEGe)-Detektoren von GERDA, haben aber um einen Faktor 3 höhere Massen. Dies führt zu einem ähnlichen Faktor bei der Verringerung des toten Materials (Kabel, Halterungen, Elektronik), das im Aufbau zur Instrumentierung der Detektoren eingesetzt wird und das eine bekannte Quelle für den Hintergrund ist.

Diese Dissertation begleitete den Übergang dieser Geometrie von einem Prototyp zu einem Basisdesign für LEGEND. Mit einer umfangreichen Modellierungskampagne wurde gezeigt, dass die kollektive Bewegung der Ladungsträger in einem Cluster Merkmale der Pulsform erzeugt, die in anderen Geometrien nicht beobachtet wurden. Diese Modellierung ermöglichte die Bewertung der Tagging-Effizienz von 0νββ-Ereignissen für die Standard-Ereignisunterscheidungstechnik in IC-Detektoren mit hoher Ganauigkeit.

Die experimentelle Charakterisierungskampagne eines Prototyps eines IC-Detektors hat gezeigt, dass diese Geometrie hervorragende Leistun-

gen in Bezug auf Energieauflösung (2.1 keV full width at half maximum (FWHM) bei 2 MeV), Ladungssammlung und pulse shape discrimination (PSD) aufweist. Diese Werte sind konkurrenzfähig mit den besten Detektoren der vorherigen Generation. Dank dieser ermutigenden Ergebnisse wurden fünf IC-Detektoren von jeweils ~2 kg aus mit 88% an ^{76}Ge angereichertem Material für den künftigen Einsatz in LEGEND hergestellt. Ihre Leistung im Kryostat des Herstellers wurde in allen untersuchten Bereichen vergleichbar mit dem Prototyp getestet. Um ihr Verhalten in LAr zu bewerten, wurden sie in der GERDA-Apparatur eingesetzt, wo sie in einem Betriebsjahr eine Exposition von 8.5 kg · yr erreichten. Sie bewiesen eine bemerkenswerte Stabilität der Energieskala und der PSD-Parameter. Die Energieauflösung im GERDA-Aufbau betrug 2.76–3.00 keV FWHM bei 2 MeV und ihre PSD Leistungen übertrafen die der meisten BEGes. Bei einem Hintergrundpegel von $(4.9^{+7.3}_{-3.4}) \cdot 10^{-4}$ cts/(keV · kg · yr), trugen sie dazu bei, GERDA im untergrundfreien Bereich zu halten und damit die Grenze der Halbwertszeit von $0\nu\beta\beta$ auf $T^{0\nu\beta\beta}_{1/2} > 1.8 \cdot 10^{26}$ yr bei 90% C.L. zu setzen.

CONTENTS

LIST OF ABBREVIATIONS

PARTICLE/NUCLEAR PHYSICS:

$0\gamma e^+ e^-$ pair-production with double escaping gammas

$0\nu\beta\beta$ neutrinoless double beta decay

$2\nu\beta\beta$ two neutrino double beta decay

$\beta\beta$ double beta

EC electron capture

BSM beyond the Standard Model

CC Compton Continuum

DEP double escape peak

FEP full energy peak

IO inverted ordering

NME nuclear matrix element

NO normal ordering

NSM nuclear shell model

PMNS Pontecorvo-Maki-Nakagawa-Sakata

SEP single escape peak

GERMANIUM RELATED:

BEGe broad energy germanium

HPGe high purity germanium

IC inverted coaxial

ICaro inverted coaxial application for rare observations

LD low depleted

MSE multi-site event

PPC p-type point contact

PSA pulse shape analysis

PSD pulse shape discrimination

SAGe small anode germanium

SP survival probability

SSE single-site event

EXPERIMENTS:

Gerda Germanium Detector Array

Legend Large Enriched Germanium Experiment for Neutrinoless double beta Decay

MJD Majorana Demonstrator

CUORE Cryogenic Underground Observatory for Rare Events

CUPID CUORE Upgrade with Particle IDentification

EXO Enriched Xenon Observatory

HdM Heidelberg-Moscow

IGEX International Germanium Experiment

KamLAND-Zen KamLAND - Zero Neutrino double beta decay search

KATRIN Karlsruhe Tritium Neutrino Experiment

NEMO Neutrino Ettore Majorana Observatory

nEXO next-generation Enriched Xenon Observatory

SNO Sudbury Neutrino Observatory

LABORATORIES:

HADES High Activity Disposal Experimental Site

HEROICA Hades Experimental Research Of Intrinsic Crystal Appliances

HZDR Helmholtz-Zentrum Dresden-Roßendorf

LNGS Laboratori Nazionali del Gran Sasso

MPIK Max Planck Institut für Kernphysik

TUM Technical University of Munich

GERDA–SPECIFIC:

AC detector anti-coincidence

BI background index

SOFTWARE / CODE:

GEANT4 GEometry ANd Tracking

BAT Bayesian Analysis Toolkit

MaGe Majorana-Gerda

MISCELLANEOUS:

ROI region of interest

BSI Baltic Scientific Instruments

cps counts per second

DAQ data acquisition

DSP digital signal processing

FADC flash analog-to-digital converter

FWHM full width at half maximum

HV high voltage

LAr liquid argon

LMFE low mass front-end electronics

LN$_2$ liquid nitrogen

MCA Multi-Channel Analyzer

PEN polyethylene naphtalate

PMT photomultiplier tube

SiPM silicon photomultiplier

TPB tetraphenyl butadiene

TPC time projection chamber

VME VERSABUS Module Eurocard

WLS wavelength-shifting

WLSR wavelength-shifting reflector

Part I

THEORETICAL AND EXPERIMENTAL BACKGROUND
ON DOUBLE-BETA DECAY

1 | A NUCLEAR DECAY FOR PARTICLE PHYSICS

Our understanding of the physics of neutrinos followed a tortuous history, where *accidental* discoveries boosted to the development of robust theoretical infrastructures. Over time, the theories have somehow adapted and merged to build a uniform description of all the forces of nature (but gravity), which we now call the Standard Model of particle physics. This has proven to be robust in both explaining experimental phenomena, as well as predicting not yet observed ones. As physics milestones piled up on its shoulders, the room once occupied by accidental discoveries has been filled by decade-long experimental efforts aimed at observing phenomena which could provide evidence of beyond the Standard Model (BSM) physics. An important evidence of physics BSM would be the observation of the simultaneous beta-decay of two neutrons inside a nucleus without accompanying neutrinos: this has been called *neutrinoless double beta decay ($0\nu\beta\beta$)* for decades and, if observed, would imply that neutrinos and antineutrinos are the same particle. In addition, it would be the first experimental evidence that processes creating matter without producing anti-matter do exist in nature.

In this chapter, the present knowledge of the neutrino physics will be briefly reviewed. In particular, key concepts will be provided to understand the implications that an observation of $0\nu\beta\beta$ would have on particle physics. The status, at the time of writing, of the worldwide experimental effort in its search will also be presented, together with considerations on how its observation might contribute to the determination of the absolute neutrino mass scale.

1.1 INTRODUCING NEUTRINOS

Neutrinos were first hypothesized in 1930 by Pauli, as a remedy to preserve energy conservation in beta-decays, and then put into the rigorous formalism of weak interactions by Fermi in 1933 [1]. Although both Pauli and Fermi considered neutrinos so elusive that no experiment could ever reach a detection, the first free neutrino was detected in 1956 by Cowan and Reines [2, 3] through inverse beta-decay. Thanks to the advancements of accelerators and detectors, we now know that those detected by Cowan and Reines were electron neutrinos, ν_e, and that in general neutrinos come in three varieties, called *flavours*, one for each family of quarks and leptons: ν_e, ν_μ and

ν_τ [4–6]. Considered to be massless for more than 50 years, neutrinos are nowadays known to have a tiny mass, though neither the exact value nor the theoretical mechanism which generates it has been determined, yet.

1.2 MASSIVE NEUTRINOS

All the fundamental particles in the standard model are spin 1/2 particles and their dynamics is described by the Dirac theory of fermions [7, 8], extended by the work of Feynman and Gell-Mann [9]. In this context, mass terms appear in the lagrangian $\mathcal{L}_D$ in the form:

$$\mathcal{L}_D^{mass} = M_D \overline{\psi}\psi = M_D(\overline{\psi}_L \psi_R + \overline{\psi}_R \psi_L) \tag{1.1}$$

The Standard Model does not predict a mass for neutrinos

where M_D is called a Dirac mass, the field operators $\psi_{L,R}$ and $\overline{\psi}_{L,R}$ respectively annihilate and create a fermion with left- or right-chirality. A mass term of the type of Equation 1.1 requires the existence of fermions of both left and right chirality, which is experimentally verified for all charged fermions. In the neutrino sector, however, a right-handed neutrino has not been detected (yet), and it would be a particle which does not interact through any force described in the standard model. It was also for this reason that neutrinos have been considered massless for several decades.

However, from a fundamental point of view, the masslessness of the neutrino does not have solid bases. Photons and gluons, the only massless particles in the standard model, cannot be massive because terms of the type of Equation 1.1 would violate the gauge symmetry which governs the whole dynamics of the interactions of bosons with fermions. No such a fundamental symmetry requests a zero value for the neutrino mass.

Oscillation experiments proved neutrinos to be massive

Indeed, oscillation experiments starting at the end of the millennium [10–18] showed that the (flavour) neutrinos ν_α detected in correspondence to a lepton $\alpha = e, \mu, \tau$ are superpositions of states with non-vanishing physical masses, hence called mass eigenstates ν_i. In formulas:

$$\nu_\alpha = \sum_{i=1}^{3} U_{\alpha i} \nu_i \tag{1.2}$$

where the index α indicates the lepton families ($\alpha = e, \mu, \tau$), i runs over 3 mass eigenstates ν_i with definite mass m_i and $U_{\alpha i}$ is a unitary matrix, called the Pontecorvo-Maki-Nakagawa-Sakata (PMNS) matrix, whose elements are the probability amplitude for a ν_α to be in the stationary state ν_i. This proved neutrinos to have mass and was the first evidence of physics BSM.

As can be easily proved, oscillation experiments are not directly sensitive to the values of the neutrino masses, but rather to their (squared) difference

$\Delta m_{ij}^2 = m_i^2 - m_j^2$. Also, while the sign of Δm_{12}^2 has been determined from solar neutrinos, that of Δm_{32}^2 has not, yet. For these reasons, neither the mass eigenvalues nor their ordering are currently known: with the present knowledge, their values could be ordered both as $m_1 < m_2 < m_3$, which is normally referred to as *normal ordering (NO)*, and as $m_3 < m_1 < m_2$, called *inverted ordering (IO)*.

1.3 DIRAC OR MAJORANA NEUTRINOS?

Being electrically neutral, a neutrino can be distinguished from an antineutrino only by its lepton number L. It is known, however, that the global $U(1)$ symmetry which gives the conservation of L is *accidental*, meaning that it does not rule the dynamics of fermions and is rather a *consequence* of the dynamics and the field contents of the standard model. In other words, there is no fundamental reason why the neutrino and the antineutrino should not be exactly the same particle. As this was first pointed out by E. Majorana in [19], we talk in this case of *Majorana* particles.

Whether neutrinos are Majorana or Dirac particles, like all other fermions, is still an unanswered question, which could be clarified by experiments looking for processes violating the conservation of lepton number, like $0\nu\beta\beta$, as we shall see in Section 1.4.2. If observed, they would reveal the Majorana nature of neutrinos.

In either case, a mass term for neutrinos can be accounted for with minimal extensions in the fermionic sector of the Standard Model. We shall see in the following sections how this is done for Dirac (Section 1.3.1) and Majorana (Section 1.3.2) neutrinos. For the sake of completeness, one could account for a neutrino mass also by extending the Higgs sector, though this won't be discussed in this dissertation, and we refer to [20] for further clarifications.

1.3.1 Dirac neutrinos

The standard model contains left and right chiral projections of all fermions, except the neutrino. A minimal extension would then be to let the neutrino be a Dirac particle like other fermions and add right-handed neutrinos in the game. In this scenario, spontaneuos symmetry breaking would give rise to the Dirac mass term of Equation 1.1.

A Dirac neutrino would be a particle like all other fermions...

Despite its simplicity, in the sense that it treats the neutrino masses in the same way as other fermions, this model does not give any information on the Yukawa coupling included in the mass matrix M_D. Specifically, there is

...though with unnaturally small Yukawa coupling

no physical reasons why the elements in M_D should be orders of magnitude lower than for the other fermions of the same family.

1.3.2 Majorana neutrinos

A Majorana neutrino is equal to an antineutrino

In 1937 Majorana opened up the possibility for neutrinos to be their own anti-particles [19]. He showed that, with a proper choice for the γ matrices of the Dirac equation, a neutrino field ψ could be costructed, which is equal to its charge conjugated $\hat{\psi}$. Moreover, considering the chiral projections, he showed that the charge conjugate of a left (right) field is right (left), allowing to build non-zero mass terms of the type:

$$\mathcal{L}_{MB}^{mass} = M_B(\overline{\hat{\psi}}_R \psi_R + \overline{\psi}_R \hat{\psi}_R) \tag{1.3}$$

Although these terms obviously violate $U(1)_L$, there is no fundamental principle which should prevent it, for electrically neutral particles. Charged fermions, conversely, cannot have terms such as in Equation 1.3, as this would violate the conservation of electric charge. Neutrons, as explicitly pointed out by Racah [21], cannot be Majorana particles, as the evidence of a neutron magnetic moment prevents the construction of a field ψ which satisfies the Majorana formalism. Also, from the experimental point of view, Majorana neutrons could decay to anti-protons through β^+ with the same probability as they decay β^- to protons, which is not observed.

The see-saw mechanism

An important consequence of this scenario is that it can provide a reason for the smallness of the neutrino mass, as we shall now see. In the most general case, the lagrangian can have both a Dirac and a Majorana mass term:

$$\mathcal{L}^{mass} = \mathcal{L}_{MD}^{mass} + \mathcal{L}_{MB}^{mass} \tag{1.4}$$

Of course, writing such mass terms implies the existence of a right-handed neutrino. Equation 1.4 can be re-written in matrix form (here in the simplified case of 1 generation of leptons, so that the mass terms M are 1-dimensional scalars):

$$\mathcal{L}^{mass} = \begin{pmatrix} \overline{\hat{\psi}}_L & \overline{\psi}_R \end{pmatrix} \begin{pmatrix} 0 & M_D/2 \\ M_D/2 & M_B \end{pmatrix} \begin{pmatrix} \psi_L \\ \hat{\psi}_R \end{pmatrix} + \text{h.c.} \tag{1.5}$$

From Equation 1.5 the physical masses of neutrinos can be found by diagonalizing the central matrix. It can be easily found that the resulting eigenvalues are:

$$m_{1,2} = \frac{1}{2}\left(M_B \pm \sqrt{M_B^2 + 4 \cdot M_D^2}\right) \tag{1.6}$$

If we now recall that M_D comes from the Yukawa coupling, it is natural to assume that it is of the same order as for the other fermion in the same gene-

ration. Conversely, no constraints apply on M_B, which could be arbitrarily large. Assuming $M_B \gg M_D$, the eigenvalues of the matrix of Equation 1.6 are:

$$m_1 \simeq M_D^2/M_B \qquad m_2 \simeq M_B \qquad (1.7)$$

This gives the desirable property that $m_1 \ll M_D$, which means that the neutrino mass is much smaller than the mass of the fermions of the same generation, without any fine-tuning on the Yukawa coupling. On the other hand, to accomplish this goal, the introduction of a heavy right-handed neutrino is necessary. This mechanism of making one particle light at the expense of creating another heavy one is called the *see-saw mechanism* [22, 23].

1.4 DOUBLE BETA DECAY AND THE CREATION OF MATTER

1.4.1 Double beta decay

All radioactive decays proceed towards final states which are more tightly bound than the initial states. So is the case for the standard β^- decay, where a neutron turns into a proton via the emission of an electron and an antineutrino. The process for a nucleus N with mass number A and atomic number Z reads:

$$N(A, Z) \rightarrow N(A, Z+1) + e^- + \bar{\nu}_e \qquad (1.8)$$
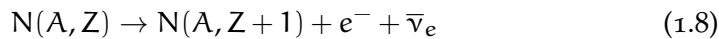
In this way, β-decaying nuclei move on isobars towards a minimum in the energy. In the case where the mass number A is even, a particular pattern appears for the isobars, which is shown in Figure 1.1 for nuclei with $A = 76$. Due to the peculiar stability of α-particles [24], nuclei with even-even number of protons-neutrons are more stable than those with an odd-odd number, so that the formers are distributed on a curve which is lower than the curve for the latter by a roughly constant amount. In this configuration, β-decay marks the passage between one curve and the other, in the direction of the minimum in the energy. In particular cases, such as the one shown in Figure 1.1 for ^{76}Ge, (all possible cases are listed in [25]), single β-decay is energetically forbidden[1], so the run towards the minimum can proceed only if two simultaneous β-decays occur. For an initial nucleus N with mass number A and atomic number Z, it reads:

$$N(A, Z) \rightarrow N(A, Z+2) + 2e^- + 2\bar{\nu}_e \qquad (1.9)$$

---
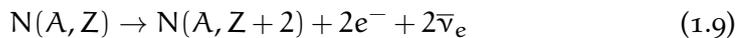
1 This is not always the case. Single beta decay can also be strongly suppressed by a large difference of angular momentum between mother and daughter nuclei [26].
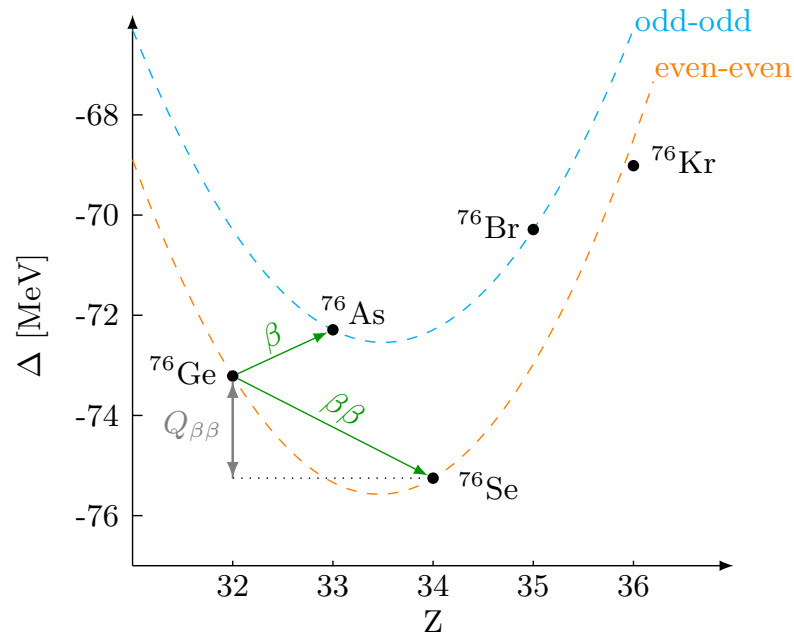
Figure 1.1: Mass excess $\Delta = (m_A - A) * u$ for nuclei with mass m_A and mass number $A = 76$, with u being the atomic mass unit. Taken from [28].

with a Q-value which ranges between 1 and 4 MeV according to the isotope. Goeppert-Mayer was the first to conceive such a process and calculated the theoretical rate in 1935 [27]. She first named it *double beta-disintegration* and is now commonly referred to as *two neutrino double beta decay (2νββ)*. Its Feynman diagram is shown on the left side of Figure 1.2. Being a second-order weak process, its half-life is extremely long, ranging from 10^{17} to 10^{24} years according to the double-beta isotope. For this reason, the first direct detection had to wait almost 50 years, until 1987, when Elliott et al. provided the first tracks of the two electrons from the double-beta decay of ^{82}Se in a time projection chamber (TPC) [29]. To date, double-beta decay has been measured with high precision in several isotopes, using different experimental techniques [30–35].

1.4.2 A particular double beta decay

As the reader might have already noticed, the theory of Majorana for neutrinos implies that in a single β-decay the emission of an electron can be accompanied by *either* a neutrino or an antineutrino. This was pointed out by Racah in 1937, who ventilated the hypothesis for (anti)neutrinos to induce inverse (β⁻) β⁺ decays [21]. A few years later, Furry combined this idea with the double disintegration of Goeppert-Mayer and conceived a particular double-beta decay "in which only the two charged particles are emitted,

a)

b)
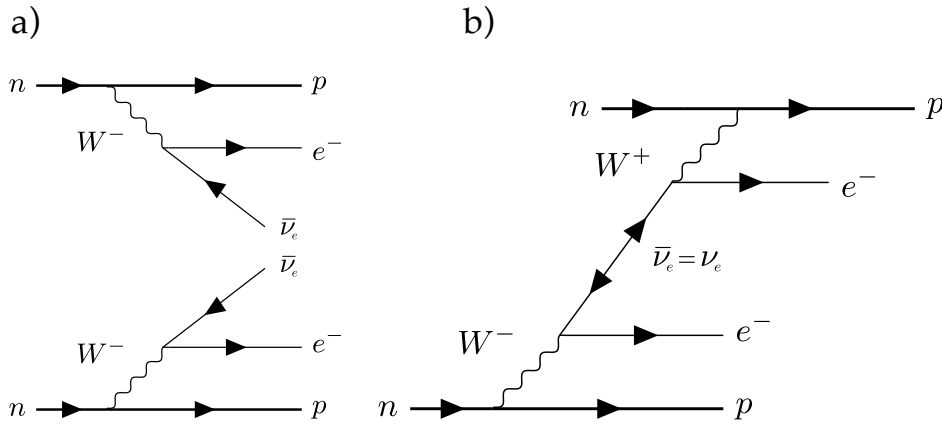
Figure 1.2: Feynman diagrams for a) $2\nu\beta\beta$ and b) $0\nu\beta\beta$ as emission and absorption of a Majorana neutrino, as it was first conceived.

unaccompanied by neutrinos" [36]. Keeping the same description as above, the process reads:

$$N(A, Z) \rightarrow N(A, Z + 2) + 2e^-　　　　(1.10)$$

which is obsviously the same as 1.9, with the exception that no antineutrinos are emitted. It was originally considered as an emission and absorption of a neutrino, made possible by its Majorana nature, as shown in Figure 1.2. For its similarity with Equation 1.9, with an unfortunate choice for the naming, it was later called *neutrinoless double beta decay (0\nu\beta\beta)*. As Equation 1.10 suggests, and as a consequence of the Majorana theory for neutrinos, it violates lepton number by two units: it creates matter particles, without compensation of anti-matter. Building on this idea, in the last years there has been a small (and rising) consensus among the scientific community to drop the formally correct name *neutrinoless double-beta decay* in favor of a more evocative *creation of matter* [28]. The interesting (and somewhat provocative) argument used in [28] is that, as we don't define a hippo as a "trunkless elephant", we should not describe Equation 1.10 for being "neutrinoless".

The spectra of the summed energy of the 2 electrons from the processes of Equation 1.9 and Equation 1.10 are shown in Figure 1.3. As a consequence of the kinematics, the $2\nu\beta\beta$ spectrum is continuous from 0 to the full $Q_{\beta\beta}$-value, and peaks at $Q_{\beta\beta}$ for $0\nu\beta\beta$.

Given the much larger parameter space available for the electrons compared to the $2\nu\beta\beta$ case, $0\nu\beta\beta$ was originally considered to proceed with much shorter half-lives. However, after the discovery of the maximal variation of parity from Wu [38] and the consequent formulation of the $V - A$ nature of the weak interaction [9], it became clear that the process as simple as the one shown on the right side of Figure 1.2 could not proceed, as the massless virtual neutrino emitted in the first step always has the wrong helicity to interact with the second neutron and produce the second electron. Today we know that a mass term for the neutrino enables the transition to

Why $0\nu\beta\beta$ is suppressed
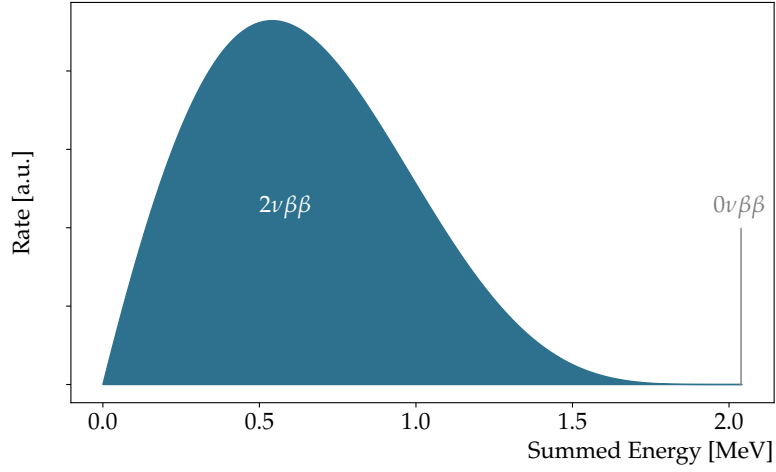
Figure 1.3: Spectrum on the summed energy of the two electrons emitted in $2\nu\beta\beta$ (blue) and $0\nu\beta\beta$ (grey). The energy shown here refers to the $Q_{\beta\beta} = 2039\,\text{keV}$ of ^{76}Ge. The ratio of the rates for the two processes is unknown. The analytical formula for $2\nu\beta\beta$ was taken from [37].

states with opposite helicity, whose probability is proportional to the square of this tiny mass, making $0\nu\beta\beta$ possible, though suppressed [39].

Rate of $0\nu\beta\beta$ with exchange of light neutrinos

As $0\nu\beta\beta$ violates lepton number, physics BSM is needed to describe the interaction. The minimal and most natural extension is to consider the process as mediated by the light neutrinos of which we have experience. The Feynman diagram for this case is shown in Figure 1.4. Using Fermi's Golden Rule, we can write the rate of the decay, which thus gets the form:

$$\Gamma^{0\nu} = \frac{\ln(2)}{T_{1/2}^{0\nu\beta\beta}} = G^{0\nu} \cdot g_A^4 \left|\mathcal{M}^{0\nu}\right|^2 \cdot \frac{m_{\beta\beta}^2}{m_e^2} \tag{1.11}$$

where $G^{0\nu}$ is the phase space factor, which can be calculated with high accuracy [40, 41], g_A is the weak axial vector coupling constant, m_e the mass of the electron and $\mathcal{M}^{0\nu}$ the nuclear matrix element (NME) for the decay, which is calculated considering the initial and final states, as well as the virtual states of the intermediate odd-odd nucleus; as the process has not been observed, $\mathcal{M}^{0\nu}$ can only be calculated. For the $0\nu\beta\beta$ isotopes, exact calculations are not feasible at the moment and different approximations and truncations are made, leading to results which differ of about a factor 2 to 3 [42]. The last term $m_{\beta\beta}$ is called the *effective Majorana neutrino mass*

$m_{\beta\beta}$ is the link between nuclear and neutrino physics

and it contains the information on the physics of the neutrinos, in the form of a coherent sum of the mass eigenvalues m_i and the mixing matrix U_{ei},
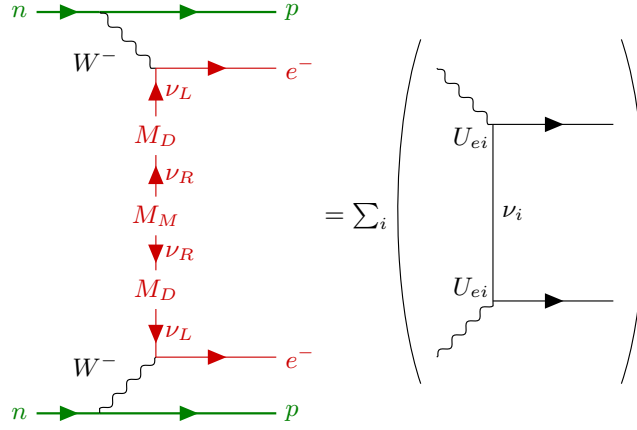
Figure 1.4: Complete Feynman diagram for $0\nu\beta\beta$ with light neutrino exchange. On the left, the mass mechanism is highlighted. A Majorana mass term M_M induces the non conservation of the leptonic current (in red) and a Dirac mass term M_D couples the left-handed neutrino ν_L to its right-handed counterpart ν_R. On the right, the mixing of the electron neutrino ν_e is explicit through the probability amplitude, in every vertex, of the neutrino eigenstate ν_i to couple to the electron, U_{ei}. Taken from [28].

which represents the probability amplitude that the virtual neutrino in the mass eigenstate ν_i couples to the electron. Explicitly:

$$m_{\beta\beta} = \left| \sum_{i=1}^{3} U_{ei}^2 m_i \right| = $$
$$= \left| |U_{e1}|^2 m_1 + |U_{e2}|^2 e^{2i\alpha} m_2 + |U_{e3}|^2 e^{2i\beta} m_3 \right| \tag{1.12}$$

The parameters $|U_{e1}|$, $|U_{e2}|$, and $|U_{e3}|$ are known from oscillation experiments, but no information is available for the phases α and β, called Majorana phases, which could in principle lead to (with some severe fine tuning) cancellation effects and make the observation of $0\nu\beta\beta$ impossible. Nevertheless, since the $|U_{ei}|$ are rather large (in the range of 0.8, 0.6 and 0.2, respectively for $i = 1, 2, 3$ [43]), Equation 1.11 and Equation 1.12 imply that a measurement of $0\nu\beta\beta$ gives information on the mass scale of neutrinos (in the assumption that the decay is mediated by a light neutrino exchange).

1.5 EXPERIMENTAL SEARCH FOR NEUTRINOLESS DOUBLE–BETA DECAY

As Equation 1.11 suggests, the higher the sensitivity of an experiment on $T_{1/2}^{0\nu\beta\beta}$ is, the smaller values of $m_{\beta\beta}$ can be probed. Following the discussion

on [44], we shall now briefly see how the experimental parameters contribute to push the sensitivity $S_{0\nu}$ on the half-life $T_{1/2}^{0\nu\beta\beta}$.

Let us now call n_s and n_b the expected number of signal and background events of a generic experiment with a live time t. The number of expected signal events n_s from a number N_0 of double-beta decaying nuclei with decay time $\tau = T_{1/2}^{0\nu\beta\beta}/\ln(2)$ is:

$$n_s = \epsilon\, N_0 \left(1 - e^{-t/\tau}\right) \simeq \epsilon\, N_0\, \frac{t \cdot \ln(2)}{T_{1/2}^{0\nu\beta\beta}} \qquad (1.13)$$

where ϵ the detection efficiency of the experimental setup, and the approximation leading to the last term in Equation 1.13 is allowed for $t \ll \tau$. The number of expected background events n_s is normally given in terms of the background index (BI), which is extracted from data and is often given in units of $\mathrm{cts}/(\mathrm{keV} \cdot \mathrm{kg} \cdot \mathrm{yr})$. With this quantity, the number of expected background events n_b in the energy region ΔE in the time t is:

$$n_b = BI \cdot \Delta E \cdot M \cdot t \qquad (1.14)$$

Background-free experiments   In the best-case-scenario, no background event is in the dataset and $n_b < 1$. The limit that can be placed in this case is given by the maximum signal rate that is consistent at some confidence level with zero observed events. In Poisson statistics, the probability of observing 0 events for expected n_s is:

$$P = e^{-n_s} \qquad (1.15)$$

Setting Equation 1.15 to be greater than a certain threshold P_0 (for instance 90%) implies that

$$n_s < -\ln(P_0) \qquad (1.16)$$

which is the limit for n_s at the confidence level set by P_0. This in turns gives the sensitivity on $T_{1/2}^{0\nu\beta\beta}$:

$$S_{0\nu} = \epsilon N_0 t \frac{\ln(2)}{-\ln(P_0)} \propto \epsilon \cdot Mt \qquad (1.17)$$

where in the last step we used the mass M of the decaying isotope instead of the number of nuclei N_0, as the quantity Mt, called *exposure* and given in $\mathrm{mol} \cdot \mathrm{yr}$, is often used in experiments searching for rare-events. Equation 1.17 is of particular importance for double-beta experiments as it says that, in case of no background, the sensitivity scales linearly with the exposure.

Experiments with background   The presence of background events makes the analysis more complicated. In the approximation of a gaussian distributed background ($\sigma_b \propto \sqrt{n_b}$), however, an analitical relation between the sensitivity and the exposure can also be found. In this approximation, the limit on the number of signal

events is set at the value determined by random fluctuations of the background:

$$n_s < \sigma_b = \sqrt{n_b} = \sqrt{BI \cdot \Delta E \cdot M \cdot t} \qquad (1.18)$$

which means that the sensitivity will be:

$$S_{0\nu} \propto \frac{\epsilon \cdot Mt}{\sqrt{BI \cdot \Delta E \cdot M \cdot t}} = \epsilon \sqrt{\frac{Mt}{BI \cdot \Delta E}} \qquad (1.19)$$

Compared to Equation 1.17, in case of background the sensitivity increases with the square root of the exposure, and is inversely proportional to the background level (through BI) and the energy range where the peak is searched for.

As it's clear from the general case of Equation 1.19, different approaches can be adopted to increase the sensitivity for the decay:

1. *High detection efficiency ϵ:* in most of the experiments, the detector is built out of the double-beta decaying isotope, thus maximizing the containment efficiency of the decay products

2. *High exposure* Mt*:* next-generation experiments will target exposures of 10^3–10^4 mol yr

3. *Excellent energy resolution:* as $Q_{\beta\beta} \pm 2\sigma$ contains 95% of the signal, small energy resolutions allow a peak search in narrow windows

4. *Low background index (BI):* the experimental goal is to reach the background-free regime in the region around $Q_{\beta\beta}$ (often referred to as the region of interest (ROI)), so that the sensitivity increases linearly with the exposure

As we shall see in Section 1.5.1, the experimental campaigns succeeded in setting the strongest limits on the half-life of $0\nu\beta\beta$ by targeting these challenges.

1.5.1 Double–beta experiments

A very complete and extensive description of the present status and future plans for $0\nu\beta\beta$ experiments has been recently presented in [28]. In the following we shall give an overview of the diverse technologies adopted in the global search, which presently includes:

- *Large liquid scintillators*

- *Time projection chambers*

- *Cryogenic calorimeters*

- *Tracking calorimeters*

- *Germanium detectors*

All of them, but tracking calorimeters, use the concept of coupling the source and the detector together to maximize the detection efficiency, either in the source=detector paradigm (as it is the case for Xenon TPCs, cryogenic calorimeters and germanium detectors), or by loading the $\beta\beta$-decaying isotope in a liquid scintillator.

LARGE LIQUID SCINTILLATORS   Liquid scintillators use photomultiplier tubes (PMTs) to measure the scintillation photons produced by any energy deposition within the medium to extract the energy, location and topology of the event. Liquid scintillators can be loaded with relative ease with isotopes which undergo double-beta decay, so high exposures can be reached without particular effort. That's the approach of the KamLAND - Zero Neutrino double beta decay search (KamLAND-Zen) and Sudbury Neutrino Observatory (SNO)+ experiments, looking for the $0\nu\beta\beta$ of ^{136}Xe and ^{130}Te, respectively [45, 46]. Despite their great scalability, liquid scintillators have energy resolutions $\mathcal{O}(100)$ keV at $Q_{\beta\beta}$, meaning that, in addition to potential environmental background, their ROI always includes a population of $2\nu\beta\beta$ events.

TIME PROJECTION CHAMBERS   A similar approach is to use Xe in a TPC. In this case, additionally to the scintillation light, the ionization products are also collected through a strong electric field, so that the topology of the event can be reconstructed with higher precision. The Enriched Xenon Observatory (EXO)-200 experiment has proved that the energy resolution in Xe TPCs can be as small as 30 keV [47], and could be even improved [48]. The next-generation Enriched Xenon Observatory (nEXO) experiment, the successor of EXO-200, plans to use 5 tons of liquid Xe enriched in ^{136}Xe, with a foreseen energy resolution of 20 keV at $Q_{\beta\beta}$ [49].

CRYOGENIC CALORIMETERS   The approach of cryogenic calorimeters, also called bolometers, is to operate crystals at a temperature of 10–20 mK and measure the heat induced by phonon recombination, which occurs after an energy deposition. The Cryogenic Underground Observatory for Rare Events (CUORE) experiment is presently taking data with crystals containing natural Te (i.e. with an abundance of 34% in the double-beta decaying ^{130}Te), and obtained an excellent energy resolution of 3.2 keV at $Q_{\beta\beta}$. Given an average mass of 0.2–0.8 kg per detector, experiments with bolometers are not easily scalable. Also, having 100% of sensitive volume, these detectors are very sensitive to α decays from the (many) open surfaces. However, using crystals with scintillating properties, like $ZnSe$ or Li_2MoO_4, the CUORE

Upgrade with Particle IDentification (CUPID)-0 and CUPID-Mo experiments showed that αs can be tagged and rejected with high efficiency [50, 51], opening the space for the future experiment CUPID, which plans to use 472 kg of Li_2MoO_4 enriched in ^{100}Mo [52].

TRACKING CALORIMETERS   Tracking calorimeters are the only experimental approach in which the source is completely decoupled from the detector. The source comes in thin foils, which are sandwiched in drift chambers, where a magnetic moment is applied to discriminate electrons and positrons, after which calorimeters are placed to measure the energy of the event. These experiments will probably never reach high exposures, but are those providing the biggest information on the kinematics of the decay products. Examples of this technology are the Neutrino Ettore Majorana Observatory (NEMO)-3 and Super-NEMO experiment, looking for the $0\nu\beta\beta$ of ^{100}Mo and ^{82}Se [53, 54].

GERMANIUM DETECTORS   Among the others, experiments with germanium detectors provide the best energy resolution, which is $\sigma = 1.1\,keV$ at $Q_{\beta\beta}$² [55]. The detectors are high purity germanium (HPGe) crystals, enriched in the double-beta decaying ^{76}Ge, with intrinsically low levels of radio-impurities [56]. Their use in combination with a surrounding scintillating liquid argon (LAr), which is the approach of the Germanium Detector Array (GERDA) experiment, has proven to be the most efficient technology in rejecting background events, indeed allowing to reach the lowest background levels in the field [57] and operate in the background-free scenario. After the successful results of GERDA and Majorana Demonstrator (MJD) [55], the Large Enriched Germanium Experiment for Neutrinoless double beta Decay (LEGEND) experiment [58, 59] is presently being commissioned at the Laboratori Nazionali del Gran Sasso (LNGS) in its first stage with 200 kg of detectors, while its second stage, with 1 t of enriched material, is already partly funded. More details on the GERDA and LEGEND experiments will be given in Chapter 2.

1.6   NEUTRINO MASS ABSOLUTE SCALE

We have seen in Section 1.4.2 that, in the assumption of light neutrino exchange, the observation of $0\nu\beta\beta$ provides information on the neutrino mass eigenvalues, through $m_{\beta\beta}$. The value of $m_{\beta\beta}$ is normally given in combination with the other experimental mass observables, coming from kinematic

---

2 In gamma spectroscopy, the resolution is commonly given in full width at half maximum (FWHM), which is a factor 2.35 higher than the σ of the normal distribution fitting the peak.
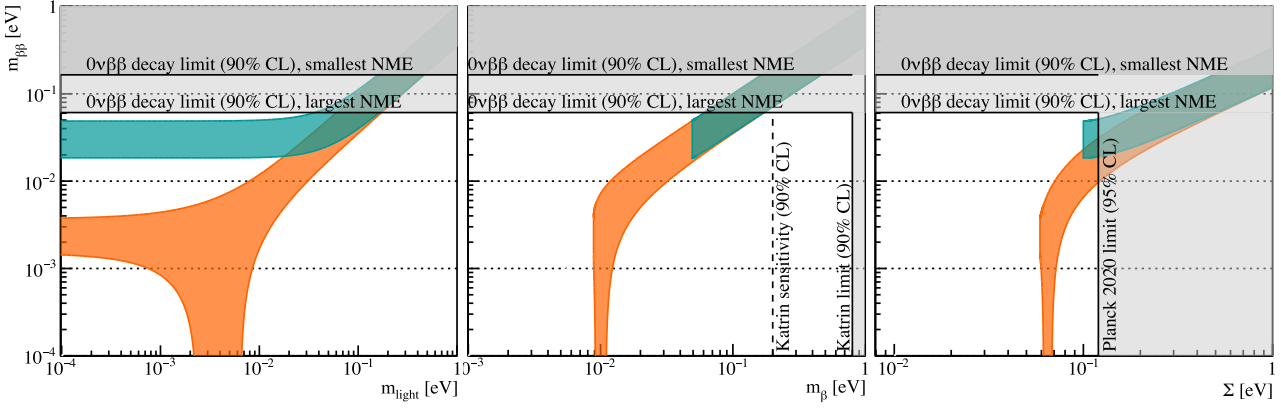
Figure 1.5: Maximally allowed parameter space for $m_{\beta\beta}$ as a function of the other mass observables m_{light}, m_β and Σ, using the central value for the oscillation parameters from [60]. The orange and green areas show the parameter space allowed assuming normal and inverted ordering, respectively. The shaded areas indicate the already excluded regions from $0\nu\beta\beta$ experiments (for the most and least favorable scenarios of the nuclear matrix element (NME)) [61], cosmology [62] and β-decay [63]. On the central panel, the projected sensitivity of the KATRIN experiment is also reported [64]. Taken from [28].

tests and cosmology, to provide an overall picture of the absolute scale of the neutrino mass. This defines a set of parameter spaces, according to the chosen observable, where limits from various experiments can be combined. This is shown in Figure 1.5, where $m_{\beta\beta}$ is given as a function of the mass m_β from kinematic experiments and the sum of neutrino masses Σ, coming from cosmology; often, $m_{\beta\beta}$ is also given as a function of the mass of the lightest neutrino m_{light}, which is not directly constrained by cosmology or kinematic experiments. Because of the lack of knowledge on the Majorana phases in Equation 1.12, the relation between the mass observables is not determined by a line, but rather by a range of allowed values. The colored bands in Figure 1.5 define the sets of maximally allowed parameter spaces in case of normal (orange) and inverted (green) ordering.

1.6.1 Cosmology

Astrophysical observations on energy and matter distribution in our Universe at different scales give information on the neutrino mass. These normally include the temperature anisotropies in the cosmic microwave background (CMB) [62] as well as the distribution of the galaxies, the so-called *large scale structures (LSS)*. The reason why an information on the mass of neutrinos can be extracted from such observations is that massive neutrinos, interacting only weakly, could have had a significant impact on the stream-
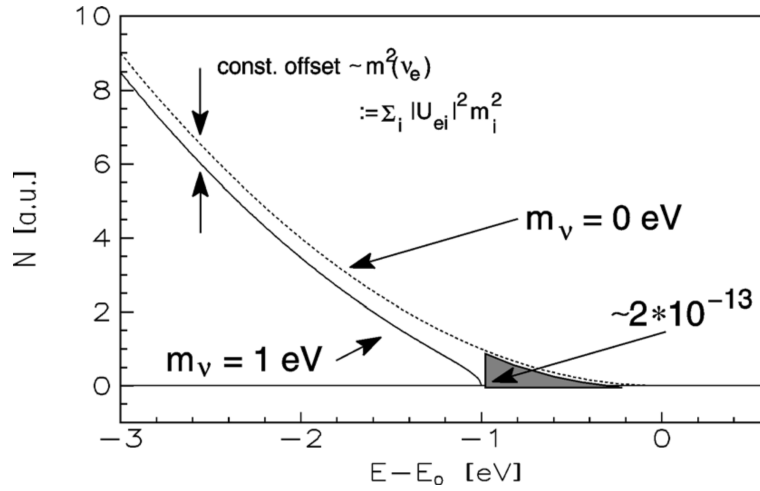
Figure 1.6: Endpoint of the energy spectrum of the electron from β-decay of Tritium. The mass observable for this kind of experiments is an incoherent sum of the mass eigenvalues m_i (here set to $1\,eV$ as example), which gives an offset between the experimental count rate and the prediction for $m_\nu = 0$. Note that the shaded area is $2 \cdot 10^{-13}$ of the total integral. Taken from [68].

out of materials from clusters, and thus in their gravitational evolution. For this reason, cosmology is sensitive to the sum of the neutrino masses:

$$\Sigma = \sum_i m_i \tag{1.20}$$

The strongest limit up-to-date is provided by the Planck survey [62], where the sum of neutrino masses is constrained to $\sum_i m_i < 0.12\,eV/c^2$. An important point is that the neutrino mass extracted from Planck data relies on the existence of the cosmic neutrino background, the footprint of neutrinos when they decoupled from matter, for which we don't have a direct evidence, yet [65].

1.6.2 Kinematic tests

In contrast with the other methods, kinematic tests don't need further assumptions to extract the neutrino mass observable. These are experiments, allowed in the standard model with $m_\nu = 0$, involving a neutrino in the final state. The determination of the mass m_ν is obtained by measuring the kinematic variables in the final state and imposing energy-momentum conservation.

In β-decays, which historically have set the most stringent limits on the neutrino masses among all kinematic tests [66, 67], the presence of a non-zero mass for the neutrino would manifest as a distortion at the endpoint of the energy spectrum of the electron, as shown in Figure 1.6. The mass

observable β-decay experiments are sensitive to can be obtained from the phase space factor of the process:

$$\rho(E) \propto p_e E_e (Q - E_e) \cdot \sqrt{(Q - E_e)^2 - m_{\nu_e}^2} \tag{1.21}$$

where p_e and E_e are the momentum and energy of the electron, Q is the Q-value of the decay and m_{ν_e} is the mass of the electron neutrino, which, as we know from Section 1.2, is not a well defined quantity. As it is a superposition of mass eigenstates ν_i, each with a probability $|U_{ei}|^2$ to couple to the electron, the energy spectrum is the sum of the contributions from every eigestate, so that Equation 1.21 reads:

$$\rho(E) \propto p_e E_e (Q - E_e) \cdot \sum_{i=1}^{3} |U_{ei}|^2 \sqrt{(Q - E_e)^2 - m_i^2} \tag{1.22}$$

Now, in an ideal experiment, one could distinguish the contributions from the different eigenstates as three kinks in the proximity of the endpoint. In reality, both the energy resolution (which presently is $\mathcal{O}(1)\,\text{eV}$) and a poor signal-to-background ratio in the proximity of the endpoint prevent such a precise determination. The analysis compares the theoretical prediction with the experimental spectrum further in the β spectrum, where $(Q - E) \gg m_i$. This allows for a series expansion of the root argument in Equation 1.22, and gives the final proportionality of the count rate on m_β, which is then the incoherent sum of the mass eigenvalues and is normally referred to as the *electron neutrino mass*:

$$m_\beta = \sqrt{\sum_i |U_{ei}^2| m_i^2} \tag{1.23}$$

The stringest upper limit for m_β has been recently set by the Karlsruhe Tritium Neutrino Experiment (KATRIN) collaboration, which for the first time explored mass scales below $1\,eV$: $m_\beta < 0.8\,eV/c^2$ (90% C.L.) [69].

1.7 SUMMARY

$0\nu\beta\beta$ is a second-order weak process in which two neutrons decay into two protons with only two electrons in the final state. If observed, it would reveal that neutrinos and antineutrinos are the same particle. In the assumption of light neutrinos mediating the process, it would also provide information on the neutrino mass scale. The worldwide search for $0\nu\beta\beta$ includes several isotopes, embedded in many different experimental tecniques. Experiments with ^{76}Ge provide the best energy resolution and background level in the field, and will be described in detail in Chapter 2.

REFERENCES

[1] E. Fermi, "Tentativo di una Teoria Dei Raggi β," *Il Nuovo Cimento (1924-1942)*, vol. 11, no. 1, p. 1, 1933. DOI: 10.1007/bf02959820.

[2] C. L. Cowan *et al.*, "Detection of the Free Neutrino: a Confirmation.," *Science (New York, N.Y.)*, vol. 124, no. 3212, pp. 103–4, 1956. DOI: 10.1126/science.124.3212.103.

[3] F. Reines and C. L. Cowan, "Detection of the Free Neutrino," *Physical Review*, vol. 92, no. 3, pp. 830–831, 1953. DOI: 10.1103/physrev.92.830.

[4] G. Danby *et al.*, "Observation of High-Energy Neutrino Reactions and the Existence of Two Kinds of Neutrinos," *Physical Review Letters*, vol. 9, no. 1, pp. 36–44, 1962. DOI: 10.1103/physrevlett.9.36.

[5] K. Kodama *et al.*, "Observation of tau neutrino interactions," *Physics Letters B*, vol. 504, no. 3, pp. 218–224, 2001. DOI: 10.1016/s0370-2693(01)00307-0.

[6] N. A. e. al, "Observation of a first ν_τ candidate in the OPERA experiment in the CNGS beam," *arXiv*, 2010. DOI: 10.1016/j.physletb.2010.06.022.

[7] P. A. M. Dirac, "The quantum theory of the electron," *Proceedings of the Royal Society of London. Series A, Containing Papers of a Mathematical and Physical Character*, vol. 117, no. 778, pp. 610–624, 1928. DOI: 10.1098/rspa.1928.0023.

[8] P. A. M. Dirac, "The quantum theory of the Electron. Part II," *Proceedings of the Royal Society of London. Series A, Containing Papers of a Mathematical and Physical Character*, vol. 118, no. 779, pp. 351–361, 1928. DOI: 10.1098/rspa.1928.0056.

[9] R. P. Feynman and M. Gell-Mann, "Theory of the Fermi Interaction," *Physical Review*, vol. 109, no. 1, pp. 193–198, 1958. DOI: 10.1103/physrev.109.193.

[10] Y. Fukuda *et al.*, "Measurement of the Flux and Zenith-Angle Distribution of Upward Throughgoing Muons by Super-Kamiokande," *Physical Review Letters*, vol. 82, no. 13, pp. 2644–2648, 1998. DOI: 10.1103/physrevlett.82.2644.

[11] B. T. Cleveland *et al.*, "Measurement of the Solar Electron Neutrino Flux with the Homestake Chlorine Detector," *The Astrophysical Journal*, vol. 496, no. 1, pp. 505–526, 1998. DOI: 10.1086/305343.

[12] K. Eguchi *et al.*, "First Results from KamLAND: Evidence for Reactor Anti-Neutrino Disappearance," *arXiv*, vol. 90, no. 2, p. 021 802, 2002. DOI: 10.1103/physrevlett.90.021802.

[13] S. Collaboration, "Direct Evidence for Neutrino Flavor Transformation from Neutral-Current Interactions in the Sudbury Neutrino Observatory," *arXiv*, 2002. DOI: 10.1103/physrevlett.89.011301.

[14] M. H. Ahn *et al.*, "Measurement of neutrino oscillation by the K2K experiment," *Physical Review D*, vol. 74, no. 7, p. 072 003, 2006. DOI: 10.1103/physrevd.74.072003.

[15] S. Abe *et al.*, "Precision Measurement of Neutrino Oscillation Parameters with KamLAND," *Physical Review Letters*, vol. 100, no. 22, p. 221 803, 2008. DOI: 10.1103/physrevlett.100.221803.

[16] K. Abe *et al.*, "Indication of Electron Neutrino Appearance from an Accelerator-Produced Off-Axis Muon Neutrino Beam," *Physical Review Letters*, vol. 107, no. 4, p. 041 801, 2011. DOI: 10.1103/physrevlett.107.041801.

[17] Y. Abe *et al.*, "Indication of Reactor $\overline{\nu}_e$ Disappearance in the Double Chooz Experiment," *Physical Review Letters*, vol. 108, no. 13, p. 131 801, 2012. DOI: 10.1103/physrevlett.108.131801.

[18] F. P. An *et al.*, "Observation of electron-antineutrino disappearance at Daya Bay," *arXiv*, vol. 108, no. 17, p. 171 803, 2012. DOI: 10.1103/physrevlett.108.171803.

[19] E. Majorana, "Teoria simmetrica dell'elettrone e del positrone," *Il Nuovo Cimento*, vol. 14, no. 4, pp. 171–184, 1937. DOI: 10.1007/bf02961314.

[20] R. N. Mohapatra and P. B. Pal, "Massive Neutrinos in Physics and Astrophysics," *World Scientific Lecture Notes in Physics*, 2004. DOI: 10.1142/5024.

[21] G. Racah, "Sulla Simmetria Tra Particelle e Antiparticelle," *Il Nuovo Cimento*, vol. 14, no. 7, pp. 322–328, 1937. DOI: 10.1007/bf02961321.

[22] P. Minkowski, "$\mu \to e\gamma$ at a rate of one out of 10^9 muon decays?" *Physics Letters B*, vol. 67, no. 4, pp. 421–428, 1977. DOI: 10.1016/0370-2693(77)90435-x.

[23] M. Gell-Mann, P. Ramond, and R. Slansky, "Complex Spinors and Unified Theories," *arXiv*, 2013.

[24] W. Heisenberg, "Über den Bau der Atomkerne. II," *Zeitschrift für Physik*, vol. 78, no. 3-4, pp. 156–164, 1932. DOI: 10.1007/bf01337585.

[25] C. Giunti and C. W. Kim, "Fundamentals of Neutrino Physics and Astrophysics," pp. 67–105, 2007. DOI: 10.1093/acprof:oso/9780198508717.003.0003.

[26] S. Finch and W. Tornow, "Search for the β decay of 96Zr," *Nuclear Instruments and Methods in Physics Research Section A: Accelerators, Spectrometers, Detectors and Associated Equipment*, vol. 806, pp. 70–74, 2016. DOI: 10.1016/j.nima.2015.09.098.

[27] M. Goeppert-Mayer, "Double Beta-Disintegration," *Physical Review*, vol. 48, no. 6, pp. 512–516, 1935. DOI: 10.1103/physrev.48.512.

[28] M. Agostini *et al.*, "Toward the discovery of matter creation with neutrinoless double-beta decay," *arXiv*, 2022.

[29] S. R. Elliott, A. A. Hahn, and M. K. Moe, "Direct evidence for two-neutrino double-beta decay in Se82," *Physical Review Letters*, vol. 59, no. 18, pp. 2020–2023, 1987. DOI: 10.1103/physrevlett.59.2020.

[30] M. Agostini *et al.*, "Results on $\beta\beta$ decay with emission of two neutrinos or Majorons in ^{76}Ge from GERDA Phase I," *The European Physical Journal C*, vol. 75, no. 9, p. 416, 2015. DOI: 10.1140/epjc/s10052-015-3627-y.

[31] J. B. Albert *et al.*, "Improved measurement of the $2\nu\beta\beta$ half-life of ^{136}Xe with the EXO-200 detector," *Physical Review C*, vol. 89, no. 1, 2014. DOI: 10.1103/physrevc.89.015502.

[32] A. Caminata *et al.*, "Results from the Cuore Experiment †," *Universe*, vol. 5, no. 1, p. 10, 2019. DOI: 10.3390/universe5010010.

[33] O. Azzolini *et al.*, "Evidence of Single State Dominance in the Two-Neutrino Double-β Decay of ^{82}Se with CUPID-0.," *Physical review letters*, vol. 123, no. 26, p. 262 501, 2019. DOI: 10.1103/physrevlett.123.262501.

[34] E. Armengaud *et al.*, "Precise measurement of $2\nu\beta\beta$ decay of ^{100}Mo with the CUPID-Mo detection technology," *arXiv*, vol. 80, no. 7, 2019. DOI: 10.1140/epjc/s10052-020-8203-4.

[35] A. Gando *et al.*, "Precision Analysis of the ^{136}Xe Two-Neutrino $\beta\beta$ Spectrum in KamLAND-Zen and Its Impact on the Quenching of Nuclear Matrix Elements," *arXiv*, vol. 122, no. 19, 2019. DOI: 10.1103/physrevlett.122.192501.

[36] W. H. Furry, "On Transition Probabilities in Double Beta-Disintegration," *Physical Review*, vol. 56, no. 12, pp. 1184–1193, 1939. DOI: 10.1103/physrev.56.1184.

[37] V. Tretyak and Y. Zdesenko, "Tables of double beta decay data," *Atomic Data and Nuclear Data Tables*, vol. 61, no. 1, pp. 43–90, 1995. DOI: 10.1016/s0092-640x(95)90011-x.

[38] C. S. Wu *et al.*, "Experimental Test of Parity Conservation in Beta Decay," *Physical Review*, vol. 105, no. 4, pp. 1413–1415, 1957. DOI: 10.1103/physrev.105.1413.

[39] K. M. Case, "Reformulation of the Majorana Theory of the Neutrino," *Physical Review*, vol. 107, no. 1, pp. 307–316, 1957. DOI: 10.1103/physrev.107.307.

[40] J. Kotila and F. Iachello, "Phase-space factors for double-β decay," *Physical Review C*, vol. 85, no. 3, p. 034316, 2012. DOI: 10.1103/physrevc.85.034316.

[41] S. Stoica and M. Mirea, "Phase Space Factors for Double-Beta Decays," *Frontiers in Physics*, vol. 7, p. 12, 2019. DOI: 10.3389/fphy.2019.00012.

[42] J. Engel and J. Menéndez, "Status and future of nuclear matrix elements for neutrinoless double-beta decay: a review," *Reports on Progress in Physics*, vol. 80, no. 4, p. 046301, 2017. DOI: 10.1088/1361-6633/aa5bc5.

[43] I. Esteban *et al.*, "The fate of hints: updated global analysis of three-flavor neutrino oscillations," *Journal of High Energy Physics*, vol. 2020, no. 9, p. 178, 2020. DOI: 10.1007/jhep09(2020)178.

[44] A. Caldwell and K. Kröninger, "Signal discovery in sparse spectra: A Bayesian analysis," *Physical Review D*, vol. 74, no. 9, p. 092003, 2006. DOI: 10.1103/physrevd.74.092003.

[45] S. Abe *et al.*, "First Search for the Majorana Nature of Neutrinos in the Inverted Mass Ordering Region with KamLAND-Zen," *arXiv*, 2022. DOI: https://doi.org/10.48550/arXiv.2203.02139.

[46] V. Albanese *et al.*, "The SNO+ experiment," *Journal of Instrumentation*, vol. 16, no. 08, P08059, 2021. DOI: 10.1088/1748-0221/16/08/p08059.

[47] M. Auger *et al.*, "The EXO-200 detector, part I: detector design and construction," *Journal of Instrumentation*, vol. 7, no. 05, P05010, 2012. DOI: 10.1088/1748-0221/7/05/p05010.

[48] E. Conti *et al.*, "Correlated fluctuations between luminescence and ionization in liquid xenon," *Physical Review B*, vol. 68, no. 5, p. 054201, 2003. DOI: 10.1103/physrevb.68.054201.

[49] G. Adhikari *et al.*, "nEXO: neutrinoless double beta decay search beyond 10^{28} year half-life sensitivity," *Journal of Physics G: Nuclear and Particle Physics*, vol. 49, no. 1, 2022. DOI: 10.1088/1361-6471/ac3631.

[50] O. Azzolini *et al.*, "Search for neutrinoless double beta decay of ^{64}Zn and ^{70}Zn with CUPID-0," *The European Physical Journal C*, vol. 80, no. 8, p. 702, 2020. DOI: 10.1140/epjc/s10052-020-8280-4.

[51] E. Armengaud *et al.*, "New Limit for Neutrinoless Double-Beta Decay of ^{100}Mo from the CUPID-Mo Experiment," *Physical Review Letters*, vol. 126, no. 18, p. 181802, 2021. DOI: 10.1103/physrevlett.126.181802.

[52] T. C. I. Group, "CUPID pre-CDR," *arXiv*, 2019.

[53] R. Arnold *et al.*, "Results of the search for neutrinoless double-β decay in ^{100}Mo with the NEMO-3 experiment," *Physical Review D*, vol. 92, no. 7, 2015. DOI: 10.1103/physrevd.92.072011.

[54] F. Piquemal, "The SuperNEMO project," *Physics of Atomic Nuclei*, vol. 69, no. 12, pp. 2096–2100, 2006. DOI: 10.1134/s1063778806120131.

[55] C. E. Aalseth *et al.*, "Search for Neutrinoless Double-β Decay in ^{76}Ge with the Majorana Demonstrator," *Physical Review Letters*, vol. 120, no. 13, p. 132 502, 2018. DOI: 10.1103/physrevlett.120.132502.

[56] M. Agostini *et al.*, "Limits on uranium and thorium bulk content in GERDA Phase I detectors," *Astroparticle Physics*, vol. 91, pp. 15–21, 2017. DOI: 10.1016/j.astropartphys.2017.03.003.

[57] M. Agostini *et al.*, "Final Results of GERDA on the Search for Neutrinoless Double-β Decay," *Physical Review Letters*, vol. 125, no. 25, p. 252 502, 2020. DOI: 10.1103/physrevlett.125.252502.

[58] N. Abgrall *et al.*, "The large enriched germanium experiment for neutrinoless double beta decay (LEGEND)," *AIP Conference Proceedings*, vol. 1894, no. 1, p. 020 027, 2017. DOI: 10.1063/1.5007652. [Online]. Available: https://aip.scitation.org/doi/abs/10.1063/1.5007652.

[59] N. Abgrall *et al.*, "LEGEND-1000 preconceptual design report," *arXiv*, 2021.

[60] P. D. Group *et al.*, "Review of Particle Physics," *Progress of Theoretical and Experimental Physics*, vol. 2020, no. 8, p. 083C01, 2020. DOI: 10.1093/ptep/ptaa104.

[61] A. Gando *et al.*, "Search for Majorana Neutrinos Near the Inverted Mass Hierarchy Region with KamLAND-Zen," *Physical Review Letters*, vol. 117, no. 8, p. 082 503, 2016. DOI: 10.1103/physrevlett.117.082503.

[62] N. Aghanim *et al.*, "Planck 2018 results," *Astronomy & Astrophysics*, vol. 641, A6, 2020. DOI: 10.1051/0004-6361/201833910.

[63] M. Aker *et al.*, "First direct neutrino-mass measurement with sub-eV sensitivity," 2021. DOI: 10.21203/rs.3.rs-544214/v1.

[64] M. Aker *et al.*, "Improved Upper Limit on the Neutrino Mass from a Direct Kinematic Method by KATRIN," *Physical Review Letters*, vol. 123, no. 22, p. 221 802, 2019. DOI: 10.1103/physrevlett.123.221802.

[65] M. G. Betti *et al.*, "Neutrino physics with the PTOLEMY project: active neutrino properties and the light sterile case," *arXiv*, vol. 2019, no. 07, pp. 047–047, 2019. DOI: 10.1088/1475-7516/2019/07/047.

[66] C. Kraus *et al.*, "Final results from phase II of the Mainz neutrino mass searchin tritium decay," *The European Physical Journal C - Particles and Fields*, vol. 40, no. 4, pp. 447–468, 2005. DOI: 10.1140/epjc/s2005-02139-7.

[67] V. N. Aseev *et al.*, "Upper limit on the electron antineutrino mass from the Troitsk experiment," *Physical Review D*, vol. 84, no. 11, p. 112 003, 2011. DOI: 10.1103/physrevd.84.112003.

[68] C. Weinheimer, "Direct determination of the neutrino masses," *Comptes Rendus Physique*, vol. 6, no. 7, pp. 768–777, 2005. DOI: 10.1016/j.crhy.2005.07.005.

[69] M. Aker *et al.*, "Direct neutrino-mass measurement with sub-electron-volt sensitivity," *Nature Physics*, vol. 18, no. 2, pp. 160–166, 2022. DOI: 10.1038/s41567-021-01463-1.

2 | THE EXPERIMENTAL APPROACH OF GERDA AND LEGEND

The GERDA experiment has operated bare germanium detectors enriched in the double-beta decaying ^{76}Ge in LAr from 2011 to 2019 and, as will be presented in Chapter 8, provided among the most stringent constraints on the half life of $0\nu\beta\beta$. In this chapter the experimental setup of GERDA Phase II will be described, with emphasis on the advantages of using germanium in $\beta\beta$-decay searches. The experimental approach and status of the next-generation experiment LEGEND will also be reviewed.

2.1 GERMANIUM AS DOUBLE–BETA DECAY DETECTOR

Since the invention of transistors in 1948 [1], germanium has been used in a broad variety of applications, ranging from gamma-ray detection [2] and fiber optics [3, 4], to measurement of the coherent neutrino-nucleus scattering [5] and search for dark matter [6–8]. The state-of-the-art technology allows the production of detector blanks with lengths and diameters of 8–9 cm using the Czochralski method. With a level of impurities of $\mathcal{O}(10^{10})$ atoms/cm^3, such crystals can be converted into HPGe detectors. A HPGe detector is a semiconductor device, where two electrodes on the crystal surface are used to apply a bias voltage and extend the semiconductor junction throughout the full detector volume. When a gamma-ray or charged particle interacts within the detector it creates a large number of charge carriers, i.e. electrons and holes. Charge carriers of the same sign drift together towards the electrodes as a cluster, following the electric field lines. Their motion induces a signal at the electrodes that is typically read-out by a charge sensitive amplifier. Similar to a time projection chamber, the analysis of the time structure of the read-out signal contains information on the topology of the event, i.e. on the number and location of the energy depositions.

In Section 1.4 we have seen that the signature of a $\beta\beta$-decay is the emission of two electrons, which, summed, have an energy E in the range $E \in [0, Q_{\beta\beta}[$ for $2\nu\beta\beta$ events, or exactly $Q_{\beta\beta}$ for $0\nu\beta\beta$. Fiorini et al. recognized in 1967 that such a signature could be detected with high precision using HPGe detectors [9], which naturally contain 7.75(12)% [10] of the $\beta\beta$-decaying isotope ^{76}Ge. This approach offers several advantages: Ge detectors have negligible radioactive internal contaminations [11], a per mil energy resolu-

tion, and advanced event reconstruction capabilities [12]. In addition, the high density of germanium crystals ensures that the two electrons sharing $Q_{\beta\beta} = 2039.061(7)$ keV [13] are absorbed within a few millimeters from the decay vertex, generating well localized energy depositions which are fully contained within the detector. Also, in the 1990s, the Heidelberg-Moscow (HdM) [14] and International Germanium Experiment (IGEX) experiments [15] showed that HPGe could be built from material isotopically enriched to $\sim 90\%$ in ^{76}Ge, opening the way to large scale double-beta experiments with germanium.

2.2 THE GERDA EXPERIMENT

The GERDA experiment benefited from the success of the HdM and IGEX experiments and developed a novel experimental concept to pursue the search for $0\nu\beta\beta$: the operation of bare HPGe detectors in a LAr bath, acting both as cooling material as well as a passive and active shield, as we shall see in more details in Section 2.2.1.

The experiment was designed to reach an exposure of $100 \, \mathrm{kg \cdot yr}$ with a BI of $\mathcal{O}(10^{-3}) \, \mathrm{cts/(keV \cdot kg \cdot yr)}$, with the goal of exploring half-lives beyond 10^{26} yr [16]. The data taking began in November 2011 with Phase I, which operated 18 kg of enriched material from the HdM and IGEX experiments [17]. Phase II started in December 2015, after a major hardware upgrade where novel broad energy germanium (BEGe) detectors [18] (for a total mass of 35.6 kg) and improved veto techniques have been deployed in the setup [19]. Additionally, in May 2018, 10 kg of detectors with the inverted coaxial (IC) geometry [20] have been added to the experiment [21], marking the transition to Phase II$^+$. Their testing in the vendor's cryostats and their performances in the GERDA environment are described in Chapter 6 and Chapter 7. After reaching the targeted exposure of $100 \, \mathrm{kg \cdot yr}$, the data taking stopped in November 2019. The final results will be presented in Chapter 8.

2.2.1 The experimental apparatus

The HdM and IGEX experiments proved that the highest contribution to the background budget is not internal to the detectors (intrinsic bulk contamination or cosmogenically activated nuclei) but rather from environmental radioactivity. For this reason, the GERDA setup was optimized for the suppression of background from external sources.

The Gran Sasso massif is part of the experiment

The experimental apparatus was located in Hall A of the LNGS, shielded by 1400 m of rock overburden (corresponding to 3500 m.w.e.), which reduces the muon flux to $1.25 \, \mathrm{m^{-2} \, h^{-1}}$ [19].

(a) Overview of the apparatus   **(b)** LAr veto   **(c)** Detector array
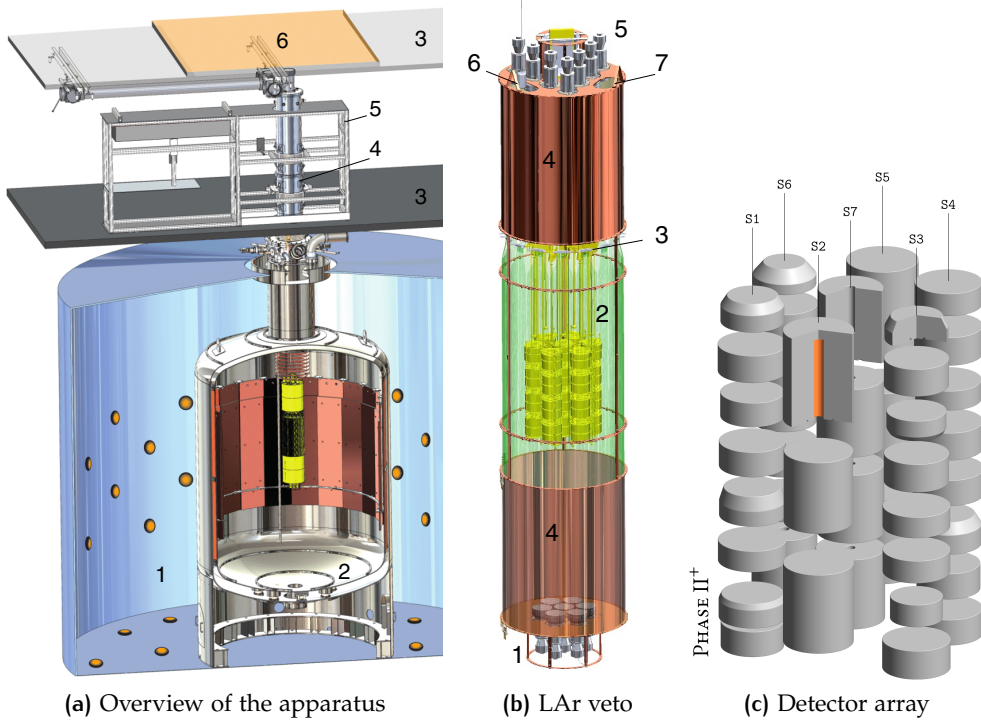
Figure 2.1: GERDA Phase II experimental setup. (a): 1. Water cherenkov detector
(590 m^3 with 10 m diameter), equipped with 66 PMTs; 2. LAr cryostat
(64 m^3 with 4 m diameter); 3. Floor and roof of clean room; 4. Lock
system; 5. Glove-box; 6. Plastic scintillators. (b): 1. Bottom plate, with 7
PMTs; 2. Fiber curtain; 3. Optical coupling and silicon photomultipliers
(SiPMs); 4. Thin-walled Cu cylinder; 5. Top plate, with 9 PMTs; 6.
Calibration source entering slit; 7. Second slit for calibration sources.
(c): HPGe detectors are arranged in 7 *strings*, labeled with *S*, which
make up the *array*; here is the layout after the upgrade of May 2018. (a)
and (b) were taken from [22]. (c) was produced with [23].

Germanium detectors are shielded from residual muons and environmen-   *Muon veto*
tal radioactivity by a shell structure, which is shown in Figure 2.1. The
outer layer is a 10 m diameter water tank, equipped with 66 PMTs, aimed
at detecting the Cherenkov radiation produced by the passage of charged
radiation. For the same purpose, plastic scintillators are placed on top of the
experiment [24, 25].

Inside the water tank is a 4 m diameter cryostat containing high-purity   *LAr veto*
LAr, which acts as both a cooling medium for germanium and a passive
shield. After the upgrade to Phase II, the cryostat was equipped with light
sensors, exploiting the scintillating properties of Ar and thus allowing its
usage as an *active* shield: its scintillation light is collected by PMTs lo-
cated above and below the detectors, and by a system of wavelength-shifting
(WLS) fibers surrounding germanium and optically coupled to silicon photo-
multipliers (SiPMs). Together, they constitute the *LAr veto* system sketched
in Figure 2.1b, which acts in anti-coincidence with a signal in the germa-

nium. An excellent description of the LAr veto system and its triggering scheme is given in [26].

At the innermost core of the setup, germanium detectors are arranged in vertical columns, referred to as *strings*, as is shown in Figure 2.1c. Altogether they form the *array* which gives the experiment its name.

Located on top of the experiment is a clean room, where detectors are assembled in strings and can be deployed into the setup through the lock system.

2.3 THE GERDA DETECTORS

(a) Semi-coaxial   **(b)** BEGe   **(c)** Inverted coaxial
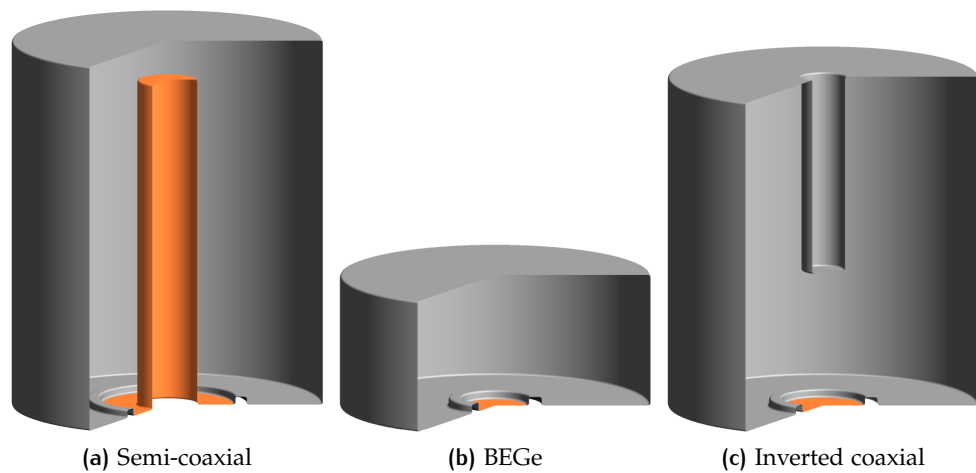
Figure 2.2: Detector geometries used in the GERDA experiment. The p^+ electrode is colored in orange and the n^+ covers the rest of the surface, except for the small groove that guarantees the electrical insulation. Produced with [23].

The detectors used in GERDA are p-type HPGe detectors, with a Lithium-diffused n^+ electrode and a B-implanted p^+ electrode. The formation of the electrodes creates a *dead* layer where the electric field is zero and therefore charges are not collected. In case of the p^+ electrode, it consists in $\mathcal{O}(100)\,\mathrm{nm}$ while for the n^+ electrode it extends for $\mathcal{O}(1)\,\mathrm{mm}$.

GERDA used three different germanium detector geometries, which are shown in Figure 2.2:

- *Semi-coaxials* (Figure 2.2a): these detectors have a cylindrical shape and a hole along the symmetry axis which extends over almost the full length. The entire surface of the hole (marked in orange in Figure 2.2a) is B-implanted and makes up the p^+ electrode, which extends also to the bottom horizontal surface, until a passivated groove, whose thickness and depth are $\sim 3\,\mathrm{mm}$. The rest of the detector surface is Li-diffused and makes up the n^+ electrode. This structure ensures a

strong field along the full crystal length, allowing the production of long detectors (8 to 10 cm), which can be operated with voltages in the order of a few kV. Seven detectors of this type have been acquired from the HdM and IGEX experiments and were used, after refurbishment, in GERDA Phase I and Phase II. With the upgrade to Phase II$^+$, one of these detectors, which had poor background discrimination performances, has been discarded. Their masses summed up to 15.6 kg in GERDA Phase I and II and 14.6 kg in Phase II$^+$.

- *Broad energy germanium (BEGe) detectors* (Figure 2.2b) [18, 27]: compared to semi-coaxials, BEGe detectors are much shorter and the structure of the elecrodes is different. No hole is present on BEGes and the p^+ electrode covers only the flat surface enclosed by the passivated groove, which has a diameter of up to ~15 mm. As for semi-coaxials, the BEGe detectors' n^+ electrode extends down to the groove, wrapping around the crystal on all surfaces. This structure of the electrodes has a strong impact on the trajectories of charge carriers, which, as we shall see in Section 2.4, allows for a very efficient signal and background discrimination. A total of 30 BEGes have been produced out of enriched material for GERDA Phase II [28], for a mass of 20.0 kg.

- *Inverted coaxial (IC) detectors* (Figure 2.2b) [20, 29]: these detectors have the same electrode structure as a BEGe, though they are about two to three times as long. To ensure a high electric field throughout the whole volume, a hole is drilled from the top surface to within 25 to 35 mm from the p^+ electrode and forms part of the n^+ electrode. This geometry was developed to achieve the performance of BEGes in terms of signal and background discrimination, with a factor 3 higher mass per detector. This ensures a reduction of the same factor of the dead material surrounding the detectors (cables, holders...), which is a known source of background events. In the framework of the upgrade to Phase II$^+$, five IC detectors have been added to the GERDA array, with a summed mass of 9.6 kg.

2.4 PULSE SHAPE ANALYSIS WITH THE GERDA DETECTORS

With the information from the muon and the LAr veto, the GERDA experiment can efficiently tag events from environmental radioactivity. Nonetheless, some background events could produce a signal only in germanium (for instance, a γ-ray from nearby the detector array, not depositing energy in LAr). In these cases, germanium detectors offer the possibility to distin-

guish potential $0\nu\beta\beta$ events from background through the analysis of the shape of the electrical signals. This kind of analysis is commonly referred to as pulse shape analysis (PSA) or pulse shape discrimination (PSD). As this will be heavily used over the course of this dissertation, details on signal formation in germanium and on the PSA technique used in GERDA will be given in the following.

2.4.1 Signal formation in the GERDA detectors

When gamma-rays or charged particles interact within the germanium detector they release energy. About 10^6 electron-hole pairs are created for each MeV deposited in the active detector volume. Once produced, the two kinds of charge carriers drift as two clusters in opposite directions following the electric field lines until they reach the electrodes. The signal induced by the motion of these charges can be modeled by the Shockley–Ramo theorem

The Shockley–Ramo theorem [30, 31]. The theorem states that the instantaneous current $I(t)$ induced at a given electrode by a drifting cluster of charge q is given by

$$I(t) = q\,\mathbf{v}(\mathbf{x}(t)) \cdot \mathbf{E}_\omega(\mathbf{x}(t)) \tag{2.1}$$

where $\mathbf{v}(\mathbf{x}(t))$ is the instantaneous drift velocity, which is determined by the electric field, and $\mathbf{E}_\omega(\mathbf{x}(t))$ is the weighting field at position $\mathbf{x}(t)$. The weighting field is defined as the electric field created by the considered electrode set at $1\,\mathrm{V}$, all other electrodes grounded and all charges inside the device removed. A visual representation of the quantities involved in Equation 2.1 is given in Figure 2.3. The signal generation is the product of its two rows (times the cosine of the angle between the vectors). As the weighting field spans over 3 to 4 orders of magnitude, while the values of the drift velocity are within a factor 2 range, it is the former that primarily determines the shape of the signal.

Semi-coaxial detectors feature big volumes where the weighting field is high and roughly homogeneous. Since both electrons and holes drift in these regions, they both contribute significantly to the signal formation. However, due to the higher drift velocity of electrons, their contribution is a factor 2 higher. Because the drift paths of the two charge carriers change significantly according to the starting position, these detectors feature a mild dependence of the pulse shape on the interaction position.

The structure of the electrodes in a BEGe detector, conversely, creates a region of high weighting field only in the volume surrounding the p^+ electrode. This means that the pulse shape is mostly determined by the holes drifting in that region, while the contribution of electrons is almost negligible. Since in the region of high weighting field, thanks to the wrap-around

(a) Module of the weighting field $\mathbf{E}_\omega$

(b) Module of the drift velocity $\mathbf{v}_d$ of holes
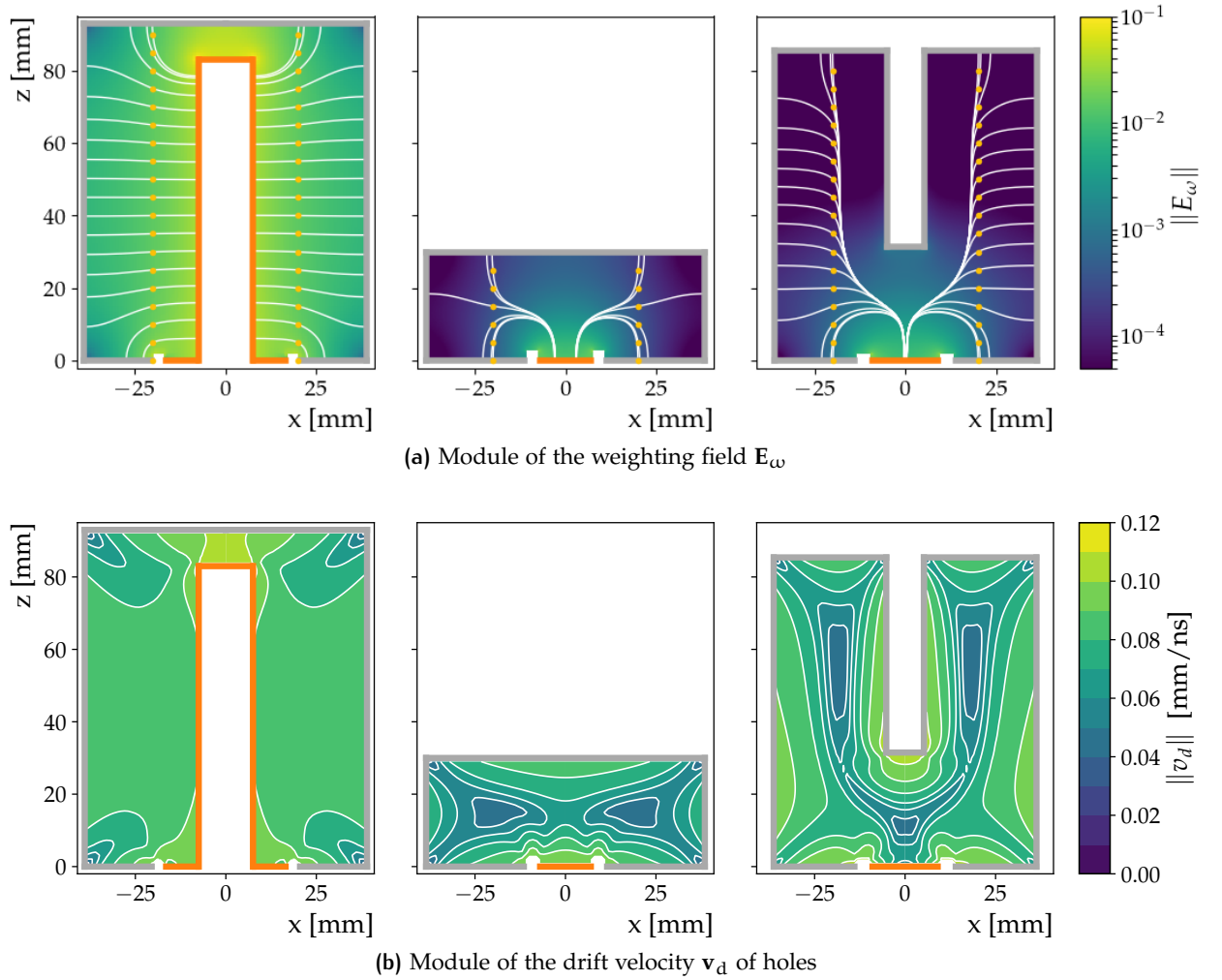
Figure 2.3: Module of (a) the weighting field $\mathbf{E}_\omega$ and (b) the drift velocity $\mathbf{v}_d$ of holes on a cross section of the three geometries used in GERDA: (from left) semi-coaxial, BEGe and inverted coaxial. The orange and gray borders mark the p^+ and n^+ electrode, respectively. The golden circles are locations of an energy deposition, the white trajectories connecting them to the p^+ electrode are the drift paths of holes and those connecting them to the n^+ electrode are the drift paths of electrons.

of the n^+ electrode, holes are pushed to the same trajectories (this is called the *funnel* effect), all pulses are alike, independently on the interaction position. The only exception is for interactions occurring directly in the region of high weighting field, where the drifting of the electrons also contributes significantly to the pulse shape.

Thanks to the same electrode structure, IC detectors show the same features of a BEGe. Being a factor 2 to 3 longer, they feature a much bigger volume where the weighting field is low. Although this has a minimal impact on the pulse shape, it could prevent a precise determination of the start time of the drift.

2.4.2 The A/E technique

As mentioned, one of the advantages of using germanium on the search for $0\nu\beta\beta$ is that the decay occurs inside the detector and the electrons are absorbed within $\mathcal{O}(1)\,mm$. Therefore, a potential $0\nu\beta\beta$ event consists of a point-like energy deposition, what is often referred to as single-site event (SSE).

Conversely, background events can have different origins and exhibit different topologies. For instance, a γ-ray in the MeV range is likely to deposit energy in germanium through multiple Compton scatterings, what is often referred to as multi-site event (MSE). For $\beta\beta$-experiments it is hence of primary interest to discriminate single-site from multiple-site energy depositions. Moreover, because the p^+ and n^+ electrodes have a thickness of $\mathcal{O}(100)\,nm$ and $\mathcal{O}(1)\,mm$, respectively, they are susceptible to α- (on the p^+) and β- (on both) decays from surface contaminations. To discriminate MSE and surface events, GERDA exploits PSA techniques, which are based on the recognition of a few specific features in the signal time evolution [12].

The fact that semi-coaxial detectors exhibit a position dependence of the pulse shape makes the features which could separate a $0\nu\beta\beta$ from background less recognizable. For this reason, the analysis for these detectors yields worse discrimination performances than in BEGes. Since this is not relevant for the present work, we refer to [12] for further details on this analysis. Consequently, the rest of this section will be dedicated to the PSA technique used for BEGes and ICs, which is the standard in the field and will be used in the whole dissertation: the A/E technique.

The A/E technique   The A/E technique is based on a single parameter that is the maximum value of the current signal (A), normalized to the total deposited energy (E) *A/E for $0\nu\beta\beta$* (or q in Equation 2.1). In case of a single energy deposition, the signal has a single peak structure with amplitude A, which corresponds to the moment when the cluster of holes crosses the region of maximum weighting field. Such an event is shown in grey in Figure 2.4: an energy $E = 2039\,keV$ is deposited in the grey circle on the left side of the detector, creating holes and electrons which follow the dashed and dotted trajectories, respectively, until collection at the electrode. The current signal $I(t)$ generated by such event is shown in grey on the right side: its maximum value is marked with A_{SSE} and its energy E is the shaded area below the curve.

A/E for γ-rays   If the same energy E is deposited in multiple locations, like the two orange circles on the left side of Figure 2.4, multiple clusters are simultaneously created and the total signal is the superposition of the signals induced by the motion of each of them. Different clusters will reach the region of maximum weighting field at different times, creating a multiple peak structure, as visible on the right side of Figure 2.4, with the orange curve. Since the
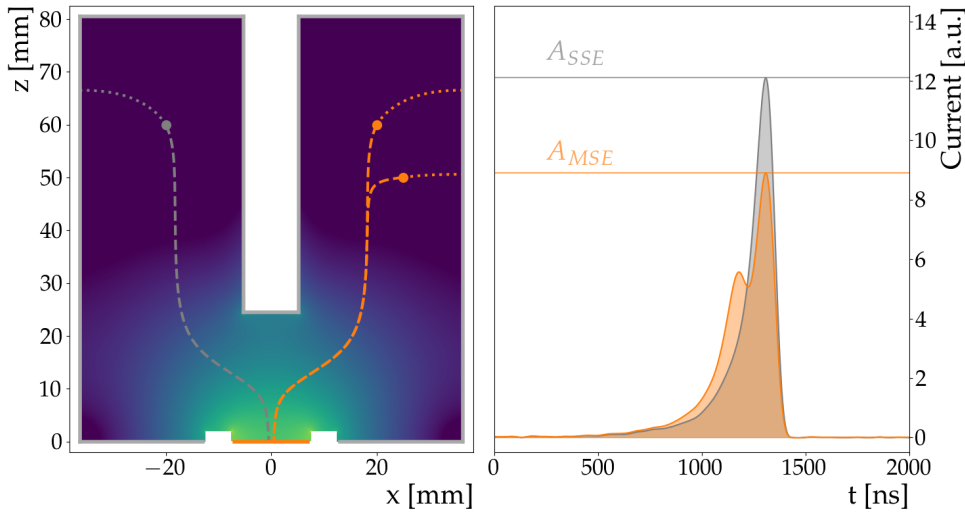
Figure 2.4: Topology and A/E of a SSE (grey) and a MSE (orange). An energy deposition of $E = 2039\,\text{keV}$ in the grey circle on the left side creates a cluster of electrons and a cluster of holes which, drifting to the electrodes following respectively the dotted and dashed lines, generate the grey current signal on the right side, with a maximum A_{SSE}. If the same energy E is deposited in two sites, as marked in orange, the area below the current signal is the same, but the maximum A_{MSE} is lower.

amplitude of each peak is proportional to the total charge in the relative cluster, events with multiple energy depositions $E_i \propto q_i < q$ will have a lower A value compared to single-site events in which all energy is contained in a single cluster $E \propto q = \sum_i q_i$. This is also shown on the right side of Figure 2.4, where the signal generated by a multiple site interaction, marked in orange, exhibits a maximum A_{MSE}, which is lower than the case where the same energy is deposited in one single point, A_{SSE}. The normalization to the total energy E allows to extend the concept to all energies.

The A/E parameter is independent of the interaction position and its discrimination efficiency is constant throughout the whole detector volume [32]. As mentioned in Section 2.4.1, the only exception is for interactions nearby the read-out electrode, for which A/E is larger than usual because of the extra contribution of the electrons: moving in a region of strong electric and weighting field, they give in this case a contribution to the signal shape which is not negligible as in the rest of the detector. Since this volume region is separated from the external world only by a thin layer of inactive material ($\mathcal{O}(100)\,\text{nm}$), these regions are susceptible to α or β decays. A detailed study of the rejection of events in the region surrounding the p^+ electrode can be found in [33]. A work to extend those results will be presented in Section 5.4.

A/E for surface αs

Furthermore, β-particles can occasionally penetrate the $\mathcal{O}(1)\,\text{mm}$ Li-diffused layer and deposit part of their energies into the sensitive region of the detector. Since the transition from the n^+ electrode to the active vol-

A/E for (n⁺) surface βs

ume is not step-like, the energy can be deposited in a layer between the two regions, where the electric field is nearly zero. If this occurs, the only way charges can be collected is by diffusing into the region of high electric field. For this reason, events of this type induce signals which are characterized by the slow time-scale of the diffusion process (of the order of several μs); they have therefore been called *Slow pulses* and exhibit very low A/E values [32].

To strongly suppress background events from α, β and γ-rays, the PSA is calibrated on 0νββ-like events to set lower and upper thresholds and thus select a range of accepted A/E values. Samples of 0νββ-like events can be produced by irradiating the Ge detectors with a ^{228}Th calibration source, which provides a 2.6 MeV gamma-ray due to the decay of ^{208}Tl. The 2.6 MeV gamma-rays can interact through pair-production, creating an electron and positron that share the whole energy. If the secondary gamma-rays emitted by the positron annihilation escape the detector, the pair-production events have a topology similar to 0νββ. These events are often called double escape peak (DEP) events after the peak they produce in the energy spectrum. They can be tagged through a selection based on their energy, which is precisely equal to $2614 - 2 \cdot 511 = 1592$ keV, i.e. the difference between the incoming photon energy and the energy of the two annihilation photons escaping the detector. A second sample of 0νββ-like events is created by the 2.6 MeV gamma-rays scattering only once within the detector. This second samples is composed of events with energy values between zero and the Compton edge at 2382 keV. The standard analysis makes use of single Compton events to calibrate the energy dependence of the A/E parameter (see Chapter 4 for a detailed study on its origin). After the correction, a lower threshold is set on A/E at the value which accepts 90% of DEP events: this is referred to as low or 1-sided cut. In addition, in order to reject surface events from regions which are close to the p^+ electrode, the mean $\mu_{A/E}$ and width $\sigma_{A/E}$ of the A/E distribution of DEP events are used to set an upper threshold to the value of $\mu_{A/E} + 3\sigma_{A/E}$. The setting of both thresholds results in a range of accepted A/E values and is referred to as 2-sided cut.

Both DEP and single Compton samples come with a certain contamination of undesired events, whose topology is not 0νββ-like: the contamination in the sample of single-Compton-scattered events is due to multiple-Comptons, which typically account for about 50% of the sample size; multiple-Compton-scattered events contaminate the pair-production sample, too, but at the level of just a few percent, thanks to the strict energy cut used to select the events. The difference between calibration samples and the actual 0νββ signal might lead to biases which are difficult to evaluate and are the focus of Chapter 4.

^{228}Th also provides samples of background-like events on which PSD can be tested. These are the γ-lines from ^{208}Tl and ^{212}Bi at 2.6 MeV and

1.62 MeV, respectively, which are mainly composed of multiple Compton scatterings, and the single escape peak (SEP) from the 2.6 MeV γ-ray, which includes those pair-production events where only one annihilation γ escapes detection, hence producing a peak at $2614 - 511 = 2103$ keV; being composed of an energy deposition of a 511 keV photon in addition to the electron and the positron, SEPs are intrinsically MSEs. Last, but certainly not least, ^{228}Th being a daughter nucleus of the primordial ^{232}Th, is expected to be present (although with very low concentrations) in the materials surrounding the detector array in GERDA. Its 2.6 MeV γ can deposit part of its energy in a dead material and exactly $Q_{\beta\beta}$ in germanium. Therefore, the fraction of events surviving the A/E cut at $Q_{\beta\beta}$ from a ^{228}Th source is an important information for the background budget of the experiment.

2.5 THE LEGEND EXPERIMENT

In 2016 the GERDA and MJD experiments joined their efforts and formed the LEGEND collaboration. The LEGEND experiment will pursue the search for $0\nu\beta\beta$ towards a ton-scale experiment with ^{76}Ge, in a phased approach: LEGEND-200 and LEGEND-1000, which will operate 200 kg and 1 t of enriched detectors, respectively.

The initial phase LEGEND-200 aims at a BI $\leqslant 2 \cdot 10^{-4}$ cts/(keV · kg · yr) to operate in the background-free regime, which, as we will see in Chapter 8, is a modest improvement to the GERDA result and hence within reach. At this background level, LEGEND-200 will reach a 3σ discovery sensitivity of 10^{27} yr with an exposure of 1 t yr within five years. This corresponds to an upper limit on $m_{\beta\beta}$ in the range 34–78 meV, which does not yet probe the full parameter space corresponding to the inverted neutrino mass ordering.

The ultimate goal of the LEGEND experiment is to cover it completely and to explore a large fraction of the parameter space corresponding to the normal ordering. To do that, its second phase LEGEND-1000 requires a significant improvement in the BI, which should not be higher than $1 \cdot 10^{-5}$ cts/(keV · kg · yr). With this background level, as shown in Figure 2.5, the LEGEND experiment will reach a 3σ discovery sensitivity of $1.3 \cdot 10^{28}$ yr within 10 years of operation. This converts to a value of $m_{\beta\beta}$ which covers the whole parameter space corresponding to the inverted neutrino mass ordering within a few standard deviations, for the state-of-the-art values of the NMEs [34, 35]. In addition to the values reported in [35], in March 2022 the first results from nuclear shell model (NSM) calculations for ^{100}Mo have been published [36], which correspond to a 99.7% C.L. discovery sensitivity for $m_{\beta\beta}$ of 33.8 meV and a 90% C.L. exclusion sensitivity of 28.9 meV.
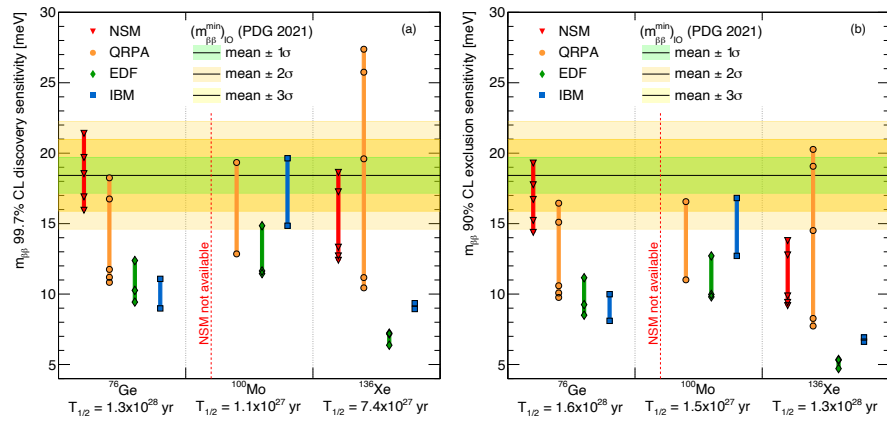
Figure 2.5: Comparison of $m_{\beta\beta}$ (a) 99.7% C.L. discovery sensitivity and (b) 90% C.L. median exclusion sensitivity for different isotopes for given half-life sensitivities, for different values of NMEs. The horizontal line shows the smallest value for $m_{\beta\beta}$ in inverted neutrino mass ordering, and the colored bands indicate the standard deviations coming from the uncertainties in the determination of the oscillation parameters. Taken from [35]. The new NSM calculations for ^{100}Mo [36] correspond to a 99.7% C.L. discovery sensitivity for $m_{\beta\beta}$ of 33.8 meV and a 90% C.L. exclusion sensitivity of 28.9 meV.

The LEGEND experiment adopts the successful GERDA experimental concept, i.e. the operation of bare HPGe immersed in LAr, instrumented as an active veto. The experimental challenge will be to operate many more detectors in the background-free regime, so that the sensitivity scales linearly with the exposure. Among the numerous strategies being pursued for this goal, the most relevant in the framework of this thesis is the development of the IC geometry [29]. As mentioned in Section 2.3, the goal for IC detectors is to achieve the same PSD performances as for BEGes, with a factor 3 higher mass per detector. This would result in a factor 3 fewer detectors for the same isotope mass, thus reducing the background from the surrounding *dead* material (cables, holders, electronics) by the same factor.

The understanding of the response of IC detectors to radiation has largely benefited from the present dissertation. Their extensive modeling will be discussed in Chapter 3 and Chapter 4, and the characterization of one of the first prototypes in Chapter 5. After the positive results from such characterization and from [37], five IC detectors have been produced from enriched material and have been deployed in the GERDA apparatus. Their characterization in the vendor's cryostat will be presented in Chapter 6 and their performances in the GERDA setup in Chapter 7.

2.5.1 Present status of LEGEND

The first phase, LEGEND-200, is being commissioned at LNGS at the time of writing and is scheduled to start taking data in 2022. The technical draw-

ing of its LAr cryostat is shown in Figure 2.6a. LEGEND-200 uses most on the existing GERDA infrastructure, though several upgrades have also taken place. First, the number of detector strings increased from 7 to 12, which will be arranged in a ring-shaped structure, as shown in Figure 2.6b, with the possibility to add an additional string at the center. This design was selected as it allows the installation of both an inner and outer fiber shroud, resulting in a more efficient collection of the scintillation light from Ar. With the same purpose, a thin copper shroud covered with tetraphenyl butadiene (TPB) [38] coated Tetratex [39], which has been called wavelength-shifting reflector (WLSR), surrounds the detector array and serves the task to reflect light back in the direction of the fibers. Additionally, detector base plates made out of polyethylene naphtalate (PEN) [40] will be used, in combination with a holding structure made out of electroformed copper [41]. Both these materials have extremely low level of radioactive impurities; moreover, PEN being a scintillating material, it will provide additional light for events originating in the proximity of the detectors (or from PEN itself), increasing the probability that they will be tagged by the LAr veto. Finally, the joint expertise on electronics of GERDA and MJD allowed to develop low mass front-end electronics (LMFE) which will guarantee lower electronics noise levels and possibly better signal and background discrimination.

2.6 SUMMARY

The GERDA experiment has searched for the $0\nu\beta\beta$ of ^{76}Ge, by operating bare HPGe detectors in an instrumented LAr bath. The choice of germanium offers several advantages, such as the intrinsic radio-purity of germanium crystals, the possibility to be used in the source=detector paradigm, the high containment efficiency for the electrons in the final state and the possibility to do PSD. The LEGEND experiment will use the same experimental concept as GERDA and, with the expertise from the MJD experiment on electroformed copper and LMFE, will continue the search for $0\nu\beta\beta$ with a factor 5 more mass in its first stage, LEGEND-200, and a factor 25 in the second, LEGEND-1000. With about a factor 50 improvement in the background level with respect to GERDA, LEGEND will cover the whole parameter space corresponding to the inverted ordering of the neutrino masses and explore a large fraction of the normal ordering.
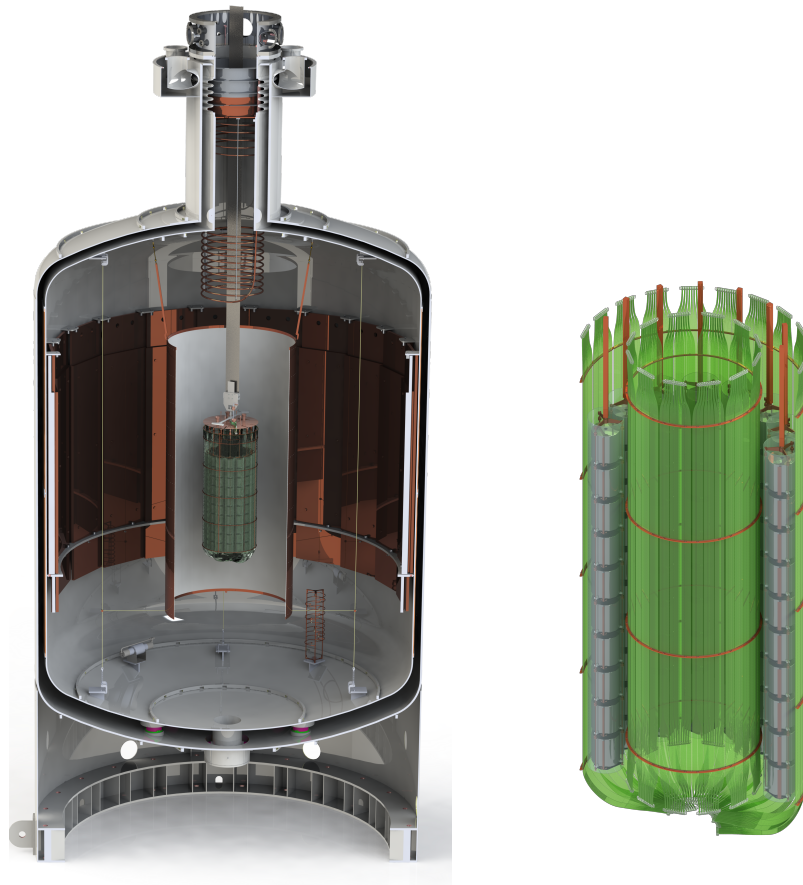
(a) Technical drawing of the LAr cryostat. (b) Detector array and fiber shroud (6 strings are removed from the drawing for clarity).

Figure 2.6: The LEGEND-200 cryostat and detector array. Image courtesy of Patrick Krause.

REFERENCES

[1]   J. Bardeen and W. H. Brattain, "The Transistor, A Semi-Conductor Triode," *Physical Review*, vol. 74, no. 2, pp. 230–231, 1948. DOI: `10.1103/physrev.74.230`.

[2]   R. D. Baertsch and R. N. Hall, "Gamma Ray Detectors Made from High Purity Germanium," *IEEE Transactions on Nuclear Science*, vol. 17, no. 3, pp. 235–240, 1970. DOI: `10.1109/tns.1970.4325695`.

[3]   E. J. Friebele, D. L. Griscom, and G. H. Sigel, "Defect centers in a germanium-doped silica-core optical fiber," *Journal of Applied Physics*, vol. 45, no. 8, pp. 3424–3428, 1974. DOI: `10.1063/1.1663795`.

[4]   J. Ballato *et al.*, "Glass-clad single-crystal germanium optical fiber," *Optics Express*, vol. 17, no. 10, p. 8029, 2009. DOI: `10.1364/oe.17.008029`.

[5] H. Bonet *et al.*, "Constraints on Elastic Neutrino Nucleus Scattering in the Fully Coherent Regime from the CONUS Experiment," *Physical Review Letters*, vol. 126, no. 4, p. 041 804, 2021. DOI: `10.1103/physrevlett.126.041804`.

[6] N. Abgrall *et al.*, "New Limits on Bosonic Dark Matter, Solar Axions, Pauli Exclusion Principle Violation, and Electron Decay from the Majorana Demonstrator," *Physical Review Letters*, vol. 118, no. 16, p. 161 801, 2016. DOI: `10.1103/physrevlett.118.161801`.

[7] C. E. Aalseth *et al.*, "CoGeNT: A search for low-mass dark matter using p-type point contact germanium detectors," *Physical Review D*, vol. 88, no. 1, p. 012 002, 2013. DOI: `10.1103/physrevd.88.012002`.

[8] T. Aralis *et al.*, "Constraints on dark photons and axionlike particles from the SuperCDMS Soudan experiment," *Physical Review D*, vol. 101, no. 5, p. 052 008, 2020. DOI: `10.1103/physrevd.101.052008`.

[9] E. Fiorini *et al.*, "A search for lepton non-conservation in double beta decay with a germanium detector," *Physics Letters B*, vol. 25, no. 10, pp. 602–603, 1967. DOI: `10.1016/0370-2693(67)90127-x`.

[10] J. Meija *et al.*, "Isotopic compositions of the elements 2013 (IUPAC Technical Report)," *Pure and Applied Chemistry*, vol. 88, no. 3, pp. 293–306, 2016. DOI: `10.1515/pac-2015-0503`.

[11] M. Agostini *et al.*, "Limits on uranium and thorium bulk content in GERDA Phase I detectors," *Astroparticle Physics*, vol. 91, pp. 15–21, 2017. DOI: `10.1016/j.astropartphys.2017.03.003`.

[12] M. Agostini *et al.*, "Pulse shape analysis in GERDA Phase II," *The European Physical Journal C*, vol. 82, no. 4, p. 284, 2022. DOI: `10.1140/epjc/s10052-022-10163-w`.

[13] B. J. Mount, M. Redshaw, and E. G. Myers, "Double-β-decay Q values of ^{74}Se and ^{76}Ge," *Physical Review C*, vol. 81, no. 3, 2010. DOI: `10.1103/physrevc.81.032501`.

[14] H. V. Klapdor-Kleingrothaus *et al.*, "Latest results from the HEIDELBERG–MOSCOW double beta decay experiment," *The European Physical Journal A - Hadrons and Nuclei*, vol. 12, no. 2, pp. 147–154, 2001. DOI: `10.1007/s100500170022`.

[15] C. E. Aalseth *et al.*, "Recent results of the IGEX ^{76}Ge double-beta decay experiment," *Physics of Atomic Nuclei*, vol. 63, no. 7, pp. 1225–1228, 2000. DOI: `10.1134/1.855774`.

[16] S. Schönert *et al.*, "The GERmanium Detector Array (Gerda) for the search of neutrinoless $\beta\beta$ decays of ^{76}Ge at LNGS," *Nuclear Physics B - Proceedings Supplements*, vol. 145, pp. 242–245, 2005. DOI: `10.1016/j.nuclphysbps.2005.04.014`.

[17] M. Agostini *et al.*, "Results on Neutrinoless Double-β Decay of ^{76}Ge from Phase I of the GERDA Experiment," *Physical Review Letters*, vol. 111, no. 12, p. 122 503, 2013. DOI: 10.1103/physrevlett.111.122503.

[18] Mirion, *Broad Energy Germanium detectors*. [Online]. Available: https://www.mirion.com/products/bege-broad-energy-germanium-detectors (visited on 03/08/2022).

[19] M. Agostini *et al.*, "Upgrade for Phase II of the GERDA experiment," *The European Physical Journal C*, vol. 78, no. 5, p. 388, 2018. DOI: 10.1140/epjc/s10052-018-5812-2.

[20] Mirion, *SAGe Well Detectors*. [Online]. Available: https://www.mirion.com/%5Ctextbackslash-well-detectors.

[21] M. Agostini *et al.*, "Characterization of inverted coaxial ^{76}Ge detectors in GERDA for future double-β decay experiments," *The European Physical Journal C*, vol. 81, no. 6, p. 505, 2021. DOI: 10.1140/epjc/s10052-021-09184-8.

[22] M. Agostini *et al.*, "Background-free search for neutrinoless double-β decay of ^{76}Ge with GERDA," *Nature*, vol. 544, no. 7648, pp. 47–52, 2017. DOI: 10.1038/nature21717.

[23] L. Pertoldi, *gedet-plots*, 2019. [Online]. Available: https://github.com/gipert/gedet-plots (visited on 03/08/2022).

[24] M. Knapp *et al.*, "The Gerda muon veto Cherenkov detector," *Nuclear Instruments and Methods in Physics Research Section A: Accelerators, Spectrometers, Detectors and Associated Equipment*, vol. 610, no. 1, pp. 280–282, 2009. DOI: 10.1016/j.nima.2009.05.115.

[25] K. Freund *et al.*, "The performance of the Muon Veto of the Gerda experiment," *The European Physical Journal C*, vol. 76, no. 5, p. 298, 2016. DOI: 10.1140/epjc/s10052-016-4140-7.

[26] C. Wiesinger, "No neutrinos not found: First exploration of neutrinoless double beta decay half-lives beyond 10^{26} years," Ph.D. dissertation, 2020.

[27] D. Budjáš *et al.*, "Pulse shape discrimination studies with a Broad-Energy Germanium detector for signal identification and background suppression in the GERDA double beta decay experiment," *Journal of Instrumentation*, vol. 4, no. 10, P10007, 2009. DOI: 10.1088/1748-0221/4/10/p10007.

[28] M. Agostini *et al.*, "Production, characterization and operation of ^{76}Ge enriched BEGe detectors in GERDA," *The European Physical Journal C*, vol. 75, no. 2, p. 39, 2015. DOI: 10.1140/epjc/s10052-014-3253-0.

[29] R. Cooper *et al.*, "A novel HPGe detector for gamma-ray tracking and imaging," *Nuclear Instruments and Methods in Physics Research Section A: Accelerators, Spectrometers, Detectors and Associated Equipment*, vol. 665, pp. 25–32, 2011. DOI: 10.1016/j.nima.2011.10.008.

[30] W. Shockley, "Currents to Conductors Induced by a Moving Point Charge," *Journal of Applied Physics*, vol. 9, no. 10, pp. 635–636, 1938. DOI: 10.1063/1.1710367.

[31] S. Ramo, "Currents Induced by Electron Motion," *Proceedings of the IRE*, vol. 27, no. 9, pp. 584–585, 1939. DOI: 10.1109/jrproc.1939.228757.

[32] M. Agostini *et al.*, "Signal modeling of high-purity Ge detectors with a small read-out electrode and application to neutrinoless double beta decay search in Ge-76," *Journal of Instrumentation*, vol. 6, no. 03, P03005–P03005, 2011. DOI: 10.1088/1748-0221/6/03/p03005.

[33] A. Lazzaro, "Signal processing and event classification for a background free neutrinoless double beta decay search with the GERDA experiment," Ph.D. dissertation, 2019.

[34] N. Abgrall *et al.*, "LEGEND-1000 preconceptual design report," *arXiv*, 2021.

[35] M. Agostini *et al.*, "Testing the inverted neutrino mass ordering with neutrinoless double-β decay," *Physical Review C*, vol. 104, no. 4, p. L042501, 2021. DOI: 10.1103/physrevc.104.l042501.

[36] L. Coraggio *et al.*, "Shell-model calculation of ^{100}Mo double-β decay," *Physical Review C*, vol. 105, no. 3, p. 034 312, 2022. DOI: 10.1103/physrevc.105.034312.

[37] A. Domula *et al.*, "Pulse shape discrimination performance of inverted coaxial Ge detectors," *Nuclear Instruments and Methods in Physics Research Section A: Accelerators, Spectrometers, Detectors and Associated Equipment*, vol. 891, pp. 106–110, 2018. DOI: 10.1016/j.nima.2018.02.056.

[38] V. Gehman *et al.*, "Fluorescence efficiency and visible re-emission spectrum of tetraphenyl butadiene films at extreme ultraviolet wavelengths," *Nuclear Instruments and Methods in Physics Research Section A: Accelerators, Spectrometers, Detectors and Associated Equipment*, vol. 654, no. 1, pp. 116–121, 2011. DOI: 10.1016/j.nima.2011.06.088.

[39] V. Boccone *et al.*, "Development of wavelength shifter coated reflectors for the ArDM argon dark matter detector," *Journal of Instrumentation*, vol. 4, no. 06, P06001, 2009. DOI: 10.1088/1748-0221/4/06/p06001. [Online]. Available: https://doi.org/10.1088/1748-0221/4/06/p06001.

[40] Y. Efremenko *et al.*, "Use of poly(ethylene naphthalate) as a self-vetoing structural material," *Journal of Instrumentation*, vol. 14, no. 07, P07006–P07006, 2019. DOI: 10.1088/1748-0221/14/07/p07006.

[41] N. Abgrall *et al.*, "The Majorana Demonstrator radioassay program," *Nuclear Instruments and Methods in Physics Research Section A: Accelerators, Spectrometers, Detectors and Associated Equipment*, vol. 828, pp. 22–36, 2016. DOI: 10.1016/j.nima.2016.04.070.

Part II

MODELING GERMANIUM DETECTORS FOR LEGEND

3 | CHARGE CLUSTER EVOLUTION AND SIGNAL DEVELOPMENT

In this chapter we investigate the collective effects in a cluster of charge carriers and their impact on signal formation in the detector geometries of interest for $0\nu\beta\beta$ searches. We performed comprehensive simulations of germanium detectors and validated them against the data acquired with the custom designed IC detector of Chapter 5. Its geometry is the one used as reference for this chapter. Our work builds on the results of [1], which reports the first observation of such collective effects in p-type point contact (PPC) detectors and discusses how to accurately model them. Our simulations have been carried out with the Majorana-Gerda (MaGe) [2] software framework based on GEometry ANd Tracking (GEANT4) [3], and a modified version of the SigGen software package [4] which already included the modeling of the collective effects and was used in [1]. More details on simulations are given in Appendix A.

This work has been published in [5].

3.1 CHARGE–CARRIERS COLLECTION AND SIGNAL FORMATION IN GERMANIUM DETECTORS

In Section 2.4.1 we have seen that the signal formation in germanium is described by the Shockley–Ramo theorem [6, 7], which we recall here:

Shockley-Ramo for point-like cluster

$$I(t) = q\, \mathbf{v}(\mathbf{x}(t)) \cdot \mathbf{E}_\omega(\mathbf{x}(t)) \tag{3.1}$$

(with q being the charge generated by an energy deposition, $\mathbf{v}(\mathbf{x}(t))$ the instantaneous drift velocity and $\mathbf{E}_\omega(\mathbf{x}(t))$ the weighting field at position $\mathbf{x}(t)$) and we have evaluated the weighting field $\mathbf{E}_\omega$ appearing in the equation on the three geometries used in the GERDA experiment. In this chapter we will drop the analysis for semi-coaxials and consider p-type point contact (PPC) detectors used in the MJD experiment [8], for their similarities with BEGes and ICs. The three detector types are shown in Figure 3.1 along with the resulting weighting field and illustrative trajectories.

The PPC detectors are also small contact p-type detectors, with a Li-diffused n^+ electrode and a B-implanted p^+ electrode; they have a cylindrical shape and masses up to $1\,\mathrm{kg}$. Their geometry is characterized by a
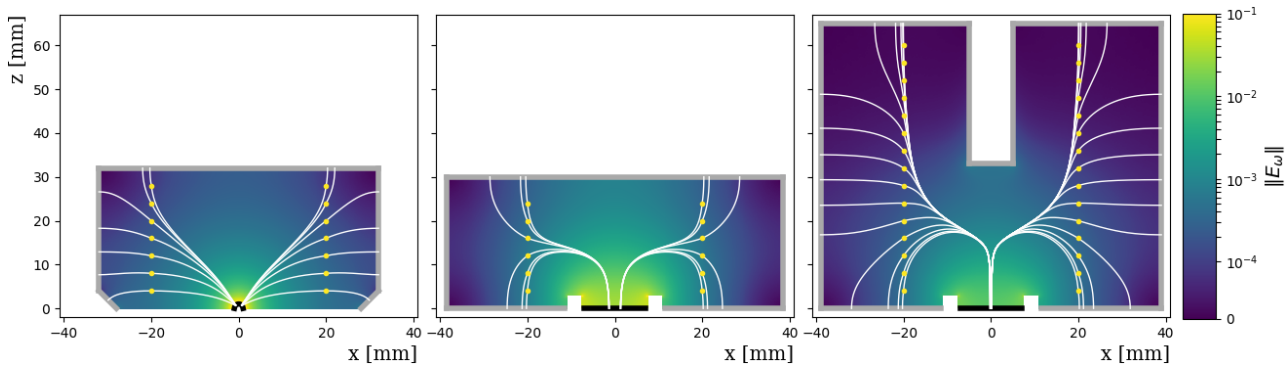
Figure 3.1: Weighting field E_ω for a cross section of the three geometries used in current and future $0\nu\beta\beta$ experiments: (from left) PPC, BEGe and inverted coaxial. The thick black and gray lines are the p^+ and n^+ electrode, respectively. The yellow points are locations of an energy deposition, the white trajectories connecting them to the p^+ electrode are the drift paths of holes and those connecting them to the n^+ electrode are the drift paths of electrons.

small (~2 mm diameter) p^+ electrode on one of the flat surfaces, while the rest of that flat surface is passivated. The remaining surface of the detector is covered by the n^+ electrode. Electrons are collected on the n^+ electrode that is kept at a few kV operational voltage, while holes on the p^+ electrode, that is grounded and used to read-out the signal. This geometry creates a weighting field that increases rapidly in the immediate vicinity of the p^+ electrode, resulting in a characteristic peak-like structure in the current signal when the hole clusters approach the p^+ electrode.

Compared to PPCs, BEGe detectors are shorter but have a larger radius. The major difference between the two geometries is the structure of the electrodes: the p^+ electrode is larger for BEGes (up to ~15 mm diameter) and surrounded by a passivated groove with typical depths of ~3 mm. The BEGe detectors' n^+ electrode extends down to the groove, wrapping around the crystal on all surfaces. As mentioned in Section 2.4.1, this structure creates the *funnel* effect [9]: holes are pushed towards the center of the detector and then move to the p^+ electrode along a fixed path that is independent of their starting point. Since that is the volume in which the weighting field is highest, according to Equation 3.1, the majority of the induced signals in a BEGe detector share the same maximum value of the current $I(t)$.

The IC detector has the same electrode structure as a BEGe, though it is about twice as long. In order to keep a high electric field throughout the whole volume, a hole is drilled on the opposite side of the p^+ electrode and constitutes part of the n^+ contact. It normally extends down to within 25–35 mm from the p^+ electrode. With the wrap-around n^+ electrode, the funneling is preserved and the trajectories converge in the region of high weighting field.

3.2 CHARGE–CARRIER COLLECTIVE EFFECTS

The modeling of the signal formation presented in the previous section does not account for the cluster spatial extension that is $\mathcal{O}(1)\,\mathrm{mm}$ for a MeV energy deposition. It can be extended to account for the non-null dimensions of the cluster. If we define $\mathbf{r}(t)$ as the distance of every charge in the cluster from the center of the distribution, the instantaneous signal induced at the electrode will be the integral of Equation 3.1 over the spatial charge distribution $Q(\mathbf{r}(t))$ of the cluster:

Shockley-Ramo for extended cluster

$$\widetilde{I}(t) = \int d\mathbf{r}\, Q(\mathbf{r}(t))I(t) \tag{3.2}$$

If the electric field varies on scales similar to the cluster size, charges at the opposite side of the cluster will experience different forces (accelerations), leading to a deformation of the cluster during its drift towards the electrodes. Moreover, the stochastic diffusion and self-interaction of the charge carriers will progressively increase the size of the cluster during its motion. The diffusion consists of a random thermal motion of the carriers while the self-interaction is the result of the Coulomb force. In this work, such processes are treated as collective effects [4]. That allows an analytical treatment and keeps the computational requirements to an affordable level. We compared this approximated collective description with a full multi-body simulation[1] and found that it does not introduce noticeable inaccuracies, as will be shown further down (Figure 3.3).

Charge-carrier collective effects modify the size of the cluster during the drift

In our collective treatment, we consider the effects of mutual repulsion and diffusion separately from those of acceleration, because the formers act in all directions, while the latter breaks the spherical symmetry and acts exclusively in the direction of motion.

The dynamics of drifting charges in the presence of mutual repulsion and diffusion can be treated assuming spherical symmetry, and is described by the continuity equation [10]:

$$\frac{\partial^2 Q}{\partial r^2} - \frac{2}{r}\frac{\partial Q}{\partial r} - \frac{1}{D}\frac{\partial Q}{\partial t} - Q\frac{\partial Q}{\partial r}\frac{1}{V_T}\frac{1}{4\pi\epsilon r^2} = 0 \tag{3.3}$$

where D is the diffusion coefficient, ϵ the permittivity in germanium and V_T the thermal voltage $V_T = k_B T/q$ with q being the elementary charge, k_B the Boltzmann constant and T the temperature of the crystal. The general solution of Equation 3.3 when the Coulomb repulsion term is neglected describes a gaussian profile for the charge cluster, whose width is

Impact of diffusion

$$\sigma_D = \sqrt{2Dt} \tag{3.4}$$

---

1 We simulated the individual motion of 10000 charges in the field generated by the detector and the instantaneous configuration of the other charges.

When charges drift in an electric field, the diffusion coefficient D has a longitudinal and transverse component. Both are calculated in `SigGen` [4] in the respective direction, but only the longitudinal is the responsible for the deformation of the signal. As reported in [11], this component is lower as the electric field strength increases. This implies that, with a sufficiently high impurity concentration, the effect of diffusion can be strongly limited (as stated also in [1]).

Impact of Coulomb self-repulsion   Neglecting the first two terms of Equation 3.3 and considering only the Coulomb self-repulsion, we obtain a solution in which the charge distribution behaves like an expanding sphere of radius σ_R:

$$\sigma_R = \sqrt[3]{\frac{3\mu q}{4\pi\epsilon}Nt} \tag{3.5}$$

where N is the number of charge carriers in the distribution and μ is the mobility of the carrier, which is related to the diffusion coefficient by the Einstein equation $D = \mu k_B T/q$. Both Equation 3.4 and Equation 3.5 describe a distribution which gets monotonously broader with time, with the difference that Equation 3.4 is completely determined by the detector properties, while Equation 3.5 depends on the deposited energy.

Impact of acceleration   The drifting in the electric field of the detector, on the other hand, enlarges or decreases the size of the cluster, according to whether it experiences accelerations or decelerations. The modeling of such effect is obtained from basic kinematics, and can be easily calculated for each time-step t_i as:

$$\sigma_A(t_{i+1}) = \sigma_A(t_i) \cdot \frac{v(t_{i+1})}{v(t_i)} \tag{3.6}$$

where $v(t_i)$ is the drift velocity at the time-step t_i. It is clear that in the direction of motion there is a strong interplay between the three described effects, which can give rise to non-linear effects on the cluster size.

Figure 3.2 displays the contribution of the mentioned processes to the charge cluster deformation[2]. The top-left plot shows the drift velocity field on an IC detector cross section, where superimposed in brown is the trajectory of holes for an energy deposition on the position marked with the star. As holes travel through the detector, they experience accelerations (decelerations) according to the electric field, stretching (shrinking) the cluster size in the direction of motion as shown in the top-right panel (light blue curve). In the same plot, the broadening effect due to the described Coulomb and diffusion processes are shown with the yellow and green curves, respectively: as described by Equation 3.4 and Equation 3.5, their effect is a monotonic enlargement of the cluster size, which, for an initial size of 0.5 mm, produce a

---

2 The initial cluster size is given here in Full Width Half Maximum, and it has been determined as a function of energy through Monte Carlo simulation.
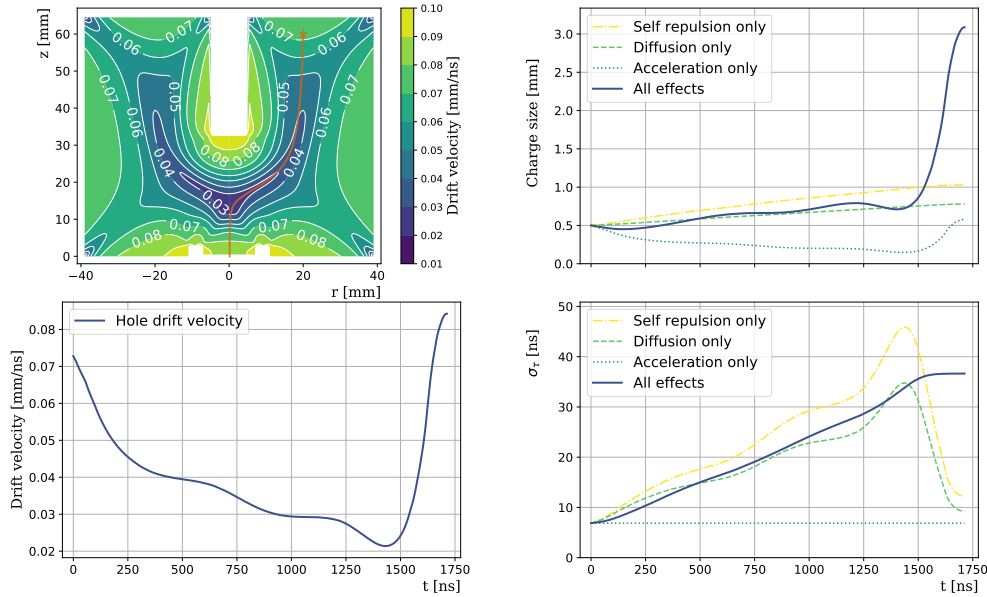
Figure 3.2: Breakdown of the collective effects on a charge cluster. The top-left plot shows the drift velocity field of an IC detector with superimposed in brown the drift path of the holes' cluster for an interaction location marked by the star. The cluster's drift velocity along the path is shown in the bottom-left plot. The evolution of the cluster's size and σ_τ is displayed in the top-right and bottom-right plot, respectively. The initial size of the cluster is 0.5 mm, the average for energy depositions of 1.6 MeV.

final cluster of about 1 mm. Finally, the dark blue curve shows the evolution of the cluster dimensions, when all effects act simultaneously. This results in extremely elongated clusters, which can reach sizes of about 3 mm. As anticipated, the total size is not just the simple sum of the three contributions, as they are not independent: an enlargement of the cluster size, for instance due to Coulomb or diffusion effects, emphasizes the difference in the drift velocity field of charges at the edge of the distribution, thus amplifying the effect of acceleration.

This amplification effect has been benchmarked with a full multi-body simulation. To keep the computational time to an affordable level, we limited the study to ∼ 7000 charges (corresponding to an energy deposition of 20 keV), whose motion has been simulated individually from creation in the upper volume of an IC detector until collection at the electrode. Their initial distribution has been approximated to have a gaussian profile with a standard deviation given by dedicated Monte Carlo simulations. The motion of every charge in such configuration is determined by the electric field generated by the position of the other charges, superimposed to the detector internal field. While the latter is a constant property of the detector, the former obviously depends on the instantaneous configuration of all charges and has been calculated, for a charge at distance r_i from the center of the distribution, as the Coulomb field generated by the charges contained in a

*Collective approach benchmarked with full multi-body simulation*
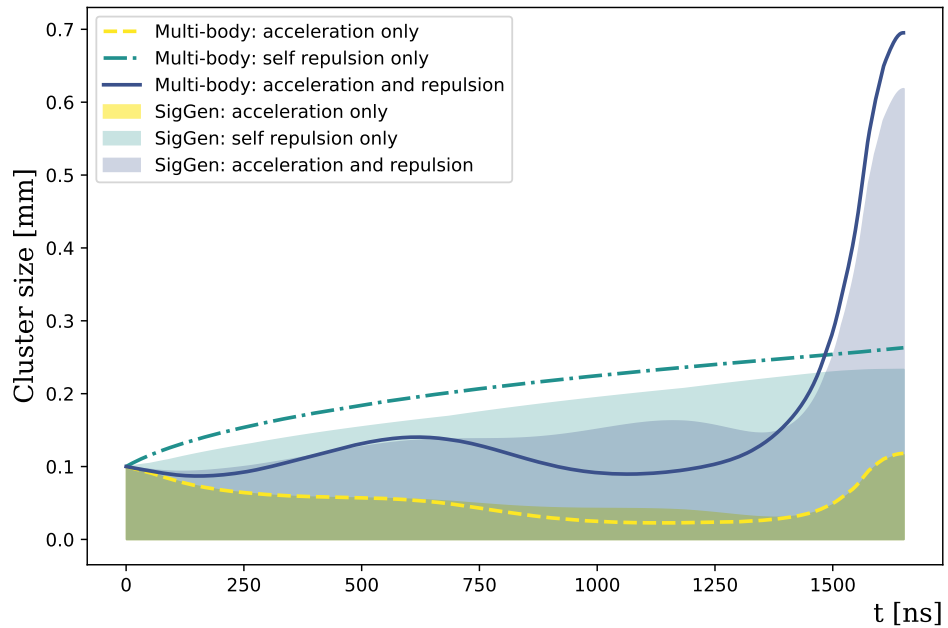
Figure 3.3: Comparison of the evolution of the cluster size as calculated by `SigGen` and by a dedicated multi-body simulation. In both cases, an energy deposition of 20 keV was simulated. The amplification effect of acceleration and self repulsion is well reproduced in `SigGen`.

radius $r \leqslant r_i$. The conversion from the resulting electric field to drift velocity has been performed using the same parametrization as in `SigGen` and the instantaneous position of charges has been calculated on a time step of 1 ns. Considering either of the electric fields or both at the same time allowed to evaluate the impact of acceleration and repulsion on the cluster size, both separately and together. Random scattering leading to diffusion was not implemented, as it would impact the results only quantitatively. The results of the full multi-body approach are shown in Figure 3.3 in comparison to those calculated by the collective approach of `SigGen`. Both the approaches produce results which are in good agreement when considering acceleration and self repulsion effects separately. More interestingly, the multi-body simulation reproduces the amplification effect coming from their interplay and therefore confirms the collective approach of `SigGen`.

From cluster deformations to signal formation

As seen in Section 2.4.2, the pulse shape for small anode detectors is mostly determined by the cluster of holes approaching the p^+ electrode. Therefore, its size at collection is the parameter which mostly affects it. More precisely, as the readout signal is in the time domain, its *time* profile depends on the *time* spread of the cluster (rather than its spatial extension), which we define in the following as $\sigma_\tau(t)$. The evolution in time of such parameter is displayed in the bottom right plot of Figure 3.2. The light blue curve shows that σ_τ is constant if only acceleration effects are considered. As other effects are switched on, their interplay gives a total time spread which can be up to a factor 5 larger than the initial value, reaching values of about 40 ns.
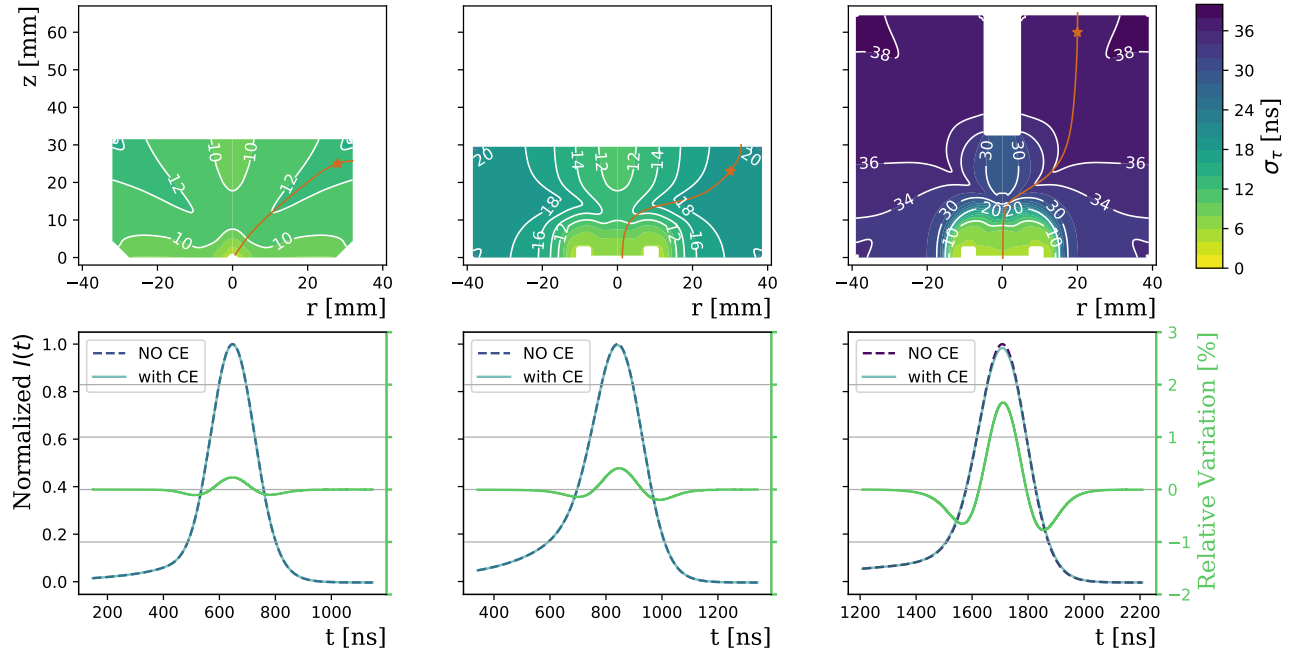
Figure 3.4: Top: values of the σ_τ parameter as a function of the interaction position, for the three geometries considered. Bottom: simulated signals for the interactions and drift paths indicated by the brown point and curve, with and without Collective Effects (CE). Higher values of σ_τ, as in inverted coaxial detectors, imply lower values of the current I(t).

The enlargement of the cluster size through the parameter σ_τ as a function of the interaction position is shown in Figure 3.4 (top), separately for the three considered geometries. For PPC detectors, the maximum enlargement is for interactions in the corners, where σ_τ reaches about 15 ns. The corners are the part of the detector from which the hole drift path is the longest. For BEGe detectors the maximum is slightly larger, up to 20 ns for radii larger than 30 mm. For inverted coaxial detectors the effect is much stronger, up to a factor 2 and it affects more than half of the detector volume. The impact on the signal shape is shown in the bottom row of Figure 3.4, where signals are shown with (light blue) and without (dark blue) the deformation caused by collective effects. The difference between the two cases is less than 0.5% of the signal amplitude in BEGe and PPC detectors (see green curve), but it is larger for inverted coaxials, where the maximum of the current signal is lowered by $\sim 2\%$ when collective effects are switched on.

The collective effects described in this section are expected for all detector geometries. Their impact on the signal shape, however, depends on the geometry and the impurity profile. In the second part of this chapter, we will evaluate such impact on advanced event reconstruction techniques such as those for $0\nu\beta\beta$ experiments.

3.3 EVENT DISCRIMINATION IN $0\nu\beta\beta$ EXPERIMENTS

3.3.1 Event discrimination in standard A/E analysis

$0\nu\beta\beta$ experiments using HPGe detectors rely heavily on PSA in order to reconstruct the topology of the energy deposition and thus discriminate between $0\nu\beta\beta$ and background. The effects discussed in Section 3.2 have the net result of blurring any features on the pulse shapes and, consequently, of worsening the performance of any PSA technique. In this section we evaluate their impact on the A/E method, the standard PSA technique in $0\nu\beta\beta$ experiments, which we have described in Section 2.4.2.

Collective effects and A/E   The A/E parameter is independent of the interaction position and its discrimination efficiency is constant throughout the whole detector volume. This is due to the fact that the holes approach the region of maximum weighting field along the same trajectory[3], regardless of the original location where the cluster was created. Without considering the collective effects, the A/E parameter is expected to have the same value for clusters with a given energy generated in most of the detector volume (The only exception, as we have seen in Section 2.4.2, is for interactions nearby the read-out electrode). Collective effects do depend on the interaction position (as shown by the σ_τ parameter in Figure 3.4) and this creates an A/E dependence from the interaction position.

Figure 3.5 shows the value of the A/E parameter for mono-energetic energy depositions simulated throughout the whole detector volume considering the collective effects described in Section 3.2. The A/E value varies by a few percent between the corners and the center of the detector in the BEGe and PPC geometry. As already mentioned, the value is significantly amplified only in about 3% of the detector volume around the p+ electrode. For inverted coaxial detectors, while the bottom half of the volume exhibits features similar to the BEGe geometry, the upper part shows a consistent 0.3% reduction of the A/E value.

Maximizing the detector volume is of primary importance for $0\nu\beta\beta$ experiments. However, the larger the collection path, the stronger the impact of these collective effects will be. In the following we evaluate the event-reconstruction performance of inverted coaxial detectors and discuss possible analysis techniques to correct for these collective effects. To quantify the performance we focus on the acceptance of $0\nu\beta\beta$-like events and of typical backgrounds of the experiments.

---

3 This is true for BEGe and IC detectors. The funneling effect is not present in the PPCs, because for that geometry the weighting field at the p^+ electrode is spherical, hence the signal does not depend on the angle from which the holes arrive.
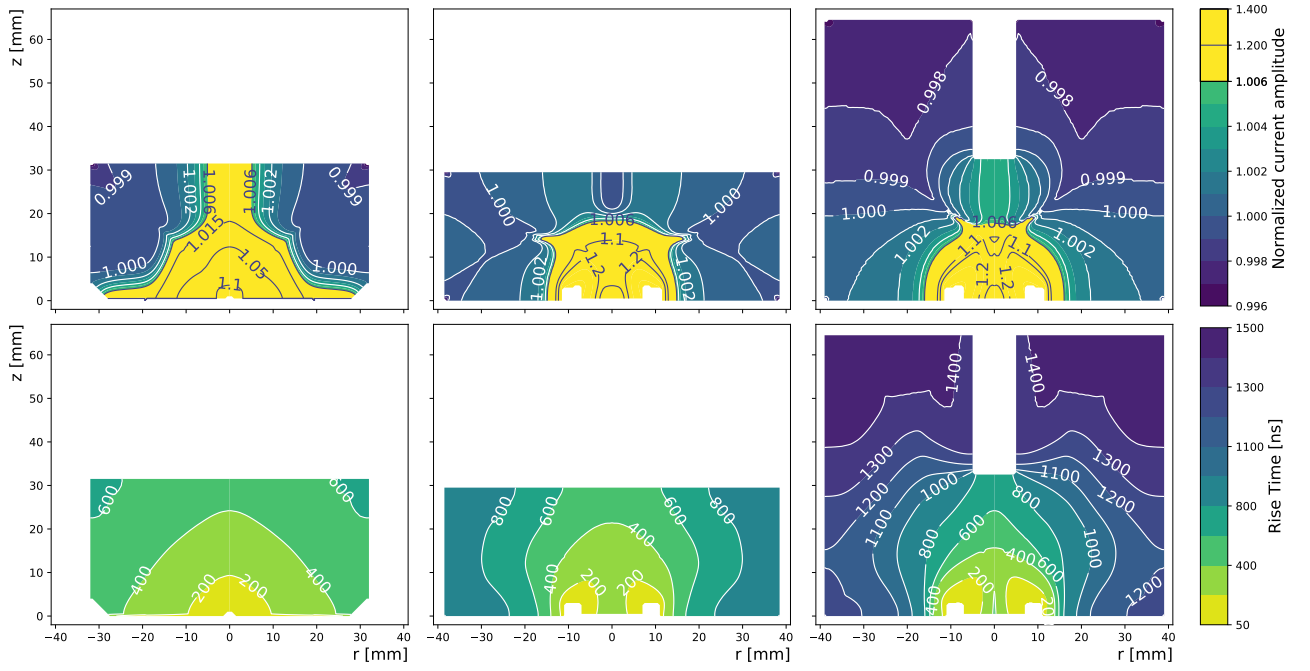
Figure 3.5: A/E (top) and rise time (bottom) values for the three analyzed geometries. In PPC and BEGe detectors rise times range up to 600–800 ns, while for inverted coaxials they can be twice as big, and saturate for high z-positions, where the threshold at 0.5% is no longer a good approximation of the beginning of charge collection. A correlation between A/E and rise time is visible for the inverted coaxial detector.

3.3.1.1 0νββ *acceptance*

We have seen in Section 2.4.2 that the event discrimination based on the A/E parameter is calibrated using DEP events from ^{208}Tl. The A/E distribution of DEP events is used to set a cut value which keeps 90% of their total number. This value cannot be directly translated to 0νββ acceptance, for two reasons: the first is that DEP and 0νββ events have a different energy. The second, DEP events are concentrated on corners, 0νββs are homogeneously distributed. Chapter 4 will be dedicated to the investigation of their topological differences and the impact on signal acceptance.

In order to estimate the 0νββ acceptance, we performed a Monte Carlo simulation of the energy deposited in 300 000 0νββ and DEP events. The Monte Carlo simulation takes into account all the physical differences between the two classes of events and their spatial distribution within the detector. For each event, the total signal is computed using the modeling described in Section 3.1 and Section 3.2 and analyzed to extract the A/E parameter. From the A/E distribution of DEP events, we set the cut value and applied it to the 0νββ population. This resulted in a final 0νββ acceptance of $(86.1 \pm 0.1(\text{stat}))\%$, which is compatible with the typical values for BEGe detectors [12] (see Table 3.1). Technical details on Monte Carlo and

From DEP to 0νββ with Monte Carlo simulations

| | **Simulations** | | |
| | IC | | BEGe [9, 12] |
Event class	*Standard*	*RT corr*	*Standard*
^{208}Tl DEP	90.00 (8)	90.08 (8)	90 (1)
^{208}Tl SEP	5.1 (3)	5.8 (3)	8 (1)
^{208}Tl FEP	7.4 (1)	8.1 (1)	12 (2)
CC @Q$_{\beta\beta}$ (^{208}Tl)	45.1 (3)	46.7 (3)	42 (3)
CC @Q$_{\beta\beta}$ (^{214}Bi)	20.3 (4)	21.8 (4)	–
$0\nu\beta\beta$	86.07 (6)	85.47 (6)	88 (2)

| | **Data** | | |
| | IC | | BEGe [9, 13] |
Event class	*Standard*	*RT corr*	*Standard*
^{208}Tl DEP	90.1 (8)	90.1 (8)	90 (1)
^{208}Tl SEP	5.0 (3)	5.3 (3)	5.5 (6)
^{208}Tl FEP	7.64 (5)	7.92 (5)	7.3 (4)
CC @Q$_{\beta\beta}$ (^{208}Tl)	32.3 (2)	33.1 (2)	34 (1)
CC @Q$_{\beta\beta}$ (^{214}Bi)	–	–	21 (3)

Table 3.1: Percentage of events classified as single-site for different event samples and detectors, taken from simulations and experimental data. For inverted coaxial detectors, the results are given both before (*Standard*) and after a correction based on the rise time (*RT corr*).

pulse shape simulation, as well as on the signal processing can be found in Appendix A.

3.3.1.2 *Background rejection*

From the Monte Carlo simulation of ^{208}Tl, we also extracted the A/E distributions of events from ^{208}Tl full energy peak (FEP), ^{208}Tl SEP as well as from the Compton continuum (CC) at Q$_{\beta\beta}$ from ^{208}Tl and ^{214}Bi. We applied the cut obtained from DEP events to these distributions and obtained the survival fraction of $(5.1 \pm 0.3)\%$ and $(7.4 \pm 0.1)\%$ for SEP and FEP events, respectively (see Table 3.1), and $(45.1 \pm 0.3)\%$ and $(20.3 \pm 0.4)\%$ for the Compton continuum at Q$_{\beta\beta}$ from ^{208}Tl and ^{214}Bi, respectively. The values, reported in Table 3.1, are in agreement with the typical theoretical values for BEGe detectors [9].

3.3.2 **Event discrimination after A/E correction based on the rise time**

As pointed out above, the impact of the collective effects is correlated with the time needed to collect the hole cluster. Following the proposal of [14], we tested a correction on the A/E parameter based on the reconstructed collection time of the signals, in order to restore the position independence.

In this work we reconstruct such a quantity by taking the time between two arbitrary thresholds on the signal, i.e. what is called the rise time[4]. Noise conditions can prevent accurate determination of the start time for thresholds below 0.5% at the energies of interest for $0\nu\beta\beta$ search. Hence, for this work we refer to rise time as the time between 0.5% and 90% of signal development[5]. A map of the mean rise time as a function of the interaction position within the detector is shown in Figure 3.5 for the three geometries considered. These rise time and A/E values are correlated in the inverted coaxial geometry. This is shown explicitly in Figure 3.6 for DEP (3.6a) and $0\nu\beta\beta$ (3.6b) events. Both plots suggest that a linear correlation could be used to align the A/E values in the bottom and top part of the detector volume.

A/E and charge collection time are correlated in IC detectors

This double peak structure has been first reported in [15, 16]. Its origin is connected by our work to the collective effects and the spatial distribution of DEP events within the detector. Indeed, the configuration of the inverted coaxial detector creates a region on the top and one on the bottom part of the detector in which rise time and A/E saturate to a limit value, which gets more represented than the others. This effect is even more pronounced for DEP events, which are more likely to occur on the detector edges.

A/E has a double-peak structure in IC detectors

Motivated by the correlation shown in Figure 3.6, we explored the impact of a first order linear correction of the A/E value based on the rise time for each event. The A/E maps before and after such correction are shown in Figure 3.7. The linear correction reduces the difference among A/E values: the volume that exhibits an A/E value of (1.000 ± 0.002) increases from 71% before correction to 89% after. At the same time, it creates a bulk volume where A/E values get lowered by almost 0.5%. This is due to the interplay between collective effects, which combine in such a way that the cluster deformation (hence A/E) is not univocally associated to the length of the drift paths. In order to determine whether it is convenient to apply the rise time correction or not, we tested it on the simulations of ^{208}Tl and $0\nu\beta\beta$. The results are reported in the second column of Table 3.1. The survival fraction of $0\nu\beta\beta$ events decreases after rise time correction from a value of (86.1 ± 0.1)% to (85.5 ± 0.1)%. In terms of background, the rise time correction increases the survival fraction of events at $Q_{\beta\beta}$ by (1.5 ± 0.3)%. The correction does not improve the overall efficiencies, but reduces the volume dependence of the PSA performance, possibly reducing the systematic uncertainties of the experiment.

A/E correction on rise time

---

4 Normally, the thresholds are set on the signal which is experimentally accessible, which means the output of the charge sensitive pre-amplifier. That is the charge signal $V(t)$, which is the integral of the current signal $I(t)$.

5 Other techniques, based on the convolution of the signal function with a well tuned impulse response function (e.g. an asymmetric trapezoidal filter), could lead to the identification of lower thresholds, such as 0.1% of the signal amplitude.
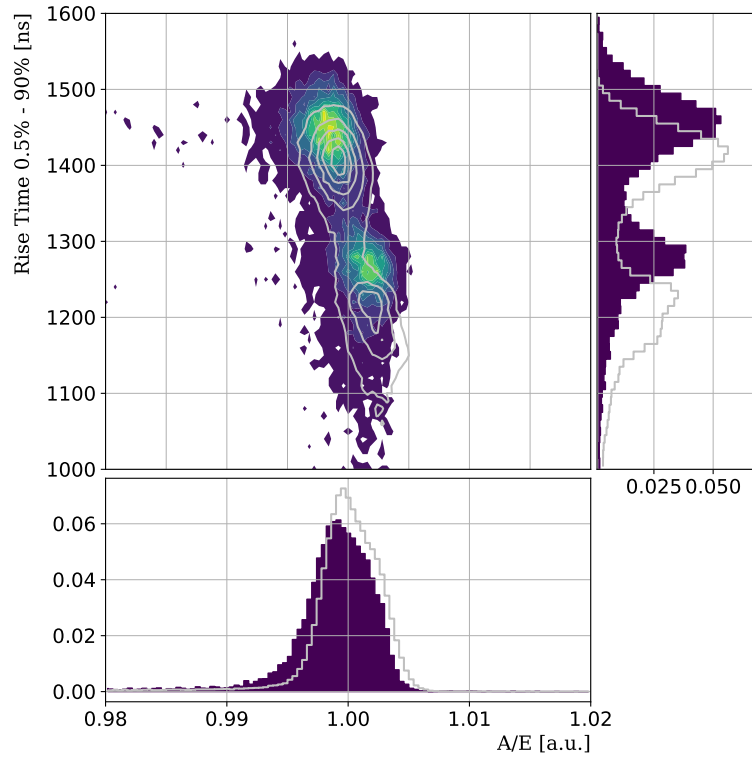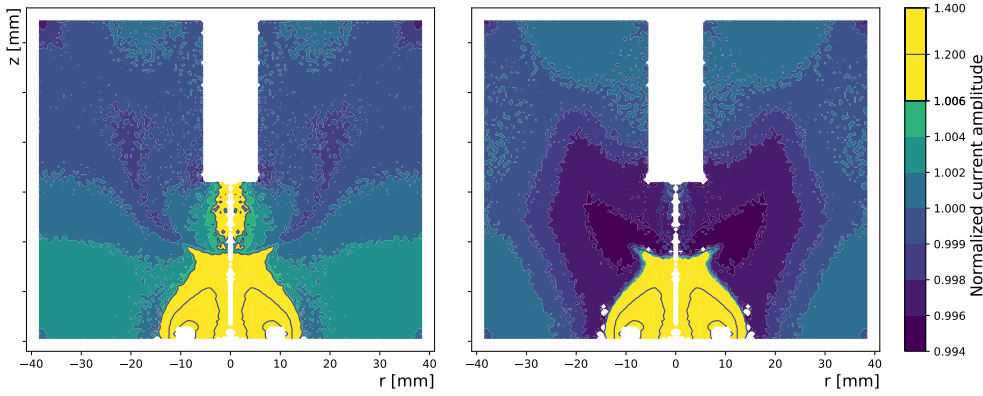
(a) DEP events from data (filled colored contour) and simulations (gray contour lines)
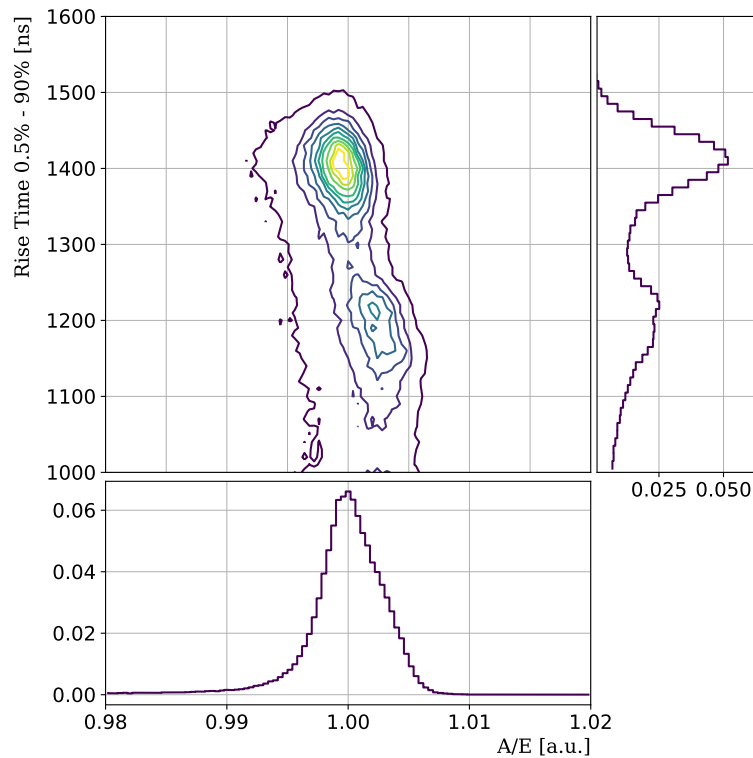
(b) $0\nu\beta\beta$ events from simulations

Figure 3.6: Distribution of the A/E and rise time for (3.6a) DEP events and (3.6b) $0\nu\beta\beta$ events. The distributions are shown for experimental data (color maps) and simulated data (contour lines).

Figure 3.7: A/E maps from Monte Carlo $0\nu\beta\beta$ events. The left plot shows the values of A/E normalized to 1 and the right plot shows the values after rise time correction.

3.3.3 Validation of the simulation

The distribution of the A/E and rise time from experimental data is shown in the coloured filled contour of Figure 3.6a, in comparison with simulations, represented by the gray contour lines. The 0.3% displacement in A/E between the two blobs is well reproduced by our work. This is not the case if collective effects are not included. The excess in data at low values of A/E is expected, as DEP events cluster on corners, where a fraction of events occurs in a transition layer where there is no electric field and the charge carriers move because of diffusion. This effect is not included in our simulation. The rise time is systematically underestimated by ~ 30 ns in our simulation. This disagreement does not affect the conclusions of our work and could in principle be improved by tuning the unknown parameters of the crystal, such as the impurity profile along the symmetry axis, or the temperature of the crystal, which impacts the hole mobility.

Experimental data for ^{208}Tl have been collected using a ^{228}Th source, which we described in Section 2.4.2, and used to extract the survival fractions of the different classes of events, both before and after rise time correction. The numbers, reported in Table 3.1, show an agreement $< 0.5\%$ with simulations for SEP and FEP events. Some tension appears when comparing the survival fractions of the Compton continuum at $Q_{\beta\beta}$. This can been traced back to inaccuracies in the positioning of the source. The distance between radioactive source and detector changes the fraction of multiple-site events from cascade of gammas (this was also observed in [9]). This does not affect the populations of SEP and FEP events, since for them a knowledge of the underlying background is available from the side-bands (details in [17, 18]). The impact of the rise time correction on data, even if not statistically significant, reflects what is found with simulations, namely that it increases the acceptance of FEP and SEP events, as well as of background

Data and simulations agree if collective effects are considered
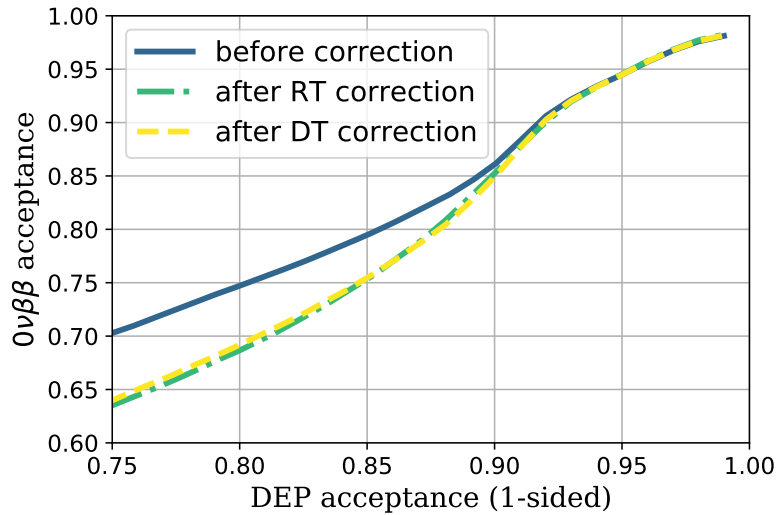
Figure 3.8: Acceptance of $0\nu\beta\beta$ events as a function of DEP's, in the case of no-correction on A/E (blue curve), or after rise time (green curve) and drift time (yellow curve) correction.

at $Q_{\beta\beta}$. In summary, the modeling developed reproduces the A/E results within 0.2% and hence its systematic uncertainties are lower than the impact of the collective effects that we wanted to study.

3.4 CONCLUSIONS AND DISCUSSION

In this chapter we discussed the collective effects in clusters of charge carriers in germanium detectors and the impact of such effects on signal formation, with particular focus on the consequences for $0\nu\beta\beta$ experiments with ^{76}Ge. We determined that the deformation of the signal due to collective effects is relevant for detectors with long drift paths. In particular, we observed in the inverted coaxial geometry a position dependence of the standard pulse shape discrimination parameter used in $0\nu\beta\beta$ experiments (A/E). With the combined use of Monte Carlo and pulse shape simulations of ^{208}Tl and $0\nu\beta\beta$s of ^{76}Ge, we determined that such volume dependence does not impact the pulse shape discrimination performances significantly. This proved to be the case both using the standard A/E analysis, and implementing a correction based on the reconstruction of the drift path.

Detector performances should be compared at the same $0\nu\beta\beta$ acceptance

As detector volumes keep on increasing, the impact of collective effects on A/E might become stronger (see Chapter 6). Moreover, the background composition at $Q_{\beta\beta}$ will change, too, for different detector geometries. With such conditions, it is meaningful to compare detector performances at the same $0\nu\beta\beta$ acceptance. This could be used in the future to fix the A/E cut on DEP events. A visual representation of the $0\nu\beta\beta$ acceptance as a function of the acceptance of DEP events is displayed in Figure 3.8, both before and

after rise time correction. No appreciable difference was observed when the true drift time (extracted from the simulations) was used for the correction.

As planned by LEGEND, inverted coaxial detectors will be deployed in environments which are more challenging than a vacuum cryostat and exhibit different electronics noise conditions. In this work we explored the impact of a factor 5 higher noise level. This has the effect of blurring the features on the pulse shape (resulting in a higher A/E resolution) and of worsening the precision on the determination of charge collection time. The impact on PSD is (for a cut at 90% DEP acceptance) an increase in the $0\nu\beta\beta$ acceptance of 3%, but at the same time an increase of 5% in the background events surviving the A/E cut at $Q_{\beta\beta}$. This is compatible with values of other BEGe detectors already in use in GERDA [12]. We also explored the performances of inverted coaxial detectors with lengths in the range 8–9 cm and determined that are still compatible with those presented here.

REFERENCES

[1] S. Mertens *et al.*, "Characterization of high purity germanium point contact detectors with low net impurity concentration," *Nuclear Instruments and Methods in Physics Research Section A: Accelerators, Spectrometers, Detectors and Associated Equipment*, vol. 921, pp. 81–88, 2019. DOI: 10.1016/j.nima.2018.09.012.

[2] M. Boswell *et al.*, "MaGe-a Geant4-Based Monte Carlo Application Framework for Low-Background Germanium Experiments," *IEEE Transactions on Nuclear Science*, vol. 58, no. 3, pp. 1212–1220, 2011. DOI: 10.1109/tns.2011.2144619.

[3] S. Agostinelli *et al.*, "Geant4—a simulation toolkit," *Nuclear Instruments and Methods in Physics Research Section A: Accelerators, Spectrometers, Detectors and Associated Equipment*, vol. 506, no. 3, pp. 250–303, 2003. DOI: 10.1016/s0168-9002(03)01368-8.

[4] D. C. Radford, `fieldgen` and `siggen` *software*, 2014. [Online]. Available: https://github.com/radforddc/icpc%5C_siggen.

[5] T. Comellato, M. Agostini, and S. Schönert, "Charge-carrier collective motion in germanium detectors for $\beta\beta$-decay searches," *The European Physical Journal C*, vol. 81, no. 1, p. 76, 2021. DOI: 10.1140/epjc/s10052-021-08889-0.

[6] W. Shockley, "Currents to Conductors Induced by a Moving Point Charge," *Journal of Applied Physics*, vol. 9, no. 10, pp. 635–636, 1938. DOI: 10.1063/1.1710367.

[7] S. Ramo, "Currents Induced by Electron Motion," *Proceedings of the IRE*, vol. 27, no. 9, pp. 584–585, 1939. DOI: 10.1109/jrproc.1939.228757.

[8] C. E. Aalseth *et al.*, "Search for Neutrinoless Double-β Decay in ^{76}Ge with the Majorana Demonstrator," *Physical Review Letters*, vol. 120, no. 13, p. 132 502, 2018. DOI: 10.1103/physrevlett.120.132502.

[9] M. Agostini *et al.*, "Signal modeling of high-purity Ge detectors with a small read-out electrode and application to neutrinoless double beta decay search in Ge-76," *Journal of Instrumentation*, vol. 6, no. 03, P03005–P03005, 2011. DOI: 10.1088/1748-0221/6/03/p03005.

[10] E. Gatti *et al.*, "Dynamics of electrons in drift detectors," *Nuclear Instruments and Methods in Physics Research Section A: Accelerators, Spectrometers, Detectors and Associated Equipment*, vol. 253, no. 3, pp. 393–399, 1987. DOI: 10.1016/0168-9002(87)90522-5.

[11] C. Jacoboni *et al.*, "Electron drift velocity and diffusivity in germanium," *Physical Review B*, vol. 24, no. 2, pp. 1014–1026, 1979. DOI: 10.1103/physrevb.24.1014.

[12] M. Agostini *et al.*, "Probing Majorana neutrinos with double-β decay," *Science*, vol. 365, no. 6460, pp. 1445–1448, 2019. DOI: 10.1126/science.aav8613.

[13] D. Budjáš *et al.*, "Pulse shape discrimination studies with a Broad-Energy Germanium detector for signal identification and background suppression in the GERDA double beta decay experiment," *Journal of Instrumentation*, vol. 4, no. 10, P10007, 2009. DOI: 10.1088/1748-0221/4/10/p10007.

[14] D. C. Radford, *Personal communication*, 2018.

[15] A. Domula *et al.*, "Pulse shape discrimination performance of inverted coaxial Ge detectors," *Nuclear Instruments and Methods in Physics Research Section A: Accelerators, Spectrometers, Detectors and Associated Equipment*, vol. 891, pp. 106–110, 2018. DOI: 10.1016/j.nima.2018.02.056.

[16] T. Comellato *et al.*, "Performance of custom designed inverted coaxial HPGe detectors for GERDA and LEGEND," *Nuclear Instruments and Methods in Physics Research Section A: Accelerators, Spectrometers, Detectors and Associated Equipment*, vol. 936, pp. 247–248, 2018. DOI: 10.1016/j.nima.2018.10.042.

[17] M. Agostini *et al.*, "Pulse shape analysis in GERDA Phase II," *The European Physical Journal C*, vol. 82, no. 4, p. 284, 2022. DOI: 10.1140/epjc/s10052-022-10163-w.

[18]   V. E. Wagner, "Pulse Shape Analysis for the GERDA Experiment to Set a New Limit on the Half-life of $0\nu\beta\beta$ Decay of ^{76}Ge," Ph.D. dissertation, 2017.

4 | TOPOLOGIES OF $0\nu\beta\beta$ EVENTS AND CALIBRATION PROCEDURE BIASES

A $0\nu\beta\beta$ event in Ge detectors would manifest as a mono-energetic and well-localized energy deposition inside the detector. The whole decay energy is transferred to the two emitted electrons, whose summed kinetic energy is equal to the Q-value of the decay, i.e. $Q_{\beta\beta} = 2039\,\text{keV}$ for ^{76}Ge. The two electrons are likely to share evenly the decay energy, but extreme cases in which one electron takes most of the energy are also possible. Electrons at these energies have an absorption length of about a millimeter in Ge. However, secondary Bremsstrahlung photons produced during the electron absorption can occasionally travel several millimeters from their production vertex before interacting, producing secondary energy deposition sites. Thus, the topology of $0\nu\beta\beta$ events is complex and its understanding is fundamental to develop techniques for discriminating the sought-after events from those due to background, for instance gamma-rays scattering multiple times within the detector.

The results of this chapter are ready for submission as [1].

4.1 CHARACTERIZATION OF THE EVENT SPATIAL DISTRI–BUTION

4.1.1 Absorption of electrons in Ge

Electrons lose energy mainly through collisional losses, i.e. ionization and excitation. As the energy loss occurs via interaction with orbiting electrons, a large fraction can be lost in a single collision. For this reason, their trajectory follows a tortuous path, where the energy loss per collision is inversely proportional to the energy of the electron. An example of the path for an electron depositing $2\,\text{MeV}$ through collisions on a germanium medium is shown in Figure 4.1a. Every point in the plot corresponds to a collision, where an energy proportional to the size of the marker is transferred to the medium. The color code marks the time evolution, which flows from darker to brighter and is $\mathcal{O}(10)\,\text{ps}$. In this case, because of its starting momentum, the electron moves from left to right almost undisturbed, until its energy is comparable to that of the orbiting electrons. This occurs at a distance of

Electrons lose energy through collisions...
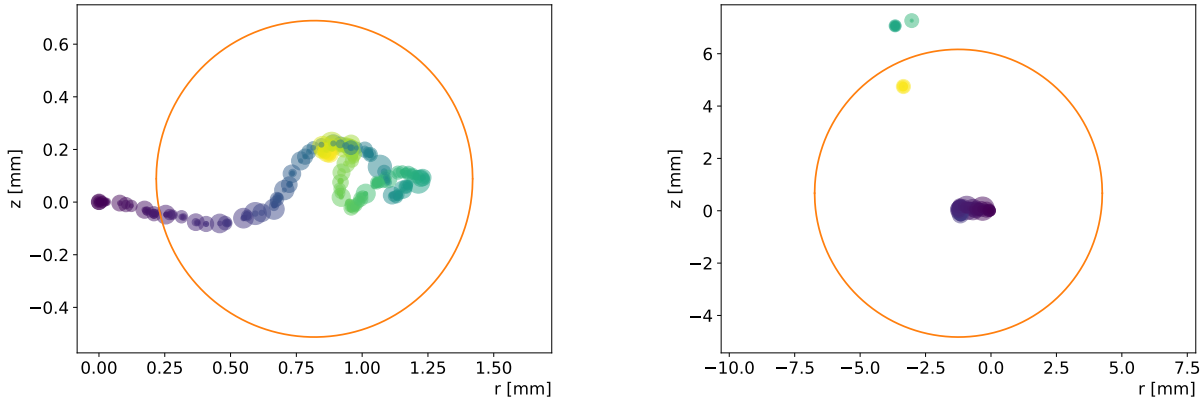
(a) Trajectory of an electron with an initial energy of 2 MeV, losing energy in germanium through collisions.

(b) Trajectory of an electron with an initial energy of 2 MeV, losing energy in germanium through collisions and radiation.

Figure 4.1: Energy depositions of a 2 MeV electron in germanium, through collisional (a) and collisional plus radiative (b) losses. The orange circle is centered around the center of energy and its radius is the R_{90} parameter described in the text. The path was simulated in 3 dimensions, and is reported here in cylindrical coordinates with respect to the starting point, which was taken as origin.

~1 mm in Figure 4.1a, where the electron begins to move in Brownian motion.
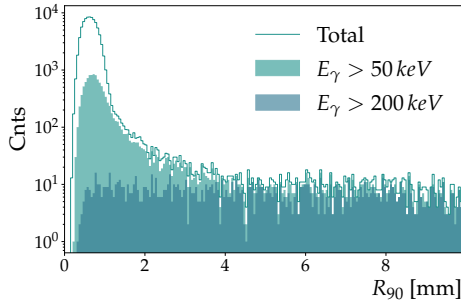
...and radiation

In addition to this, electrons, as every accelerated charged particle, lose energy also radiating Bremsstrahlung gammas, which can occasionally travel up to a few centimeters in the detector, producing secondary interaction sites. This is shown in Figure 4.1b, where a gamma with an energy of 216 keV is emitted from the cluster around the origin and travels several millimeters upwards before undergoing multiple Compton scatterings.

*Spatial distributions of electrons in a medium can be described with R_{90}*

Therefore, according to the case, energy depositions from electrons with the same energy can produce very different spatial distributions. How broad they are can be captured using the R_{90} parameter. This is defined as the minimum radius of the sphere which is centered around the energy-weighted mean of the coordinates of energy depositions (what is often referred to as center of energy), and contains 90% of the total deposited energy. Although we have seen that the spatial distributions of electrons are not a perfect sphere, R_{90} does give an effective indication of their broadness: as shown in Figure 4.1, in the case of energy loss through collisions (Figure 4.1a) this parameter is ~0.6 mm, while it can increase by an order of magnitude if a gamma-ray with sufficient energy is also emitted (Figure 4.1b).

Collisional losses produce a peak in R_{90} distributions

We can thus use this definition to parametrize the size of the spatial distributions of electrons depositing energy in germanium and estimate both qualitatively and quantitatively how they are affected by the emission of Bremsstrahlung gammas. As an example, we extracted the R_{90} parameter for energy depositions of electrons with an initial energy of 2 MeV. As shown with the empty histogram in Figure 4.2a, the majority of events have
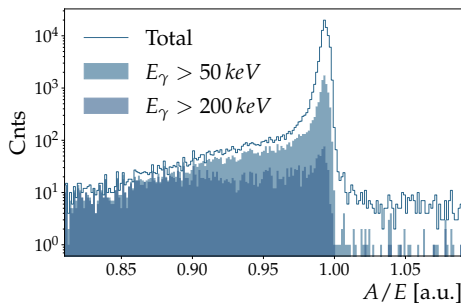
(a) R_{90} distribution from a primary electron with an energy of 2 MeV. The line histogram shows the total distribution, and the filled ones represent the subsets of events where an energy E_γ higher than 50 and 200 keV is converted into Bremsstrahlung radiation.
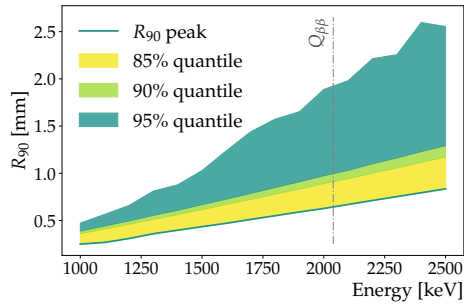
(b) Dependence of the R_{90} distributions on energy. The green line follows the dependence of the peak, the yellow, light and dark green bands the 85%, 90% and 95% quantiles, respectively

(c) A/E distribution from a primary electron with an energy of 2 MeV. The line histogram shows the total distribution, and the filled ones represent the subsets of events where an energy E_γ higher than 50 and 200 keV is converted into Bremsstrahlung radiation.
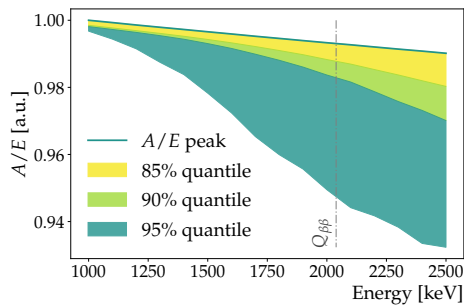
(d) Dependence of the A/E distributions on energy. The green line follows the dependence of the peak, the yellow, light and dark green bands the 85%, 90% and 95% quantiles, respectively

Figure 4.2: R_{90} and A/E distributions from absorption of monoenergetic electrons in germanium, and their dependence on energy.

an R_{90} value centered around 0.6 mm, and a fraction of them populate a tail at higher values. In order to confirm the radiative origin of such tail, we built the R_{90} distributions of the subset of events where a gamma-ray with energy higher than 50 keV and 200 keV is emitted. These are the filled histograms of Figure 4.2a, which show that these events are entirely responsible for the tail in the R_{90} distributions.

Radiative losses produce a tail in R_{90} distributions

The event topology is affected by the electron initial kinetic energy, both in the collisional and in the radiative sector. As summarized in Table 4.1 and as we shall see in the following, this has an impact on both the peak and the tail of R_{90} distributions.

As the scattering length of electrons increases with energy, the spatial distributions get on average broader. This is captured by the position of the R_{90} peak (shown with the green line labeled with R_{90} *peak* in Figure 4.2b), which shifts from a value of 0.2 mm at 1 MeV, to 0.8 mm at 2.5 MeV. Obviously, the

Collisional losses with higher energy shift R_{90} peak position

Energy [MeV]	R_{90} peak [mm]	$\sigma_{R_{90}}$ [mm]	peak-to-tail [%]
1.0	0.25	0.07	4.7
1.5	0.43	0.13	5.4
2.0	0.63	0.18	6.5
2.5	0.84	0.24	6.5

Table 4.1: Summary of the parameters of interest for the description of spatial distributions of electrons in germanium, and their evolution with energy.
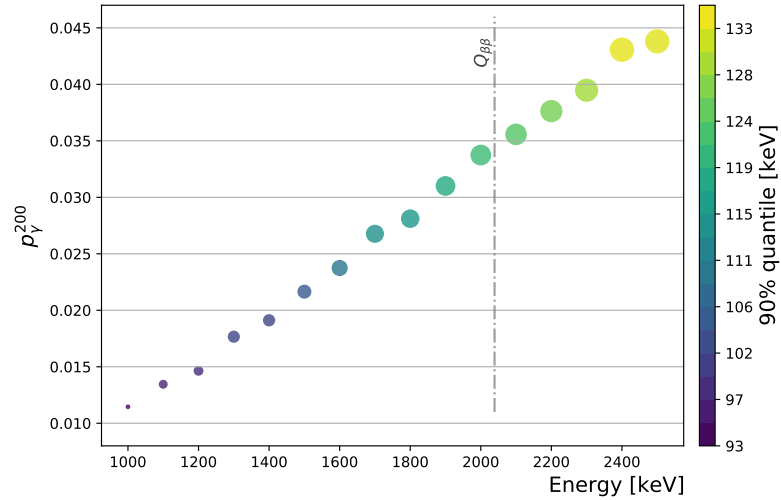
Figure 4.3: Probability of emitting a photon with energy greater than 200 keV, as a function of the energy of the primary electron. Both the marker size and color indicate the 90% quantile of the photons' energy spectrum.

variance $\sigma_{R_{90}}$ of the peak also increases, as reported in Table 4.1. Moreover, with increasing energy of the electron, the emission probability for a high energetic gamma-ray increases, too. This is shown in Figure 4.3, where the fraction of events p_γ^{200} where an energy greater than 200 keV[1] is converted into Bremsstrahlung is given as a function of the energy of the primary electron. From 1 to 2.5 MeV, this fraction increases from 1 out of 100 events, to 1 out of 25. With the help of the color scheme and the marker size, both indicating the 90% quantile of the Bremsstrahlung energy spectrum, Figure 4.3 also shows that, with increasing primary energy, Bremmstrahlung gammas are also more energetic. Therefore, with increasing energy, not only the spatial distributions get on average broader, but the fraction of exceptionally enlarged ones increases, as well. This is reflected in the R_{90} distributions as a shift of events from the peak to the tail, as is shown in Table 4.1, under the peak-to-tail label[2]. This change in the shape of the R_{90} distributions can be captured tracking the evolution of their quantiles with energy. As shown in

Radiative losses with higher energy change peak-to-tail ratio in R_{90}

---

1 200 keV is the energy threshold which corresponds to photon scattering length of ≈ 10 mm in germanium

2 This value is calculated taking the ratio of the integral outside and inside the main R_{90} peak. The delimiting point was arbitrarily taken 4σ away from the centroid of the peak.
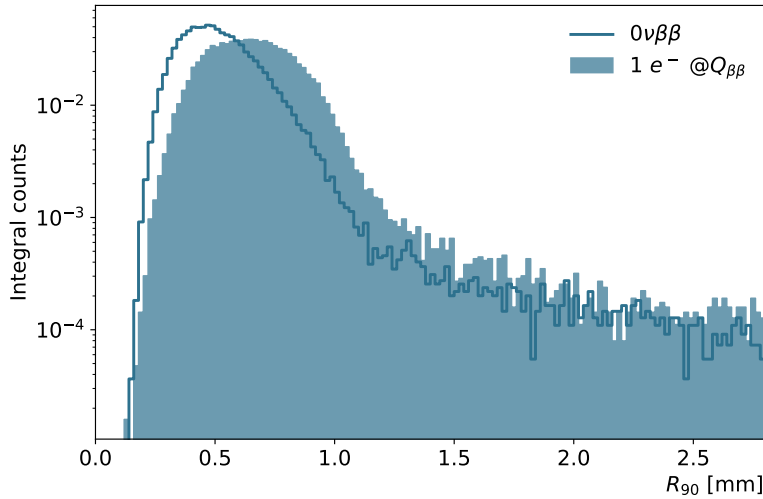
Figure 4.4: Comparison of the R_{90} distribution from $0\nu\beta\beta$ (empty histogram) and a single electron with initial energy equal to $Q_{\beta\beta}$ (filled histogram).

Figure 4.2b, the quantiles of the distributions increase with energy, although, because of the shift of events from the peak to the tail, with different proportionality constants than the R_{90} peak centroid.

R_{90} peak and quantiles follow different energy dependences

4.1.2 From single electron to $0\nu\beta\beta$

The experimental signature of $0\nu\beta\beta$ is an energy deposition of 2 electrons sharing the full Q-value of the decay ($Q_{\beta\beta} = 2039\,\text{keV}$). The two electrons are likely to share evenly the decay energy, though extreme cases in which one carries most of it are also possible. According to the energy share, their spatial distributions can exhibit features which are typical of those of a 1 MeV electron as well as those of a 2 MeV. Overall, as shown in Figure 4.4, the R_{90} distribution of $0\nu\beta\beta$ events and a single electron with an initial energy equal to $Q_{\beta\beta}$ largely overlap, meaning that their spatial distributions have *on average* the same size and that a discrimination between the two cannot be pursued based on this parameter.

Single and double electron cannot be distinguished

Every technique aiming to select $0\nu\beta\beta$ events must be calibrated with samples with a topology which is similar to $0\nu\beta\beta$. The topological differences between these samples and the actual $0\nu\beta\beta$ signal can lead to biases which are the focus of the next sections.

4.2 $0\nu\beta\beta$–EVENT IDENTIFICATION TECHNIQUES

4.2.1 Event reconstruction with A/E and correlation with R_{90}

According to what we have said in Section 2.4.2 on the A/E technique, electron events characterized by only collisional losses will produce point-like energy depositions, i.e. SSEs. Those accompanied by hard Bremsstrahlung are MSEs and thus will be characterized by A/E values lower than the average, signaling a larger spatial distribution with secondary interaction sites. This is shown explicitly in Figure 4.2c, where the A/E reconstruction of the events of Figure 4.2a is reported. As for the R_{90} distribution, the majority of the events fall into a narrow peak at $A/E \sim 1$. The Bremsstrahlung gamma events populating the tail at large R_{90} values are now responsible for the tail at low A/E values.

Similarly to what we have done for the R_{90} parameter, we studied the energy dependence of the centroid and a few quantiles of the A/E distributions. Figure 4.2d shows that the peak in the A/E distribution decreases linearly with energy by about 1% per MeV. The quantiles of the distribution decrease faster and non-linearly with the energy.

With a similar approach as in [2], we studied explicitly the correlation between R_{90} and A/E plotting in Figure 4.5 one against the other for the absorption of electrons between 1 and 2.5 MeV. The main feature is the
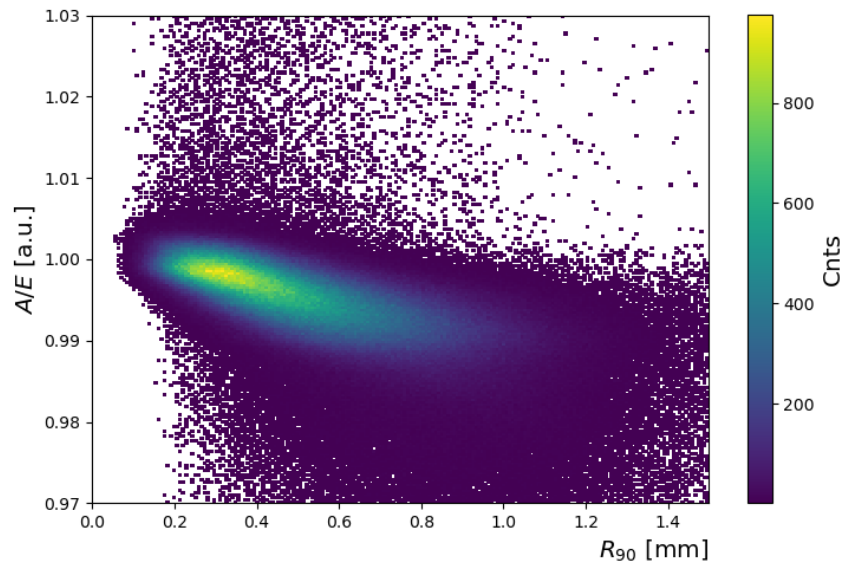
Collisional losses produce a SSE, radiative losses produce a MSE

A/E peak and quantiles follow different energy dependences

Figure 4.5: Correlation between A/E and R_{90} for absorption of electrons between 1 and 2.5 MeV.

densely populated band with A/E values between 0.99 and 1, and R_{90} between 0.2 mm and 0.8 mm, representing the correlation between the narrow peaks of R_{90} and A/E. This reflects that, as R_{90} gets larger, the energy depositions tend to be less localized, thus giving lower values of A/E. Outside the

band, we observe events with $A/E > 1$, which are known to be generated by interactions in the volume surrounding the anode [3], and Bremsstrahlung events, populating the region of $A/E < 0.99$ and $R_{90} > 0.3$ mm.

Though an inverse proportionality between A/E and R_{90} is expected for all small anode detectors, the magnitude depends on the detector geometry and the resulting electric field. For this work, the inverted coaxial detector studied in Chapter 3 (and which will be characterized in Chapter 5) was taken as a reference.

4.2.2 Standard A/E calibration samples and limitations

As we have seen in Section 2.4.2, the standard calibration samples are obtained by irradiating the detectors with a ^{228}Th source. The 2.6 MeV gammas from its daugher ^{208}Tl can provide two classes of 0νββ-like events in the interaction with the detector:

- *Single Compton Scattering*: events in which the gammas scatter only once in the detector, before leaving the active volume. In such cases the energy between zero and the Compton edge at 2.4 MeV is transferred to a single electron

- *Pair-production with double escaping gammas ($0\gamma e^+ e^-$)*: events in which the 2.6 MeV gammas interact through pair-production inside the detector creating an electron-positron pair[3]. If the two photons from the annihilation of the positron escape the detector, the energy deposition occurs only through the electron and the positron, which deposit $2614 - 2 \cdot 511 = 1592$ keV in the detector

As the first class provides samples of 0νββ-like events at all energies up to the Compton edge, it is used to calibrate the energy dependence of A/E and correct for it. The correction is performed by tracking the centroid of the A/E peak for samples of selected energies between 1 and 2.4 MeV, and fit its energy dependence with a linear function. Such samples come with a contamination of multiple-Compton scatterings that populate the tails of the A/E distributions. For this reason, the energy dependence of the peak value of A/E can be tracked, but the quantiles, like we have done in Section 4.2, cannot.

On the other side, $0\gamma e^+ e^-$ events always deposit the same energy, hence the contamination of single- and multiple-Compton-scattered events can be limited to a few percents by selecting a strict energy range. This can be further reduced using the knowledge of the sides of the energy peak, and

Single Compton events are used to calibrate the A/E energy dependence...

...but they have an unknown contamination of multiple Compton

$0\gamma e^+ e^-$ events are used to fix the A/E cut...

---

3 In the rest of the dissertation these events are referred to as DEP after the peak they produce in the energy spectrum. In the present chapter we use this new terminology to emphasize their similarity with the two electrons of 0νββ events.

an almost pure sample of $0\nu\beta\beta$-like events can be obtained. For this reason, $0\gamma e^+e^-$ events are taken as main proxy of signal-like events and the A/E cut is set to the value corresponding to their 90% quantile. The drawback of this procedure is that $0\gamma e^+e^-$ events from ^{228}Th deposit an energy which is ~500 keV lower than $Q_{\beta\beta}$.

...but they occur at energy lower than $Q_{\beta\beta}$

4.3 $0\nu\beta\beta$–TAGGING EFFICIENCY AND SYSTEMATIC UN– CERTAINTIES

Differences between $0\gamma e^+e^-$ and $0\nu\beta\beta$

The 90% quantile of $0\gamma e^+e^-$ events does not translate directly into a $0\nu\beta\beta$-tagging efficiency, because using $0\gamma e^+e^-$ events as a proxy of $0\nu\beta\beta$ has two biases. First, the former occurs at 1592 keV, while the latter at $Q_{\beta\beta} = 2039$ keV. As the standard A/E correction follows the energy dependence of the peak value and not of the quantiles, the different composition of the tails (which, in turn, depends on the Bremsstrahlung composition and changes with energy) is not taken into account. Ideally, in order to keep the tagging efficiency of $0\nu\beta\beta$-like events constant through energy, one would need to correct for the energy dependence of the chosen quantile (e.g. 90%) and not of the peak value. However, such a tracking would require pure samples of point-like events at all energies, which are not accessible with ^{228}Th. Second, $0\gamma e^+e^-$ and $0\nu\beta\beta$ have a different geometrical distribution. Given the dynamics of $0\gamma e^+e^-$ events, they are more likely to occur on detector lateral surfaces and corners, where the probability for the annihilation photons to escape detection is maximal. Conversely, $0\nu\beta\beta$ events are homogeneously distributed within the detector.

The differences between calibration samples from a ^{228}Th source and $0\nu\beta\beta$ were early recognized [3], and have been accounted for in the computation of the systematic uncertainties of the $0\nu\beta\beta$-tagging efficiency in the GERDA experiment [4]. In the next section, we will present a precise measurement of these systematic uncertainties, which represent the biases introduced in the $0\nu\beta\beta$-tagging efficiency by using ^{228}Th as a calibration source. Additionally, by adopting a two steps approach, we will estimate quantitatively how the two sources of bias separately impact the central value of the $0\nu\beta\beta$-tagging efficiency. Specifically, we will study:

1. The difference between $0\gamma e^+e^-$ events at 1.6 MeV and at $Q_{\beta\beta}$

2. The difference between $0\gamma e^+e^-$ at $Q_{\beta\beta}$ and $0\nu\beta\beta$.

The first step studies the bias of a calibration based on a sample of events with different kinetic energy than $0\nu\beta\beta$. The advantage of breaking down the two contributions is that this step can be investigated experimentally using a ^{56}Co source, which provides $0\gamma e^+e^-$ events below and above $Q_{\beta\beta}$.

The second step quantifies how the 0νββ-tagging efficiency is biased when using a calibration sample with a different geometrical distribution than 0νββ and will be discussed with the support of Monte Carlo simulations.

4.3.1 Energy dependent 0νββ–tagging with a ^{56}Co source

For this study, a custom-made ^{56}Co source was produced by the Jagiellonian University in Krakow. Its decay is characterized by several high-energy gamma-lines up to 3.6 MeV. For this reason, it was early recognized as a valuable source to calibrate germanium detectors [5, 6]. In the framework of our study, 5 gammas with energy higher than 2.5 MeV and branching ratio bigger than 1% are particularly interesting, as the probability of creating electron-positron pairs for them is high enough to give statistically significant samples of $0\gamma e^+e^-$ events (an additional gamma line at 3451 keV also produces a $0\gamma e^+e^-$ event at 2429 keV, which was however excluded from the analysis for a peculiar shape of its A/E distribution). Their energies, listed in Table 4.2 next to their original gamma-lines, lie in the range between 1.5 and 2.5 MeV, which means they constitute samples of almost pure 0νββ-like events both below and above $Q_{\beta\beta}$. Therefore, ^{56}Co offers the unique opportunity to interpolate the tagging efficiency of signal-like events at $Q_{\beta\beta}$.

The ^{56}Co source

The ^{56}Co source provided by the Jagiellonian University had a starting activity of 90 kBq at the beginning of the data taking. In order to gain sufficient statistics, we acquired data for 2 weeks with the source positioned at 20 cm from the lateral surface of our inverted coaxial detector. The resulting spectrum is shown in the top plot of Figure 4.6, in the range where the $0\gamma e^+e^-$ events occur. The empty grey and filled blue histograms show the spectrum respectively before and after the A/E cut calibrated on ^{228}Th. The ratio between the two is shown in the middle plot, where the 6 peaks from $0\gamma e^+e^-$ events are clearly visible. The bottom plot shows how all the events from the decays of ^{56}Co populate the A/E spectrum. Its description is analogous to Figure 4.5: the high density horizontal band centered around 1 represents all the energy depositions which occurr in a single location, while the band below contains all the events which deposit energy in more than one site, and the region where A/E is higher than 1 represents those which occur in the volume surrounding the anode. In this spectrum, $0\gamma e^+e^-$ and single Compton events are distributed around A/E = 1, while multiple Compton scatterings populate the region where A/E < 1.

In order to quantify the biases in the standard 0νββ-tagging efficiency, data from ^{56}Co have been calibrated with a ^{228}Th source. Specifically, the energy correction was performed using the energy dependence of the Compton samples from ^{228}Th, and the cut value was set on the 90% quantile of

Analysis followed standard calibration with ^{228}Th
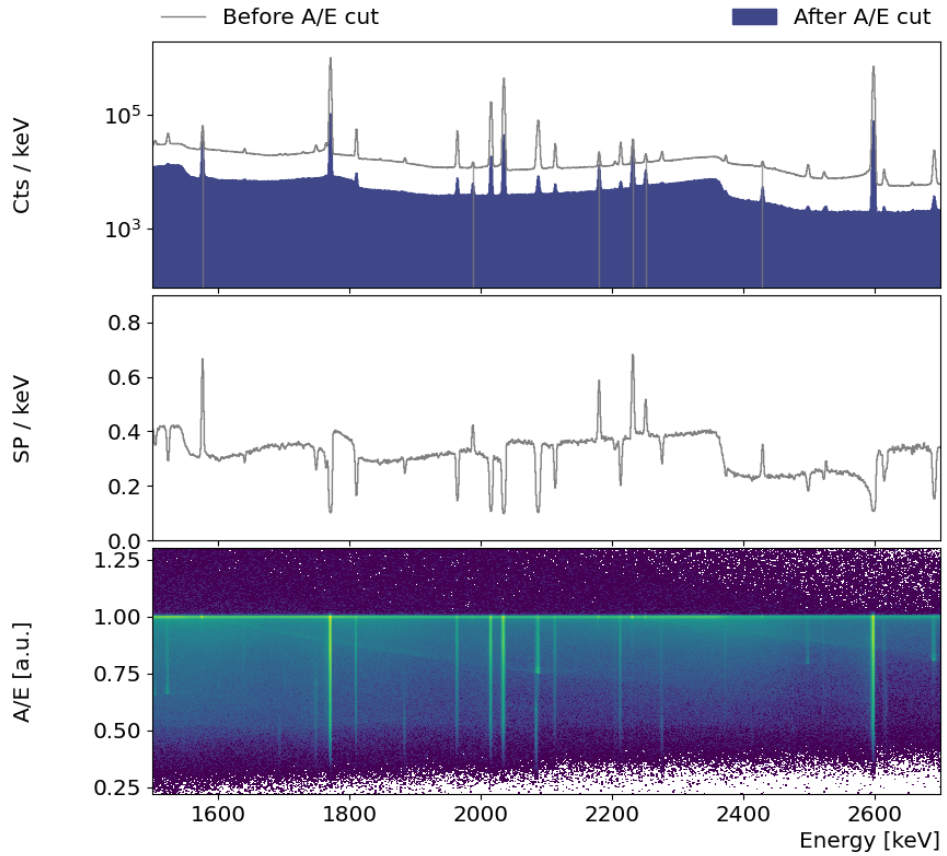
Figure 4.6: Region of interest of the energy (top) and A/E (bottom) spectrum obtained from a ^{56}Co source. The middle plot shows the Survival Probability (SP) of every energy bin after an A/E cut calibrated on a ^{228}Th source. The position of the $0\gamma e^+e^-$ events in the energy spectrum are marked with a solid gray line.

the A/E distribution of the $0\gamma e^+e^-$ events at 1592 keV. The resulting tagging efficiencies for the $0\gamma e^+e^-$ events from ^{56}Co are listed in the fourth column of Table 4.2, under the *Data* label, and shown with the light blue squares in Figure 4.7.

The fraction of tagged events is systematically lower than 90%, even at 1576 keV. Even though a small decrease is expected due to the effect of the higher A/E threshold, the tagging efficiency for this peak is 1% smaller than the value at 1592 keV from the calibration on ^{228}Th. This constitutes a limitation of the analysis, which, due to the complexity of the ^{56}Co spectrum (which exhibits many different features in the A/E space, see Figure 4.6), does not select a completely pure sample of $0\gamma e^+e^-$ events. For this reason, we take 1% as systematic uncertainty of the method. Additionally, the tagging efficiency decreases as a function of the energy, reaching a value of $(86.3 \pm 0.4)\%$ at $Q_{\beta\beta}$. This behaviour was expected, as the energy correction based on ^{228}Th tracks the centroid of the A/E distributions, but not the 90% quantile.

In view of extending the discussion to $0\nu\beta\beta$ itself, we crosschecked the

*Signal-tagging efficiency decreases with energy because calibration with ^{228}Th tracks energy dependence of the A/E peak and not of the quantiles*

Simulation of a ^{56}Co source agrees with data

E (FEP) [keV]	E (DEP) [keV]	BR %	**Data** SP %	**Simulations** SP %
2598.5	1576.5	17	88.8 (5)	88.6 (4)
3009.6	1987.6	1	86.0 (30)	87.4 (27)
3202.0	2180.0	3	84.6 (11)	85.9 (10)
3253.5	2231.5	8	85.6 (6)	85.0 (5)
3273.1	2251.1	2	83.9 (18)	85.4 (16)

Table 4.2: Energies of the DEPs used in our ^{56}Co analysis and respective Survival Probability (SP) after A/E cut. Information on the energy and Branching Ratio (BR) of the relative FEPs are also given as reference.
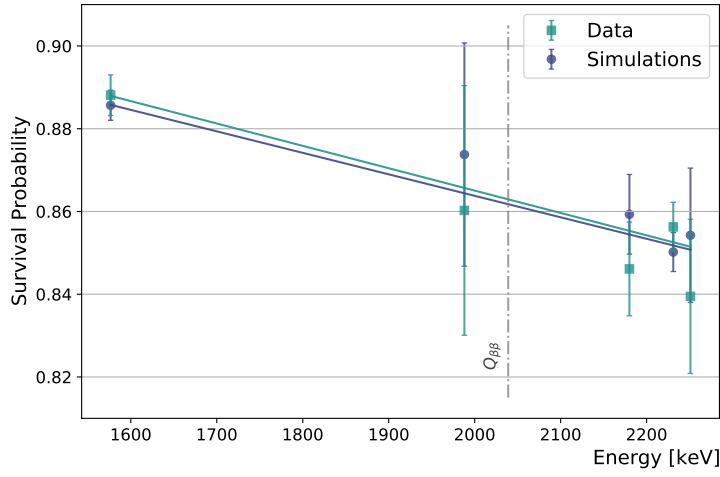
Figure 4.7: Survival probability of $0\gamma e^+ e^-$ events from ^{56}Co after A/E cut. Light blue squares indicate results from simulated data, dark blue circles from simulations.

accuracy of our simulations tools with these data. We performed a Monte Carlo simulation of a ^{56}Co source shining on the side of our detector and produced the electrical signals accordingly, including the collective effects of Chapter 3. After the calibration of A/E with a (simulated) ^{208}Tl source, we obtained the efficiencies for ^{56}Co events listed in the fifth column of Table 4.2, under the *Simulations* label, and shown with the dark blue circles in Figure 4.7. Simulations agree with data within the statistical uncertainties, yielding a tagging efficiency of $(86.2 \pm 0.3)\%$ at $Q_{\beta\beta}$, which is in good agreement with the experimental value.

As a corroboration of this result, we explicitly simulated a $0\gamma e^+ e^-$ event occurring directly at $Q_{\beta\beta}$. The tagging efficiency for such an event is $(86.5 \pm 0.4)\%$, in excellent agreement with the value from the interpolation. Furthermore, this simulation allows to compare directly the A/E distributions of $0\gamma e^+ e^-$ events at 1.6 MeV and $Q_{\beta\beta}$, as shown in Figure 4.8 with the yellow and dark blue lines, respectively. Though some discrepancies are expected in the shape of the A/E peak because of the different volumes sampled by

Simulation of a $0\gamma e^+ e^-$ event at $Q_{\beta\beta}$ and comparison with $0\nu\beta\beta$

the primary gamma rays, we observe that the difference in energy between the two samples impacts most significantly the tails for A/E values around 0.95, but not at very low values.
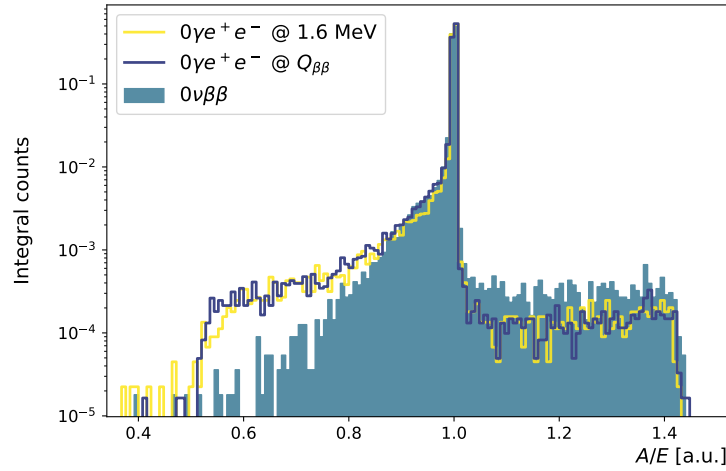

Figure 4.8: A/E distributions of pair production events and $0\nu\beta\beta$.

Comparing the tagging efficiency of $0\gamma e^+ e^-$ events at $Q_{\beta\beta}$ with $0\nu\beta\beta$ gives the estimation of the bias of calibrating the $0\nu\beta\beta$-tagging using a $0\gamma e^+ e^-$ event, which has a different geometrical distribution than $0\nu\beta\beta$. The value for $0\nu\beta\beta$ has been determined through Monte Carlo simulation, similarly to how it was done in Chapter 3, yielding an acceptance of $(85.2 \pm 0.4)\%$[4], i.e. a further reduction of 1% in the tagging efficiency. As can be seen from the comparison of the A/E distributions in Figure 4.8, this further reduction is a complex balance of features at low and high A/E values. First, $0\gamma e^+ e^-$ events exhibit a higher tail at very low A/E values. Being present for $0\gamma e^+ e^-$ events at 1.6 MeV as well, it suggests its origin to be intrinsically related to the dynamics of pair-creation. Regarding the high A/E side, being $0\nu\beta\beta$ homogeneously distributed, a higher fraction of events occurs in the volume surrounding the p^+ electrode, which gives electrical signals with higher A/E.

As a final remark, the discrimination efficiency depends also on the electronics noise. In order to be comparable with the GERDA noise environment, we injected a factor 5 higher electronics noise into our dataset and performed the same analysis. This yielded a $0\nu\beta\beta$-tagging efficiency of $(87.1 \pm 0.4)\%$[5], which is consistent within the systematic uncertainties shown in [4].

At the end of Phase I, an experimental effort with a ^{56}Co source was carried out with semi-coaxial detectors in the GERDA infrastructure, and no evidence for an energy dependence of the $0\nu\beta\beta$-tagging efficiency was even-

---

4 The value here shows some tension with what we reported in Chapter 3, as it has been obtained with a slightly changed analysis routine.

5 Though an increase in the $0\nu\beta\beta$-tagging efficiency is desirable, this comes at the expense of a higher increase in the acceptance of background, as also stated in [7]

tually stated [8]. However, the pulse shape analysis to reject multiple-site interactions in semi-coaxial detectors is based on an artificial neural network and not on the A/E parameter [4]. Also, for that work, the experimental conditions were far more challenging than a vacuum cryostat, which led the statistical fluctuations to be larger than the effect we observed in this work.

4.4 CONCLUSIONS AND OUTLOOK

In this chapter we characterized the spatial distributions of the energy deposition of electrons in germanium and studied their evolution as a function of their initial kinetic energy. We identified a connection between the spatial distributions and the estimator used in $0\nu\beta\beta$ experiments to discriminate single and multiple interaction sites. We used these information to investigate the topological differences between $0\nu\beta\beta$ events and those used to calibrate its tagging, and evaluate the consequent biases in the standard calibration procedures. With the help of a ^{56}Co source, we determined that the bias of a calibration based on ^{228}Th is a 5% reduction in the $0\nu\beta\beta$-tagging efficiency, in the best noise conditions of a vacuum cryostat. We estimated that, using an electronics noise comparable to the level in the GERDA environment, this reduces to 3%. In the future LEGEND experiment, which aims at intermediate noise levels between the two configurations, a $0\nu\beta\beta$-tagging efficiency within 85% and 87% could be foreseen.

With the support of simulations, we found that, out of the 5% reduction, a 4% contribution comes from the procedure for the energy dependence correction of A/E, which follows the centroid of the A/E distributions and does not track the different number of events in the tails due to Bremsstrahlung events. We also found that the remaining 1% comes from the difference in the geometrical distribution between $0\gamma e^+ e^-$ events and $0\nu\beta\beta$. Although in the GERDA analysis this bias is accounted for in the systematic uncertainties, we have also shown that, with a proper detector modeling, the central value of the $0\nu\beta\beta$-tagging efficiency can be accurately estimated.

In view of future experiments, ^{56}Co offers the opportunity to estimate experimentally the tagging efficiency of $0\nu\beta\beta$ events, without relying heavily on a single-detector basis Monte Carlo. Indeed, as it provides samples of almost pure $0\nu\beta\beta$-like events in a broad energy range, the 90% quantile can be tracked as a function of energy, and used as correction of the energy dependence of A/E instead of Compton events. Using this procedure would still suffer from the geometrical bias, but would be bias-free in terms of the difference in energy. As three out of five $0\gamma e^+ e^-$ events of ^{56}Co come from very low branching ratio γ-rays, a calibration with sufficient statistics to observe the $2 - 4\%$ reduction in the tagging efficiency requires very

long acquisition times. For a ton-scale experiment like LEGEND-1000, which is scheduled to acquire data for a decade, the required counting statistics could be gained with multiple or periodical calibration campaigns. Given ^{56}Co's half-life of only 77.3 days, this would require a regular production of radioactive sources and a calibration plan optimized for this application, which is beyond the scope of this work.

REFERENCES

[1] T. Comellato, M. Agostini, and S. Schönert, "Topologies of ^{76}Ge $0\nu\beta\beta$-decay events and calibration procedure biases," *Ready for submission*, 2022.

[2] B. Schweisshelm, "Influence on the charge cloud size on germanium detector pulse shapes in the GERDA experiment," M.S. thesis, 2018.

[3] M. Agostini *et al.*, "Signal modeling of high-purity Ge detectors with a small read-out electrode and application to neutrinoless double beta decay search in Ge-76," *Journal of Instrumentation*, vol. 6, no. 03, P03005–P03005, 2011. DOI: 10.1088/1748-0221/6/03/p03005.

[4] M. Agostini *et al.*, "Pulse shape analysis in GERDA Phase II," *The European Physical Journal C*, vol. 82, no. 4, p. 284, 2022. DOI: 10.1140/epjc/s10052-022-10163-w.

[5] P. Barker and R. Connor, "^{56}Co as a calibration source up to 3.5 MeV for gamma ray detectors," *Nuclear Instruments and Methods*, vol. 57, pp. 147–151, 1967. DOI: 10.1016/0029-554x(67)90513-7.

[6] R. Gehrke, J. Cline, and R. Heath, "Determination of relative photo-peak efficiency and system linearity for Ge(Li) gamma-ray spectrometers," *Nuclear Instruments and Methods*, vol. 91, no. 3, pp. 349–356, 1971. DOI: 10.1016/s0029-554x(71)80009-5.

[7] T. Comellato, M. Agostini, and S. Schönert, "Charge-carrier collective motion in germanium detectors for $\beta\beta$-decay searches," *The European Physical Journal C*, vol. 81, no. 1, p. 76, 2021. DOI: 10.1140/epjc/s10052-021-08889-0.

[8] M. Agostini *et al.*, "Limit on Neutrinoless Double Beta Decay of ^{76}Ge by GERDA," *Physics Procedia*, vol. 61, pp. 828–837, 2015. DOI: 10.1016/j.phpro.2015.06.002.

Part III

PRODUCTION AND PERFORMANCE OF NOVEL
DETECTORS FOR LEGEND

5 | PERFORMANCE OF A PROTOTYPE INVERTED COAXIAL DETECTOR

We have seen in Chapter 2 that the baseline detector geometry for the Legend experiment is the IC. The final decision on this geometry followed a few milestones which we shall now briefly discuss. In 2011, D. Radford et al. [1] proposed the IC geometry as a promising candidate for $0\nu\beta\beta$ experiments. Following this idea, Mirion started producing commercial IC detectors, which were called small anode germanium (SAGe)-Well detectors [2]. In 2017 the Dresden group purchased two of such commercially available detectors and carried out a first characterization campaign in the framework of $0\nu\beta\beta$ experiments [3]. Thanks to the encouraging results from this first campaign in terms of energy resolution and PSD, the Gerda collaboration placed an order of enriched material with the plan to convert it into IC detectors to be deployed in the Gerda apparatus during the upgrade of 2018. In parallel, the Max Planck Institut für Kernphysik (MPIK) and Technical University of Munich (TUM) groups purchased two custom designed prototypes IC detectors, which were then thoroughly characterized to benchmark the geometry. The final decision on the adoption of enriched IC detectors in Gerda (and on the manufacturer) was taken after the expertise acquired in these characterization campaigns.

This chapter reports on the characterization of the TUM prototype, a 1.6 kg IC detector to which we will refer as ICaro. A deep understanding of IC detectors was gained from the experimental data presented in this Chapter, in combination with the simulations of Chapter 3 and Chapter 4. These results, in addition to the performances of the enriched IC detectors in the vendor's cryostat and in the Gerda apparatus (which will be presented in Chapter 6 and Chapter 7, respectively) corroborated the choice of the IC geometry for Legend.

5.1 DETECTOR PRODUCTION

The feedstock for the production of non-enriched HPGe detectors is widely available electronic-grade polycrystalline germanium, which normally comes with a level of impurities of 10^{13} to 10^{14} cm^{-3}. For a working detector, this needs to be lowered to $\sim\!10^{10}$ cm^{-3}, and is normally done via zone refining [4]. This technique uses the principle that most impurities *Zone refining* tend to concentrate in the liquid phase as the material begins to freeze. A
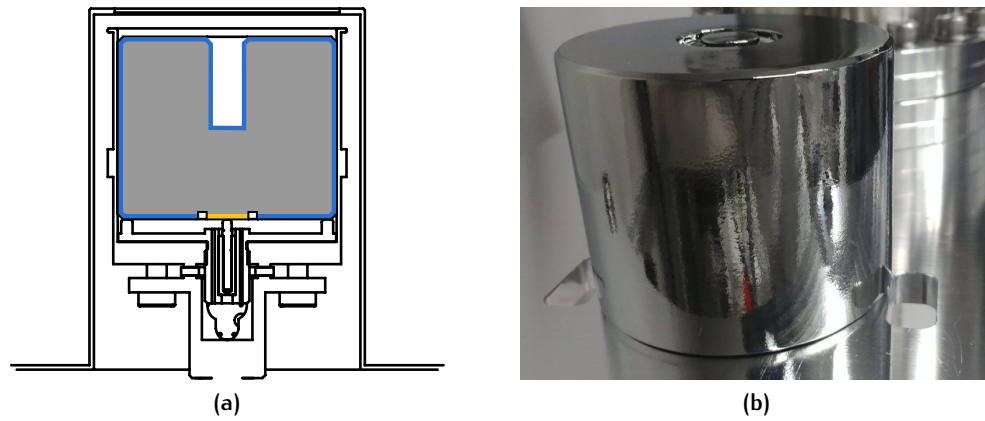
Figure 5.1: (a) Sketch of ICaro in the vacuum cryostat provided by the vendor. Marked in yellow is the B-implanted p^+ electrode and in blue the Li-diffused n^+. (b) Close look of bare ICaro.

small section of the germanium ingot is melted with radiofrequency heating coils, which are then moved slowly along the length of the ingot, causing the liquid phase to move along with them. In this way, the impurities tend to follow the coils and are thus *swept* to one end of the ingot, which can eventually be cut off. By following this procedure many times, the impurity concentration can be reduced by several orders of magnitude.

Crystal pull   The ingot resulting from the zone refining operation is the starting material to pull single large germanium crystals using the Czochralski technique. This consists of dipping a seed crystal into germanium kept slightly above the freezing point and slowly withdrawing it while rotating it [4].

Crystal cutting and electrode formation   The crystal pulled with the Czochralski method, which can have diameters of up to 9–10 cm and lengths of tens of cm, is then cut according to the selected geometry. A Lithium-diffused and a Boron implanted layer are then formed on the selected surfaces of the crystal to form respectively the n^+ and p^+ electrodes of the detector, thus completing the fabrication process.

ICaro: history and specifications   For the detector studied in this chapter, the germanium crystal was pulled from standard electronic-grade germanium by Umicore, Olen (Belgium) in March 2017 and the conversion to diode was assigned to Baltic Scientific Instruments (BSI). The detector geometry is a small-anode inverted coaxial, where the p^+ electrode (marked in yellow in Figure 5.1a) extends on the entire surface enclosed by the circular groove, while the n^+ electrode (marked in blue in Figure 5.1) covers the rest of the surface, wrapping up the detector down until the groove, which physically separates the electrodes. In order to guarantee its electrical and chemical neutrality, a passivation is normally carried out, which in most of the cases consists of a layer of either SiO_2 or amorphous germanium on the surface of the detector [5]. Alternatively, the GERDA collaboration proved that stable operation of detectors without a passivation layer is also possible [6]. As no information was given regarding
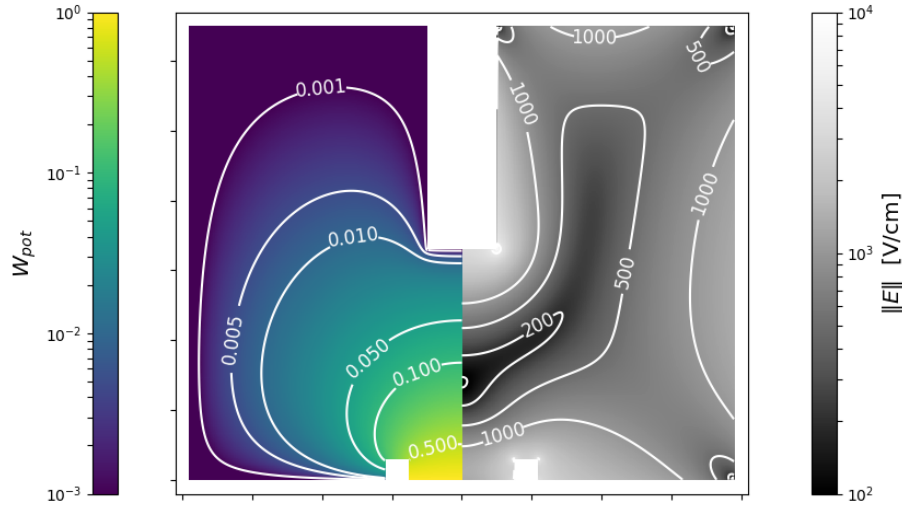
Figure 5.2: Weighting potential W_{pot} and strength of the electric field E for a cross section of ICaro.

ICaro, a visual inspection of the groove only led to the conclusion that it is not passivated with SiO_2, as no colored shades typical of such process are visible (see Figure 5.17c).

The dimensions of ICaro have been customized at TUM (with a great contribution at this stage by Y. Kermaïdic from the MPIK in Heidelberg) to allow a depletion voltage lower than 4 kV and minimize the regions of low electric field (< 200 V/cm). The values of the electric field on a cross section of ICaro are shown on the right side of Figure 5.2. The left side shows the weighting potential W_{pot}, the quantity which, according to the Shockley–Ramo theorem [7, 8], determines the time profile of the signal[1]. Like for all small anode detectors, the weighting potential of ICaro exhibits a small region around the p^+ electrode with a high gradient, and is roughly homogeneous in the rest of the volume (color maps in Figure 5.2 are in logarithmic scale). As we have seen in Section 2.4.1, this guarantees that the largest contribution to the signal formation comes from the region close to the p^+ electrode, where holes follow the same trajectories for collection, independently of the starting position. Quantitatively, in the top part of the detector W_{pot} takes values $< 0.1\%$, which means that charges drifting in this region contribute in less than one part out of thousand to the total signal.

As BSI did not have in 2017 the facility to perform the B-implantation of the p^+ electrode on such big crystals, this operation has been carried out with a joint effort of the TUM group and the Helmholtz-Zentrum Dresden-

B-implantation as a joint effort of TUM and HZDR

---

1 The weighting potential is the integral of the weighting field E_ω used in Chapter 2 and Chapter 3.
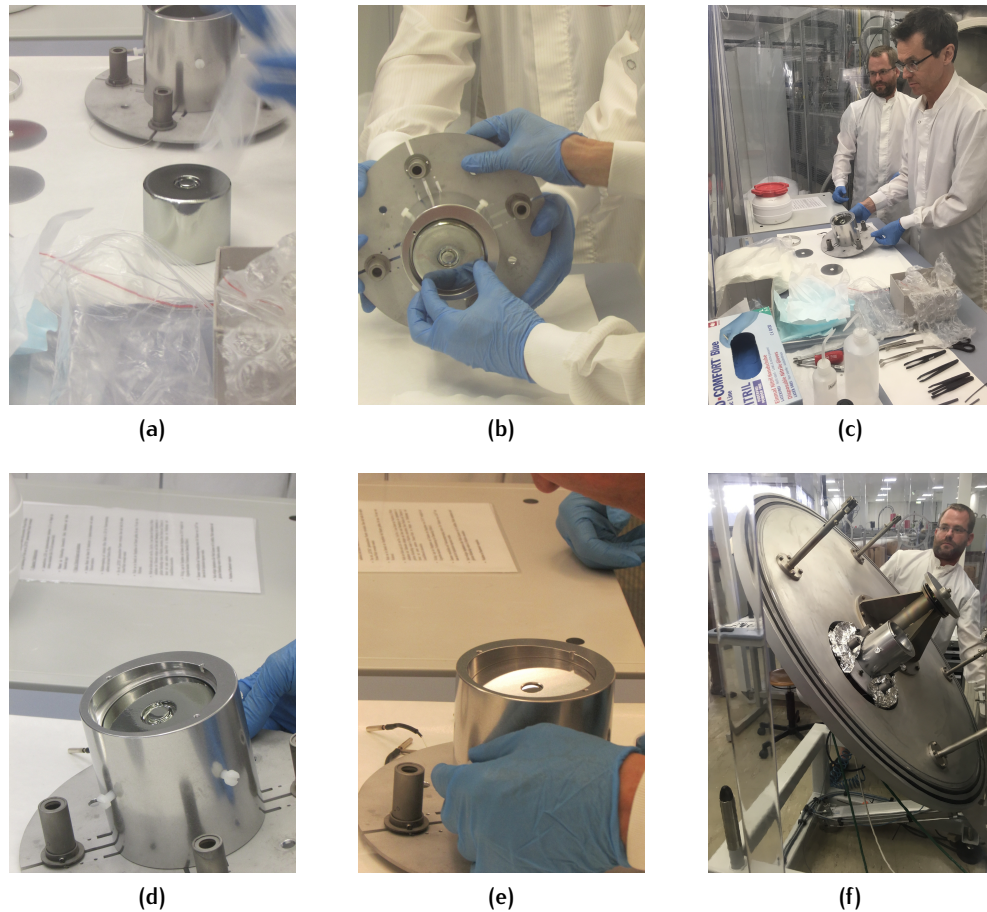
(a)   (b)   (c)

(d)   (e)   (f)

Figure 5.3: ICaro (a), was mounted on a mockup frame ((b), (c), and (d)) and masked (e) for B-implantation of the p^+ electrode (f) .

Roßendorf (HZDR), in June 2017. A few pictures from the implantation campaign are shown in Figure 5.3.

After the B-implantation, the crystal was sent back to BSI for final manufacturing of the detector. After that, in August 2017, ICaro was shipped to Munich, where the characterization took place.

5.2 DETECTOR CHARACTERIZATION

5.2.1 Experimental setup

ICaro was shipped to Munich inside the vendor's vacuum cryostat (which has been used for all the measurements of this work) and cooled down via a cold finger immersed in liquid nitrogen (LN_2). Two electronics data acquisition (DAQ) chains have been used for the data taking:

- *Digital chain*: the output from the detector is amplified by a non shaping amplifier (Genius II) and digitized at 100 MHz by the VERSABUS

Module Eurocard (VME) Struck 3301 flash analog-to-digital converter (FADC). For each triggered event, a 10 µs long trace with a 10 ns sampling step, and a down-sampled 160 µs long trace with a 40 ns sampling step are recorded for offline analysis.

- *Analog chain*: the output from the detector is shaped and amplified by a Spectroscopy Amplifier (ORTEC 672) for analysis with a Multi-Channel Analyzer (MCA) (ORTEC ASPEC 927), which provides as output an energy spectrum and no information on the pulse shape.

5.2.2 Operational voltage and list of measurements

For the present characterization, positive voltage was applied to the n^+ electrode while the p^+ was grounded and used as read-out. Full depletion voltage was found by increasing the high voltage (HV) in steps from 1 kV to 3.3 kV and tracking the main parameters (peak position, energy resolution in FWHM and counts per second (cps)) of the 1.3 MeV energy peak from a ^{60}Co source. Full depletion is defined at the voltage where such parameters reach their maximal (minimal) and stable value. As shown in Figure 5.4, this was estimated to be 2.3 kV. The operational voltage for the following measurements in vacuum cryostat was set at the value of 3 kV as recommended by the manufacturer, which is 700 V above depletion. At the operational voltage, the following sources have been used for the characterization:

Depletion voltage at 2.3 kV, operational voltage at 3 kV

- ^{60}**Co,** ^{241}**Am,** ^{228}**Th,** ^{56}**Co** to determine the energy resolution and linearity of the detector-electronics system (Section 5.2.3)

- ^{241}**Am** to scan the detector surface and investigate the response (in terms of charge collection and pulse shape) as a function of the interaction position (Section 5.2.4)

- ^{22}**Na** for a measurement of the charge collection time (Section 5.2.5)

- ^{228}**Th** for PSA (Section 5.3)

In addition, an Autunite ore has been used as a constant ^{222}Rn emanator to create a population of ^{210}Po on the p^+ surface of the detector and study its response to α decays. Details in Section 5.4.

5.2.3 Energy resolution and linearity

5.2.3.1 *Energy Resolution*

At the operational voltage, ^{60}Co, ^{241}Am and ^{228}Th have been used without collimation to study the energy resolution of the detector. The main
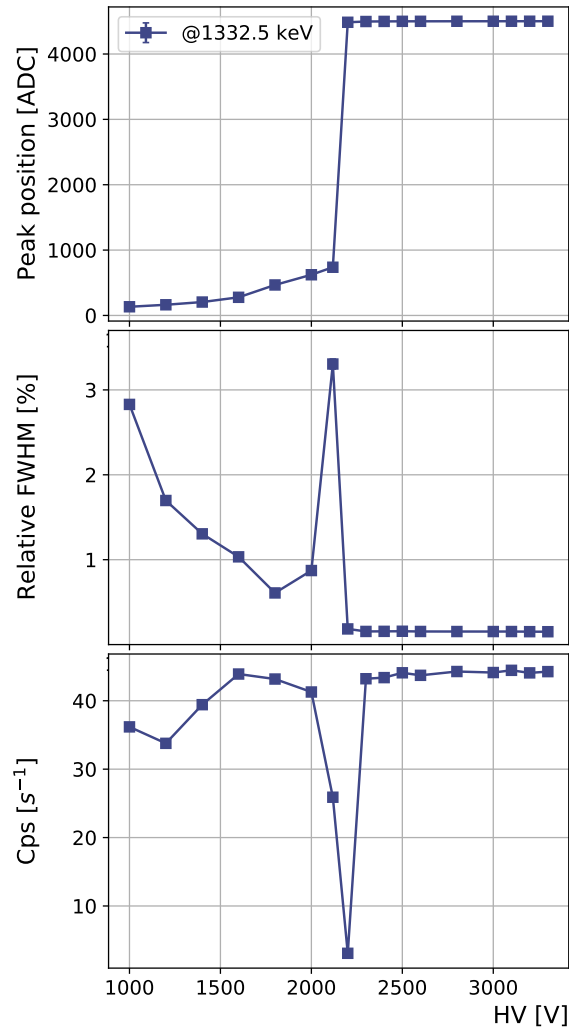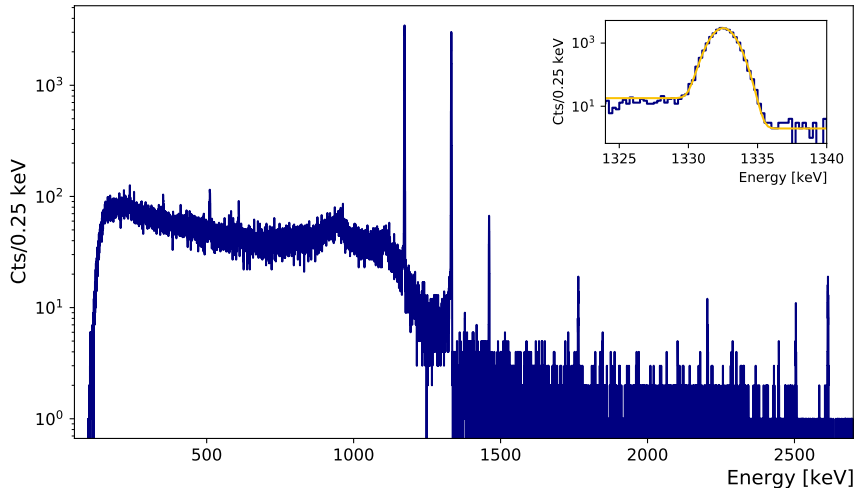
Energy resolution: 2.1 keV FWHM @ $Q_{\beta\beta}$

Figure 5.4: HV scan of ICaro. From top to bottom: peak position, FWHM normalized to 1.3 MeV and cps for the 1.3 MeV peak of ^{60}Co as a function of the applied HV. The uncertainties are smaller than the size of the markers.

peaks from the sources have been fitted with a gaussian function plus a sigmoid. The spectra from ^{60}Co and ^{228}Th are shown in Figure 5.5a and Figure 5.5b, where a fit of the highest energy peak is also shown in the inset. The resolution (in FWHM) was found to be 1.8 keV @1.3 MeV and 2.5 keV @2.6 MeV. A plot of the FWHM as a function of energy is shown in Figure 5.5c. A function of the type $FWHM(E) = \sqrt{a + b \cdot E}$ was used to interpolate the energy resolution at $Q_{\beta\beta}$, which resulted in $FWHM(Q_{\beta\beta}) = 2.1$ keV.

5.2.3.2 Linearity

Given the abundance of γ lines from 1 to 3.6 MeV, the ^{56}Co source of Chapter 4 was also used to determine the linearity of the detector-electronics system. This has been done by comparing the deviations of the peak position from a 1st and 2nd order polynomial calibration curve. As shown in

(a) ^{60}Co energy spectrum for ICaro with fit on the 1.3 MeV peak.
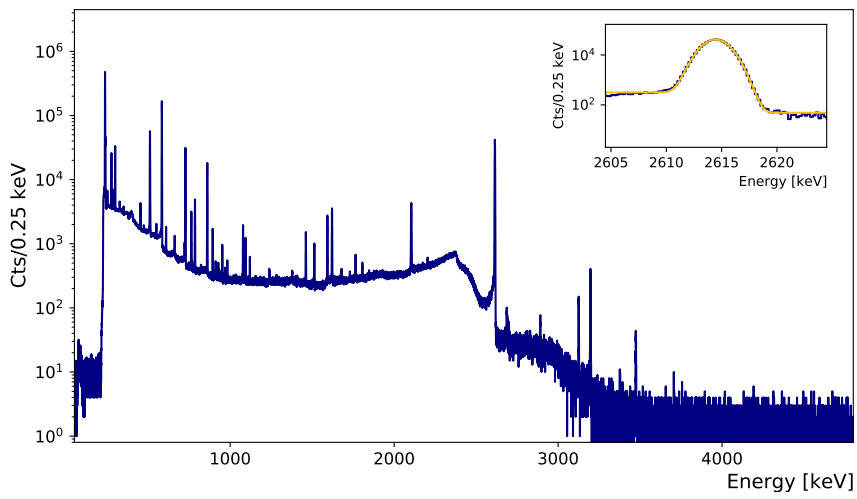
(b) ^{228}Th energy spectrum for ICaro with fit on the 2.6 MeV peak.
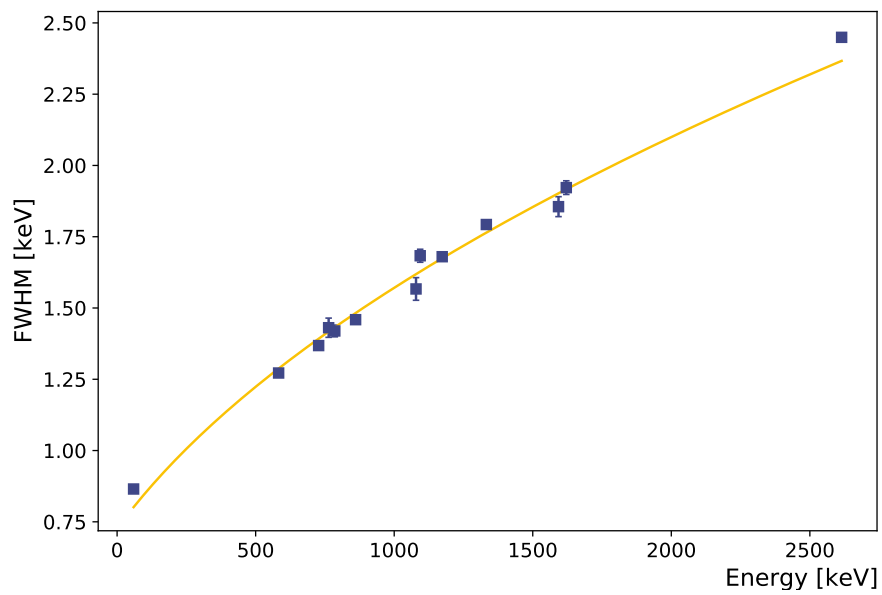
(c) Energy resolution (in FWHM) as a function of energy for ICaro.

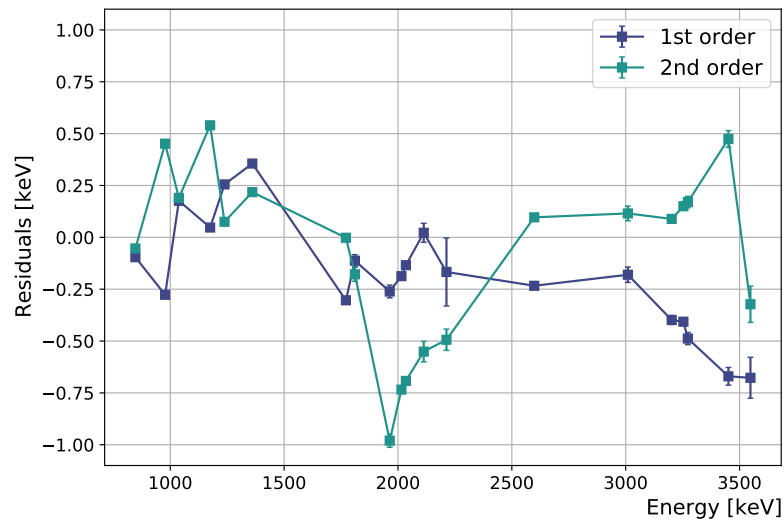**Figure 5.5:** Energy spectra ((a) and (b)) and resolution in FWHM (c) for ICaro.

Figure 5.6: Plot of the residuals for 1st (dark blue) and 2nd (light blue) order energy calibration

.

Figure 5.6, deviations from linearity slowly increase (within the specifications from BSI ($< 0.04\%$)) for incident energy exceeding ~2.6 MeV, which is not the case when a 2nd order term is added. As in the present chapter the energies of interest are $\leqslant 2.6$ MeV, a linear calibration is used. For the experimental part of Chapter 4, which involved higher energy γ-rays, a quadratic term was added to the calibration curve.

5.2.4 Surface response homogeneity

Side and top surface scanned with 60 keV γ-rays

The homogeneity of the detector response along the surface has been inspected by means of a collimated 60 keV γ-beam from a ^{241}Am source. As a collimator, a 26 mm long copper cylinder with a 2 mm diameter hole was used, resulting in a 2.8 mm diameter spot on the detector surface. Since 95% of the 60 keV γ-rays are absorbed within the first 3 mm of germanium, such a setup allows for a study of the parameters of interest with a reasonably precise knowledge of the interaction position. Specifically, the countrate and the position of the 60 keV peak have been monitored to investigate charge collection efficiency and charge trapping as a function of the interaction position. Also, the rise time $0.5\% - 90\%$ and A/E for the events in the range $(60 \pm 2\sigma)$ keV have been extracted to study how the pulse shape changes as a function of the interaction position.

Two main sets of measurements have been taken: a longitudinal scan of the side of the detector and a radial scan of the top surface, and the results are shown in Figure 5.7, on the left and right column, respectively. The shape of the detector (and its holder in case of the side scan) is also superimposed for quick identification of the source position relative to the detector.

In Figure 5.7 the coloured lines indicate *obstacles*, coordinates where some inhomogeneity in the parameters is expected: the yellow lines indicate the edges of the detector, the blue lines the thicker ring on the side of the detector holder (see Figure 5.1a), and the green ones the borehole[2].

5.2.4.1 Side longitudinal scan

The charge collection efficiency has been investigated by monitoring the countrate of events at $(60 \pm 2\sigma)$ keV for every scanned position (Figure 5.7a). A 15% lower countrate was observed at around Z $=20$ mm, which reflects the structure of the detector internal holder. A $\sim$ 22% reduction was also observed in the top half of ICaro, corresponding to an additional 0.1 mm layer with respect to the bottom half, which is probably due to how the detector is handled during Li-diffusion at BSI. The visual difference in the reflectivity of the two halves of the bare detector in Figure 5.1b is a hint in this direction. A detailed study of the pulse shape of events in the upper half of ICaro allowed to conclude that this additional layer is not completely *dead*, as a higher fraction of *slow pulses* (see Section 2.4.2) is generated there with respect to the case in which an additional dead material (yielding the same attenuation) was manually added in front of the bottom half.

Thicker Li layer in the top half

It is well know that traps in semiconductor devices and, specially, large volume germanium detectors, lead to partial reconstruction of the incident energy [9, 10]. For the present measurement, it would result in a lower reconstruction of the position of the 60 keV energy peak for longer paths (higher Z positions). Its mean position has thus been monitored along the scan using a fixed calibration (Figure 5.7c) and no evidence for a dependence on the Z coordinate was observed. Given some electronics instabilities for this measurement, this measurement set an upper limit for charge trapping on $\leqslant 0.05\%$.

No evidence for charge trapping from side scan

As expected from the simulations in Chapter 3, the rise time $(0.5\% - 90\%)$ of events occurring along the surface for Z below 20 mm is constant at the value of 1200 ns (see Figure 3.5), it increases rapidly with increasing Z values, and reaches a plateau of 1350 ns for Z above 40 mm, where the 0.5% threshold is not sensitive to the beginning of charge collection (Figure 5.7e).

Rise time 150 ns longer in top half

Finally, the mean value of the A/E parameter was extracted for every scanned position. As seen in Chapter 3, charge carriers' collective effects combine in such a way that interactions occurring in the upper part of the detector exhibit lower A/E than those occurring in the lower part. The results of the side scan confirm the effect, showing a 0.2% lower A/E for events occurring in the top part of ICaro (Figure 5.7g), compared to those occurring in the bottom part.

A/E 0.2% lower in top half

---

2 The lines are slightly shifted compared to the coordinates of the *obstacle* because they indicate when the edges of the γ-ray beam start shining on it.
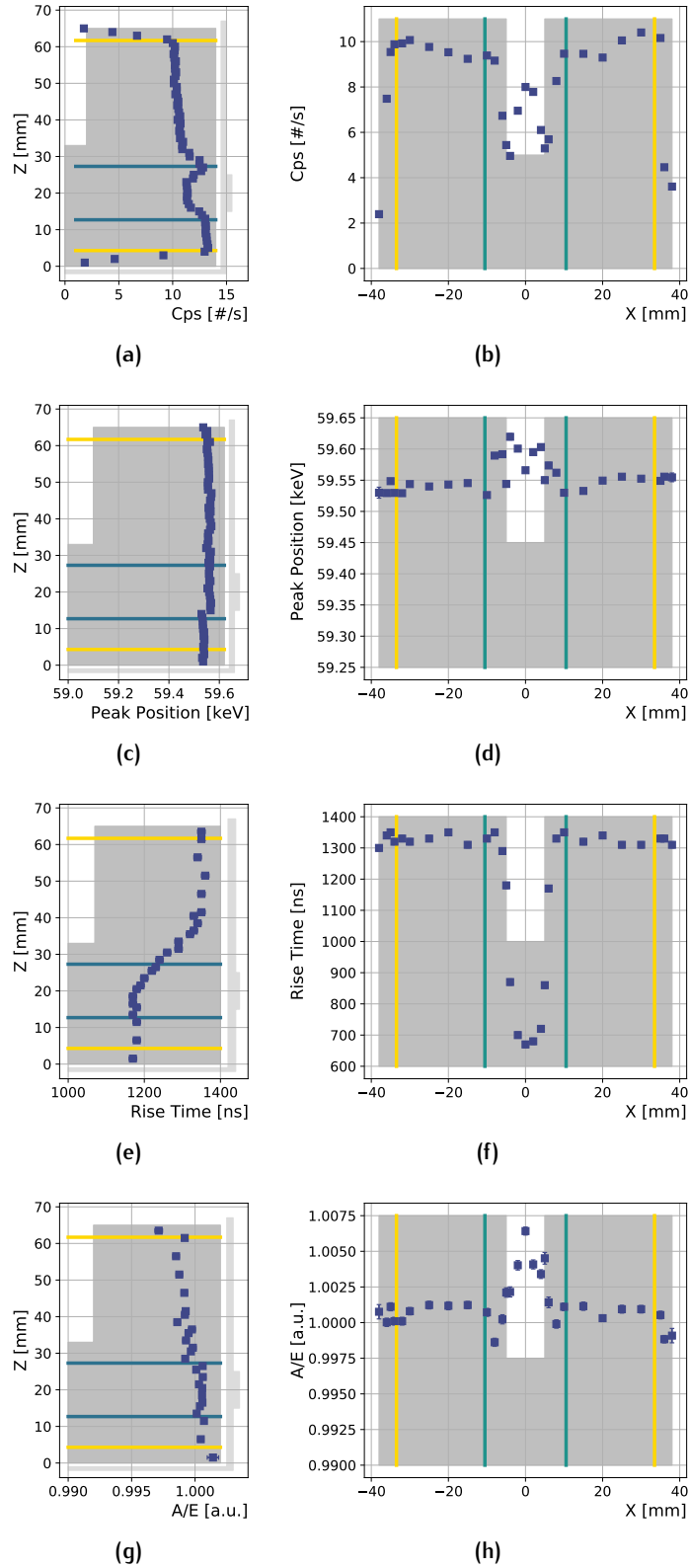
Figure 5.7: Results of the side longitudinal (left) and top radial (right) scan of ICaro for the 60 keV γ-rays from ^{241}Am. The colored lines indicate the coordinates for which the γ-beam is expected to encounter an *obstacle* (see text).

5.2.4.2 Top radial scan

Charge collection on the top surface of ICaro is compatible with the values of the side scan for high Z values and exhibits two prominent features (Figure 5.7b). The most significant is the countrate around the center of the detector, which is strongly reduced on the sides of the borehole and increases at the very center. This reflects the geometry of the beam, which, shining diagonally on the vertical surfaces, *sees* thicker layers of dead material before getting into the active volume. Moving towards the center, this effect is reduced. The second prominent feature is that the charge collection is less efficient already for radii smaller than 30 mm, which is not close enough to the borehole to experience its effects. This suggests that a second Li-diffusion was performed around the position of the borehole after the mechanical drilling.

Thicker Li layer around borehole

The analysis of the peak position gives indication of trapping of $\sim 0.08\%$ of the deposited charge, as a higher reconstructed energy was observed for events occurring on the bottom of the borehole compared to those on the top surface (Figure 5.7d). Indeed, for the formers the charge collection path is more than twice shorter than the latters. This value is higher than the limit set from the side scan, as the difference in the collection paths is maximal when comparing events occurring on the top surface and at the bottom of the borehole.

Indication of small charge trapping (0.08%)

With no surprise, the rise time (Figure 5.7f) takes the constant value of 1350 ns (in agreement with the highest Z values of the side scan) for events on the detector top surface and it decreases to 700 ns for interactions in the borehole.

Rise time agrees with upper position of side scan

Finally, the A/E distributions have the same peak value for all interactions occurring on the top surface of the detector (Figure 5.7h). At the bottom of the borehole, A/E is 0.5% higher as in the top surface. As for the side scan, this difference comes from collective effects, as no difference is seen in simulations without implementation of the charge cloud dynamics.

A/E is 0.5% higher in the borehole

5.2.5 Estimation of charge collection time

As detector dimensions keep on increasing, charge trapping can have a significant impact on the reconstruction of the event true energy [10]. As this is intrinsically proportional to the charge collection path, a correction on the energy can be carried out using the charge collection time, which is often referred to as *drift time*. Its experimental determination is equivalent to the identification of the rising edge of the electrical signal, what is normally called the t_0, which, for interactions occurring in regions of low weighting field, can be at (or below) the edge of the electronics noise. An important
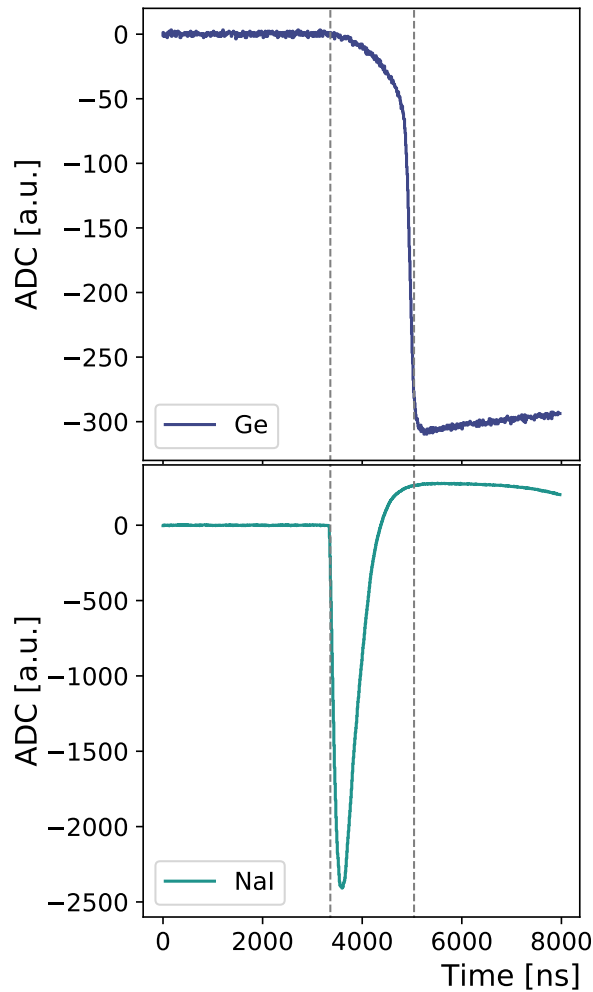
Figure 5.8: Coincident 511 keV γs in ICaro (top) and NaI(Tl) crystal (bottom).

parameter for IC detectors is thus how precise the determination of the t_0 is. For ICaro, this accuracy has been determined by comparing the rise time $0.5\% - 90\%$ with the drift time obtained using a ^{22}Na source and a NaI(Tl) crystal, following and adapting the procedure of [11].

Signal in NaI(Tl) marks the t_0

The two 511 keV photons following the β^+ decay of ^{22}Na have been used to select coincident events in germanium and NaI(Tl). Exploiting the fact that signal generation is an order of magnitude faster in NaI(Tl) than in germanium, the 10% threshold on the signal from the scintillator was used as an estimation of the t_0. The end of charge collection in germanium was then considered as the 90% of the signal. An example of a coincidence is shown in Figure 5.8, where the dashed lines mark the beginning and the end of charge collection, as selected in our analysis.

Determination of the drift time for four interaction positions

In the present work the source was placed in a double 4 cm long copper collimator between ICaro and the NaI(Tl) crystal at 4 different Z-positions ($Z = 17$ mm, $Z = 27$ mm, $Z = 37$ mm, $Z = 57$ mm) and the coincident events have been selected for each dataset to estimate the drift time as a function of
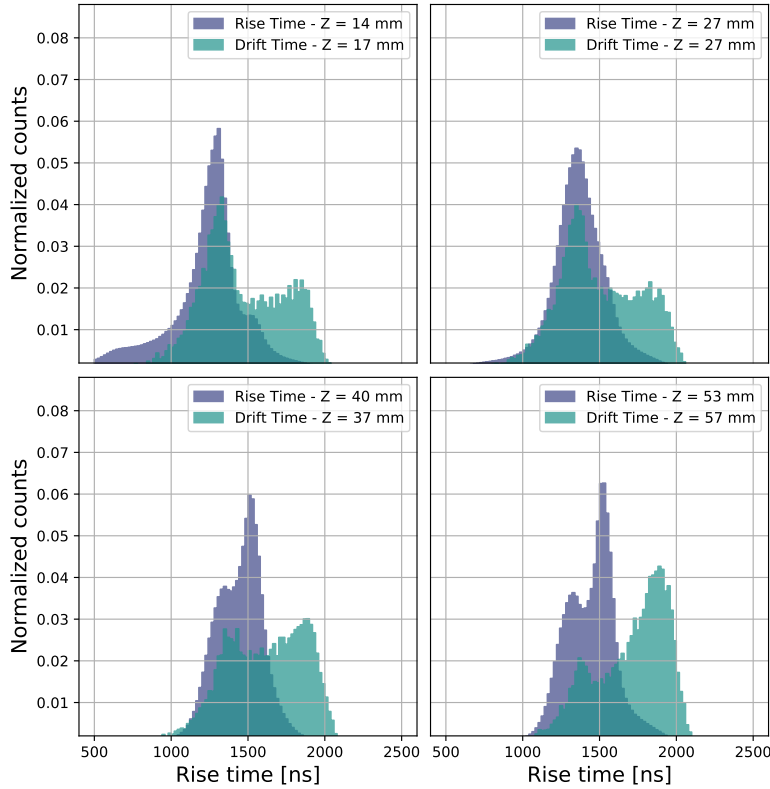
Figure 5.9: Comparison of drift time (green), estimated with a collimated ^{22}Na source, with rise time $0.5\% - 90\%$ (blue), extracted from collimated ^{228}Th data, for ICaro.

the interaction position. The distributions of the drift time for the coincident events at the 4 Z-positions are shown with the green histograms in Figure 5.9. As we saw in Chapter 3 for the rise time (Figure 3.6), drift time distributions have a two-peaks structure, where the lower peak includes the events which occur in the lower part of the detector, and the higher those occurring in the upper part. Additionally, as 511 keV γs have a non negligible multiple-site component, some events starting at low Z-values can end up in higher regions and vice-versa. As visible in Figure 5.9, the drift time in the upper volume of ICaro reaches values of 2 μs, which is roughly double the typical amount for BEGes.

A direct comparison of the rise time $0.5\% - 90\%$ and the drift time for the same events is unfortunately not possible, as the 0.5% threshold for events at 511 keV is at the edge of the electronics noise. However, since charge collection time is energy independent, DEP events from a collimated ^{228}Th source at comparable positions[3] have been used for the comparison; their rise time distributions are shown in blue in Figure 5.9. As expected, the difference between rise time and drift time is not significant for the lower

Drift time vs rise time

---

3 The difference in the position of the two collimators is at most 4 mm, and the size of collimator's hole for ^{228}Th is 10 mm.

peak, as it contains events occurring in the bottom part of the detector, where, according to the configuration of the weighting potential (see Figure 5.2), the contribution to the total signal is higher than the 0.5% threshold of the rise time. Conversely, as is visible from Figure 5.2, charges drifting at Z >35 mm give a contribution which is smaller than 0.5%. In these regions, the 0.5% threshold is not a precise determination of the real t_0. Therefore, the rise time for these events is ~300 ns shorter than the drift time, as is visible in the second row of Figure 5.9. Additionally, the comparison between rise and drift time for the lowest Z position (top-left panel in Figure 5.9) shows an excess of DEP events with low rise time values. This is due to the different volumes sampled by the 2.6 MeV gamma-ray (which interacts through pair creation and creates the DEP), compared to the 511 keV from ^{22}Na. With an attenuation length $\lambda \simeq 5$ cm, the former also probes the volume around the p^+ electrode, which the latter (with a $\lambda \simeq 2.4$ cm) only poorly accesses.

The 300 ns difference between rise time and drift time represents the uncertainty on the estimation of the charge collection time in the top part of ICaro, if a 0.5% threshold is chosen. Despite more refined digital signal processing (DSP) techniques are being developed to access lower thresholds (such as 0.1%), this uncertainty can still be significant in longer IC detectors, and could ultimately prevent a precise reconstruction of the event true energy.

5.3 PULSE SHAPE ANALYSIS

We have seen in Section 2.4.2 that PSA is a powerful tool to discriminate signal-like events from background. In this section the performances of the A/E technique for ICaro will be evaluated. The results which will follow have been partially anticipated in Chapter 3, where little emphasis was given to the experimental characterization campaign, as the main goal was to corroborate the accuracy of the modeling of collective effects in charge clusters. This section takes up the discussion on the dependence of the pulse shape on the interaction position and expands it with the support of results from multiple experimental configurations. After this discussion, the performances of ICaro in terms of background discrimination will be given for all the experimental configurations and with different analysis techniques.

5.3.1 Pulse shape dependence on the interaction position

As seen with the surface scan with ^{241}Am, an event occurring in the upper part of ICaro exhibits a smaller A/E value compared to the same event in the lower part. In the following, this effect will be investigated for SSEs
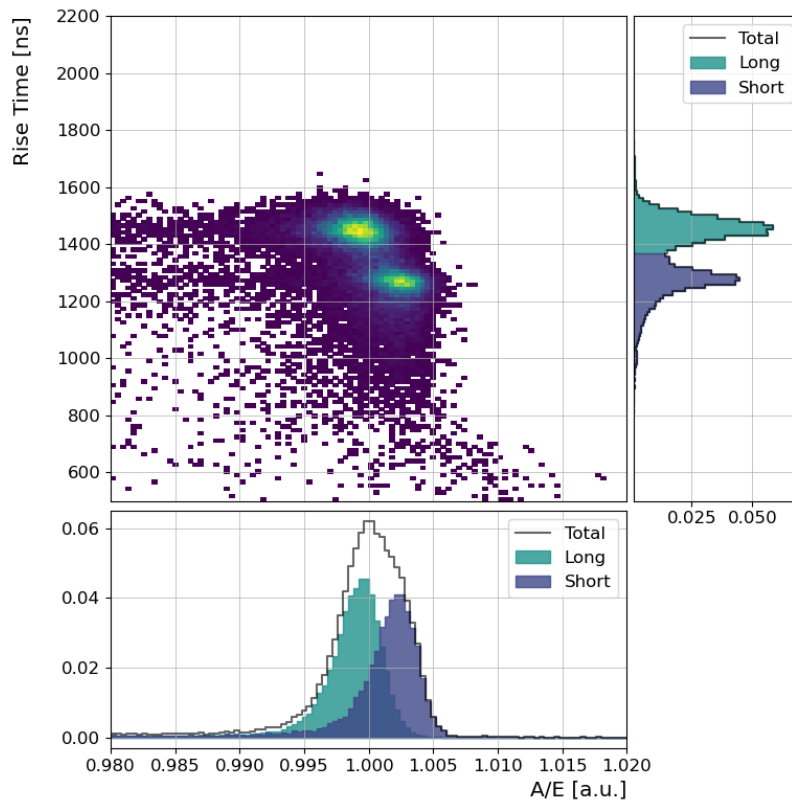
Figure 5.10: Experimental correlation of A/E on the rise time for DEP events from a flood irradiation with ^{228}Th of the lateral surface of ICaro.

at higher energy, using samples of DEP events from a ^{228}Th source in 3 different configurations:

- Flood source illuminating the full lateral surface

- Flood source illuminating the top surface

- Collimated source at 4 lateral positions

As rise time carries the information on the interaction location, its correlation with A/E makes the dependence of the pulse shape on the interaction position explicit.

This is shown for the flood lateral measurement in Figure 5.10. For this configuration, DEP events are distributed along the whole detector height, particularly on the top and bottom corners, where the chance for 2 back-to-back photons to escape detection is higher. As exhaustively explained in Section 3.3.2, the combination of charge cluster's collective effects with the geometry of ICaro creates two populations of almost constant rise time and A/E, in the bottom and top halves of the detector. The actual values of the rise time for events from ^{228}Th differ from those extracted in Section 5.2.4 with ^{241}Am. This is because the 60 keV collimated γ-rays from ^{241}Am probe a small angle of the detector, hence generating charges drifting with a veloc-
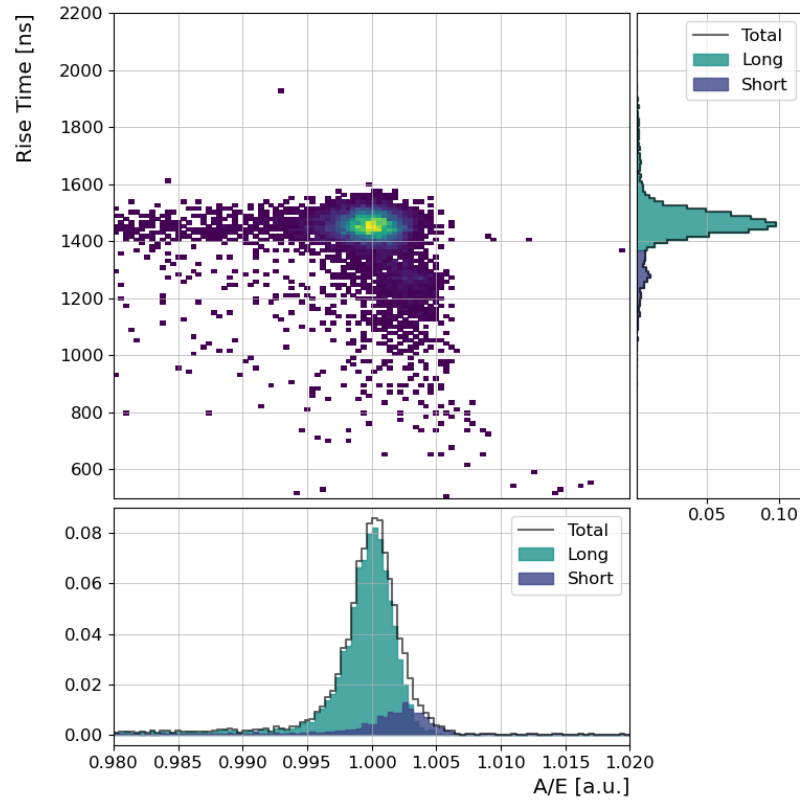
Flood lateral irradiation with ^{228}Th

Figure 5.11: Experimental correlation of A/E on the rise time for DEP events from a flood irradiation with ^{228}Th of the top surface of ICaro.

ity which is characteristic of the closest crystallographic axis, which is not the case for 2.6 MeV γ-rays from ^{228}Th.

In order to clearly distinguish the two populations in the A/E space, in Figure 5.10 DEP events have been divided into two groups, according to the median value of rise time, which have been called *Short* and *Long* (in blue and green, respectively). This emphasizes the physical origin of the two, where *Short* labels events occurring in the bottom part of the detector, and *Long* those in the top half. Furthermore, this division triggered the idea of the *Split* analysis, which will be presented in Section 5.3.2.

Flood top irradiation with ^{228}Th

The same correlation of rise time and A/E is shown in Figure 5.11 for the flood irradiation of the top surface of ICaro. For this configuration, only $\leqslant 20\%$ of the 2.6 MeV γ-rays reaches the bottom of the detector, of which only a small fraction will interact through pair creation. Hence selecting DEP events from this dataset results in probing mainly the top part of the crystal height. For this reason, Figure 5.11 does exhibit a single peak structure, with very few events in the *Short* group.

Collimated scan with ^{228}Th

In addition to the flood datasets, collimated measurements with ^{228}Th have been performed, using a 7 cm long lead collimator with a 1 cm diameter aperture (resulting in a ~1.2 cm wide spot on the detector surface) to scan the lateral surface of the detector at 4 different heights. This allowed
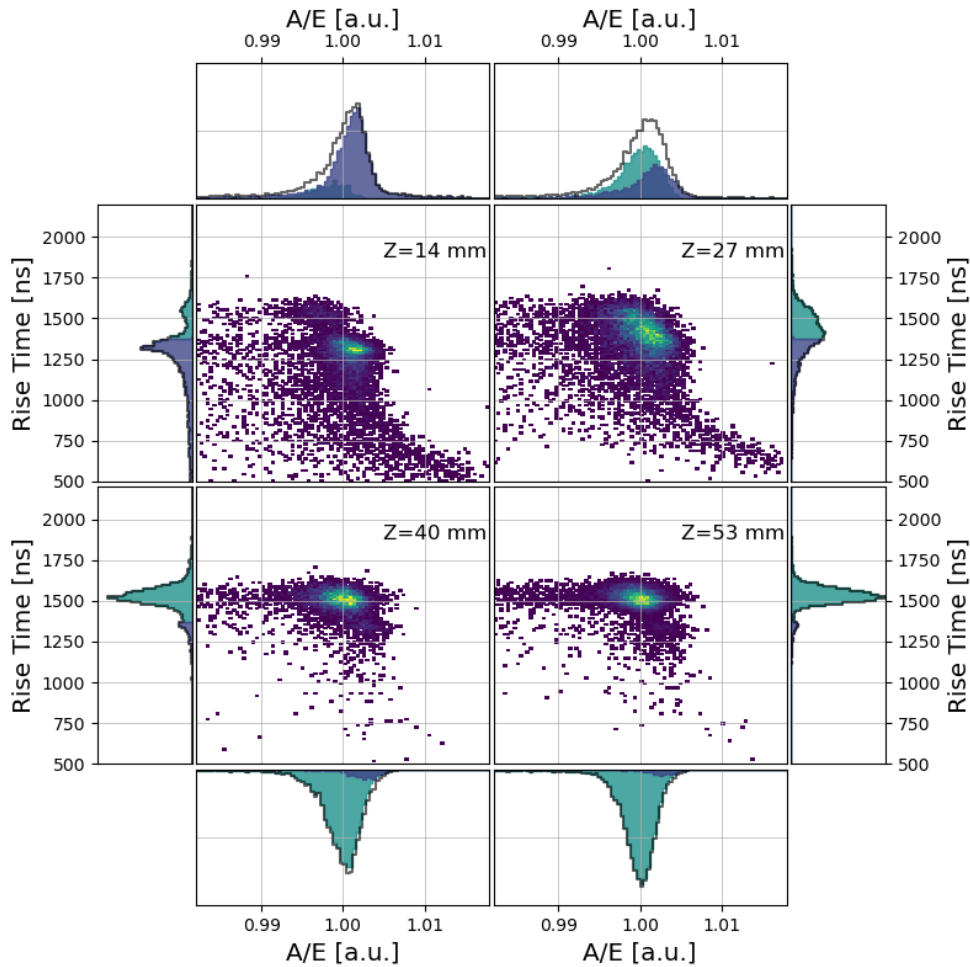
Figure 5.12: Experimental correlation of A/E on the rise time for DEP events from a collimated scan with ^{228}Th of the lateral surface of ICaro.

to have a considerably high number of DEP events in controlled volume regions. The result of this scan is shown in Figure 5.12 in the rise time - A/E space, where the collimator height is indicated in the top right corner of each plot. Moving towards higher Z-positions, DEP events gradually shift from the *Short* to the *Long* population. In particular, the $Z = 27$ mm position (top, right) probes the central part of the detector, which is only poorly represented in the flood measurements. Here the transition volume between *Short* and *Long* is probed, thus showing the gradual dependence of A/E on the rise time.

5.3.2 Event discrimination performance

The survival probability (SP) of the standard event samples from a ^{228}Th source after cut is listed in Table 5.1 and Table 5.2 for the experimental configurations with ^{228}Th presented in Section 5.3.1. In particular, the first column of Table 5.1 reports the standard PSD performance for the lateral

flood measurement. Additionally, motivated by the correlation shown in

	Side					
Event class	*Standard*		*Corrected*		*Split*	
^{208}Tl DEP	90.1	(8)	90.1	(8)	90.3	(8)
^{208}Tl SEP	5.0	(3)	5.3	(3)	5.0	(3)
^{208}Tl FEP	7.64	(5)	7.92	(5)	7.49	(5)
^{212}Bi FEP	8.9	(4)	9.1	(4)	8.8	(4)
CC @$Q_{\beta\beta}$	32.3	(2)	33.1	(2)	32.5	(2)

Table 5.1: Survival probabilities for the flood lateral measurement of ICaro with ^{228}Th.

Rise time correction of A/E Figure 5.10, a linear correction of A/E on the rise time has been investigated. This is extracted by fitting the two A/E and rise time *blobs* of DEP events, as:

$$A/E_{DEP}(RT) = a + b \cdot RT_{DEP} \qquad (5.1)$$

and then applied to all events i as:

$$A/E_i^{corr} = (A/E_i - b \cdot RT_i)/a \qquad (5.2)$$

The results of this *Corrected* analysis are listed in the second column of Table 5.1 and, as anticipated in Chapter 3, do not provide a significant improvement of the discrimination capabilities. However, such correction reduces the volume dependence of the PSA performance, possibly reducing the systematic uncertainties of the procedure.

Split analysis As suggested by the separation into *Short* and *Long* datasets made in Section 5.3.1 (and highlighted in blue and green in Figure 5.10), a different analysis, which has been named *Split*, has also been carried out: it consists of carrying out the A/E standard routines separately on the two populations, and evaluating the final SP on the total number of events, so that the performance can be directly compared to the other methods. As for the *Corrected* analysis, the *Split* method does not show a significant improvement in the MSE rejection capability. Its performance for detectors where the dependence of A/E on the rise time is stronger will be investigated in Chapter 6.

As shown in Section 5.3.1, the configurations where the ^{228}Th source sits on the top of the detector or is collimated do not exhibit a double peak in A/E, hence only the standard analysis was carried out, and its results are reported on Table 5.2.

Overall, the measurements performed with ^{228}Th show excellent rejection power of MSEs in all experimental configurations. The values for ICaro are compatible with typical values of BEGe and PPC detectors, and even better than many of them [12–14].

Event class	Flood Top		Collimated Z1		Z2		Z3		Z4	
^{208}Tl DEP	90	(2)	90.1	(7)	90.0	(7)	90.0	(6)	90.3	(5)
^{208}Tl SEP	5.7	(5)	6.1	(2)	5.8	(2)	6.8	(2)	5.9	(2)
^{208}Tl FEP	8.9	(1)	7.82	(3)	7.57	(3)	9.59	(3)	9.98	(3)
^{212}Bi FEP	7.9	(6)	8.6	(3)	7.8	(3)	9.6	(2)	10.1	(3)
CC @$Q_{\beta\beta}$	24.5	(3)	33.1	(1)	31.7	(1)	34.9	(1)	35.0	(1)

Table 5.2: Survival probabilities for the flood top measurement and for the collimated lateral scan of ICaro with ^{228}Th. The collimated Z-positions are, from the bottom of the detector, Z1 = 14 mm, Z2 = 27 mm, Z3 = 40 mm, Z4 = 53 mm.

5.4 REJECTION OF α–DECAYS

Several times throughout this dissertation we have mentioned that events in the vicinity of the p^+ electrode generate signals with high A/E values. Being separated from the external world by a $\mathcal{O}(100)$ nm thick B layer from the implantation process on the p^+ electrode, or a layer of unknown thickness from the passivation process on the groove, this volume is the only sensitive region to α-decays. This section shall present the ongoing work on the estimation of the rejection efficiency of events occurring in the region surrounding the p^+ electrode (i.e. on the surface of the electrode itself and of the groove) to which we will refer simply as p^+ events.

5.4.1 State–of–the–art alpha rejection efficiency

The rejection efficiency of p^+ events can be determined in two ways:

- **In-situ**: during the production and handling stage, germanium detectors are exposed to (tiny) concentration of ^{222}Rn. Its progeny can deposit on the surface of detectors, thereby causing a (small) contamination of the α-decaying ^{210}Po; this can be a background when detectors are operated in GERDA, as α particles can deposit an energy equal to $Q_{\beta\beta}$ in the active volume, without producing any light in LAr. The fraction of events surviving analysis cuts gives the performance of the discrimination methods.

- **Custom setups**: a detector's vacuum cryostat can be customized to host an α-decaying source shining on the p^+ electrode, thus providing a sample of *external* αs on which the rejection efficiency of different analysis techniques can be evaluated.

In-situ measurements in the GERDA setup benefit from the cleanest environment around the ^{210}Po α-peak, so that above the Q_β of ^{42}K at 3.5 MeV, only

α-decays populate the energy spectrum. At the same time, the contamination of ^{210}Po is so low that the number of the available α-decays is just a handful per detector per month (and none survive the analysis cuts in small anode detectors). Therefore, only upper limits at $\mathcal{O}(0.1)\,\%$ level are available for the α survival probability with this method [15].

The advantage of *custom setups* is that they can reach a significantly higher statistics of α events using a radioactive source. The disadvantage is, however, that ad-hoc setups are needed, which are hardly as clean as the GERDA core. A pathfinder in this direction was conducted in [16], using a collimated ^{241}Am source shining on the p^+ electrode of a modified BEGe detector (an enlarged version of a BEGe detector with extremely low level of impurities, which was called low depleted (LD)-BEGe) inside a customized vacuum cryostat. The setup was operated in the shallow underground laboratory of TUM, shielded by a 15 m.w.e. overburden. Although a scintillator panel was placed on top of the cryostat and used as an detector anti-coincidence (AC) veto, the background from cosmic rays worsened the signal-to-background ratio, and the analysis yielded survival probabilities compatible with 0, and upper limits at $\mathcal{O}(1)\,\%$ level. As the experiment was carried out using a collimated source, the analysis yielded also a qualitative study of the A/E response depending on the interaction position, which was also a milestone for the field.
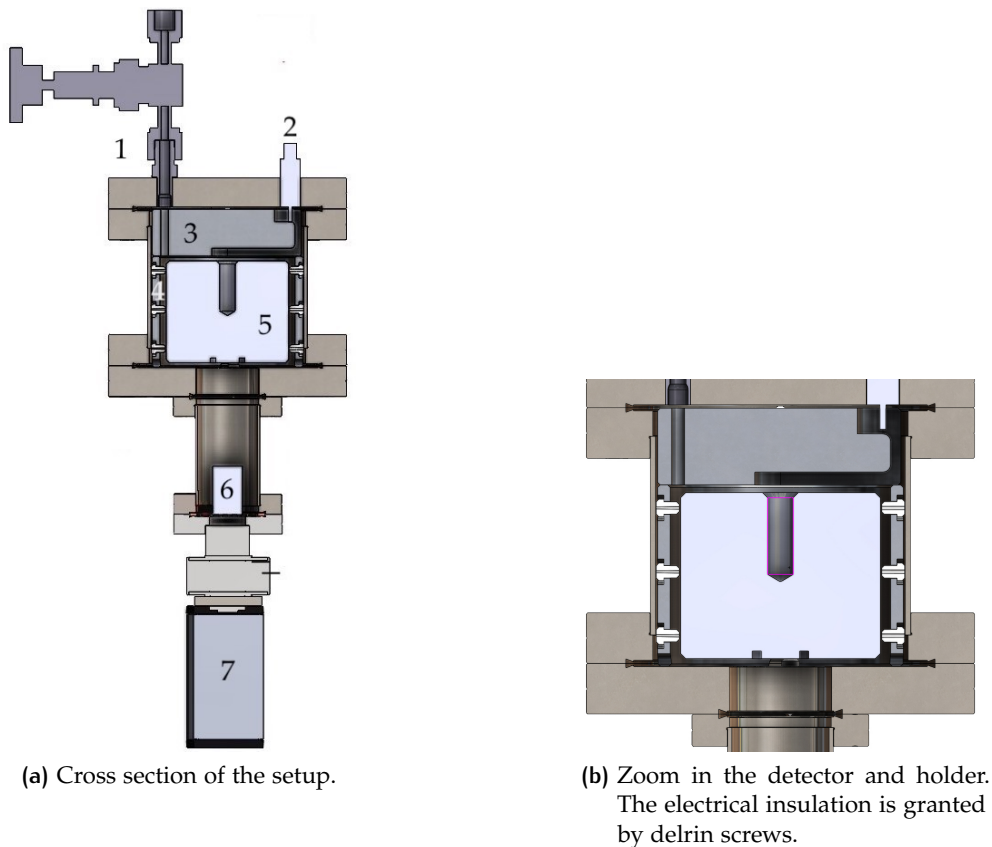
5.4.2 The p^+ spoiler

To get the best out of the two worlds, a high contamination of ^{210}Po directly on the surface of a detector would be desirable. This could be obtained by exposing it to a constant ^{222}Rn emanator, thus accelerating the *natural* process which creates the normally undesired contamination. An Autunite ore fulfills this requirement as it contains the ^{222}Rn progenitor ^{238}U in form of Uraninite (UO_2) in $\sim 50\%$ of its weight [17]. A $\sim 1\,$g ore has been purchased for this purpose, providing an activity of 25 kBq.

Autunite ore as constant ^{222}Rn emanator

The p^+ spoiler setup

With the engineering support of L. Papp at TUM, the setup shown in Figure 5.13 was designed and assembled, which could host the source in the proximity of the p^+ electrode of a generic germanium detector. The setup consists in standard CF components from Kurt J. Lesker with a VCR fitting (for flushing/pumping) and a HV feedthrough welded on the top flange, allowing to set the detector on HV. The internal components are made out of aluminum, and the electrical insulation is ensured by delrin screws on the bottom and side of the detector. The internal volume is filled with material, except for the volume region around the p^+ electrode, where ^{222}Rn can accumulate and decay. Applying a negative HV to the detector (ensuring analogous field strengths as in [18]), increases the collection efficiency of the

(a) Cross section of the setup.

(b) Zoom in the detector and holder. The electrical insulation is granted by delrin screws.

Figure 5.13: (a) Technical drawing of the p^+ spoiler setup: (1) VCR fitting for flushing or pumping. (2) HV feedthrough. (3) Aluminum volume filler (4) Cup-like aluminum detector holder. (5) ICaro. (6) Source holder with Autunite. (7) Pressure gauge. (b) Zoom in the detector surrounding volume.

progeny ions of ^{222}Rn. Once collected at the detector surface, the α-decaying nuclei of ^{218}Po and ^{214}Po can recoil in the direction of the detector and thus create a contamination of ^{210}Po[4] on its surface, which can be subsequently measured either in the vendor's cryostat or with the detector bare in LAr.

5.4.3 Preliminary results

The first deposition campaign has been carried out as a proof-of-principle on the same detector where the aforementioned scan had been performed [16]. As it developed an increasingly high leakage current during the HV ramping up, the detector could not be fully depleted, resulting in a poor energy resolution. Great experience in the deposition mechanism as well as in the technical work has been gained with this campaign. After 180 days of exposure in the p^+ spoiler setup under nitrogen gas overpressure[5], the

First campaign with LD-BEGe

---

4 The decay to ^{210}Po goes through the β-decaying ^{210}Pb, which, with an half-life of 22 yr, continuously increases the ^{210}Po population.

5 The exposure was interrupted several times to monitor the number of ^{210}Po decays and optimize the hardware configuration

detector was installed in a vacuum cryostat and, in a 30 days long measurement, a total number of ~ 60000 potential α events have been identified above 3300 keV, which are shown in Figure 5.14 in the A/E-Energy space. After a comparison with the collimated scan of [16], the events occurring ei-
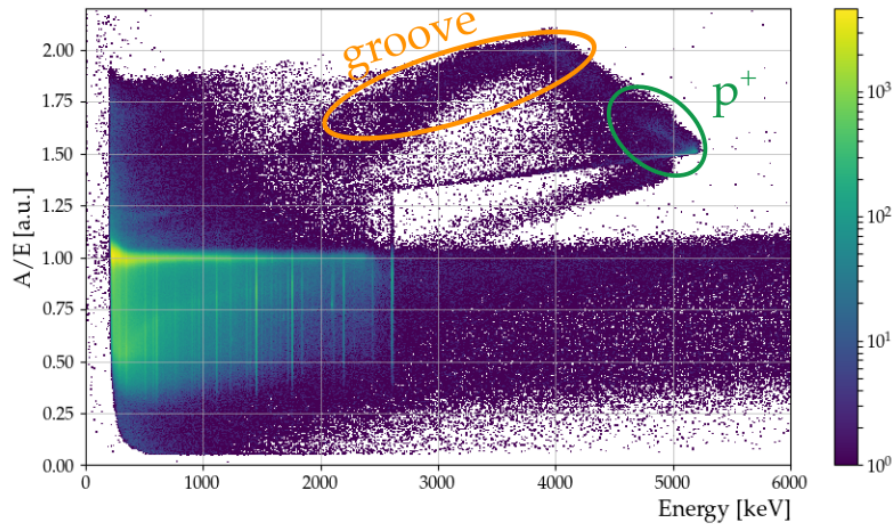

Figure 5.14: A/E vs energy for the LD-BEGe detector after 180 days of exposure in the p^+ spoiler setup and 30 days of measurement in the vacuum cryostat. The recognition of the event location was possible via comparison with the work in [16].

ther around the p^+ electrode or in the groove could be recognized; these are marked in Figure 5.14 with the green and orange circle, respectively. This has proven that the deposition of ^{210}Po was successful on both the p^+ electrode and the groove. A new low statistics population extending from the α peak towards the SSE band was identifed, whose origin could not be traced. Although the analysis of this dataset did not improve the limits of [16], because the rate of ^{210}Po decays was still comparable to the rate of background events (from cosmic or environmental background), it nonetheless fulfilled the goal of proving that a ^{210}Po deposition on the surface of a working detector is indeed achievable, and that a high count rate can be reached within a few months of exposure.

Second campaign with ICaro After the experience gained with the first campaign , ICaro was taken out from the vendor's cryostat and deployed in the p^+ spoiler setup for a long-term deposition. Pictures from the de-cryostating and deployment are given in Figure 5.17. The spoiling has started in June 2021 and is still ongoing. With the deposition efficiency extracted from the previous run, the foreseen number of α-candidates can be predicted as a function of the exposure time in the p^+-spoiler setup. This has been done using the laws of radioactive-series decay which can be found in [19] and the result is shown in Figure 5.15. As an intermediate step, the exposure was interrupted at the end of November 2021 and the number of α-events was cross-checked: it was
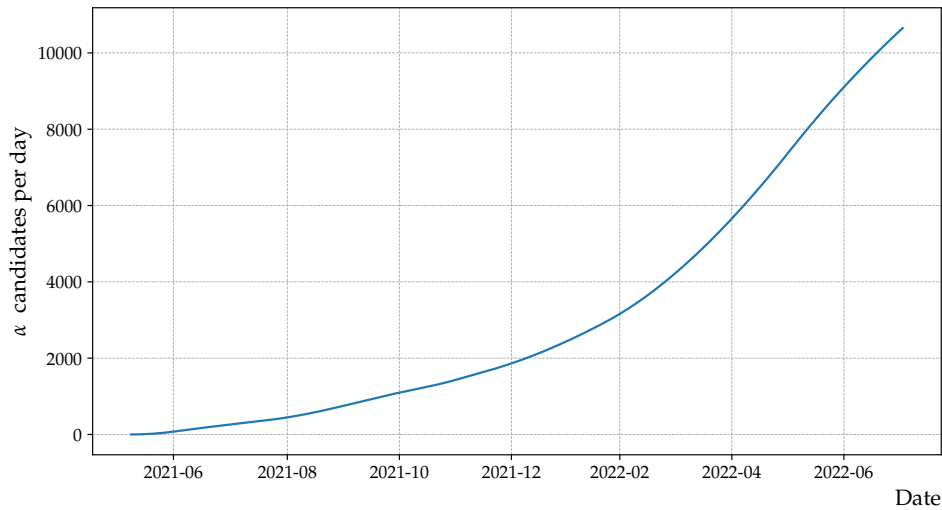
Figure 5.15: Simulation of the α candidates as a function of the exposure in the p$^+$ spoiler setup. The smooth steps are interrumptions in the exposure due to measurements or hardware exchanges.

found to be ∼ 1500/d, in agreement with simulations. A preliminary look at the results of this measurement is shown in Figure 5.16: despite having very different statistics compared to Figure 5.14, it suggests that not all the populations observed in the A/E − E space for the LD-BEGe detector can be found for ICaro. This would indicate a detector-specific response to p$^+$ events, which needs to be further investigated in future spoiling runs with more detectors. Since the two detectors have been passivated using different methods (presumably SiO$_2$ for the LD-BEGe and amorphous germanium for ICaro), further studies could possibly investigate a correlation between the A/E populations and the passivation technique.
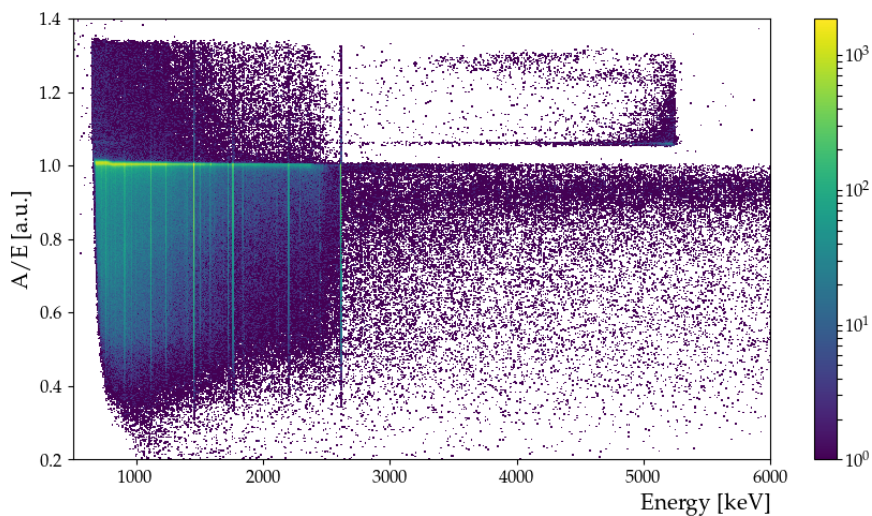
Figure 5.16: A/E vs energy for the ICaro detector after 100 days of exposure in the p$^+$ spoiler setup and 6 days of measurement in the vacuum cryostat.

As a work in progress at the time of writing, the exposure in the p^+ spoiler of ICaro will now proceed until July 2022, when the α events will get to ∼ 10000 per day. In order to maximize the signal-to-background ratio, the detector will then be operated in the LAr setup in the TUM underground laboratory, instrumented with a GERDA-like LAr veto system.

5.5 CONCLUSIONS

A 1.6 kg prototype IC detector has been custom designed and successfully produced as a result of the joint collaboration between TUM, MPIK, BSI and HZDR. It showed excellent performance in terms of charge collection and energy resolution. The peculiar double peak structure in the A/E parameter has been extensively investigated and understood thanks to the work reported here and in Chapter 3. Despite this feature, the detector showed excellent background discrimination performances in all experimental configurations. Thanks to the success of [3] and corroborated by the results of the present characterization campaign, five enriched IC detectors have been produced for deployment in the GERDA infrastructure and as a benchmark for LEGEND, as we shall discuss in Chapter 6 and Chapter 7.

REFERENCES

[1] R. Cooper *et al.*, "A novel HPGe detector for gamma-ray tracking and imaging," *Nuclear Instruments and Methods in Physics Research Section A: Accelerators, Spectrometers, Detectors and Associated Equipment*, vol. 665, pp. 25–32, 2011. DOI: `10.1016/j.nima.2011.10.008`.

[2] Mirion, *SAGe Well Detectors*. [Online]. Available: `https://www.mirion.com/%5Ctextbackslash-well-detectors`.

[3] A. Domula *et al.*, "Pulse shape discrimination performance of inverted coaxial Ge detectors," *Nuclear Instruments and Methods in Physics Research Section A: Accelerators, Spectrometers, Detectors and Associated Equipment*, vol. 891, pp. 106–110, 2018. DOI: `10.1016/j.nima.2018.02.056`.

[4] R. M. Keyser and T. W. Raudorf, "Germanium radiation detector manufacturing: Process and advances," *Nuclear Instruments and Methods in Physics Research Section A: Accelerators, Spectrometers, Detectors and Associated Equipment*, vol. 286, no. 3, pp. 357–363, 1990. DOI: `10.1016/0168-9002(90)90877-9`.
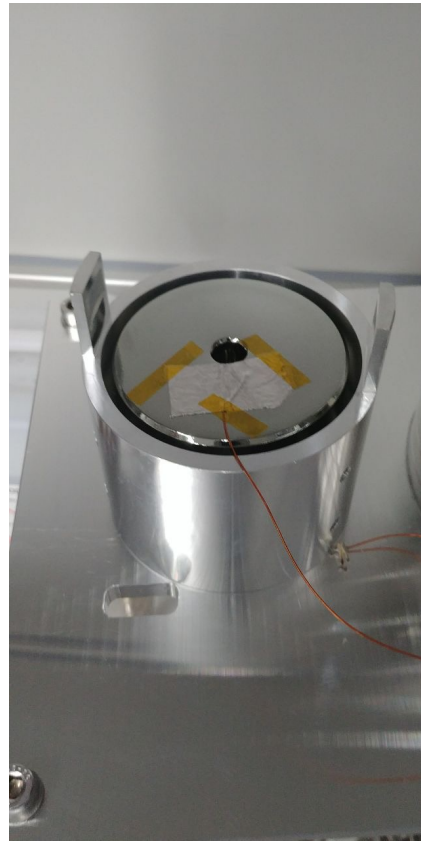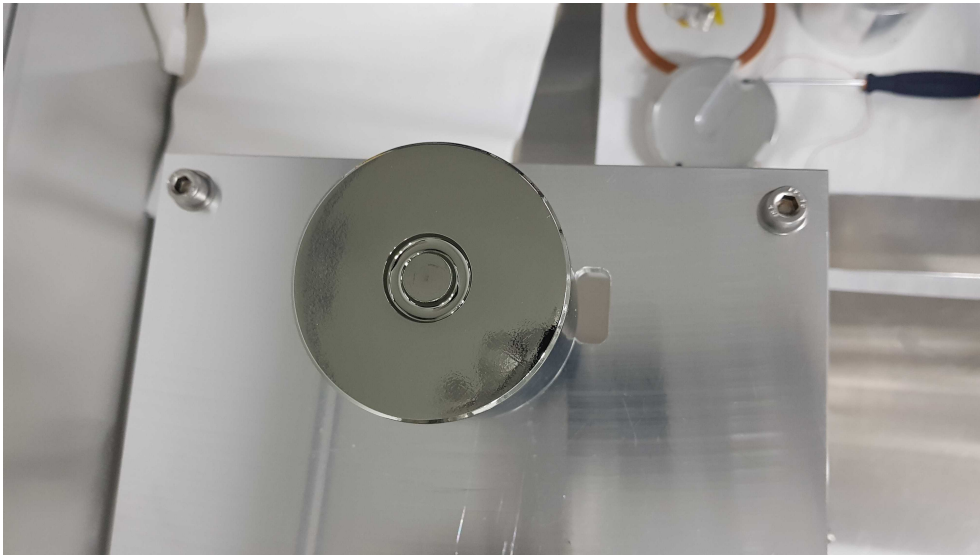
Figure 5.17: Pictures from the de-cryostating and deployment of ICaro into the p^+ spoiler. (a) The author of this dissertation holding ICaro in front of the p^+ spoiler setup. (b) Top view of ICaro in the cup-like aluminum holder, with indium patch and cable for HV connection. (c) View of the p^+ electrode of ICaro, next to the p^+ spoiler.

[5] G. Maggioni *et al.*, "Characterization of different surface passivation routes applied to a planar HPGe detector," *The European Physical Journal A*, vol. 51, no. 11, p. 141, 2015. DOI: `10.1140/epja/i2015-15141-9`.

[6] M. Agostini *et al.*, "Upgrade for Phase II of the GERDA experiment," *The European Physical Journal C*, vol. 78, no. 5, p. 388, 2018. DOI: `10.1140/epjc/s10052-018-5812-2`.

[7] W. Shockley, "Currents to Conductors Induced by a Moving Point Charge," *Journal of Applied Physics*, vol. 9, no. 10, pp. 635–636, 1938. DOI: `10.1063/1.1710367`.

[8] S. Ramo, "Currents Induced by Electron Motion," *Proceedings of the IRE*, vol. 27, no. 9, pp. 584–585, 1939. DOI: `10.1109/jrproc.1939.228757`.

[9] R. Trammell and F. Walter, "The effects of carrier trapping in semiconductor gamma-ray spectrometers," *Nuclear Instruments and Methods*, vol. 76, no. 2, pp. 317–321, 1969. DOI: `10.1016/0029-554x(69)90034-2`.

[10] T. W. Raudorf and R. H. Pehl, "Effect of charge carrier trapping on germanium coaxial detector line shapes," *Nuclear Instruments and Methods in Physics Research Section A: Accelerators, Spectrometers, Detectors and Associated Equipment*, vol. 255, no. 3, pp. 538–551, 1987. DOI: `10.1016/0168-9002(87)91225-3`.

[11] S. Mertens *et al.*, "Characterization of high purity germanium point contact detectors with low net impurity concentration," *Nuclear Instruments and Methods in Physics Research Section A: Accelerators, Spectrometers, Detectors and Associated Equipment*, vol. 921, pp. 81–88, 2019. DOI: `10.1016/j.nima.2018.09.012`.

[12] D. Budjáš *et al.*, "Pulse shape discrimination studies with a Broad-Energy Germanium detector for signal identification and background suppression in the GERDA double beta decay experiment," *Journal of Instrumentation*, vol. 4, no. 10, P10007, 2009. DOI: `10.1088/1748-0221/4/10/p10007`.

[13] M. Agostini *et al.*, "Characterization of 30 ^{76}Ge enriched Broad Energy Ge detectors for GERDA Phase II," *The European Physical Journal C*, vol. 79, no. 11, p. 978, 2019. DOI: `10.1140/epjc/s10052-019-7353-8`.

[14] S. I. Alvis *et al.*, "Multisite event discrimination for the MAJORANA DEMONSTRATOR," *Physical Review C*, vol. 99, no. 6, p. 065 501, 2019. DOI: `10.1103/physrevc.99.065501`.

[15] N. Abgrall *et al.*, "LEGEND-1000 preconceptual design report," *arXiv*, 2021.

[16] M. Agostini *et al.*, "BEGe detector response to alpha-induced energy depositions on the p+ electrode and groove surfaces," Tech. Rep., 2013.

[17] D. Barthelmy, *Autunite Mineral Data*. [Online]. Available: `http://webmineral.com/data/Autunite.shtml%5C#.Yj2UYi9aaAl` (visited on 03/25/2022).

[18] J. Kiko, "Detector for ^{222}Rn measurements in air at the 1 mBq/m^3 level," *Nuclear Instruments and Methods in Physics Research Section A: Accelerators, Spectrometers, Detectors and Associated Equipment*, vol. 460, no. 2-3, pp. 272–277, 2001. DOI: `10.1016/s0168-9002(00)01082-2`.

[19] R. D. Evans, *The Atomic Nucleus*. Tata McGraw Hill Publishing Company Limited, 1955.

6 | ENRICHED INVERTED COAXIAL DETECTORS FOR LEGEND

After the promising results from the prototypes of Chapter 5 and [1], five IC detectors made out of material enriched to 88% in ^{76}Ge have been produced in collaboration with Mirion Technologies [2], and their performances have been benchmarked in the vendor's cryostats. In preparation for the Legend experiment, they have also been deployed bare in the Gerda apparatus for long-term characterization in LAr. This chapter reports on their first characterization in the vendor's cryostats, where the performances in terms of energy resolution, charge collection and background discrimination have been investigated. Their long-term operation in LAr will be exhaustively discussed in Chapter 7.

The author of this dissertation has given a significant contribution to the measurements and results presented in this chapter, which have been published in [3, 4].

6.1 DETECTOR PRODUCTION

In 2017, the Gerda collaboration purchased ∼ 20 kg of germanium, enriched to 87.7(5)% in ^{76}Ge, in the form of GeO$_2$ powder. The enrichment has been carried out in the Production Association Electrochemical Plant (ECP) [5] of the Isotope Joint Stock Company (JSC) [6] in Zelenogorsk, Russia. As for the Gerda BEGe detectors for Phase II [7], the reduction and purification process took place at the PPM Pure Metals company in Goslar, Germany [8]. About 95% of the material had the required quality and 1.6% was lost during etching and cutting of the bars. The rest was too little for another purification process and has been stored for future processing.

20 kg of enriched GeO$_2$ powder have been reduced and zone-refined...

The enriched bars have been shipped to Mirion Technologies - Oak Ridge, US, for crystal pulling. Three detector blanks have been pulled, from which five crystals have been obtained. Their final conversion to diodes took place in February 2018 at Mirion Technologies - Olen, Belgium, where a total mass of 9.618 kg was converted into 5 working IC detectors. Their identifiers were assigned to give information on the detector geometry and the crystal where they had been cut from: being all inverted coaxial detectors and cut from crystal numbers 48, 50 and 74, they were named IC74A, IC48A, IC48B, IC50A, IC50B. More information on their dimensions and weight can be

...and converted to 5 working detectors, of ∼2 kg each

Det. ID	Diameter [mm] [±0.2]	Height [mm] [±0.3]	Well depth [mm] [±0.5]	Mass [g] [±0.5]
IC48A	74.6	80.4	47.4	1918.9
IC48B	72.6	80.5	56.0	1815.8
IC50A	74.7	80.4	40.0	1881.1
IC50B	72.6	85.4	53.9	1928.7
IC74A	76.6	82.3	52.4	2072.9

Table 6.1: Dimensions and mass of the 5 enriched IC detectors characterized during the 2018 campaign.

found on Table 6.1. Overall, the estimated mass yield was 51%, slightly below the achieved 53.3% during the previous BEGe detectors production [7].

As for ICaro in Chapter 5, the geometrical dimensions have been customized by the GERDA collaboration to allow a depletion voltage lower than 4 kV and to minimise the regions of low electric field (<200 V/cm). The resulting electric field and weighting potential are shown in Figure 6.1 for all the 5 detectors. Compared to ICaro, these IC detectors are ~2 cm longer and ~0.5 kg heavier. This creates bigger volumes where the weighting potential is very low ($W_{pot} < 0.1\%$), i.e. where the determination of the starting point of the drift is less accurate.

6.2 CHARACTERIZATION IN VACUUM CRYOSTATS

Most of the characterization campaign took place in the High Activity Disposal Experimental Site (HADES) underground facility in Mol, Belgium. It benefits from a 500 m.w.e. overburden, which is desirable to minimize the activation rate of ^{77}Ge. This campaign largely benefited from the characterization of the 30 BEGes for GERDA Phase II [9], as the same Hades Experimental Research Of Intrinsic Crystal Appliances (HEROICA) platform [10] has been used and similar protocols have been applied. Due to burocratical delays in sending a 250 kBq ^{228}Th source from TUM to HADES, the measurements with such source have been carried out at the TUM shallow underground laboratory, shielded by a 15 m.w.e. overburden.

6.2.1 Experimental setup

The detectors have been installed in vacuum cryostats and cooled down via a cold finger immersed in LN_2. A DAQ system similar to the one presented in Chapter 5 was set up:

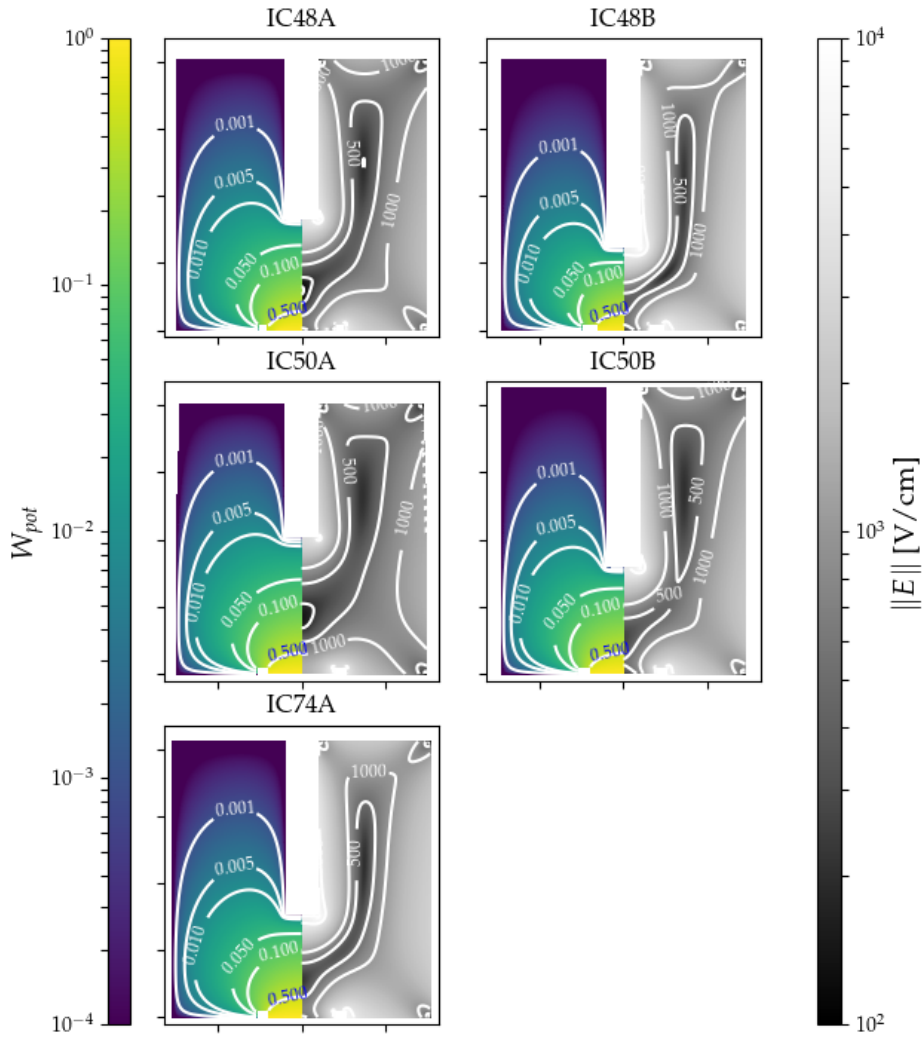**Figure 6.1:** Module of the electric field $\|E\|$ and weighting potential W_{pot} of the 5 enriched IC detectors produced in 2018.

- *Digital chain*: the signal is amplified by a non shaping amplifier (Genius II) and digitized at 100 MHz by the VME Struck 3301 FADC. For each triggered event, a 10 μs long trace at full sampling rate, and a down-sampled 160 μs long trace at 25 MHz are recorded for offline analysis.

- *Analog chain*: after a 10 μs shaping with a spectroscopy amplifier, the signal is recorded with a MCA, which provides an energy spectrum as output and no information on the pulse shape.

Most of data have been acquired using the digital chain, with full information on the trace. Due to occasional failures of the FADC, part of it was recorded with the analog chain. A sketch of the experimental setup used for the characterization is shown in Figure 6.2.
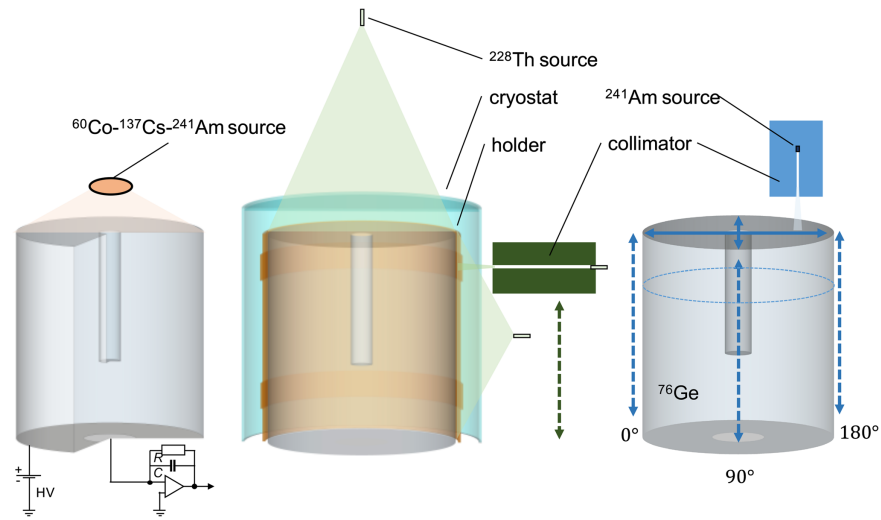
Figure 6.2: Configurations used for detector characterization. **Left**: Setup for depletion voltage estimation with a mixed 1.5 kBq source of ^{60}Co –^{137}Cs –^{241}Am. **Middle**: Setup for PSD studies with a flood top and side 13 kBq ^{228}Th source and with a collimated 250 kBq ^{228}Th source for lateral scans. The vacuum cryostat (cyan) and detector holder (orange), both made of aluminum, are added here for illustration. **Right**: Setup for scans with the collimated 4.3 MBq ^{241}Am source: lateral at 3 polar angles (dashed lines) and 2 orthogonal directions on top (solid lines).

6.2.2 Operational voltage and list of measurements

For all detectors, positive voltage was applied to the n^+ electrode while the p^+ was grounded and used as read-out. Full depletion voltage was found by increasing the HV in steps from 2 kV to 4.7 kV and tracking the main parameters (peak position, energy resolution and count rate) of the peaks from a mixed 1.5 kBq ^{60}Co - ^{137}Cs - ^{241}Am source. The resulting energy spectrum is shown in Figure 6.3 for detector IC50A at a bias voltage of 3 kV.

As in the previous GERDA campaigns, full depletion was defined at the value where the energy resolution reaches its minimal and stable value. The
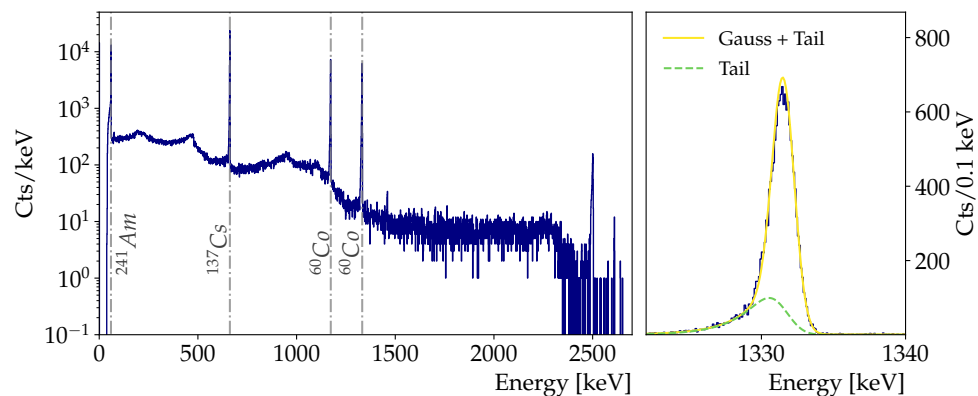

Figure 6.3: Left: Energy spectrum for IC50A with the mixed ^{60}Co-^{137}Cs-^{241}Am source. **Right:** fit of the 1332.5 keV line from ^{60}Co.

Det. ID	Exp [V]	Manufacturer [V]	Set in HADES [V]	Set in GERDA [V]
IC48A	2900	3500	4000	3300
IC48B	3200	3500	4000	3200
IC50A	2900	3000	4000	3700
IC50B	3200	3500	4000	3800
IC74A	3800	4000	4500	4400

Table 6.2: Depletion voltages extracted from the experiment (Exp), in comparison to those provided by the manufacturer, for the 5 enriched IC detectors. Operational voltages applied when the detectors were used in vacuum cryostats (in HADES) and in the GERDA setup are also reported.

results of the high voltage scan relatively to the 1.3 MeV peak from ^{60}Co are shown in Figure 6.4, and Table 6.2 reports the depletion voltages following this definition (*Exp*). As a reference, the values provided by the manufac-
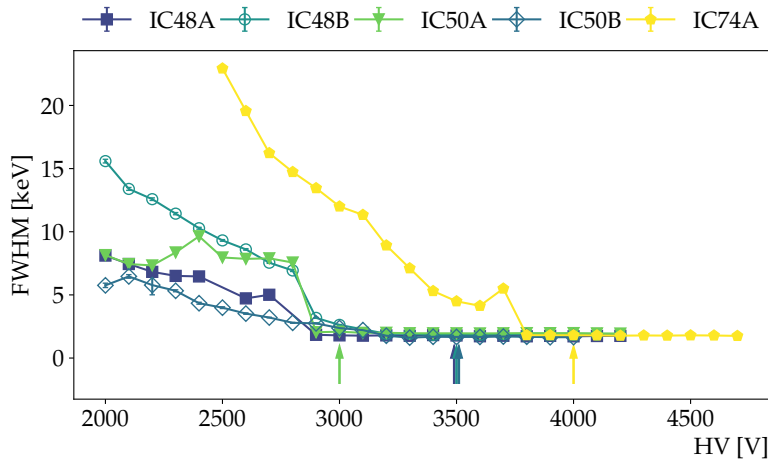
Figure 6.4: Energy resolution (in FWHM) of the 1332.5 keV line from ^{60}Co for all detectors. The arrows show the depletion voltages reported by the manufacturer.

turer and those used in HADES and GERDA are also reported. All deple- *All depletion voltages below* tion voltages were lower than 4 kV, fulfilling the required specification. For *4 kV* the characterization measurements in vacuum cryostats, the voltages recommended by the manufacturer, which are typically 500–1000 V higher than depletion, were applied (see *Manufacturer* in Table 6.2). As done in the previous campaigns, the operational voltages in the GERDA cryostat were set to 400–600 V above depletion.

At the operational voltage, the following measurements have been taken:

- **Estimate the best energy resolution achievable:** the gamma lines from the ^{60}Co –^{137}Cs –^{241}Am and ^{228}Th sources have been used to construct the energy resolution in FWHM as a function of energy in the optimal electronics noise condition of a vacuum cryostat.

- **Probe the geometrical detector response:** the homogeneity of the detector surface has been probed with a collimated 60 keV γ-beam from a 4.3 MBq ^{241}Am source embedded on a 3D movable arm [10].

- **Pulse shape analysis:** a 13 kBq ^{228}Th source was used flood on the top and the side of the detector to test the background discrimination performances. As for ICaro in Section 5.3.1, an additional 250 kBq ^{228}Th source was used collimated to study the pulse shape as a function of the interaction position. A total of 4 collimated source positions were probed along the Z-axis of each detector. As this source was located at the shallow underground laboratory of TUM, this special measurement was conducted there.

6.2.3 Energy resolution

Energy resolution:
2.04–2.19 keV FWHM @
Q$_{\beta\beta}$

The γ-lines from the ^{60}Co –^{137}Cs –^{241}Am and ^{228}Th sources have been fitted with a gaussian function sitting on a sigmoid-like background, and the resulting resolution in FWHM as a function of the γ-ray energy is shown in Figure 6.5 for all detectors. The data points have been fitted with a function of the type $f(E) = a + b \cdot \sqrt{E}$ to interpolate the resolution at Q$_{\beta\beta}$, which ranges from 2.04 to 2.19 keV (FWHM) in the vacuum cryostat.
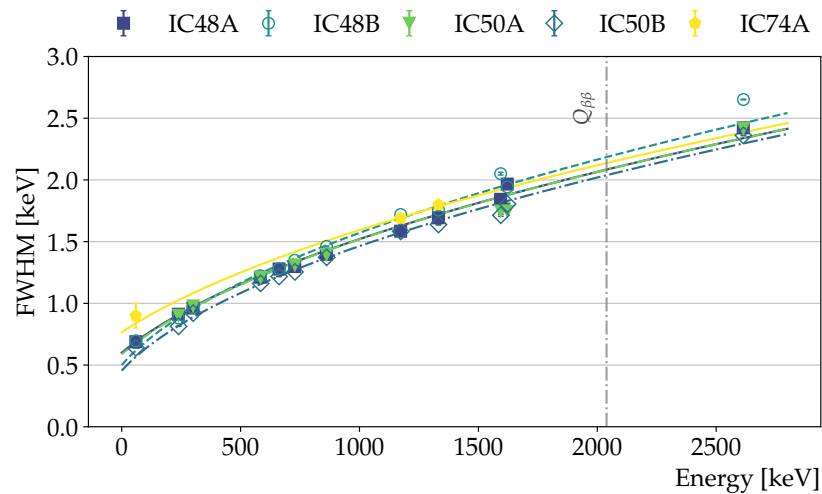

Figure 6.5: Energy resolution (in FWHM) as a function of the γ-ray energy, for all detectors. The statistical uncertainties are smaller than the marker size.

6.2.4 Surface response homogeneity

Side and top surface scanned
at different polar angles with
60 keV γ-rays

Similarly to what has been done for ICaro in Chapter 5, the homogeneity of the detector response along the surface has been investigated by means of a collimated 60 keV γ-beam from a 4.3 MBq ^{241}Am source. Compared to

Chapter 5, in the present characterization campaign the collimator consisted of a 30 mm long copper cube, with a 1 mm diameter aperture, resulting in a ~2 mm^2 diameter spot on the detector surface. The parameters of interest, as in Section 5.2.4, are the count rate and position of the 60 keV peak for the investigation of charge collection efficiency; the rise time (0.5 − 90%) and A/E for PSA.

As sketched in Figure 6.2, two main sets of measurements have been taken: a scan of the detector side over its full height, and a radial scan of the top surface. The side scan was repeated at 3 polar angles (see Figure 6.2), and the top scan at 2 orthogonal directions. The source was typically moved in steps of 1 mm every 5 minutes and a total number of approximately 1500 measurements have been taken. For the sake of conciseness, only the results for IC50A (Figure 6.6) and the common features for all the 5 detectors will be reported in the following (Table 6.3). The detailed analysis for all detectors can be found in Appendix B.

6.2.4.1 Side longitudinal scan

The count rate of events at $(60 \pm 2\sigma)$ keV (Figure 6.6a) exhibits two specific wells around $Z = 10$ and 60 mm, which reflect the two 9 mm long ditches on the detector holder (sketched in Figure 6.2, middle). This profile is well reproduced at all angles. Additionally, this specific detector shows an increased count rate starting from $Z = 40$ mm. Indeed, IC50A has a light tapering starting from that value up to the top surface, which was obtained by milling the already Li-diffused surface. As this operation removes part of the dead layer, it explains the effect.

Increased count rate in upper part of IC50A *due to tapering*

The $\sim 0.05\%$ decrease in the value of the peak position for interactions occurring further away from the p^+ electrode (Figure 6.6c) is interpreted as an indication for a modest charge trapping, analogously to Section 5.2.4.

Indication of small charge trapping (0.05%)

The rise time shown in Figure 6.6e is the mean value of all the events in the 60 keV peak. It exhibits the same features as ICaro (see Figure 5.7e), namely a plateau for $Z < 20$ mm, a linear increase in the middle region, and another plateau in the top part of the detector, characterized by values which are 200 ns higher. Compared to ICaro, however, the present IC detectors feature bigger volumes of low weighting field, which implies a larger volume of constant rise time.

Rise time 200 ns *longer in top half*

Finally, the average A/E for the 60 keV γ-rays features two plateaus with a $\Delta A/E = 0.3\%$, as visible in Figure 6.6g. This fact, and its correlation with the rise time, is explained by the charge cloud dynamics described in Chapter 3. The deviations at different polar angles are explained by small instabilities in the electronics, as no difference in the crystallographic properties is expected at angles multiple than 90°.
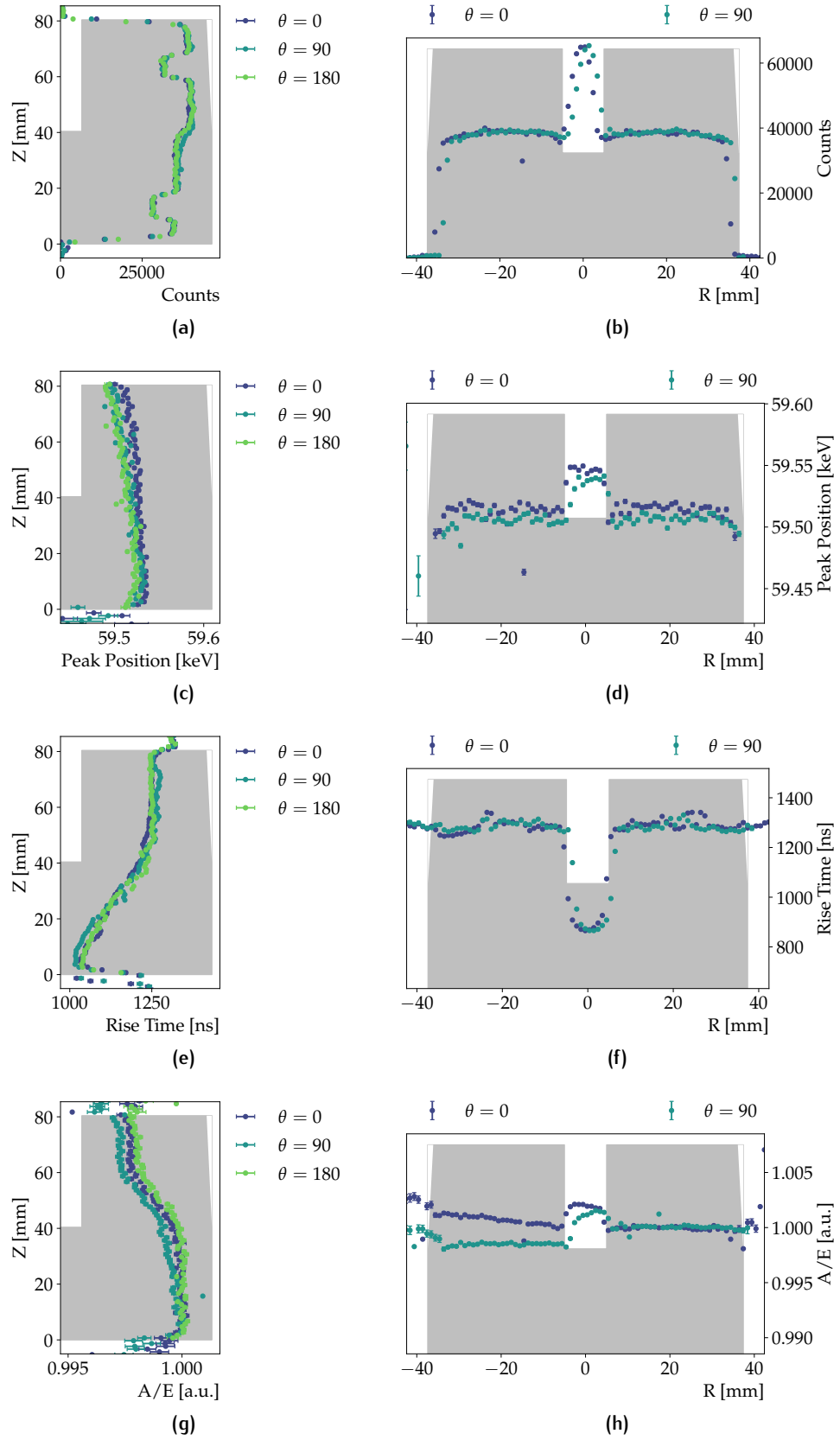
A/E 0.3% lower in top half

Figure 6.6: Results of the side longitudinal (left) and top radial (right) scan of IC50A for the 60 keV γ-rays from ^{241}Am.

6.2.4.2 Top radial scan

The top radial scan exhibits interesting features due to the presence of the borehole. While the count rate (Figure 6.6b) outside is compatible with the values for high Z from the side scan, an increase for interactions occurring inside is explained by a thinner dead layer originating from the fabrication process.

Thinner Li layer in the borehole

The analysis of the peak position (Figure 6.6d) yields, as for ICaro, indications of a slightly stronger charge trapping (0.07%) than observed in the lateral scan, which is explained considering the much shorter trajectories for interactions occurring at the bottom of the borehole.

Indication of a mild charge trapping (0.07%)

The rise time values (Figure 6.6f) outside the well are compatible with the higher plateau at ~1200 ns from the lateral scan, and decrease to 800 ns at the bottom of the borehole, as a result of the much shorter trajectories for those events.

Rise time agrees with upper position of side scan

The A/E analysis (Figure 6.6h) reproduces the increased A/E values for interactions occurring at the bottom of the borehole, which was observed for ICaro. This effect, as explained in Section 5.2.4, is due to the charge cloud dynamics. Additionally, a small angular shift in A/E is observed, which can be attributed to some instabilities in the electronics chain. Due to time constraints, it has not been investigated further.

A/E is 0.3% higher in the borehole

6.2.4.3 Remarks on the surface scan

An overview of the surface scan campaign is given with Table 6.3, which provides the maximum variation of the parameters of interest for the 5 ICs.

Charge trapping smaller than resolution in the Gerda cryostat for all detectors

Det. ID	ΔPP [%]	ΔA/E [%]	Min RT [ns]	Max RT ns
IC48A	0.06	0.16	970	1190
IC48B	0.20	0.26	925	1200
IC50A	0.08	0.25	980	1240
IC50B	—	—	—	—
IC74A	0.13	0.10	920	1150

Table 6.3: Maximal variation Δ of Peak Position (PP) and A/E for the 60 keV γ-ray events. The minimum and maximum value of the rise time (RT) are also reported for comparison with data from ^{228}Th. No information on the pulse shape of signals for IC50B is available, as data were taken with a MCA.

The values of the maximal variation of the peak position (ΔPP) suggest that the amount of charge trapping observed for these detectors is not troublesome for GERDA, as the shifts in the peak position lie in the same range of the energy resolution at Q$_{\beta\beta}$ (which, as we will see in Section 7.1.1 is ~ 0.15% in the GERDA cryostat). The A/E shifts range from 0.1% to 0.25%, which is of

A/E shift is within the resolution achievable in Gerda

the same order as, or lower than, the typical A/E resolution (which, as will be shown in Section 7.1.2, is $\mathcal{O}(1)$ %). As collective effects are energy dependent[1], however, A/E shifts need to be investigated at higher energies, too, as will be presented in Section 6.3.1. In Table 6.3 the minimum and maximum values of the rise time obtained from the lateral scan are also reported, as will be relevant to benchmark data from the ^{228}Th source. Data for IC50B were taken with a MCA due to a failure of the FADC system, hence no information on the pulse shape is available. Also, due to some instabilities, the variations in the peak positions were not considered as reliable as in the other datasets.

6.3   PULSE SHAPE ANALYSIS

For this characterization campaign, three types of data were collected with a ^{228}Th source: two flood measurements (from top and lateral position of the detectors) and a collimated lateral scan at 4 different heights, using the same collimator as in Section 5.3.1. This last set of measurements has been carried out at the TUM shallow underground laboratory.

6.3.1   Pulse shape dependence on the interaction position

A/E dependence on the interaction position confirmed for all five detectors

In order to confirm the dependence of the pulse shape on the interaction position for these detectors, the correlation between A/E and rise time for DEP events from a ^{228}Th source has been investigated for all the experimental configurations. For the sake of conciseness, only the results of the lateral collimated scan for IC50A (Figure 6.7) will be described in the following, while the plots for all detectors can be found in Appendix B.

As we have seen in Section 5.3.1, moving from lower to higher positions (marked with Z in Figure 6.7), DEP events gradually shift from the *Short* to the *Long* population. This feature was observed in all the 5 detectors in all experimental configurations, thus confirming the dependence of A/E on the interaction position for these detectors, too.

ΔA/E on average higher than for ICaro

The difference ΔA/E between the *Short* and *Long* A/E populations is reported in Table 6.4 for all detectors, next to the values of the mean rise time of both. These IC detectors, being ∼ 25% longer than ICaro, exhibit a difference in the values of the rise time between upper and lower half which is higher (∼200 ns). Due to the complex interplay between collective effects, the higher separation between these two values is responsible for a higher ΔA/E between the two populations. Indeed, the two A/E peaks could be resolved in the low noise environment of the vendor's vacuum cryostat.

---

1 Due to the Coulomb self-repulsion, see Chapter 3.
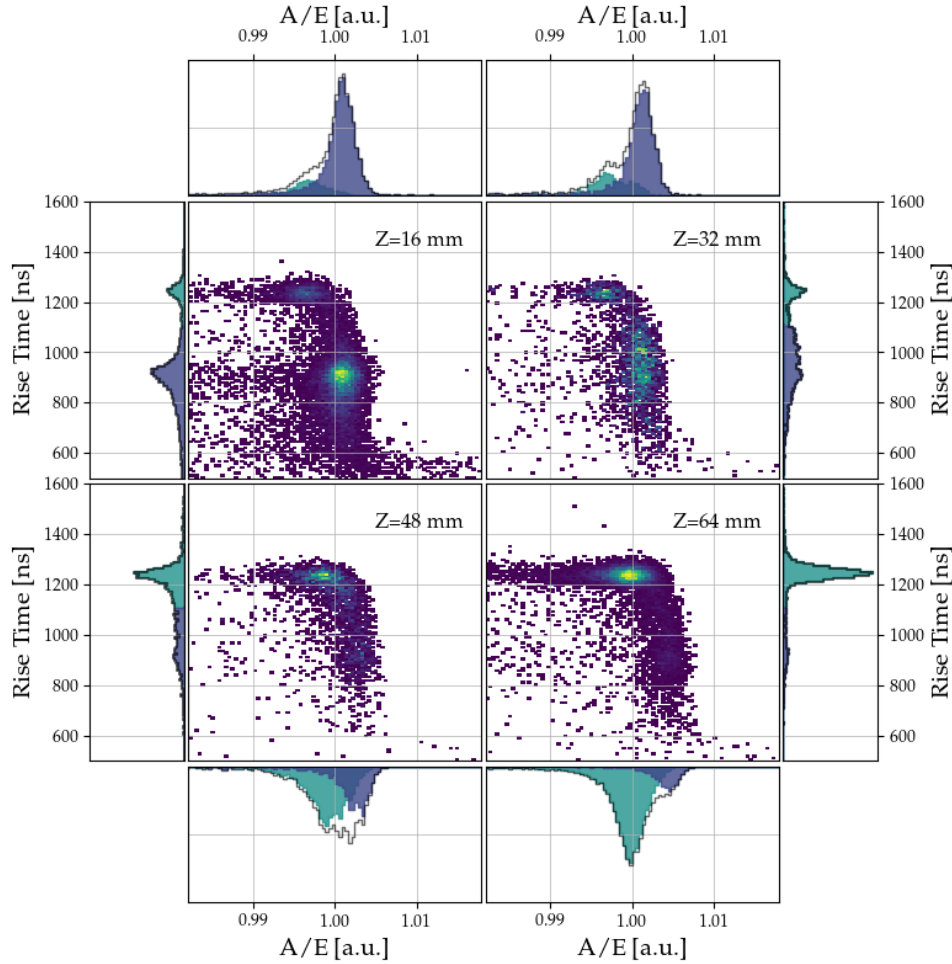
Figure 6.7: Experimental correlation of A/E on the rise time for DEP events from a collimated scan with ^{228}Th of the lateral surface of IC50A.

Compared to the maximal variations of A/E from the surface scan with ^{241}Am (Table 6.3), the $\Delta A/E$ for DEP events is larger. This is expected, as the Coulomb self-repulsion depends strongly on the number of generated carriers. Some tension also arises in the values of rise time, as was observed in Section 5.2.4, to which we refer for clarification.

Det. ID	$\Delta A/E$ [%]	*Short* RT [ns]	*Long* RT [ns]
IC48A	0.40	870	1180
IC48B	0.43	915	1205
IC50A	0.47	920	1260
IC50B	0.31	820	1080
IC74A	0.23	880	1190

Table 6.4: Parameters of interest of the *Short* and *Long* populations of DEP events from a flood lateral measurement with ^{228}Th. $\Delta A/E$ is the difference between the A/E peak positions of the *Short* and *Long* populations. The mean risetime (RT) for both is also reported.

6.3.2 Event discrimination performance

Analogously to the characterization of ICaro, a ^{228}Th source was used to investigate the event discrimination performance of the present detectors. Compared to the analysis of ICaro, however, the higher separation of the two A/E peaks in the flood lateral measurements (as can be seen in Figure 6.8) required the development of new tools to track the energy dependence of the two peaks separately. These have been fitted with a double gaussian plus the standard tail function of [11], and the energy dependence of the lower peak was chosen for the correction on A/E.

New tools developed to track energy dependence of double A/E peak
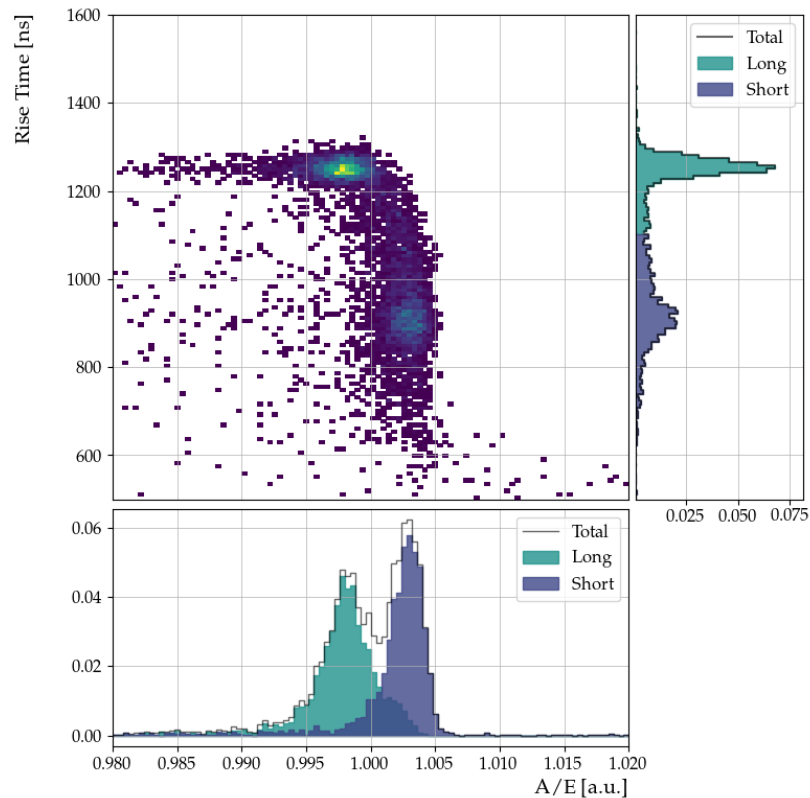
Figure 6.8: Experimental correlation of A/E on the rise time for DEP events from a flood irradiation with ^{228}Th of the lateral surface of IC50A.

The survival probability (SP) of the different event samples is reported in the first column of Table 6.5 for the analysis of the data from the flood lateral measurement for detector IC50A. As this analysis deals with a double peak in the A/E space, it was labeled as *Double*.

Energy dependent rise time correction of A/E

Additionally, the second column, labeled as *Corrected*, reports the event discrimination performance of IC50A after a correction based on the rise time, which was performed in a modified version compared to Section 5.3.2. Specifically, as these detectors feature a stronger energy dependence of the separation between the two A/E populations, the correlation between rise

time and A/E was fitted for many j Compton continuum regions above
1 MeV, as:

$$A/E(RT)_j = a_j + b_j \cdot RT_j \tag{6.1}$$

The values of a_j and b_j obtained from the fits of the j Compton continuum
regions are shown in Figure 6.9. From those, the energy dependent $a(E)$ and
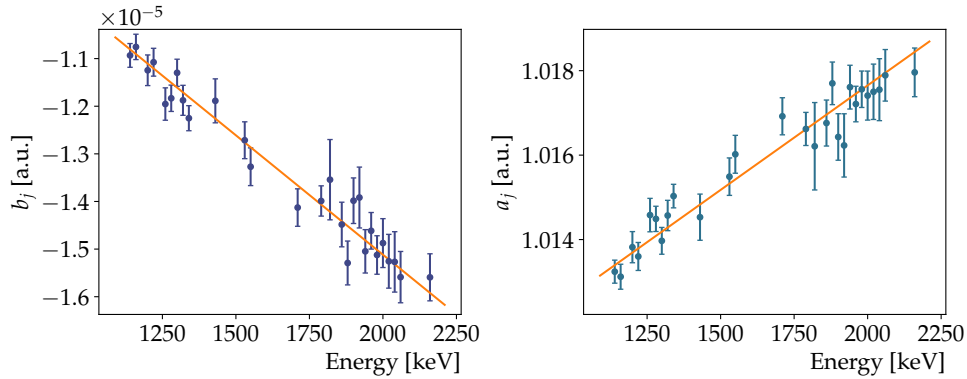
Figure 6.9: Fitting parameters of the A/E dependence on the Rise Time for all the j
Compton regions between 1 and 2.2 MeV, for detector IC50A.

$b(E)$ are determined via linear interpolation (shown with the orange curve
in Figure 6.9); these parameters have then been used to correct the A/E value
on a single event basis:

$$A/E_i^{corr} = (A/E_i - b(E) \cdot RT_i)/a(E) \tag{6.2}$$

Such a correction is physically motivated, as the collective effects which are
responsible of the double A/E populations are strongly energy dependent,
and brings *as a consequence* a minimization of the resolution of the A/E pa-
rameter. Indeed, as shown in Figure 6.10 and Figure 6.11 the A/E^{corr} after
correction does not exhibit a double peak structure anymore.   As was the
case for ICaro, the correction does not significantly improve the background
discrimination performance, nevertheless it reduces the volume dependence
of the PSA performance, possibly reducing the systematic uncertainties of
the analysis.

Event class	Side					
	Double		*Corrected*		*Split*	
^{208}Tl DEP	90	(2)	90	(2)	90	(2)
^{208}Tl SEP	6.3	(4)	6.2	(4)	6.2	(4)
^{208}Tl FEP	8.05	(8)	8.47	(8)	8.62	(8)
^{212}Bi FEP	9.3	(4)	8.3	(4)	8.7	(4)
CC @$Q_{\beta\beta}$	33.4	(6)	33.8	(6)	35.2	(6)

Table 6.5: Survival probabilities for the flood lateral measurement of IC50A with
^{228}Th for different analysis techniques.
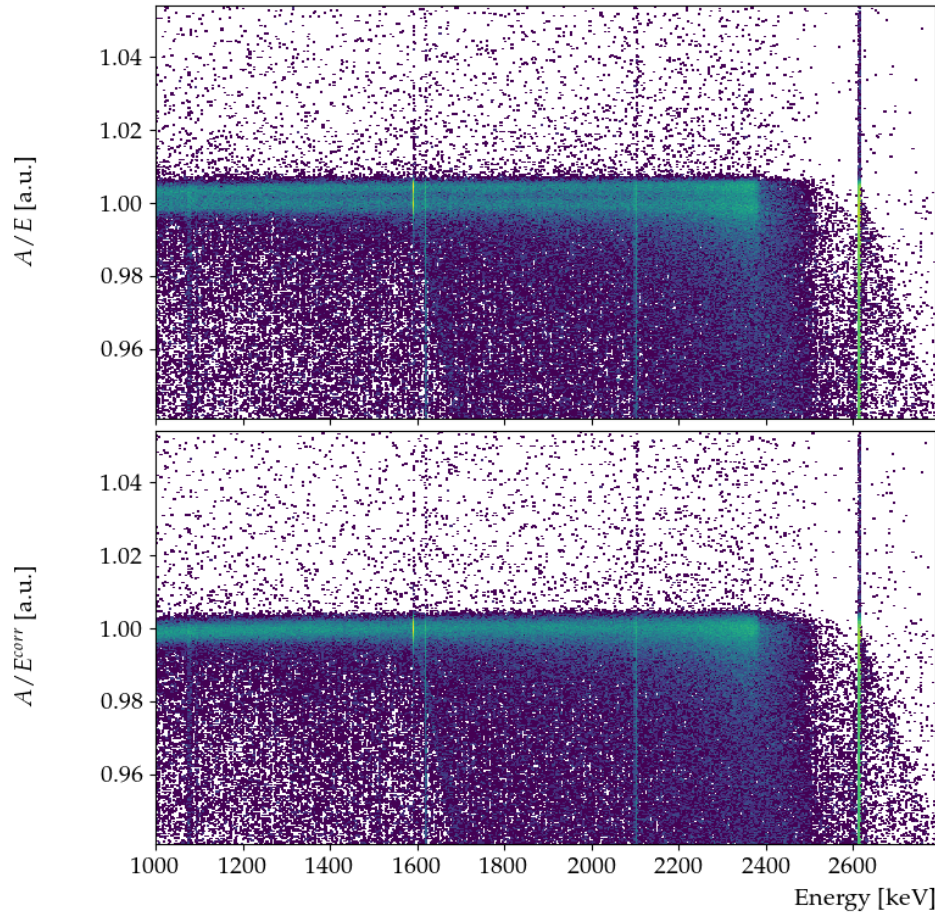
Figure 6.10: A/E spectrum from the lateral flood irradiation with a ^{228}Th source for detector IC50A before (top) and after (bottom) the correction based on the rise time described in the text.

Split analysis　　The performance of the *Split* analysis proposed in Section 5.3.2 have been investigated for these detectors, too, and the results for IC50A are reported in the last column of Table 6.5, under the *Split* label. From an overview of all detectors (available in Appendix B), we do not find strong statistical evidence of improvements in the background discrimination capabilities for this method. Considering also its technical complexity for $\mathcal{O}(100)$ detectors, we do not foresee its future use in double beta ($\beta\beta$)-decay experiments with ^{76}Ge.

For what concerns the flood measurements from the top, given the geometrical distribution of DEP events, only the *Long* population is represented, hence the standard A/E analysis has been carried out, and the results are reported in Table 6.6 for all detectors.
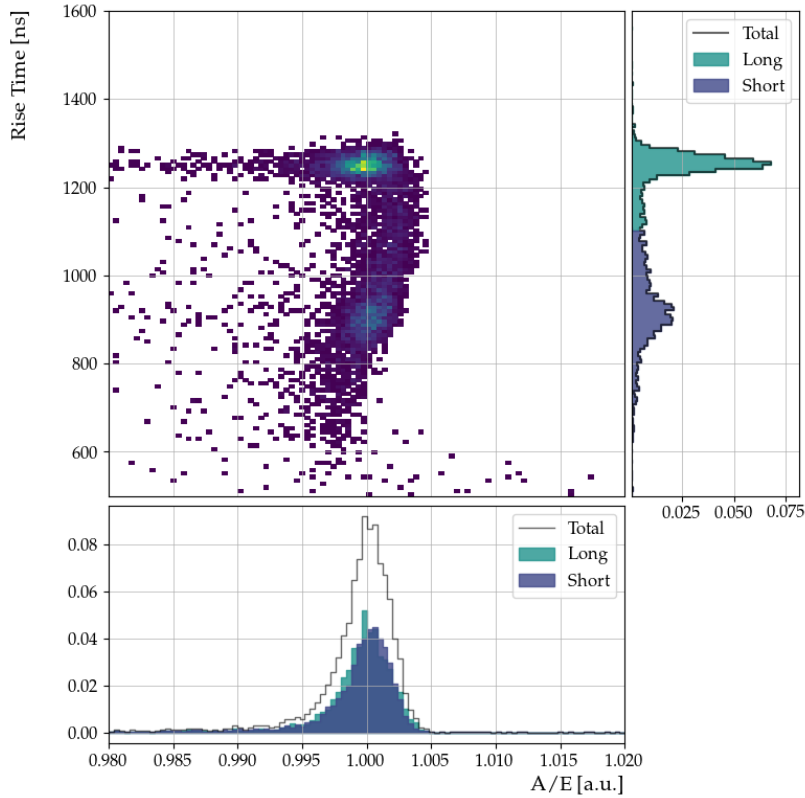
Figure 6.11: Correlation of the rise time corrected A/E^{corr} on rise time for DEP events from a flood irradiation with ^{228}Th of the lateral surface of IC50A.

Event class	Top									
	IC48A		IC48B		IC50A		IC50B		IC74A	
^{208}Tl DEP	90	(2)	90	(1)	90	(1)	90	(1)	90	(3)
^{208}Tl SEP	6.4	(7)	6.6	(3)	6.5	(3)	5.6	(3)	7.6	(6)
^{208}Tl FEP	9.8	(1)	8.70	(7)	9.28	(8)	8.51	(7)	-	-
^{212}Bi FEP	6.9	(9)	8.0	(5)	8.6	(4)	7.9	(4)	12.1	(9)
CC @$Q_{\beta\beta}$	37.1	(8)	35.8	(4)	35.7	(6)	36.6	(5)	34.5	(8)

Table 6.6: Survival probabilities for the flood top measurement of all detectors with ^{228}Th.

6.4 CONCLUSIONS

Five enriched IC detectors have been successfully produced and characterized in terms of surface response, energy resolution and background rejection capabilities. Their performances in vacuum cryostats were excellent in all the investigated fields. The dependence of the pulse shape on the interaction position found in Chapter 5 was confirmed for these detectors, too. Despite that, all the 5 enriched detectors proved an excellent level of background discrimination, fulfilling the requirements for operation in GERDA

and LEGEND. Chapter 7 will describe their long term operation in LAr, inside the GERDA cryostat.

REFERENCES

[1] A. Domula *et al.*, "Pulse shape discrimination performance of inverted coaxial Ge detectors," *Nuclear Instruments and Methods in Physics Research Section A: Accelerators, Spectrometers, Detectors and Associated Equipment*, vol. 891, pp. 106–110, 2018. DOI: 10.1016/j.nima.2018.02.056.

[2] Mirion, *SAGe Well Detectors*. [Online]. Available: https://www.mirion.com/%5Ctextbackslash-well-detectors.

[3] T. Comellato *et al.*, "Performance of custom designed inverted coaxial HPGe detectors for GERDA and LEGEND," *Nuclear Instruments and Methods in Physics Research Section A: Accelerators, Spectrometers, Detectors and Associated Equipment*, vol. 936, pp. 247–248, 2018. DOI: 10.1016/j.nima.2018.10.042.

[4] M. Agostini *et al.*, "Characterization of inverted coaxial ^{76}Ge detectors in GERDA for future double-β decay experiments," *The European Physical Journal C*, vol. 81, no. 6, p. 505, 2021. DOI: 10.1140/epjc/s10052-021-09184-8.

[5] *Electrochemical plant JSC*. [Online]. Available: https://www.ecp.ru/eng/ (visited on 04/05/2022).

[6] *Isotope Joint Stock Company*. [Online]. Available: http://www.isotop.ru/en/ (visited on 04/05/2022).

[7] M. Agostini *et al.*, "Production, characterization and operation of ^{76}Ge enriched BEGe detectors in GERDA," *The European Physical Journal C*, vol. 75, no. 2, p. 39, 2015. DOI: 10.1140/epjc/s10052-014-3253-0.

[8] *PPM Pure Metals*. [Online]. Available: https://recylex.eu/de/ppm-pure-metals/ (visited on 04/05/2022).

[9] M. Agostini *et al.*, "Characterization of 30 ^{76}Ge enriched Broad Energy Ge detectors for GERDA Phase II," *The European Physical Journal C*, vol. 79, no. 11, p. 978, 2019. DOI: 10.1140/epjc/s10052-019-7353-8.

[10] E. Andreotti *et al.*, "HEROICA: an underground facility for the fast screening of germanium detectors," *Journal of Instrumentation*, vol. 8, no. 06, P06012–P06012, 2013. DOI: 10.1088/1748-0221/8/06/p06012.

[11]   D. Budjáš *et al.*, "Pulse shape discrimination studies with a Broad-Energy Germanium detector for signal identification and background suppression in the GERDA double beta decay experiment," *Journal of Instrumentation*, vol. 4, no. 10, P10007, 2009. DOI: 10.1088/1748-0221/4/10/p10007.

7

ENRICHED INVERTED COAXIAL DETECTORS FOR LEGEND IN GERDA

After proven excellent performances in vacuum cryostat, the 5 enriched IC detectors of Chapter 6 have been integrated in the GERDA setup. Being the first time of long operation in LAr, this was a crucial benchmark for the adoption of IC detectors in the LEGEND experiment. IC detectors contributed with $8.5 \, \text{kg} \cdot \text{yr}$ exposure (i.e. 8.2%) to the total exposure of $103.7 \, \text{kg} \cdot \text{yr}$ of GERDA Phase II. They proved excellent long-term performances in LAr, and indeed showed that a high efficiency, background-free search for $0\nu\beta\beta$ is possible with big (mass $>1.5 \, \text{kg}$) detectors.

7.1 PERFORMANCES FROM CALIBRATIONS

The GERDA setup is exposed to radiation from a ^{228}Th source on a weekly basis for the calibration of the energy scale and PSD methods. Since the upgrade of 2018, when the enriched IC detectors had been deployed in LAr, ~ 50 calibrations have been carried out. A complete description of the calibration procedures for the full GERDA array can be found in [1, 2]. In the following, details on the performances (and their stability in time) evaluated with such calibration data will be given for the enriched IC detectors. Unfortunately, after deployment in LAr and due to electronics issues, detector IC48B exhibited an increasing leakage current. Notwithstanding several attempts to recover its functionality, it was operated around depletion (3200 V) and therefore used only in AC mode.

IC48B operated in AC mode

7.1.1 Energy calibration

The exhaustive description of the routines for energy calibration can be found in [1], to which we refer for technical details. The position of the prominent gamma peaks of ^{208}Tl and ^{212}Bi from a ^{228}Th source is estimated by fitting the uncalibrated spectrum with different functions according to their intensity: for those with lower statistics, a gaussian function sitting on a linear background is used. For the stronger ones, the background is modeled as a step function (which represents the asymmetric composition of Compton scatterings on the left and right side of the full-absorption peak), and a tail is added to model the effect of incomplete charge collection. The

Periodical energy calibrations with γ-peaks from a ^{228}Th source

central values from the gaussian functions are then used to obtain the calibration curve. Before the upgrade of 2018, a linear function had always proved to be the best approximation. For the enriched IC detectors (and for one single semi-coaxial detector, ANG2), however, larger deviations than in the past (~1 keV in the residuals at 1.6 MeV for IC50B and 2.5 keV for ANG2) were observed, hence a quadratic term was added in their calibration curve. After the quadratic correction, the remaining residuals were within a few tenths of a keV as for the other detectors. The combined spectrum which sums all calibration runs for detector IC48A is shown in Figure 7.1, with a zoom on the fit of the high statistics 2.6 MeV peak.
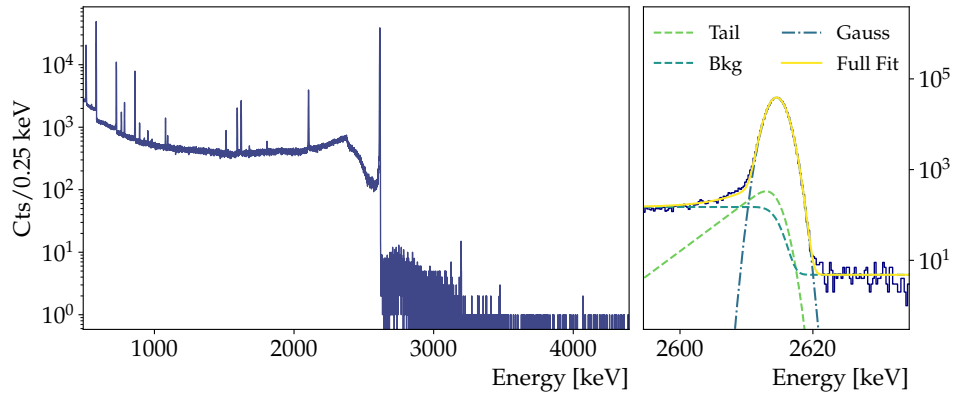
Figure 7.1: Summed energy spectrum of detector IC48A for irradiation with ^{228}Th.

The time stability of the energy calibration is carefully monitored, through the observation of the shift in the position of the (uncalibrated) 2.6 MeV peak between calibrations: datasets which come before a jump >1 keV are discarded from the analysis. As can be seen from Figure 7.2, the energy scale of IC detectors was very stable during data taking and only a couple of datasets were not considered for the $0\nu\beta\beta$ analysis.

As the final determination of the $T_{1/2}^{0\nu\beta\beta}$ (or its limit) depends on the energy resolution of the detector where it is observed, this is also monitored as a function of time. For this purpose, the 2.6 MeV peak is chosen, whose width stability (in FWHM) during the course of the data taking is shown in Figure 7.2 for the IC detectors. The fluctuations on such parameter for these detectors are comparable to the most stable BEGes [3].

As experienced in GERDA, energy resolution can potentially change significantly in time. For this reason, in order to produce resolution curves which are representative of the full data taking, the average value of each peak from the different calibration is taken, weighted with the time span for which the calibration curves are applied to physics data. The result of this operation is shown in Figure 7.3. Similarly to Section 6.2.3, data points have been fitted with a function of the type $f(E) = a + b \cdot \sqrt{E}$ to interpolate the resolution at $Q_{\beta\beta}$, which ranges from 2.76 to 3.00 keV FWHM in the
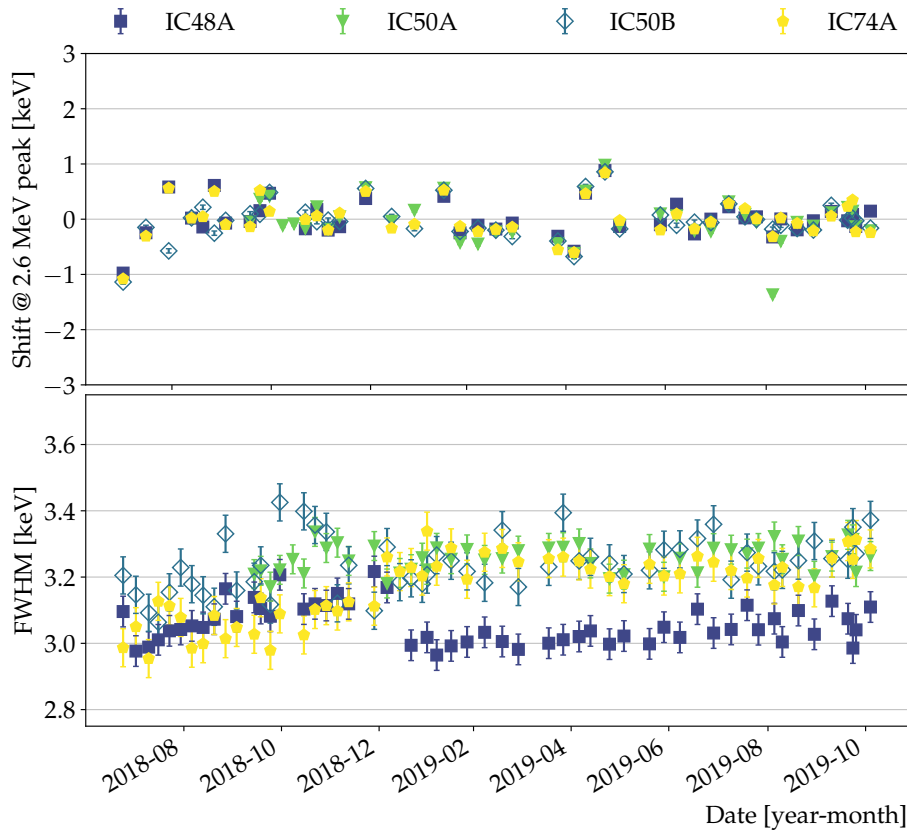
Figure 7.2: Shift of the position of the 2.6 MeV peak between calibrations, for IC detectors. Energy resolution (in FWHM) of the IC detectors during the course of the data taking. Adapted from [3].

GERDA cryostat. These values, though higher than in vacuum cryostat, are comparable to those of BEGe detectors and better than semi-coaxials' [1].

7.1.2 Calibration of PSD techniques

Compared to the A/E analysis described in the previous chapters, since detectors are operated on a long-term basis, time is an additional variable to consider. The full A/E analysis chain for long-term operation of BEGe detectors in GERDA was developed in [4]. As the double peak structure in the A/E space was not resolvable in the higher electronics noise environment of the GERDA cryostat, this same analysis was conducted for IC detectors as well.

A/E stability is also monitored in time

The first step in the calibration procedures is to check for drifts or jumps of the A/E parameter occurred during the data taking. This is done by monitoring the mean A/E value of events with energy between 1 and 1.3 MeV. A jump is classified as such when the difference between calibrations exceeds $0.4 \cdot \sigma_{A/E}$. A drift is a smaller, but constant, deviation in time. While a drift is normally compensated for, in case of a jump the dataset betwen calibrations is not considered for further analysis. The stability of A/E for the enriched
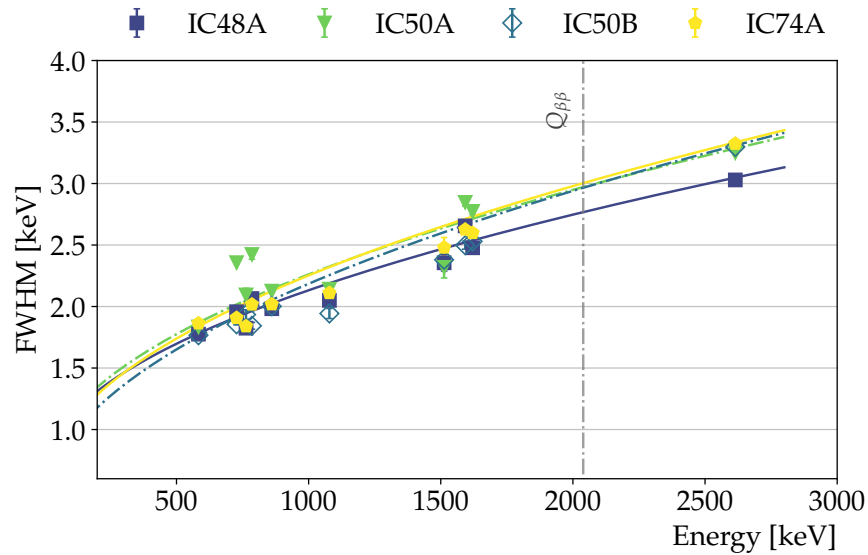
Figure 7.3: Energy resolution (in FWHM) curves for the IC detectors.

No worrisome instabilities in the A/E parameter

IC detectors is shown in the top plot of Figure 7.4. From there, we see that the ICs exhibited no constant drift. A jump occurred in November 2018 for all detectors, which followed some hardware operations. Other than that, some instabilities are present, mostly with detector IC48A, which were not related to hardware changes. The overall instabilities caused an exposure loss of 0.197 kg · yr (of which, 0.127 kg · yr due to IC48A). After these losses, the exposure gained with IC detectors was 8.541 kg · yr.

A/E resolution slightly larger than BEGes

In Figure 7.4, the resolution (in FWHM) of A/E is also plotted as a function of time. As the two peaks in A/E observed in vacuum cryostats contribute to the A/E width of the single peak observed in GERDA, such parameter is expectedly larger than for BEGe detectors. Indeed, ICs showed a ∼ 50% higher A/E resolution compared to BEGes [4]. Overall, we see that a very stable regime was achieved after ∼ 4 months of operation in the GERDA cryostat.

PSD performances stable and better than majority of BEGes

After data selection based on the stability in time, the A/E values are normalized detector-wise using the mean value of events between 1 and 1.3 MeV, and all calibrations are merged together. At this point, the dataset for every detector is analogous to that obtained from a vacuum cryostat, and indeed the analysis follows the same steps as in Chapter 6. The resulting discrimination efficiencies (2-sided) for the standard event samples from ^{228}Th are shown in Figure 7.5. Though higher than in vacuum cryostat (see Table 6.6 for comparison), these values are better than the majority of the BEGes [2]. In the same Figure 7.5, the discrimination efficiency for a sample of 2νββ events is also shown as crosscheck for the discrimination efficiency on signal-like events. This sample is defined as those events (in the physics datasets) with energy between 1 and 1.3 MeV in anticoincidence with the LAr veto, which are expected to be predominantly 2νββ events. A small fraction,
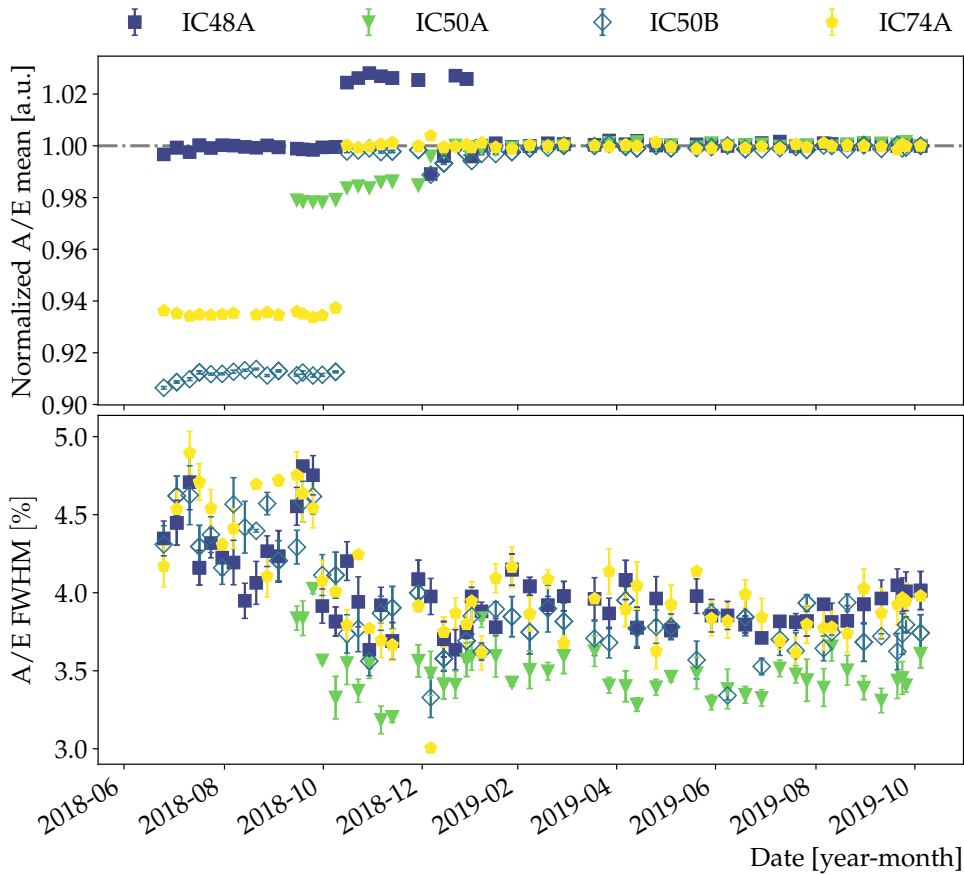
Figure 7.4: Stability in time of the A/E mean and width (in FWHM) of events between 1 and 1.3 MeV, for IC detectors.

however, consists of Compton events from the K lines which do not produce light in LAr and can have a multiple-site nature. For this reason, although not statistically significant, the efficiencies for this sample are slightly lower than for DEP events.

With the cut being the same for all calibrations, the discrimination efficiencies can also be investigated as a function of time, as a crosscheck on the time stability of the A/E analysis. This is shown in Figure 7.6, which, although with limited statistics per calibration, proves the effective stability of the PSD technique for IC detectors over the course of the whole data taking.

7.1.3 $0\nu\beta\beta$-tagging efficiencies from Monte Carlo

As we have thoroughly discussed in Chapter 4, setting the 90% acceptance of DEP events does not translate into a 90%-tagging efficiency of $0\nu\beta\beta$ events, because of the difference in energy and geometrical distributions between the two samples. As in Chapter 3 and Chapter 4, we estimated the $0\nu\beta\beta$-tagging efficiency on a single detector basis, using the MaGe [5] software framework to simulate Monte Carlo samples of ^{208}Tl and $0\nu\beta\beta$ decays and the SigGen [6] software to generate the electrical signals produced by

$0\nu\beta\beta$-tagging efficiency from Monte Carlo used in the final Gerda systematic uncertainties
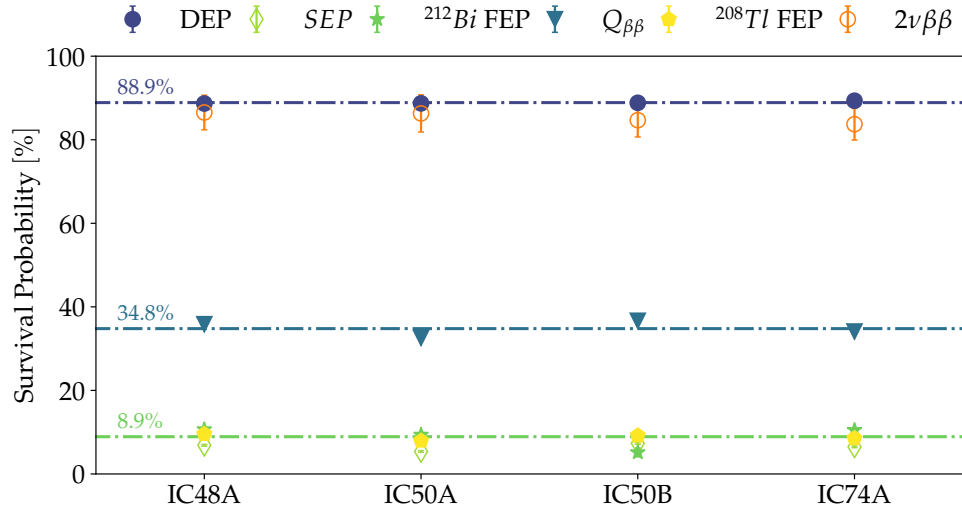
Figure 7.5: Discrimination efficiencies for the standard event samples from a ^{228}Th source and for $2\nu\beta\beta$ events for IC detectors in the GERDA cryostat. The dash-dotted lines (and the numbers above them) indicate the mean values of the efficiencies for DEP, ^{212}Bi and Compton events at $Q_{\beta\beta}$.

the interactions of their decay products with the detectors. The validation of the electrical signals was done by tuning the impurity profile of the crystals in two steps. We used as a first constraint that simulations should reproduce the depletion voltage as found in HADES (Section 6.2.2). In a second iteration, we adjusted the parameters by tuning the simulated rise time populations from DEP events on the experimental ones. After freezing the crystal parameters, we used these signals to carry out the standard A/E calibration analysis on ^{208}Tl and extract the efficiency of tagging $0\nu\beta\beta$ events, which are reported in Table 7.1 and shown in Figure 7.7 for all detectors.

	IC48A		IC50A	
Event class	*Experiment*	*Simulation*	*Experiment*	*Simulation*
^{208}Tl DEP	89.0 (6)	89.3 (1)	87.7 (7)	88.3 (1)
^{208}Tl SEP	6.7 (3)	4.8 (2)	5.5 (3)	4.4 (2)
^{208}Tl FEP	9.43 (8)	8.58 (3)	7.62 (9)	7.79 (3)
$0\nu\beta\beta$	-	88.19 (4)	-	86.55 (4)

	IC50B		IC74A	
Event class	*Experiment*	*Simulation*	*Experiment*	*Simulation*
^{208}Tl DEP	88.7 (7)	89.1 (5)	89.0 (6)	89.3 (5)
^{208}Tl SEP	6.8 (3)	6.2 (1)	6.4 (3)	6.6 (3)
^{208}Tl FEP	8.61 (9)	10.18 (2)	8.09 (8)	9.6 (1)
$0\nu\beta\beta$	-	88.0 (1)	-	88.6 (3)

Table 7.1: Comparison of the experimental and simulated discrimination efficiencies for the standard event samples from a ^{228}Th source for IC detectors.
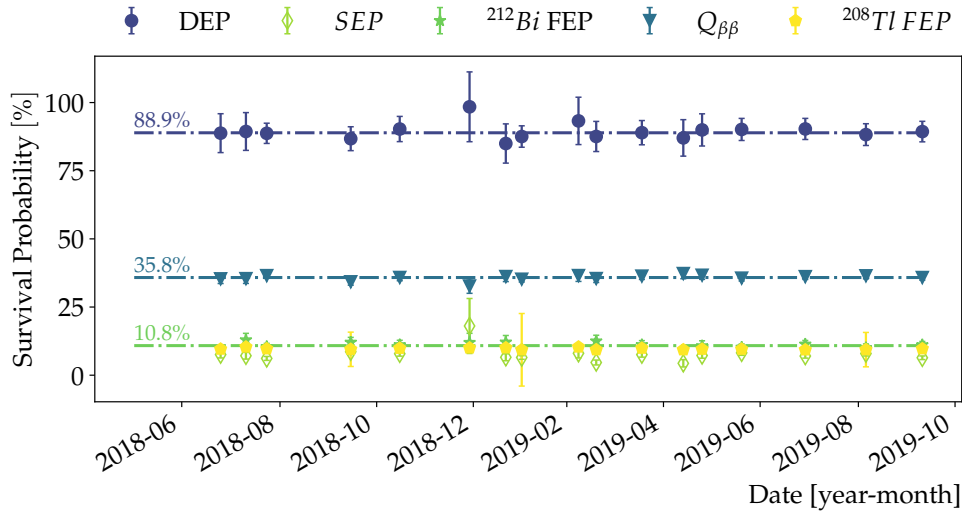
Figure 7.6: Discrimination efficiencies for the standard event samples from a ^{228}Th source over the whole data taking of detector IC48A in the GERDA cryostat. The dash-dotted lines (and the numbers above them) indicate the mean values of the efficiencies for DEP, ^{212}Bi and Compton events at $Q_{\beta\beta}$.
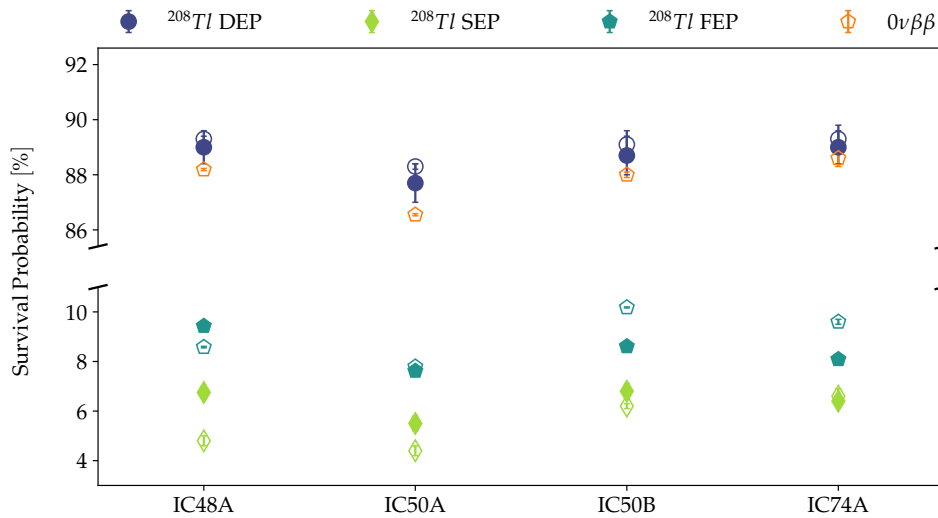
Figure 7.7: Comparison of the experimental (filled markers) and simulated (empty) discrimination efficiencies for the standard event samples from a ^{228}Th source for IC detectors.

As mentioned in Chapter 4, the final GERDA analysis does not use directly these numbers for the central value of the $0\nu\beta\beta$-tagging efficiency, but rather runs a data-driven analysis (all details are in [2]) using the electrical signals from DEP and Compton Continuum (CC) events with rescaled energy. The difference between the discrimination efficiency of $0\nu\beta\beta$ and DEP events obtained with the present work is then considered as contribution on the systematics of the method.

7.2 PHYSICS RESULTS IN THE GERDA CRYOSTAT

After each calibration, the ^{228}Th sources are moved away from the array, the LAr veto is active and the setup is ready to register all the physics events depositing energy in germanium and/or in LAr. These include signal events, like $2\nu\beta\beta$ and $0\nu\beta\beta$, and background, e.g. decays from the primordial ^{238}U and ^{232}Th chains occurring in the surrounding materials as well as radioactive decays in LAr itself. The accurate analysis of the signal and background components in the full GERDA spectrum can be found in [7–9], while details on the components relative to the IC detectors will be discussed in Section 7.2.2.

Before getting to the physics spectrum, one last crosscheck is performed on A/E, as will be described in Section 7.2.1.

7.2.1 Calibration and physics data

A/E centered at the same value for calibration and physics data

Since A/E is the combination of $\mathcal{O}(\text{year})$ of data, a quality control for the full A/E calibration procedure is carried out to ensure that the acceptance region is the same for calibration and physics data. Also, as calibration and physics data are taken using a different triggering scheme, this serves also as a crosscheck on the DAQ. Practically, this is done by checking that the A/E populations of $2\nu\beta\beta$ (from physics data) and DEP events (from calibrations) are centered on the same value. As visible in Figure 7.8, no misalignment was observed in such comparison for IC detectors, meaning that neither an inaccuracy in the calibration procedure nor any instability of the DAQ sneaked into the final IC dataset.
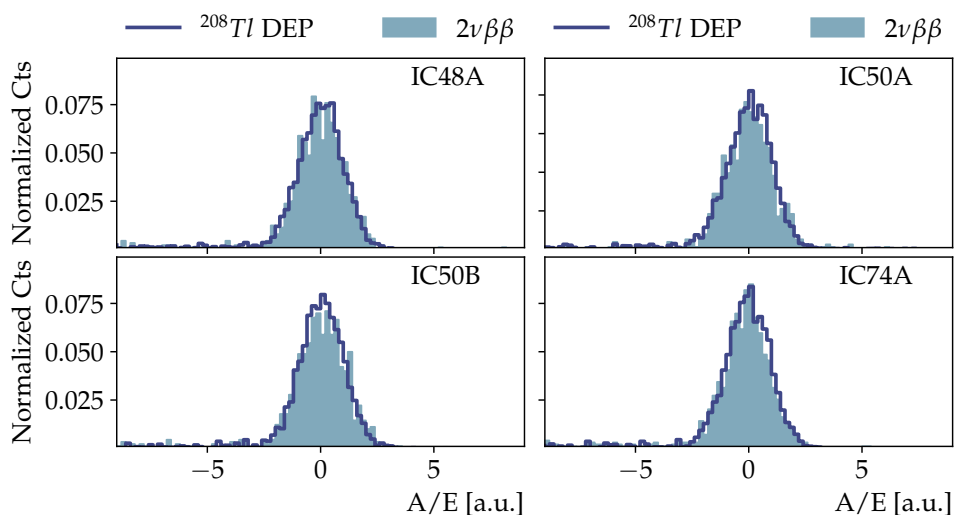
Figure 7.8: Comparison of the A/E distributions of DEP and $2\nu\beta\beta$ events for the IC detectors in GERDA.
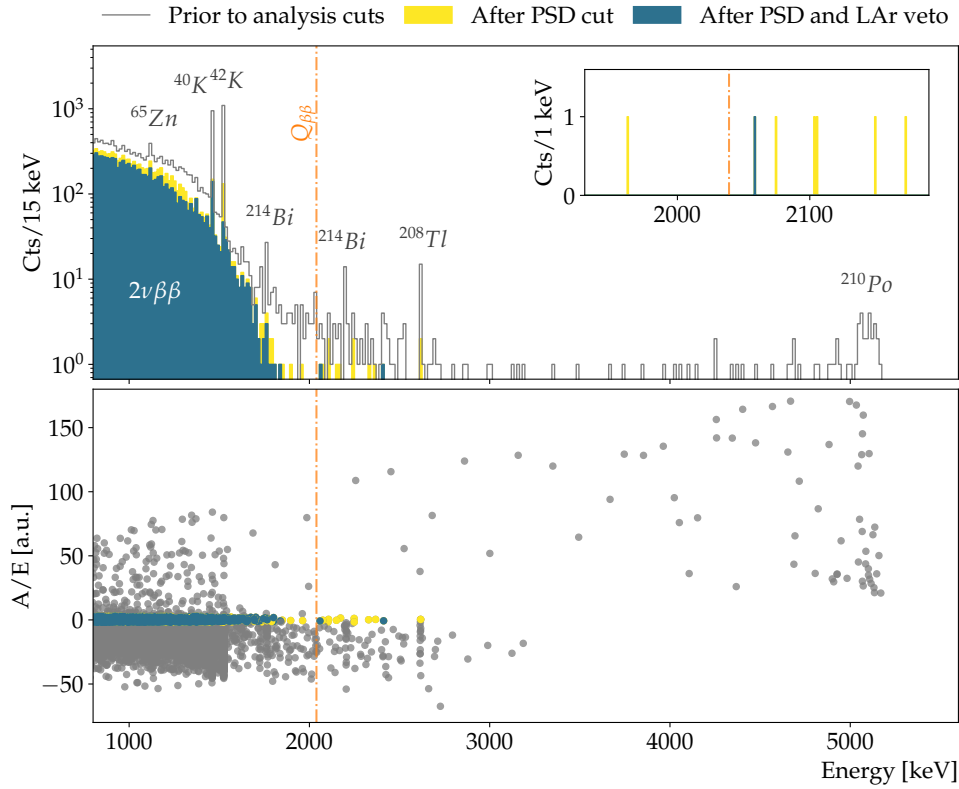
Figure 7.9: Summed energy spectrum (top) of all physics runs for the enriched IC detectors in GERDA and relative A/E values (bottom). In grey are all events after AC cut, in yellow after PSD and in blue those surviving both PSD and LAr cuts. The main features of the spectrum are labeled after the nucleus which originates them.

7.2.2 Physics spectrum of IC detectors in liquid argon

After the sets of crosschecks described above on energy scale and PSD, the summed energy spectrum before and after analysis cuts is constructed. This is shown in Figure 7.9 for the total exposure of $8.5 \, \mathrm{kg \cdot yr}$ gained from July 2018 to November 2019 with the IC detectors. For a better event identification, Figure 7.9 also shows how the events in the spectrum are distributed in the A/E space. Since the description of the main γ-lines (but one, see Section 7.2.2.2) in the energy spectrum is not IC-specific but rather depends on the surrounding materials, we refer to [7, 9] for further details, and report their count rates for IC detectors only in Table 7.2 for reference.

7.2.2.1 $2\nu\beta\beta$

With the half-life of $T_{1/2}^{2\nu\beta\beta} = (1.926 \pm 0.094) \cdot 10^{21}$ yr extracted from Phase I [10], the $2\nu\beta\beta$ of ^{76}Ge dominates the energy spectrum between 1 and 2 MeV. As it features the same topology of $0\nu\beta\beta$, this spectral component survives all cuts. The half-life of the process can be estimated with just IC detectors in several ways. The final results of GERDA Phase II uses data (from a selection of BEGe detectors) after LAr veto to minimize the impact

of background events on the analysis [11]. We report here the result from a multi-variate fit of all background components of the spectrum of IC detectors before analysis cuts [12]. This yields the results:

$$T_{1/2}^{2\nu\beta\beta} = (1.90 \pm 0.02 \, (\text{stat})) \cdot 10^{21} \, \text{yr} \tag{7.1}$$

Although compatible with the value of GERDA Phase I, this is in tension with the latest results from Phase II [11], which is

$$T_{1/2}^{2\nu\beta\beta} = (2.022 \pm 0.041) \cdot 10^{21} \, \text{yr} \tag{7.2}$$

The lower value from the multi-variate fit suggests an underestimation of the background components before analysis cuts. This is not surprising since the method used for IC detectors relies on the precise knowledge of all background components, while the GERDA approach is almost background-free. Indeed, as pointed out in [11], the historical trend on the estimation of the half-life of $2\nu\beta\beta$ shows a gradual increase as experiments succeeded in lowering their background levels.

7.2.2.2 ^{65}Zn
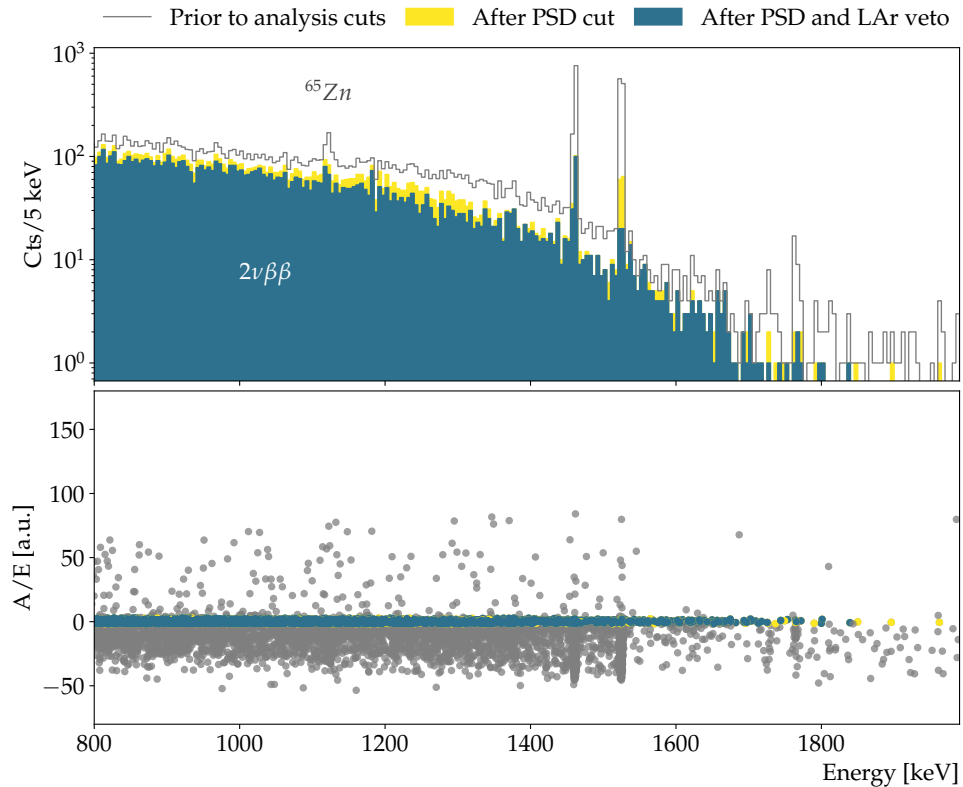
Figure 7.10: Summed energy spectrum (top) of all physics runs for the enriched IC detectors in GERDA and relative A/E values (bottom), in the energy range of $2\nu\beta\beta$. In grey are all events after AC cut, in yellow after PSD and in blue those surviving both PSD and LAr cuts.

Compared to the energy spectra of BEGes and semi-coaxials in GERDA Phase II, an additional γ-line was found at 1125 keV, before cuts, on the energy spectrum of IC detectors. This originates from the cosmogenically produced ^{65}Zn, which decays via electron capture (EC), with the emission of a γ-ray at 1116 keV in 50% of the cases. As the decay occurs internally to the detectors, the probability for an X-ray or an Auger electron to deposit the full energy in the detector active volume is high, hence its energy would add up to that of the γ. Indeed, the signal appears 9 keV higher than the energy of the γ-ray, at 1125 keV. Being instrinsically multi-site-*ish*, this line is highly suppressed by the PSD cut, as shown in Figure 7.10. Such detector bulk contamination had been reported at the beginning of the Heidelberg-Moscow experiment [13]. However, with a half-life of 244 days, this γ-line has not been observed in the other GERDA Phase II datasets since semi-coaxial and BEGe detectors had been stored at least 2 years underground before being deployed.

Internal ^{65}Zn decay suppressed by PSD

7.2.2.3 ^{210}Po

Above the Q-value of the β-decay of ^{42}K at 3.5 MeV, the spectrum is populated by α particles from the decay of ^{210}Po which penetrate through the thin p$^+$ electrode and reach the active volume of germanium detectors. Their mean path is however $\mathcal{O}(1)\,\mu$m, which means they only probe the small volume around the electrode, where, as we discussed in Chapter 2, signals with high A/E are generated. As visible in Figure 7.9, all the events above 3.5 MeV are characterized by high values of the A/E parameters, and thus discarded by the high A/E cut.

No α-decay survives analysis cuts

As these events come from a surface contamination while detectors are exposed to ^{222}Rn, their count rate is used as validation of the handling procedures. With a constant rate of 4.5α particles per month, the surface contamination of IC detectors is compatible with the typical values for BEGes, meaning that detectors have been handled in clean environments.

7.2.3 ^{238}U and ^{232}Th bulk contamination

In [14], with no candidate events over an exposure of $26.14\,\text{kg}\cdot\text{yr}$, a limit of 3 nBq/kg was derived for the ^{238}U and ^{232}Th bulk contamination of germanium crystals. For the $8.5\,\text{kg}\cdot\text{yr}$ exposure of IC detectors, this would result in 0.8 decays of the long-lived mother isotope, accompanied by the consequent decays of the daughters in secular equilibrium. On the search for such decays, the fact that αs have mean free paths which don't exceed a few μm is a powerful ally, as it brings two important consequences. Firstly, the detection efficiency for a bulk α-decay is almost 100%, which in turn implies that the whole decay chain down to the stable isotope can be tracked.

No evidence of ^{238}U and ^{232}Th internal contamination

Secondly, such a decay would have (in more than 95% of the cases) an A/E value in the SSE band. With no surprise, no hints for a bulk contamination in the 8.5 kg·yr exposure of IC detectors was observed, as no event of in the SSE band above 3.5 MeV is present in this dataset. A limit for the activity A_{IC} of ^{238}U and ^{232}Th in IC detectors has been set in [15] to $A_{IC} < 9.2$ nBq/kg.

Isotope	Energy [keV]	Count rates [cts/(kg·y)]		
		Before cuts	After LAr	Coincident with LAr
^{65}Zn	1123.5	$10.2^{+1.7}_{-1.4}$	$9.5^{+1.5}_{-1.2}$	$0.8^{+0.7}_{-0.5}$
^{40}K	1460.8	$100.6^{+3.7}_{-3.2}$	$97.8^{+3.6}_{-3.2}$	$2.8^{+0.7}_{-0.6}$
^{42}K	1524.6	$121.2^{+3.6}_{-3.2}$	$19.4^{+1.5}_{-1.6}$	$101.8^{+3.2}_{-3.7}$
^{214}Bi	1764.5	$2.3^{+0.7}_{-0.5}$	$0.8^{+0.4}_{-0.3}$	$1.5^{+0.5}_{-0.4}$
^{214}Bi	2204.1	$1.3^{+0.4}_{-0.4}$	$0.3^{+0.3}_{-0.2}$	$0.9^{+0.4}_{-0.3}$
^{208}Tl	2614.5	$1.7^{+0.5}_{-0.4}$	$0.1^{+0.2}_{-0.1}$	$1.7^{+0.5}_{-0.4}$

Table 7.2: Count rates of the main γ peaks above 1 MeV. Taken from [9].

7.2.4 $0\nu\beta\beta$ search with IC detectors

As shown in the inset of Figure 7.9, in the energy window between 1930 and 2180 keV, only one event, occurred at the energy of 2059 keV in detector IC74A, survives all analysis cut. With this event, the BI is calculated as the mode and smallest 68% interval of a Poisson signal expectation, which yields the final results of

$$\mathrm{BI_{IC}} = (4.9^{+7.3}_{-3.4}) \cdot 10^{-4} \text{ cts/(keV·kg·yr)} \tag{7.3}$$

This is compatible with the value reported in [7] for BEGe detectors, i.e. $(3.8^{+3.6}_{-2.1}) \cdot 10^{-4}$ cts/(keV·kg·yr). Compared to them, IC detectors feature a factor ~ 3 more mass per detector, hence a significantly smaller quantity of dead material (holders, cables...) per isotope mass. This means that the BI is expected to be lower by a same factor if only (or mainly) ICs are used, as foreseen in LEGEND.

The full analysis to extract the limit on the half-life of $0\nu\beta\beta$ from the complete GERDA dataset will be described in Chapter 8. Nonetheless, it's interesting at this point to use the unified approach of [16] to extract a 90% C.L. limit with IC detectors, only. With a number of expected background

counts calculated from Equation 7.3 and 0 observed events in the $Q_{\beta\beta} \pm 2\sigma$ region, the upper limit on the number of $0\nu\beta\beta$ events is set to:

$$N_{0\nu\beta\beta} < 2.40 \text{ counts} \tag{7.4}$$

In the more than reasonable approximation of a measurement time t which is much smaller than the $0\nu\beta\beta$ half-life, the number of measured decays $N_{0\nu\beta\beta}$ in time t is

$$N_{0\nu\beta\beta} \simeq N_{ge} \cdot \frac{\ln(2)}{T_{1/2}^{0\nu\beta\beta}} \cdot t \cdot \epsilon_{0\nu\beta\beta} \tag{7.5}$$

where N_{ge} is the number of ^{76}Ge nuclei and $\epsilon_{0\nu\beta\beta}$ the $0\nu\beta\beta$ detection efficiency (which folds in several factors and will be clarified in Chapter 8). Using $\epsilon_{0\nu\beta\beta} = 66\%$ (as reported in [9] for ICs), this gives the lower limit on the $0\nu\beta\beta$ half-life:

$$T_{1/2}^{0\nu\beta\beta} > 1.29 \cdot 10^{25} \text{ yr (90\% C.L.)} \tag{7.6}$$

7.3 CONCLUSIONS

This chapter has reported the first and successful long-term operation of IC detectors in LAr. The standard analysis of GERDA yielded for them a background discrimination power compatible with that of BEGe detectors, with the advantage of having a factor ~ 3 higher mass. In the 14 months of operation in the GERDA cryostat, IC detectors collected an exposure of $8.5 \, \text{kg} \cdot \text{yr}$ and reached a background level of $(4.9^{+7.3}_{-3.4}) \cdot 10^{-4} \, \text{cts}/(\text{keV} \cdot \text{kg} \cdot \text{yr})$, thus giving a significant contribution to the final and successful results of GERDA, which will be presented in Chapter 8.

REFERENCES

[1] M. Agostini *et al.*, "Calibration of the GERDA experiment," *The European Physical Journal C*, vol. 81, no. 8, p. 682, 2021. DOI: 10.1140/epjc/s10052-021-09403-2.

[2] M. Agostini *et al.*, "Pulse shape analysis in GERDA Phase II," *The European Physical Journal C*, vol. 82, no. 4, p. 284, 2022. DOI: 10.1140/epjc/s10052-022-10163-w.

[3] C. Ransom, "Energy Calibration for the GERDA and LEGEND-200 Experiments," Ph.D. dissertation, 2021.

[4]   V. E. Wagner, "Pulse Shape Analysis for the GERDA Experiment to Set a New Limit on the Half-life of $0\nu\beta\beta$ Decay of ^{76}Ge," Ph.D. dissertation, 2017.

[5]   M. Boswell *et al.*, "MaGe-a Geant4-Based Monte Carlo Application Framework for Low-Background Germanium Experiments," *IEEE Transactions on Nuclear Science*, vol. 58, no. 3, pp. 1212–1220, 2011. DOI: 10.1109/tns.2011.2144619.

[6]   D. C. Radford, `fieldgen` *and* `siggen` *software*, 2014. [Online]. Available: https://github.com/radforddc/icpc%5C_siggen.

[7]   M. Agostini *et al.*, "Final Results of GERDA on the Search for Neutrinoless Double-β Decay," *Physical Review Letters*, vol. 125, no. 25, p. 252 502, 2020. DOI: 10.1103/physrevlett.125.252502.

[8]   T. G. collaboration *et al.*, "Modeling of GERDA Phase II data," *Journal of High Energy Physics*, vol. 2020, no. 3, p. 139, 2020. DOI: 10.1007/jhep03(2020)139.

[9]   C. Wiesinger, "No neutrinos not found: First exploration of neutrinoless double beta decay half-lives beyond 10^{26} years," Ph.D. dissertation, 2020.

[10] M. Agostini *et al.*, "Results on $\beta\beta$ decay with emission of two neutrinos or Majorons in ^{76}Ge from GERDA Phase I," *The European Physical Journal C*, vol. 75, no. 9, p. 416, 2015. DOI: 10.1140/epjc/s10052-015-3627-y.

[11] M. Agostini *et al.*, "Precision measurement of the ^{76}Ge double-β decay rate with GERDA Phase II," *In preparation*, 2022.

[12] L. Pertoldi, "Search for new physics with two-neutrino double-beta decay in GERDA data," Ph.D. dissertation, 2020.

[13] A. Balysh *et al.*, "Measurement of the $\beta\beta2\nu$ decay of ^{76}Ge," *Physics Letters B*, vol. 322, no. 3, pp. 176–181, 1994. DOI: 10.1016/0370-2693(94)91103-7.

[14] M. Agostini *et al.*, "Limits on uranium and thorium bulk content in GERDA Phase I detectors," *Astroparticle Physics*, vol. 91, pp. 15–21, 2017. DOI: 10.1016/j.astropartphys.2017.03.003.

[15] F. Novak, "The search for bulk Alpha-events in GERDA Phase II Data," 2020.

[16] G. J. Feldman and R. D. Cousins, "A Unified Approach to the Classical Statistical Analysis of Small Signals," *arXiv*, 1997. DOI: 10.1103/physrevd.57.3873.

8 | FINAL RESULTS OF GERDA

With the IC detectors studied in Chapter 6 and Chapter 7 contributing with $8.5\,\text{kg}\cdot\text{yr}$, GERDA Phase II accumulated an exposure of $103.7\,\text{kg}\cdot\text{yr}$. Thanks to the experimental design and the choice of materials, GERDA succeded to operate with an unprecedentedly low background index of $\text{BI} = (5.2^{+1.6}_{-1.3})\cdot 10^{-4}\,\text{cts/(keV}\cdot\text{kg}\cdot\text{yr)}$, which fulfills the design goal [1] and makes GERDA the experiment with the lowest background in the $\beta\beta$-decay field. Combining data from Phase I and Phase II, GERDA set a limit on the half-life of the process to $T^{0\nu\beta\beta}_{1/2} > 1.8\cdot 10^{26}\,\text{yr}$. In this chapter the final energy spectrum of GERDA Phase II will be presented. An overview will also be given on the statistical analysis which combines the results of Phase I and II to set the limit on $T^{0\nu\beta\beta}_{1/2}$. These results have been published by the GERDA collaboration in [2].

8.1 DATA TAKING

GERDA phase II started taking data in December 2015 with $15.6\,\text{kg}$ of semi-coaxial and $20.0\,\text{kg}$ of BEGe detectors. In summer 2018, the 5 ICs studied in Chapter 6 and Chapter 7 were added to the array, and one semi-coaxial was taken out, so that GERDA resumed operation with $44.2\,\text{kg}$ of detectors until the end of the data taking, in November 2019. The live time fraction was higher than 90% for the vast majority of the data taking, with short interruptions due to hardware failures or to the upgrade, as can be seen in Figure 8.1. This allowed GERDA to gain a final exposure of $103.5\,\text{kg}\cdot\text{yr}$, fulfilling the exposure design goal.
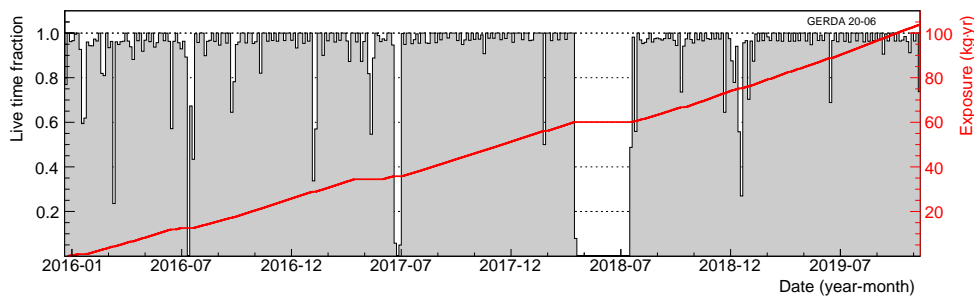
Figure 8.1: Live time fraction and cumulative exposure during the GERDA Phase II data taking.

8.2 THE FINAL SPECTRUM OF GERDA PHASE II

After a careful data selection (details can be found in [3]) and periodic calibrations of energy and PSD methods [4, 5], the energy spectrum is constructed as the sum of the single energy spectra from all detectors. This is shown in Figure 8.2 for the three detector families separately, before and after analysis cuts.
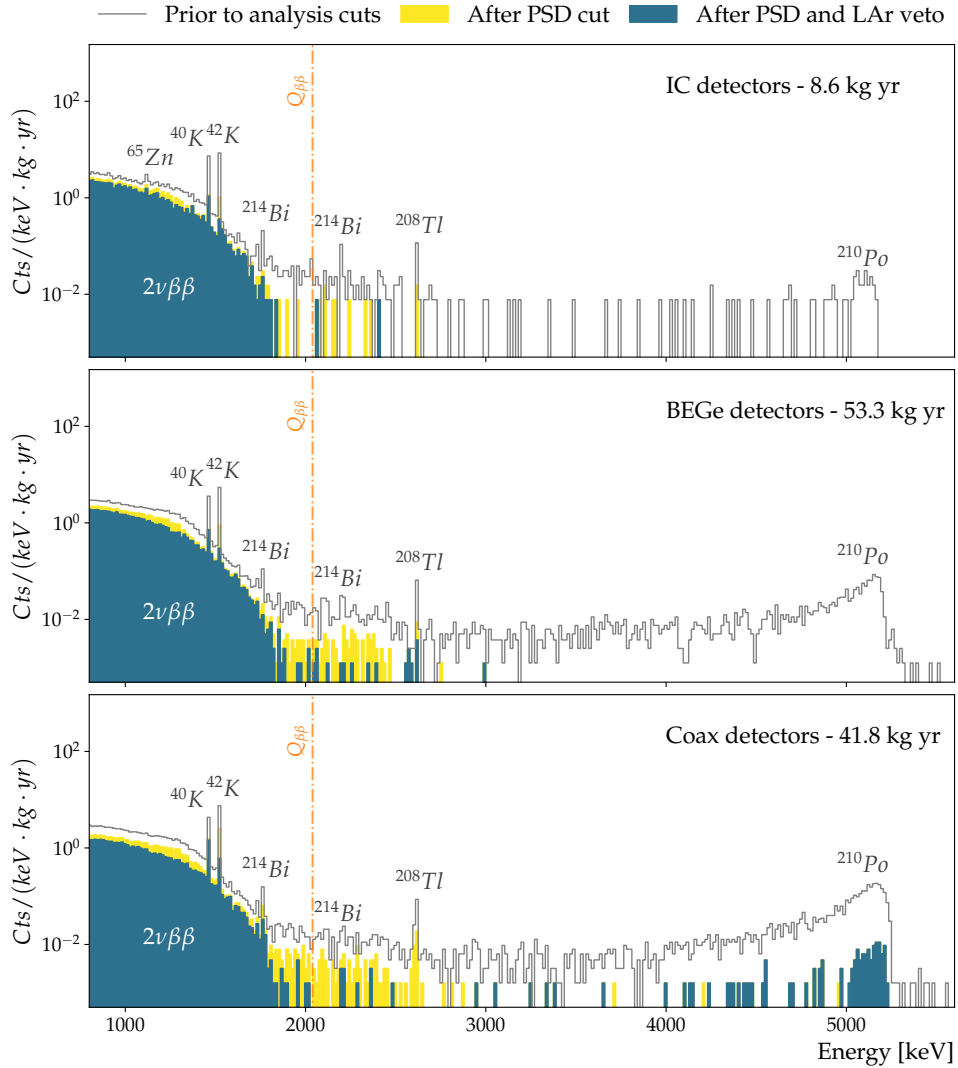
Figure 8.2: Final energy spectrum of GERDA Phase II for the three detector families, before and after analysis cuts. Its main features are labeled and described in detail in the text.

2νββ   As seen in Chapter 6, from 1 to 2 MeV the spectrum is dominated by the population of electrons from the 2νββ of ^{76}Ge. As the energy is deposited (in most of the cases) in a $\mathcal{O}(1)$ mm range in germanium (like 0νββ), these events are neither cut by PSD nor LAr veto. As can be seen from the zoom at $Q_{\beta\beta}$ of Figure 8.3, thanks to the excellent energy resolution of germanium detectors, the high energy tail of this population does not overlap with a possible peak at $Q_{\beta\beta}$.

The second most prominent feature is the presence of several gamma lines, which are labeled in Figure 8.2 according to the isotope which produces them. Their origin is attributed to a small contamination from ^{40}K and the ^{238}U/^{232}Th primordial chains of the materials surrounding the detectors. As in the MeV range the full absorption of γ-rays in germanium occurs mainly through multiple Compton scatterings, these lines are highly suppressed by PSD. Also, as the γs from ^{42}K, ^{214}Bi and ^{208}Tl follow quite energetic β-decays (3.5, 3 and 5 MeV, respectively), even when the γ is fully absorbed in the detector, light is also produced in LAr[1]. Indeed, the LAr veto strongly contributes to their suppression, too. This complementarity of PSD and LAr veto is even enhanced for events with partial energy deposition of γ-rays, as is visible in Figure 8.2, in the regions between γ peaks. These events could deposit part of their energy in germanium through single Compton scattering, thus surviving the PSD cut, but are very likely to deposit the rest in Ar, triggering the veto. The case of ^{40}K is different, because the γ-ray at 1460 keV is only emitted after EC. Therefore, if this γ is fully absorbed in germanium, the event does not produce light and the LAr veto will miss it. For this reason, this line is suppressed only by PSD.

γ lines

The last feature of the spectrum is the alpha peak at 5.4 MeV from ^{210}Po. As seen in Section 2.4.2 and Section 5.4, αs can reach the active volume of germanium detectors only through the p^{+} electrode or the groove. Since semi-coaxials' p^{+} electrode covers a surface which is a factor ∼ 30 bigger than for BEGes, most of the alphas are expected on their dataset. For BEGes and ICs, p^{+} events produce peculiar pulse shapes and are thus easily tagged. Indeed, as shown in Figure 8.2, for BEGe and IC detectors the PSD cut removes all the α-candidates above the Q$_{β}$ value of ^{42}K at 3.5 MeV. Those surviving the cut in the energy spectrum of Figure 8.2 are from semi-coaxial detectors, for which the structure of the weighting field does not allow an equally efficient tagging of surface events. Stronger analysis cuts could grant a more efficient background reduction, however, this would come at the expense of a lower acceptance of 0νββ events. Therefore, the trade-off described in [5] has been selected, leading to the spectrum of Figure 8.2.

α peak

8.2.1 The search for 0νββ

In order to avoid possible biases, a blind analysis is carried out for the search of 0νββ. For GERDA, this means that no access is given to collaborators in the blinded window Q$_{ββ}$ ± 50 keV, before all the analysis parameters (energy calibration, LAr veto, PSD thresholds...) are fixed. Once everything is frozen, data are *unblinded* and the events inside the blinded window are

---

1 This would not be true if the contamination were internal to detectors. Searches in this direction did not provide any evidence of a bulk contamination in germanium crystals [6]

used to perform the analysis for the search of $0\nu\beta\beta$. The unblinded energy spectrum in the region around $Q_{\beta\beta}$ is shown in Figure 8.3.

The statistical analysis assumes a gaussian signal on a flat background, and its free parameters are the signal strength $S = 1/T_{1/2}^{0\nu\beta\beta}$ and the BI. As we have seen in Section 7.2.4 for ICs, the number of expected $0\nu\beta\beta$ events μ_s for a measurement time t is given by

$$\mu_s \simeq N_{ge} \cdot \ln(2) \cdot S \cdot t \cdot \epsilon_{0\nu\beta\beta} \tag{8.1}$$

where N_{ge} is the number of ^{76}Ge nuclei and $\epsilon_{0\nu\beta\beta}$ the $0\nu\beta\beta$ detection efficiency. This last factor folds in several efficiencies: the active volume fraction (provided by characterization measurements with ^{241}Am), the containment efficiency of the two electrons emitted in the decay (calculated from Monte Carlo simulations) and analysis efficiencies, which include both the acceptances of the LAr veto and PSD methods. As such, it is detector specific and can change over time, according to the experimental conditions.

The number of expected background events μ_b in an energy range ΔE for an exposure Mt is given in terms of BI, as:

$$\mu_b = BI \cdot \Delta E \cdot Mt \tag{8.2}$$

The statistical analysis is carried out as an unbinned extended likelihood fit, in the energy window between 1930 and 2190 keV (excluding the two regions around the expected γ lines from the decays of ^{208}Tl and ^{214}Bi at 2103 and 2119 keV, respectively), in both a frequentist and bayesian framework. The dataset is divided in partitions, which are time intervals, for each detector, where the analysis parameters are stable. All partitions share the same signal strength S and BI (except the partition relative to GERDA Phase I, which has its own BI) but have different efficiencies $\epsilon_{0\nu\beta\beta}$ and energy resolutions. By dividing the dataset in this way, the most detailed information is available to describe an event around $Q_{\beta\beta}$. With this approach, the likelihood function for N_k events in k partitions is the product of k gaussian distributions on a flat background, weighted by a Poisson term:

$$\mathcal{L} = \prod_k \left[\frac{(\mu_{s,k} + \mu_{b,k})^{N_k} e^{-(\mu_{s,k} + \mu_{b,k})}}{N_k!} \times \right.$$
$$\left. \times \prod_{i=1}^{N_k} \frac{1}{\mu_{s,k} + \mu_{b,k}} \left(\frac{\mu_{b,k}}{\Delta E} + \frac{\mu_{s,k}}{\sqrt{2\pi}\sigma_k} e^{-\frac{(E_i - Q_{\beta\beta})^2}{2\sigma_k^2}} \right) \right] \tag{8.3}$$

Frequentist result Under the frequentist approach, the best fit for the number of signal events is zero, and the lower limit on the half-life is:

$$T_{1/2}^{0\nu\beta\beta} > 1.8 \cdot 10^{26} \text{ yr} \quad \text{at } 90\% \text{ C.L.} \tag{8.4}$$

which is also the result shown in Figure 8.3. The best fit result for the BI is:

$$BI = (5.2^{+1.6}_{-1.3}) \cdot 10^{-4} \, cts/(keV \cdot kg \cdot yr) \tag{8.5}$$

which is the lowest background level ever achieved in a $\beta\beta$-decay experiment, fulfilling (and exceeding) the design goal of GERDA [1]. Furthermore,
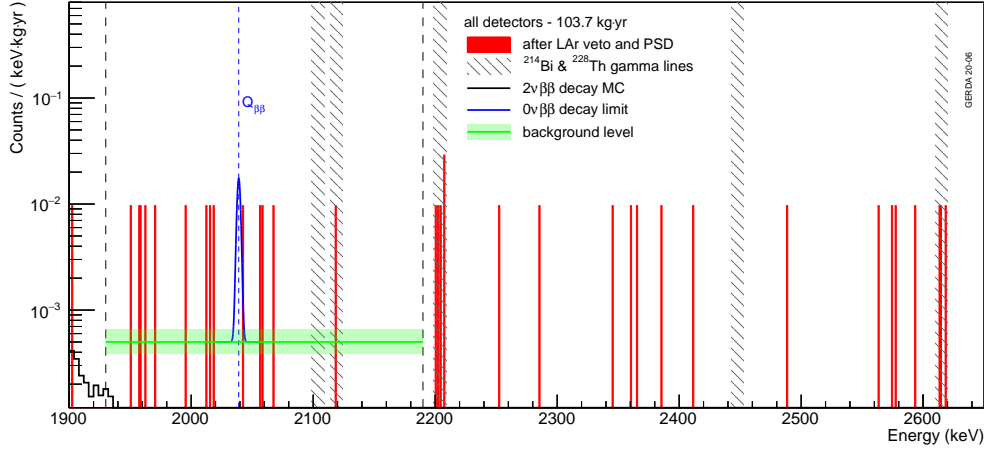

Figure 8.3: Analysis window (marked by the dashed lines) of the GERDA experiment and result of the frequentist analysis.

with this BI, GERDA Phase II succeeded in operating in the *background-free* regime for the full duration of the experiment, which allowed the sensitivity for $T^{0\nu\beta\beta}_{1/2}$ to scale linearly with the exposure, as shown in Figure 8.4.

In the bayesian framework, the prior distribution for the signal S is assumed flat between 0 and $10^{-24} \, yr^{-1}$, and the one-dimensional posterior probability density function P(S|data) of the signal strength is obtained by marginalizing over the other free parameters by using Bayesian Analysis Toolkit (BAT) [7]. The analysis yields:

Bayesian result

$$T^{0\nu\beta\beta}_{1/2} > 1.4 \cdot 10^{26} \, yr \quad \text{at 90\% C.I.} \tag{8.6}$$

as a lower limit on the half-life of the process.

Assuming a light neutrino exhange as mediator of the decay, the limit on the half-life $T^{0\nu\beta\beta}_{1/2}$ can be translated into a limit on the effective Majorana mass $m_{\beta\beta}$ using Equation 1.11. As pointed out in Section 1.4.2, the calculations for the NMEs of Equation 1.11 are only approximate, leading to results which differ of a factor 2 to 3. For this reason, the upper limit on $m_{\beta\beta}$ lies in a range, which is set by the most and least favorable scenarios of the NMEs [8, 9]:

$$m_{\beta\beta} < [79, 180] \, meV \tag{8.7}$$

Equation 8.7 is comparable to the most stringent constraints from other isotopes [10–12].
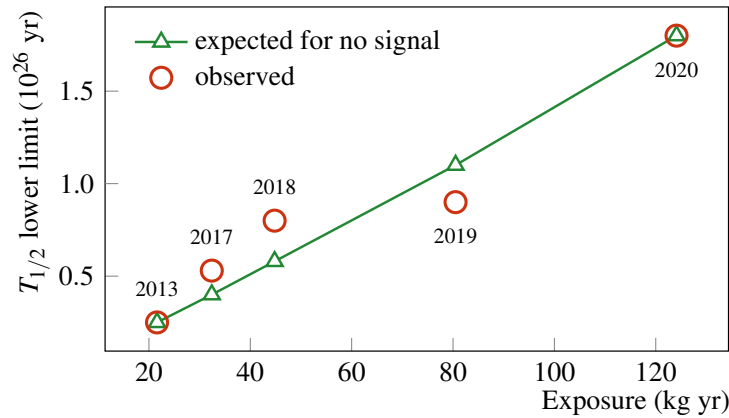
Figure 8.4: 90% C.L. limit on $T_{1/2}^{0\nu\beta\beta}$ (red circles) and median expectation for no signal (green triangles) as a function of exposure. The almost linear dependence proves the operation of GERDA Phase II in the background-free regime throughout the duration of the experiment.

REFERENCES

[1] S. Schönert *et al.*, "The GERmanium Detector Array (Gerda) for the search of neutrinoless $\beta\beta$ decays of ^{76}Ge at LNGS," *Nuclear Physics B - Proceedings Supplements*, vol. 145, pp. 242–245, 2005. DOI: 10.1016/j.nuclphysbps.2005.04.014.

[2] M. Agostini *et al.*, "Final Results of GERDA on the Search for Neutrinoless Double-β Decay," *Physical Review Letters*, vol. 125, no. 25, p. 252 502, 2020. DOI: 10.1103/physrevlett.125.252502.

[3] C. Wiesinger, "No neutrinos not found: First exploration of neutrinoless double beta decay half-lives beyond 10^{26} years," Ph.D. dissertation, 2020.

[4] M. Agostini *et al.*, "Calibration of the GERDA experiment," *The European Physical Journal C*, vol. 81, no. 8, p. 682, 2021. DOI: 10.1140/epjc/s10052-021-09403-2.

[5] M. Agostini *et al.*, "Pulse shape analysis in GERDA Phase II," *The European Physical Journal C*, vol. 82, no. 4, p. 284, 2022. DOI: 10.1140/epjc/s10052-022-10163-w.

[6] M. Agostini *et al.*, "Limits on uranium and thorium bulk content in GERDA Phase I detectors," *Astroparticle Physics*, vol. 91, pp. 15–21, 2017. DOI: 10.1016/j.astropartphys.2017.03.003.

[7] O. Schulz *et al.*, "BAT.jl: A Julia-Based Tool for Bayesian Inference," *SN Computer Science*, vol. 2, no. 3, p. 210, 2021. DOI: 10.1007/s42979-021-00626-4.

[8] L. S. Song *et al.*, "Nuclear matrix element of neutrinoless double-β decay: Relativity and short-range correlations," *Phys. Rev. C*, vol. 95, p. 024 305, 2 2017. DOI: 10.1103/PhysRevC.95.024305.

[9] L. Coraggio *et al.*, "Calculation of the neutrinoless double-β decay matrix element within the realistic shell model," *Physical Review C*, vol. 101, no. 4, p. 044 315, 2020. DOI: 10.1103/physrevc.101.044315.

[10] S. Abe *et al.*, "First Search for the Majorana Nature of Neutrinos in the Inverted Mass Ordering Region with KamLAND-Zen," *arXiv*, 2022. DOI: https://doi.org/10.48550/arXiv.2203.02139.

[11] D. Q. Adams *et al.*, "Improved Limit on Neutrinoless Double-Beta Decay in ^{130}Te with CUORE," *Physical Review Letters*, vol. 124, no. 12, p. 122 501, 2020. DOI: 10.1103/physrevlett.124.122501.

[12] G. Anton *et al.*, "Search for Neutrinoless Double-β Decay with the Complete EXO-200 Dataset," *Physical Review Letters*, vol. 123, no. 16, p. 161 802, 2019. DOI: 10.1103/physrevlett.123.161802.

SYNOPSIS

9 | CONCLUSIONS AND OUTLOOK

This dissertation has been conducted in the framework of the GERDA and LEGEND experiments, in the search for the neutrinoless double beta decay ($0\nu\beta\beta$) of ^{76}Ge.

The baseline detector design for LEGEND is the inverted coaxial (IC) geometry. These detectors have the same electrode structure as the broad energy germanium (BEGe) detectors of GERDA, but have masses which are a factor 3 higher. This gives a similar factor in the reduction of the dead material (cables, holders, electronics) deployed in the setup to instrument the detectors, which is a known source of background. The benchmarking of this geometry has been the goal of the present work.

In the first part of the dissertation a detailed modeling of the signal formation in IC detectors has been presented. The long drift paths of charge carriers in this geometry led to the observation of previously unnoticed effects on the pulse shape. These have been attributed with the present work to the collective motion of the charge carriers during the drift to the electrodes. Collective motion includes random thermal scattering, Coulomb self-repulsion and acceleration. It has been observed that their combination leads to non-linear effects on the size of the cluster of charge carriers, which ultimately determines the rate at which they are collected at the electrodes. Although this has the effect of blurring some features on the pulse shape, it nevertheless does not compromise the signal and background discrimination performance of IC detectors. The work on this topic has been published in [1].

With the information from the signal formation, the impact of different event topologies on the pulse shape has also been investigated. This allowed to study the discrimination efficiency of $0\nu\beta\beta$-like events at different energies and to evaluate possible biases of the standard calibration procedures. A custom-produced ^{56}Co source was used to corroborate the results of these simulations with experimental data. Nothwithstanding the practical difficulties of its use, its employment in the second stage of LEGEND is also proposed as an additional calibration source. This part of the work has been submitted for publication in [2].

The second part of the dissertation was dedicated to the experimental characterization of IC detectors. An IC prototype has been custom designed and produced in collaboration with an industrial partner. Its performances in terms of energy resolution, charge collection efficiency and pulse shape dis-

crimination (PSD) have been extensively investigated at TUM using γ-rays with energies between 60 keV and 3.6 MeV. The detector has demonstrated excellent performance in all the investigated fields. The effects of the collective motion of charge carriers on the pulse shape have been thoroughly evaluated with this prototype, which has been an important benchmark for the correct interpretation of the phenomenon. After the characterization campaign, the detector has been deployed in a custom setup for the deposition (still in progress) of a ^{210}Po layer on the surface of the p^+ electrode. This will allow to study the detector response to α-decays and, possibly, to determine their rejection efficiency with unprecedentedly high statistics.

Corroborated by the positive results from the characterization campaign of the prototype, five IC detectors of $\sim$2 kg each have been produced out of material enriched to 88% in ^{76}Ge. They have been characterized inside the vendor's cryostat in the HADES underground laboratory and confirmed the excellent performance of the prototype, fulfilling the requirements for Legend. As a final benchmark of the IC geometry for the Legend experiment, they have been deployed in the Gerda apparatus for long term operation in LAr. Four out of five detectors showed very stable operation both in terms of the energy scale and PSD. One IC could not be operated above depletion due to hardware issues not related to the HPGe detectors. Overall, in 14 months of operation, IC detectors collected an exposure of 8.5 kg · yr, i.e. 8.2% of the total exposure of Gerda Phase II. With a background index of $(4.9^{+7.3}_{-3.4}) \cdot 10^{-4}$ cts/(keV · kg · yr), IC detectors contributed to achieve the background-free regime for the full duration of the data taking of Gerda Phase II. This allowed the experiment to set the limit on the half-life of $0\nu\beta\beta$ in ^{76}Ge to $T^{0\nu\beta\beta}_{1/2} > 1.8 \cdot 10^{26}$ yr at 90% C.L., which is one of the strongest constraints for the process. Part of the contents of this section have been published in [3]. The author of this dissertation also gave a significant contribution to the results published in [4].

IC detectors have been extensively modeled and experimentally characterized. They proved excellent performances in all the investigated fields, and showed stable operation in LAr. The results of this dissertation contributed significantly to a deep understanding of their response to radiation, and strongly corroborated the hypothesis of adopting them as baseline detector design for Legend. Building on this knowledge, $\sim$100 kg of enriched IC detectors have been produced for deployment in the Legend experiment, which is being commissioned at LNGS at the time of writing.

REFERENCES

[1] T. Comellato, M. Agostini, and S. Schönert, "Charge-carrier collective motion in germanium detectors for ββ-decay searches," *The European Physical Journal C*, vol. 81, no. 1, p. 76, 2021. DOI: 10.1140/epjc/s10052-021-08889-0.

[2] T. Comellato, M. Agostini, and S. Schönert, "Topologies of ^{76}Ge 0νββ-decay events and calibration procedure biases," *Ready for submission*, 2022.

[3] T. Comellato *et al.*, "Performance of custom designed inverted coaxial HPGe detectors for GERDA and LEGEND," *Nuclear Instruments and Methods in Physics Research Section A: Accelerators, Spectrometers, Detectors and Associated Equipment*, vol. 936, pp. 247–248, 2018. DOI: 10.1016/j.nima.2018.10.042.

[4] M. Agostini *et al.*, "Characterization of inverted coaxial ^{76}Ge detectors in GERDA for future double-β decay experiments," *The European Physical Journal C*, vol. 81, no. 6, p. 505, 2021. DOI: 10.1140/epjc/s10052-021-09184-8.

APPENDICES

A | DETAILS ON SIMULATIONS

This section deals with the technical details of the simulations carried out for this dissertation. The physics model for $0\nu\beta\beta$ and ^{208}Tl decays has been simulated within the MaGe software framework [1], while the generation of signals in germanium detectors has been simulated using the `SigGen` software [2].

A.1 MONTE CARLO SIMULATIONS

The Monte Carlo simulations have been performed using the MaGe software, a GEANT4 based framework oriented to low background experiments. MaGe gives the opportunity to select the track precision of the simulated particles, by choosing what is called the *realm*. For this work, we used the *DarkMatter* realm, in which the precision for gamma-rays and $e^{\pm}$ are 5 μm and 0.5 μm, respectively. For a germanium detector, this means that every energy deposition of $\mathcal{O}(1)$ keV is stored as a hit.

Additionally to what explicitly mentioned in Chapter 3 and Chapter 4, we also simulated a collimated ^{241}Am source shining on the side of the detector at different heights. The low energy (59.5 keV) gammas from it have been selected as samples of known and localized interaction position. The comparison of this dataset with analogous experimental data has been used to tune the physics parameters of the detector in `SigGen`.

A.2 PULSE SHAPE SIMULATIONS

`SigGen` is a software tool to simulate signals from germanium detectors. The signal generation consists of two parts: the first one, called *fieldgen*, calculates the electric and weighting field of a given geometrical configuration. The second part, *siggen*, simulates the signals generated by the drifting charges in the detector field.

For this work, the fields from *fieldgen* are simulated on a 0.1 mm grid, and the signals fom *siggen* are generated on a time step of 0.1 ns. The crystal properties, such as the temperature and the impurity profile, are tuned using the combination of Monte Carlo and experimental data with a ^{241}Am source.

The output of MaGe is a list of hits which constitute an event. In order to build the event-waveform (e.g. a $0\nu\beta\beta$ waveform), we generate signals for every hit and sum them all up, each with a weight corresponding to the energy deposited in the hit. The waveform obtained in this way, however, does not yet include the collective effects discussed in Chapter 3, as every hit is processed separately. In order to take them into account, two steps more are needed. The first is to use the position of the first energy deposition to calculate the associated time spread of the cluster, σ_τ. The second step is to convolute the event-waveform with a gaussian function of with σ_τ.

Before the analysis, every waveform goes through the electronics response function developed by [3], whose parameters are again tuned using the combination of Monte Carlo and experimental data with a ^{241}Am source. Furthermore, electronics noise, taken from our experimental setup, is added on top of the electronics processed waveform.

The relevant parameters for the analysis are calculated from differently processed waveforms. The rise time is extracted directly from the waveforms with noise, while the A parameter has been calculated after applying 5 times a moving window average of 100 ns width. Finally, the energy E, given by Monte Carlo, has been smeared using a gaussian function whose width σ_E has been inferred from the experimental resolution curve.

For a comparison with data, the standard GERDA analysis [4, 5] has been carried out for both simulated and experimental data.

REFERENCES

[1] M. Boswell *et al.*, "MaGe-a Geant4-Based Monte Carlo Application Framework for Low-Background Germanium Experiments," *IEEE Transactions on Nuclear Science*, vol. 58, no. 3, pp. 1212–1220, 2011. DOI: 10.1109/tns.2011.2144619.

[2] D. C. Radford, *fieldgen and siggen software*, 2014. [Online]. Available: https://github.com/radforddc/icpc%5C_siggen.

[3] K. Panas, "Development of Pulse Shape Discrimination Methods as Tools for Background Suppression in High Purity Germanium Detectors used in the GERDA Experiment," Ph.D. dissertation, 2018.

[4] M. Agostini *et al.*, "GELATIO: a general framework for modular digital analysis of high-purity Ge detector signals," *Journal of Instrumentation*, vol. 6, no. 08, P08013–P08013, 2011. DOI: 10.1088/1748-0221/6/08/p08013.

[5]   M. Agostini *et al.*, "Pulse shape analysis in GERDA Phase II," *The European Physical Journal C*, vol. 82, no. 4, p. 284, 2022. DOI: `10.1140/epjc/s10052-022-10163-w`.

B | CHARACTERIZATION OF ENRICHED INVERTED COAXIAL DETECTORS

This Appendix completes the characterization described in Chapter 6 with the results of the surface scan and of PSA for the remaining four IC detectors: IC48A, IC48B, IC50B and IC74A.

B.1 PULSE SHAPE DISCRIMINATION PERFORMANCES

The PSD performances from the flood top scan with ^{228}Th are found in Table 6.6; those from the flood side scan are reported in Table 6.5 for detector IC50A and in the following for IC48A, IC48B, IC50B and IC74A. All detectors feature excellent PSD performances, in all experimental configurations, for every analysis method investigated.

	Side					
Event class	*Standard*		*Corrected*		*Split*	
^{208}Tl DEP	90	(2)	90	(2)	90	(2)
^{208}Tl SEP	6.8	(3)	6.5	(3)	6.0	(3)
^{208}Tl FEP	9.25	(8)	8.86	(8)	8.52	(8)
^{212}Bi FEP	10.0	(6)	9.6	(6)	9.2	(6)
CC @Q$_{\beta\beta}$	34.1	(6)	33.9	(6)	33.5	(6)

Table B.1: Survival probabilities for the flood lateral measurement of IC48A with ^{228}Th.

	Side					
Event class	*Standard*		*Corrected*		*Split*	
^{208}Tl DEP	90	(2)	90	(2)	90	(2)
^{208}Tl SEP	5.5	(3)	5.4	(3)	5.6	(3)
^{208}Tl FEP	8.64	(7)	8.23	(7)	8.08	(7)
^{212}Bi FEP	8.3	(4)	7.7	(4)	8.0	(4)
CC @Q$_{\beta\beta}$	35.2	(5)	35.1	(5)	35.9	(5)

Table B.2: Survival probabilities for the flood lateral measurement of IC48B with ^{228}Th.

	Side					
Event class	Standard		Corrected		Split	
^{208}Tl DEP	90	(1)	90	(1)	90	(1)
^{208}Tl SEP	6.6	(3)	6.2	(3)	6.3	(3)
^{208}Tl FEP	9.08	(6)	9.50	(6)	8.47	(6)
^{212}Bi FEP	8.9	(3)	8.4	(3)	9.4	(3)
CC @Q$_{\beta\beta}$	36.5	(5)	36.4	(5)	37.6	(5)

Table B.3: Survival probabilities for the flood lateral measurement of IC50B with ^{228}Th.

	Side					
Event class	Standard		Corrected		Split	
^{208}Tl DEP	90	(1)	90	(1)	90	(1)
^{208}Tl SEP	6.8	(3)	6.2	(3)	6.9	(3)
^{208}Tl FEP	-	-	-	-	-	-
^{212}Bi FEP	10.0	(4)	9.4	(4)	10.6	(4)
CC @Q$_{\beta\beta}$	34.6	(4)	33.4	(4)	35.9	(4)

Table B.4: Survival probabilities for the flood lateral measurement of IC74A with ^{228}Th.

B.2 PULSE SHAPE POSITION DEPENDENCE

The flood and collimated measurements with ^{228}Th, as described in Section 6.3.1, were used to investigate the dependence of the pulse shape on the interaction position. All detectors showed the transition of events from the *Short* to *Long* population for increasing Z-position of the interaction.

B.3 SURFACE RESPONSE HOMOGENEITY

The surface response homogeneity has been investigated with an ^{241}Am source. The results of the scan for detector IC50A are in Figure 6.6; those for IC48A, IC48B and IC74A are presented here. Due to time constraints, the scan of the top surface of detector IC48A and the full scan of detector IC50B have not been carried out. Except small instabilities in the electronics, all detectors exhibit the same feature described in Section 6.2.4.
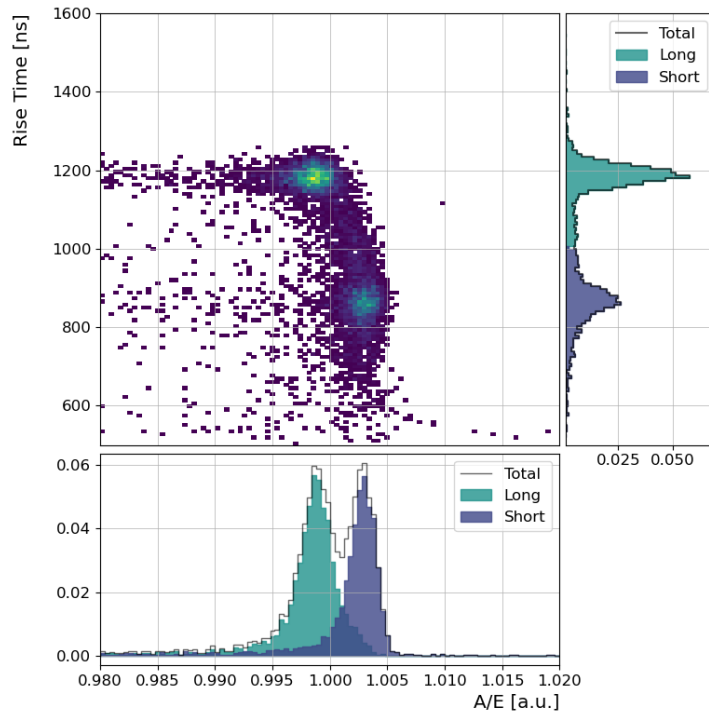
Figure B.1: Experimental correlation of A/E on the rise time for DEP events from a flood irradiation with ^{228}Th of the lateral surface of IC48A.
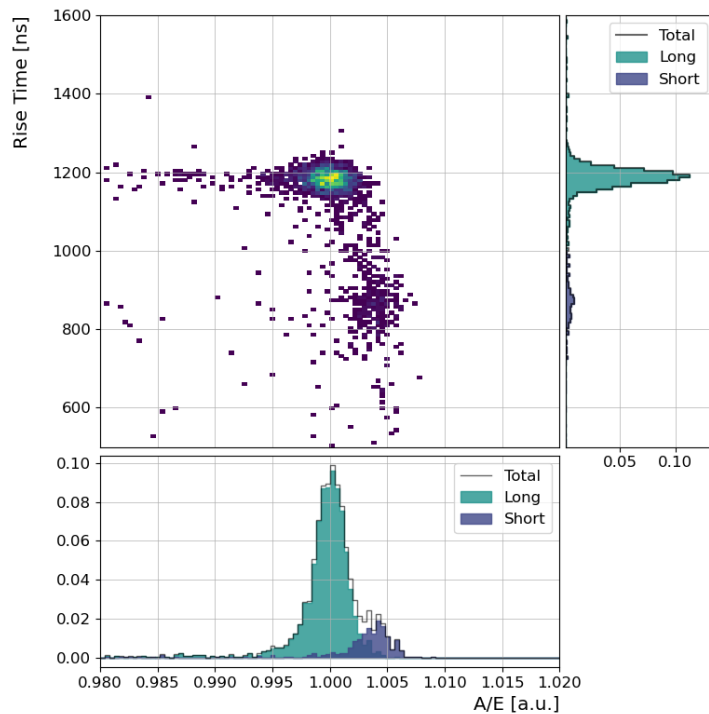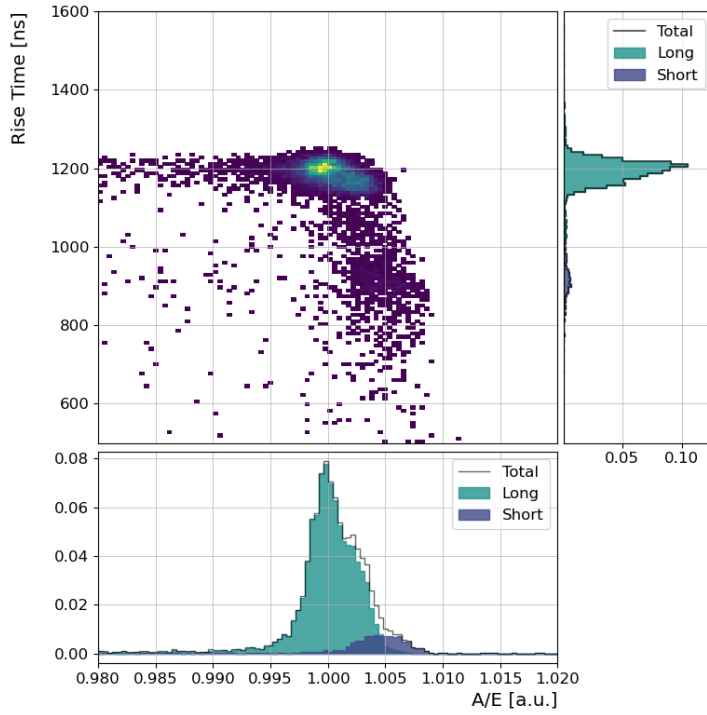

Figure B.2: Experimental correlation of A/E on the rise time for DEP events from a flood irradiation with ^{228}Th of the top surface of IC48A.
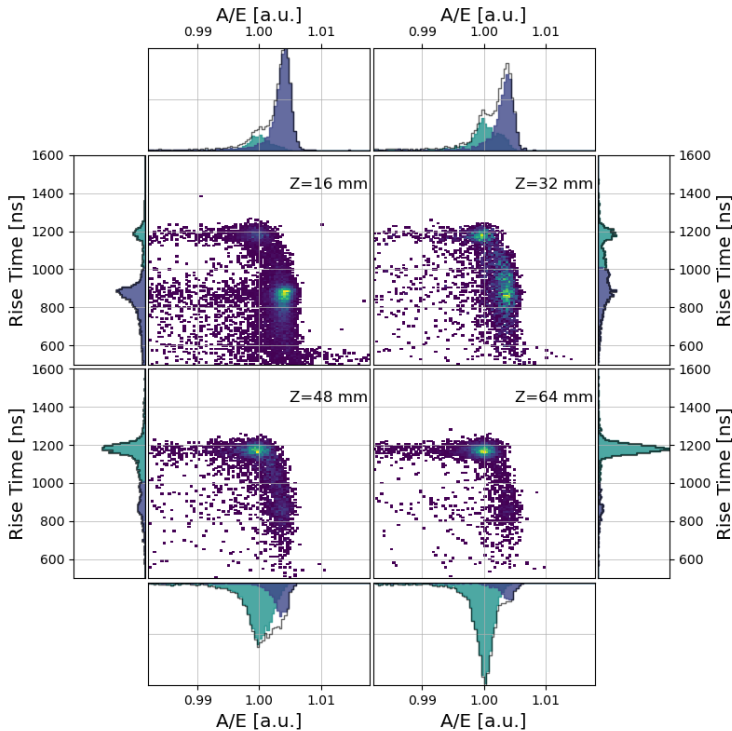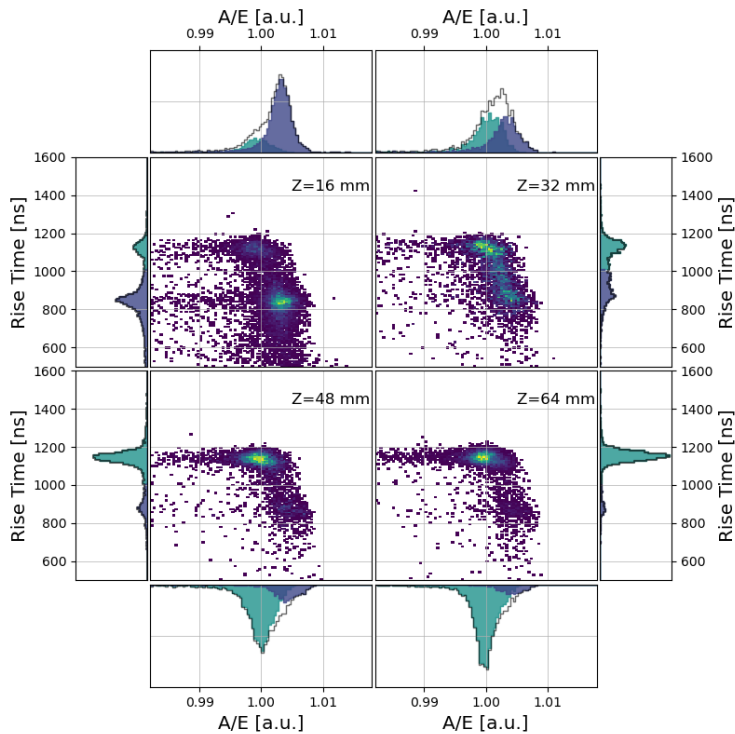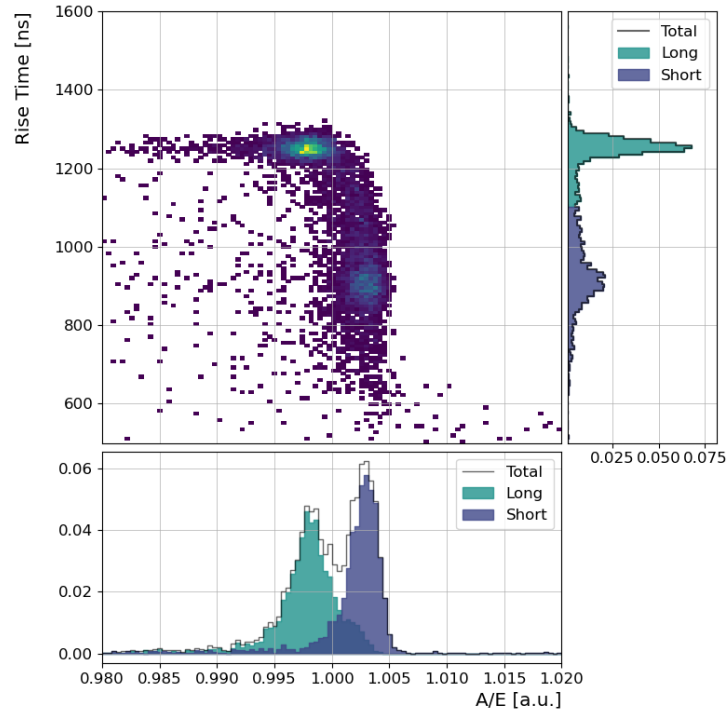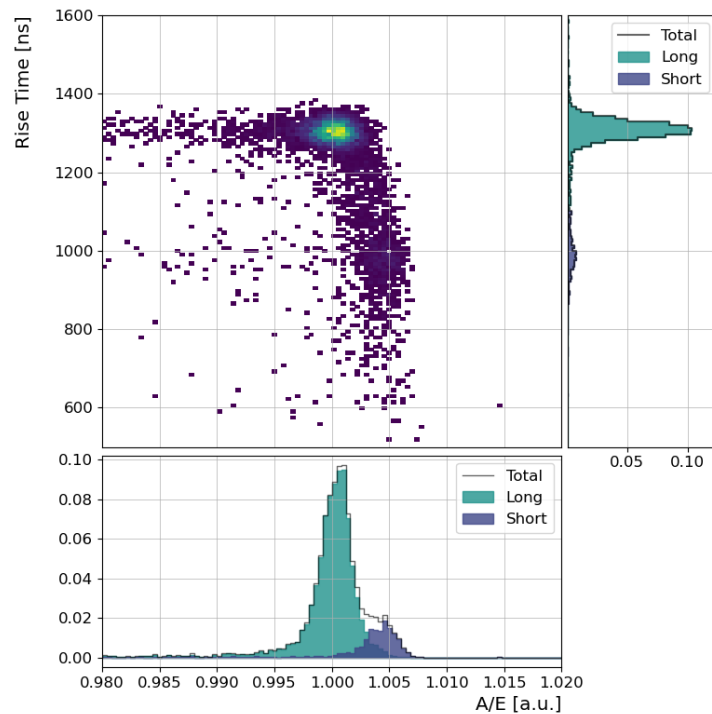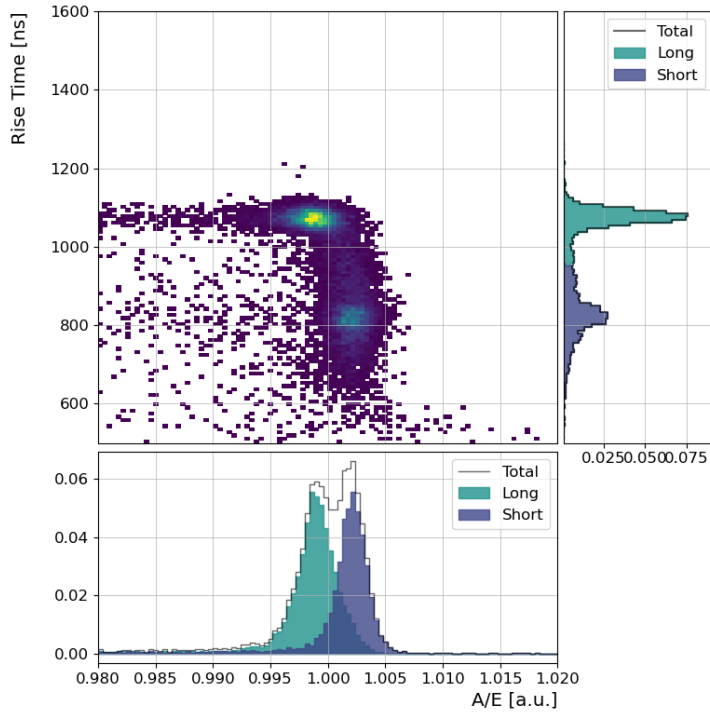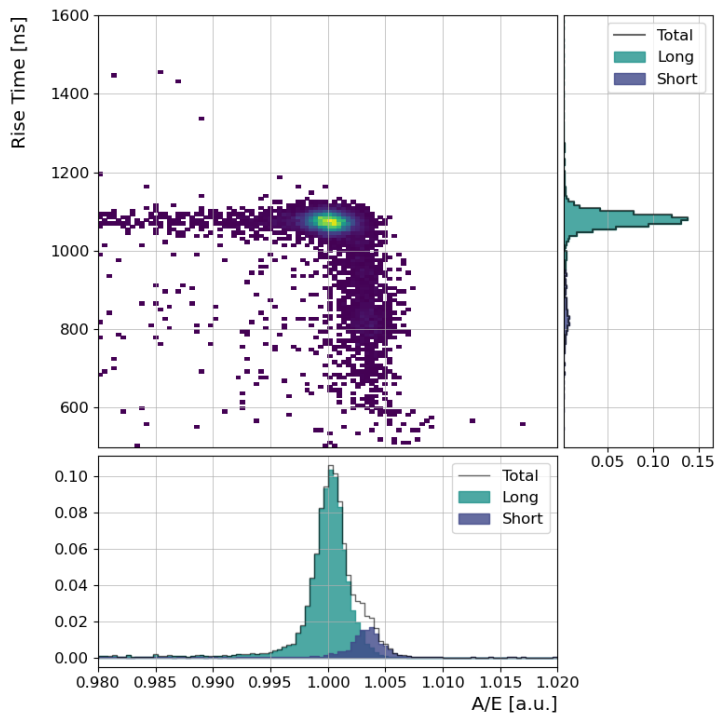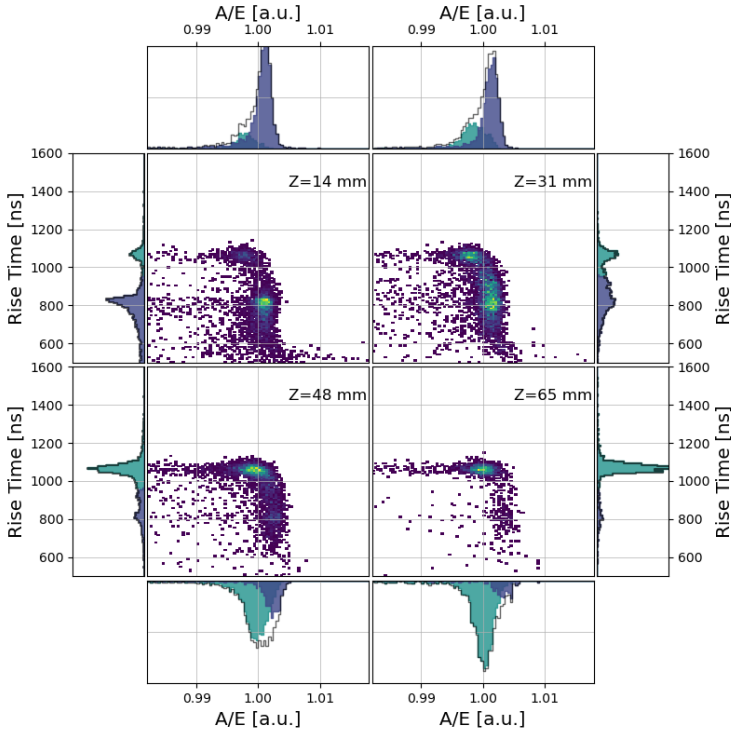
Figure B.3: Experimental correlation of A/E on the rise time for DEP events from a collimated scan with ^{228}Th of the lateral surface of IC48A.
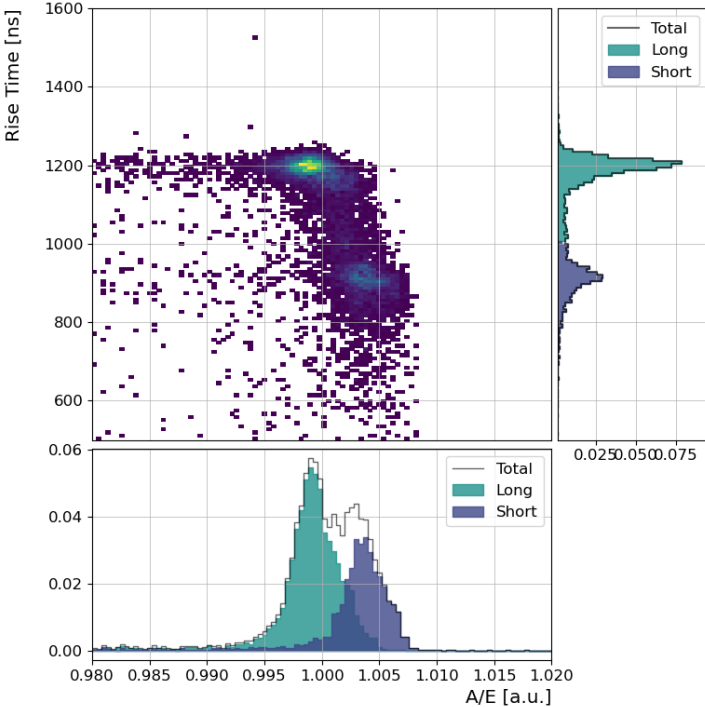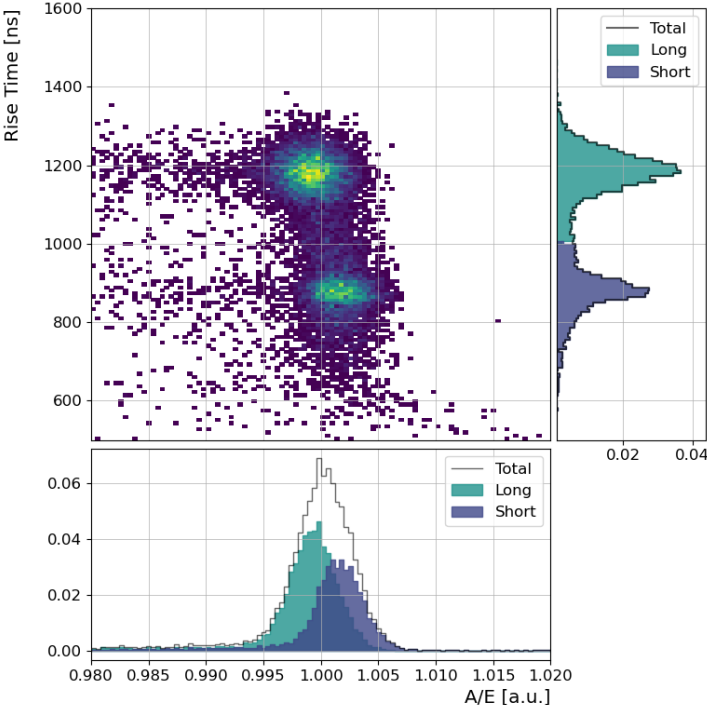

Figure B.4: Experimental correlation of A/E on the rise time for DEP events from a flood irradiation with ^{228}Th of the lateral surface of IC48B.
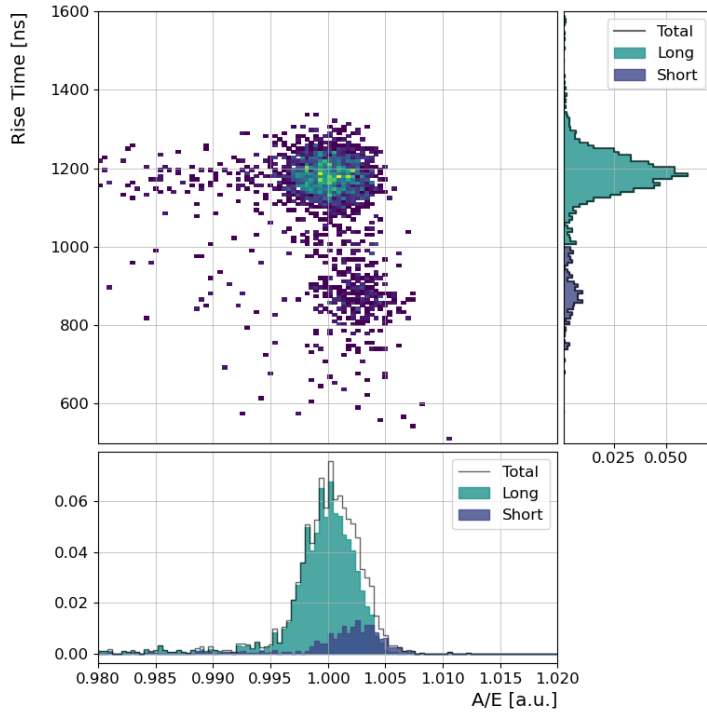
Figure B.5: Experimental correlation of A/E on the rise time for DEP events from a flood irradiation with ^{228}Th of the top surface of IC48B.

Figure B.6: Experimental correlation of A/E on the rise time for DEP events from a collimated scan with ^{228}Th of the lateral surface of IC48B.

Figure B.7: Experimental correlation of A/E on the rise time for DEP events from a flood irradiation with ^{228}Th of the lateral surface of IC50A.

Figure B.8: Experimental correlation of A/E on the rise time for DEP events from a flood irradiation with ^{228}Th of the top surface of IC50A.
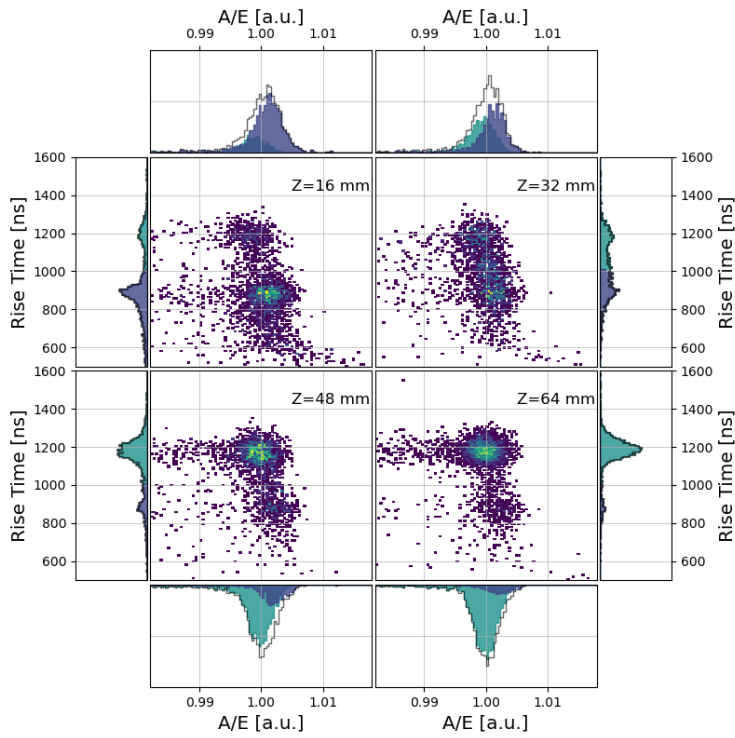
Figure B.9: Experimental correlation of A/E on the rise time for DEP events from a flood irradiation with ^{228}Th of the lateral surface of IC50B.

Figure B.10: Experimental correlation of A/E on the rise time for DEP events from a flood irradiation with ^{228}Th of the top surface of IC50B.

Figure B.11: Experimental correlation of A/E on the rise time for DEP events from a collimated scan with ^{228}Th of the lateral surface of IC50B.

Figure B.12: Experimental correlation of A/E on the rise time for DEP events from a flood irradiation with ^{228}Th of the lateral surface of IC74A.

Figure B.13: Experimental correlation of A/E on the rise time for DEP events from a flood irradiation with ^{228}Th of the top surface of IC74A.

Figure B.14: Experimental correlation of A/E on the rise time for DEP events from a collimated scan with ^{228}Th of the lateral surface of IC74A.
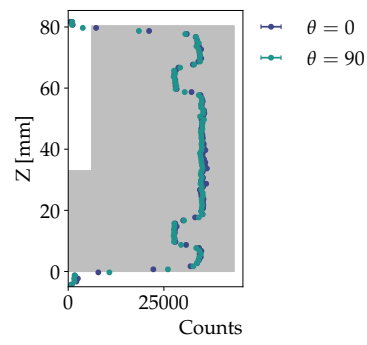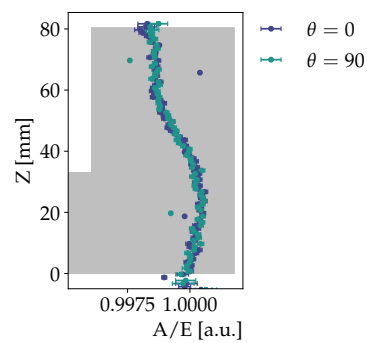
(a)
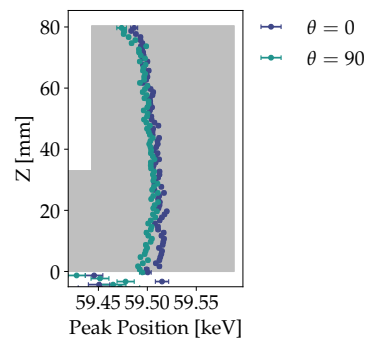
(b)
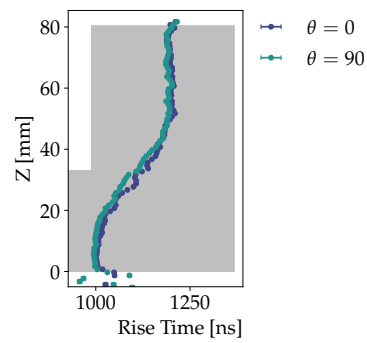
(c)

(d)

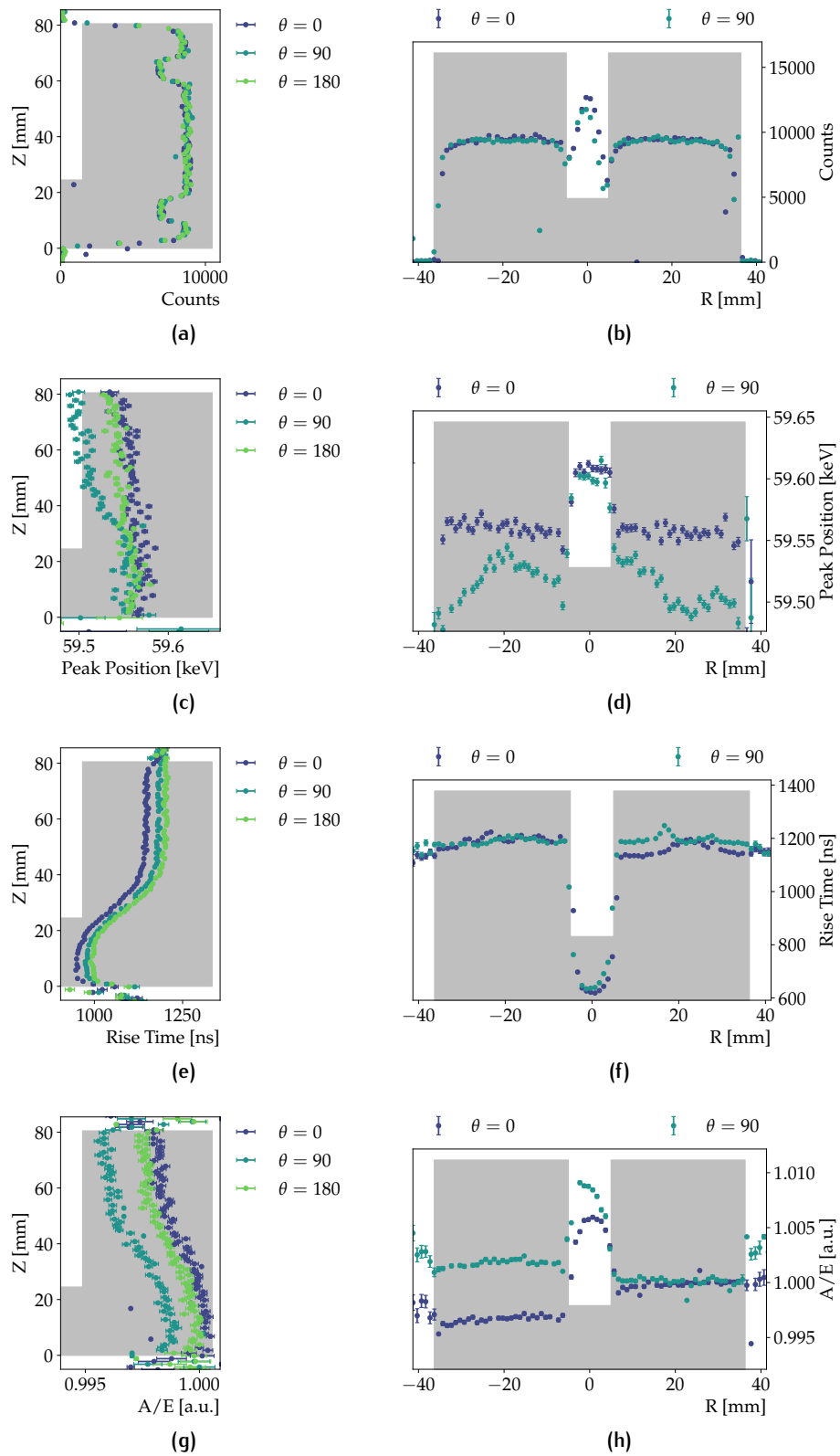**Figure B.15:** Results of the side longitudinal scan of IC48A for the 60 keV γ from ^{241}Am.

Figure B.16: Results of the side longitudinal (left) and top radial (right) scan of IC48B for the 60 keV γ from ^{241}Am.
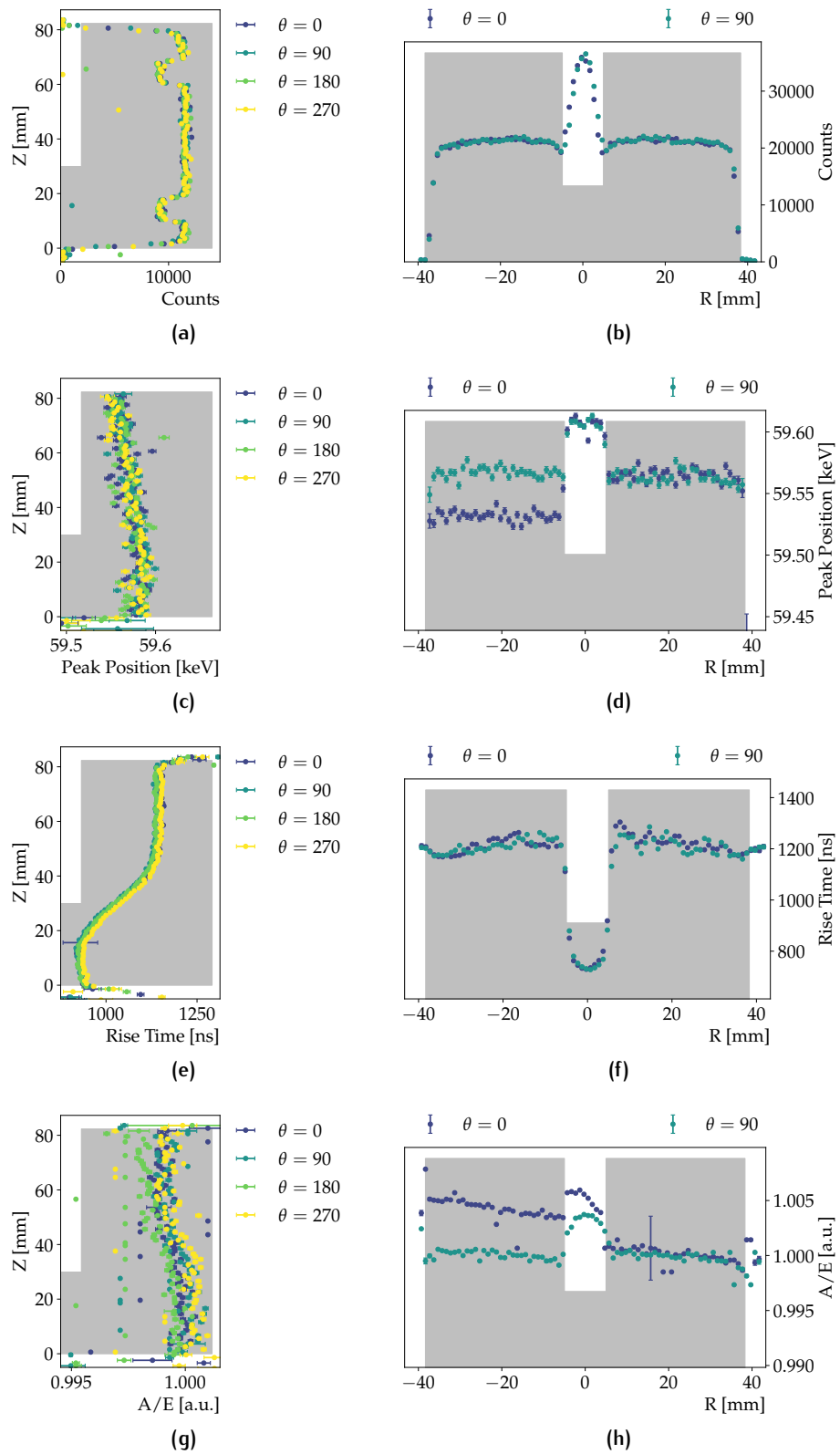
(a)

(b)

(c)

(d)

(e)

(f)

(g)

(h)

Figure B.17: Results of the side longitudinal (left) and top radial (right) scan of IC74A for the 60 keV γ from ^{241}Am.